Phenomenological implication of particle dark matter models

A thesis submitted in partial fulfillment of
the requirements for the degree of

Doctor of Philosophy

by

Sudipta Show

(Roll No. 17330033)

Under the guidance of

Dr. Partha Konar

Professor

Theoretical Physics Division

Physical Research Laboratory, Ahmedabad, India.

DEPARTMENT OF PHYSICS

INDIAN INSTITUTE OF TECHNOLOGY GANDHINAGAR

2022

Dedicated to
my family & teachers

Declaration

I declare that this written submission represents my ideas in my own words and where others' ideas or words have been included, I have adequately cited and referenced the original sources. I also declare that I have adhered to all principles of academic honesty and integrity and have not misrepresented or fabricated or falsified any idea/data/fact/source in my submission. I understand that any violation of the above will be cause for disciplinary action by the Institute and can also evoke penal action from the sources which have thus not been properly cited or from whom proper permission has not been taken when needed.

Sudipta Show
(Roll No: 17330033)

CERTIFICATE

It is certified that the work contained in the thesis titled **"Phenomenological implication of particle dark matter models"** by **Sudipta Show** (17330033), has been carried out under my supervision and that this work has not been submitted elsewhere for a degree. I have read this dissertation and that, in my opinion, it is fully adequate in scope and quality as a dissertation for the degree of Doctor of Philosophy.

Dr. Partha Konar
(Thesis Supervisor)
Professor,
Theoretical Physics Division,
Physical Research Laboratory,
Ahmedabad, India.

Thesis Approval

*

The thesis entitled

Phenomenological implication of particle dark matter models

by

Sudipta Show
(Roll No. 17330033)

is approved for the degree of

Doctor of Philosophy

Examiner	Examiner
Supervisor	Chairman

Date: ________________

Place: ________________

List of Publications

A. Publications included in the thesis :

1. *Linking the pseudo-Dirac dark matter and radiative neutrino mass in a singlet doublet scenario*
   Partha Konar, Ananya Mukherjee, Abhijit Kumar Saha, **Sudipta Show**
   Phys.Rev.D 102 (2020) 015024 [arXiv:2001.11325]

2. *A dark clue to seesaw and leptogenesis in a pseudo-Dirac singlet doublet scenario with (non)standard cosmology*
   Partha Konar, Ananya Mukherjee, Abhijit Kumar Saha, **Sudipta Show**
   JHEP 03 (2021) 044 [arXiv:2007.15608]

3. *Freeze-in Dark Matter Through Forbidden Channel in* $U(1)_{B-L}$
   Partha Konar, Rishav Roshan, **Sudipta Show**
   JCAP 03 (2022) 021 [arXiv:2110.14411]

4. *Self-interacting freeze-in dark matter in a singlet doublet scenario*
   Purusottam Ghosh, Partha Konar, Abhijit Kumar Saha, **Sudipta Show**
   JCAP 10 (2022) 017 [arXiv:2112.09057]

5. *Thermally corrected masses and freeze-in dark matter: a case study*
   Nabarun Chakrabarty, Partha Konar, Rishav Roshan, **Sudipta Show**
   arXiv:2206.02233 (Manuscript under journal review)

Acknowledgements

First and foremost, I want to take this opportunity to express my gratitude to my Ph.D. supervisor Dr. Partha Konar, for his invaluable guidance, encouragement, and support throughout this work. His continuous support and positive attitude about everything in life helped a lot.

I am fortunate to have Dr. J. Selvaganapathy in the initial stage of my Ph.D. Also, I thank all the collaborators from whom I gain a lot during my Ph.D. Firstly I would like to thank my collaborator, Dr. Abhijit Kumar Saha, for introducing me to the area of model building in the early stage of my Ph.D. I thank Dr. Ananya Mukherjee, Dr. Rishav Roshan, Dr. Purusottam Ghosh, and Dr. Nabarun Chakrabarty for collaborating and pursuing exciting physics with me.

I take this opportunity to thank my Doctoral Studies Committee, Prof. Srubabati Goswami, Prof. Hiranmaya Mishra, and Prof. Goutam Kumar Samanta for evaluating my work regularly. Their valuable comments helped me to improve scientific outcomes. I am also grateful to them for the examination of this thesis.

I would like to thank Prof. Subhendra Mohanty, Prof. Dilip Angom, Prof. Jitesh R. Bhatt, Prof. Srubabati Goswami, Prof. Namit Mahajan, and Dr. Ketan Patel for teaching many high-energy physics and cosmology course during and after the course work. I want to thank everyone in my office, my seniors Akanksha, Balbeer, my batch mate Vishal and my junior Anupam, for making the place joyful.

I am obliged to the Indian Institute of Technology, Gandhinagar (IIT Gn), for my Ph.D. registration. It would have been impossible to pass the five years without the joyful company of my dear batch mates Pravin, Ramanuj, Sovan, and all the seniors and juniors in PRL. A special mention of Samiran da, who helped me through challenging times; we have shared some challenging experiences during the pandemic. I thank some of my good friends from school, college, and University days Abinash, Apurba, Ankan, Astik, Krishna, Polash, Pritam, Rahul, Sougata, Sourav, Subhojit, Sukanta, Surajit, Tanmoy, Tufan.

I thank my father, Mr. Sachin Show, my mother, Aparna Show, and brother Saumodeep Show for their constant support, encouragement, love, and care throughout my life. Also, I am fortunate to have Koel Hazra, and her unconditional support helps me overcome different odd situations.

(Sudipta)

Abstract

The standard model of particle physics provides an elegant description of matters and forces of nature as the building block in its most fundamental form. Decades-long theoretical and experimental journey, most of them through immense collaborative efforts from Humanity, finally established a self-consistent theory of particles and their gauge interaction, depicting the strong, weak, and electromagnetic force. An enormous amount of data so far from different collider and celestial experiments measured different parameters of this model very precisely, shaping this model.

Alas, we still firmly believe this only as an effective low every theory - just revealed the tip of the iceberg. A considerable chunk remains imperceivable to us, probably describing a richer dark sector, which constitutes eighty percent of the matter of the Universe. The evidence of dark matter has spread over a wide range of scales, e.g., from the galaxy scale to the cosmological scale, in various experiments. Our standard model cannot provide any clue if it has anything to do with the particles and forces of fundamental nature. There are several other convincing results, such as matter anti-matter asymmetry and the tiny but non-zero neutrino mass, which only strengthens this impression. A fierce hunt for new physics is underway at the present high luminosity run of the Large Hadron Collider. Many exotic theories have been developed to make it work or address some of these puzzles. The present thesis studies some of these well-motivated new physics models winding around different dark matter scenarios.

The first set of analyses explores different extended realizations of the singlet doublet scenario. We start with examining a simple extension of the standard model with a pair of fermions, one singlet, and a doublet in a common thread linking the dark matter problem with the smallness of neutrino masses associated with several exciting features. In the presence of a small bare Majorana mass term, the singlet fermion brings in a pseudo-Dirac dark matter capable of evading the strong spin-independent direct detection bound by suppressing the dark matter annihilation processes mediated by the neutral current. Consequently, the allowed range of a mixing angle between the doublet and the singlet fermions is enhanced substantially. Interestingly, the presence of the same mass term in an association with singlet scalars also elevates tiny but non-zero masses radiatively for light Majorana neutrino satisfying observed oscillation data.

We further extend to study an appealing alternative scenario of leptogenesis assisted by the dark sector, which leads to the measured baryon asymmetry of the Universe. The dark sector carries a non-minimal set-up of singlet doublet

fermionic dark matter extended with copies of a real singlet scalar field. A small Majorana mass term for the singlet dark fermion, in addition to the typical Dirac term, provides the more favorable dark matter of pseudo-Dirac type, capable of escaping the direct search. Such a construction also offers a formidable scope for radiative generation of active neutrino masses. In the presence of a (non)standard thermal history of the Universe, we perform the detailed dark matter phenomenology adopting the suitable benchmark scenarios, consistent with direct detection and neutrino oscillations data. Besides, we have demonstrated that the singlet scalars can go through CP-violating out of equilibrium decay, producing ample lepton asymmetry. Such an asymmetry then gets converted into the observed baryon asymmetry of the Universe through the non-perturbative sphaleron processes owing to the presence of the alternative cosmological background considered here. Unconventional thermal history of the Universe can thus aspire to lend a critical role both in the context of dark matter and in realizing baryogenesis.

In another work, we further discuss the non-thermal production of dark matter in a scalar extended singlet doublet fermion model where the lightest admixture of the fermions constitutes a suitable dark matter candidate. The dark sector is non-minimal with the MeV scale singlet scalar, which is stable in the Universe lifetime and can mediate the self-interaction for the multi-GeV fermion dark matter, mitigating the small-scale structure anomalies of the Universe. If the dark sector is strongly coupled, it undergoes internal dark thermal equilibrium after freeze-in production. We end up with suppressed relic abundance for the fermionic dark matter in a commonly conceived radiation-dominated Universe. In contrast, the presence of a modified cosmological phase in the early era drives the fermionic dark matter to satisfy nearly the whole amount of observed relics. It also turns out that the assumption of an unconventional cosmological history can allow the GeV scale dark matter to be probed at LHC from displaced vertex signature with improved sensitivity.

In our next set of investigations, we probed the importance of thermal effects in dark matter production. To realize the same, we examine a scenario for freeze-in production of dark matter, which occurs due to the large thermal correction to the mass of a decaying mediator particle present in the thermal bath of the early Universe. We show that the decays, which are kinematically forbidden otherwise, can open up at very high temperatures and dominate the dark matter production. We explore such forbidden production of dark matter in the minimal $U(1)_{B-L}$ model, comparing dark matter phenomenology in the context of forbidden frozen-in with the standard picture.

We further investigate a freeze-in production of the dark matter considering the thermal effects in a minimally extended $U(1)_{L_\mu - L_\tau}$ framework that remains consistent with the recent muon $(g-2)$ data. Here, the scalar plays the role of the dark matter with a non-trivial charge under the additional symmetry $U(1)_{L_\mu - L_\tau}$. This scalar dark matter obtains a thermally corrected mass at high temperatures for a not-so-small self-coupling. We show that the thermal correction to the dark matter mass plays a significant role in the dark matter phenomenology.

In this thesis, we explored diverse mainstream paradigms consisting of 'weakly interacting massive particle' (WIMP) and 'feebly interacting massive particle' (FIMP) as dark matter in the context of different models. We also discuss the scope of generating observed neutrino masses and the production of baryon asymmetry via the leptogenesis mechanism. Two important aspects, such as the thermal effects in masses and cosmological evolution in the early Universe, can affect the dark matter evolution. The significance of the same is probed by looking at the subtle footprint it may have left on dark matter phenomenology.

Contents

Chapter 1

Standard Model of Particles and Quest for New Physics

The eternal curiosity of understanding the mysteries of Nature and exploring their relations to the basic building blocks of our Universe directed us into constructing a self-consistent periodic table of fundamental particles. In the course of such development, a series of theoretical formation and experimental verification over the last several decades have delivered us an incredibly successful standard model (SM) [1–4] of particle physics. This model has the potential to explain the interaction and the dynamics of the fundamental forces with the elementary particles. Over the years, the experiments have supported this model by discovering all the fundamental particles.

Although the Standard Model theory is undoubtedly very successful, it suffers from some limitations as it fails to explain dark matter (DM), neutrino mass, matter-antimatter asymmetry, etc. These shortcomings motivate us to study physics beyond the standard model. Now we briefly discuss the Standard model.

1.1 The Standard Model

The Standard Model describes the interaction of all the fundamental particles and three of the four fundamental forces of Nature: the strong force, the weak force, and the electromagnetic force. The SM does not incorporate the gravitational interaction since the quantum description is yet unknown. Moreover, it is much weaker to contribute meaningfully at the subatomic scale when other interactions play a vital role. SM is based on the gauge group $SU(3)_c \times SU(2)_L \times U(1)_Y$, where c, L and Y represent the color, left-handed isospin, and the hypercharge, respectively. The gauge symmetry $SU(3)_c$ dictates the interactions of the strong sector. The weak and the electromagnetic interaction is governed by the gauge group $SU(2)_L \times U(1)_Y$. The particle contents of the SM are listed in Table 1.1. The matter comprises six quarks and six leptons, which are distributed over three generations. Quarks are the multiplets of $SU(3)_c$ where the leptons are singlet under this group. Quarks have strong interaction mediated by the massless gauge boson gluons.

Spin	Nature	Particle	$SU(3)_c \times SU(2)_L \times U(1)_Y$
$\frac{1}{2}$	Quarks	Q_L	(3,2,$\frac{1}{6}$)
		u_R, d_R	(3,1,$\frac{2}{3}$), (3,1,$\frac{1}{3}$)
	Leptons	l_L	(1,2,$-\frac{1}{2}$)
		e_R	(1,1,-1)
1	Gauge Bosons	G^a_μ	(8,1,0)
		W^i_μ, B_μ	(1,3,0), (1,1,0)
0	Scalar	H	(1,2,$\frac{1}{2}$)

Table 1.1: The Standard Model particle spectrum and their charge assignment under the Standard Model gauge symmetry: $SU(3)_c \times SU(2)_L \times U(1)_Y$.

The weak interaction is mediated by the $W^\pm, Z$ where $W^\pm$ is responsible for charge current interaction, and the neutral current interaction involves Z, an admixture of the W^3 and B boson. The massless gauge boson photon (γ) is the force carrier for the electromagnetic interaction. The gauge bosons W and Z acquire masses after the spontaneous symmetry breaking, commonly known as Higgs Mechanism [5–8]. Due to this mechanism, a part of the SM gauge group $SU(2)_L \times U(1)_Y$ is broken to $U(1)_{em}$ while the $SU(c)_c$ remains Unbroken. Here the interaction of the gauge boson with the Higgs boson takes place through the kinetic term of the Higgs boson. The fermions interact with the Higgs via the Yukawa interaction, and they become massive after the symmetry breaking because of this interaction with the Higgs. All the interactions of the SM can be described completely by the following Lagrangian

$$\mathcal{L} = \mathcal{L}_{\text{Matter}} + \mathcal{L}_{\text{Gauge}} + \mathcal{L}_{\text{Scalar}} + \mathcal{L}_{\text{Fermion}} \tag{1.1}$$

1.1.1 Fermion Sector

The matter fields of the SM consist of the fermion fields. All the fermion fields have different charges under different groups, demonstrating the transformation under a particular gauge group. Here, the left-handed fermion fields transform as a doublet, whereas the right-handed one transforms as a singlet under $SU(2)$. The Lagrangian of the fermions can be expressed as

$$\mathcal{L}_{\text{Matter}} = \sum_f i\bar{\psi}_f \not{D} \psi_f \tag{1.2}$$

where $\not{D} = \gamma^\mu D_\mu$ and the covariant derivative of the SM gauge group and has the following structure

$$D_\mu \equiv \partial_\mu + ig_s \frac{\lambda^a}{2} G^a_\mu + ig \frac{\sigma^a}{2} W^a_\mu + ig' Y B_\mu \tag{1.3}$$

Where g_s and g are the gauge coupling constants associated with the groups $SU(3)$ and $SU(2)$ respectively and determine the interaction strengths, the g' represents the coupling constant of $U(1)_Y$. The parameter $\lambda^a(a = 1, 2...8)$ refers to the generators of $SU(3)$ which are known as Gell-Mann matrices, and σ^a are the Pauli matrices which represent the generators of $SU(2)$. Here G^a_μ, W^a_μ and B_μ are the massless field of the gauge groups $SU(3), SU(2)$ and $U(1)_Y$ respectively.

1.1.2 The Gauge Sector

The kinetic terms for the gauge fields are given by

$$\mathcal{L}_{\text{Gauge}} = -\frac{1}{4} G^a_{\mu\nu} G^{\mu\nu a} - \frac{1}{4} W^k_{\mu\nu} W^{\mu\nu k} - \frac{1}{4} B_{\mu\nu} B^{\mu\nu} \tag{1.4}$$

Where $G^a_{\mu\nu}$ and $W^k_{\mu\nu}$ are the field strengths tensor for the vector field of the non-abelian group $SU(3)$ and $SU(2)$ and $B_{\mu\nu}$ represents the same of the abelian group $U(1)_Y$. The field strength tensors have the following definition.

$$G^a_{\mu\nu} = \partial_\mu G^a_\nu - \partial_\nu G^a_\mu - g_s f^{abd} G^b_\mu G^d_\nu \tag{1.5}$$

$$W^k_{\mu\nu} = \partial_\mu W^k_\nu - \partial_\nu W^k_\mu - g\epsilon^{ijk} W^j_\mu W^k_\nu \tag{1.6}$$

$$B_{\mu\nu} = \partial_\mu B_\nu - \partial_\nu B_\mu \tag{1.7}$$

where f^{abd} is the total antisymmetric structure constants for $SU(3)$ with the color indices a, b and d. Also, ϵ^{ijk} is the total antisymmetric structure constants for $SU(2)$ where i, j and k are the generation indices.

1.1.3 Electroweak symmetry breaking and Higgs mechanism

Experimentally, it is observed that the gauge bosons and the fermions of the standard model have finite mass. But, the gauge symmetry does not allow any mass term for the gauge vector bosons. In addition, the presence of exact $SU(2)_L \times U(1)_Y$ symmetry forces the fermions to be massless. So the gauge symmetry must be broken to give masses to the gauge bosons and fermions. This can be done by the elegant mechanism of spontaneous symmetry breaking. To break the symmetry spontaneously, a $SU(2)$ complex scalar doublet is needed,

$$H = \begin{pmatrix} \phi^+ \\ \phi^0 \end{pmatrix} \tag{1.8}$$

Here both the component ϕ^+ and ϕ^0 are complex scalar. The Lagrangian for this scalar multiplet takes the following form

$$\mathcal{L}_{\text{Scalar}} = (D_\mu H)^\dagger (D^\mu H) - V(H) \tag{1.9}$$

Here the first term represents the kinetic term of the scalar, and the second term refers to the Higgs potential and can be expressed as

$$V(H) = -\mu_H^2 H^\dagger H + \lambda_H (H^\dagger H)^2 \tag{1.10}$$

One can obtain a non-zero vacuum expectation value for the Higgs potential

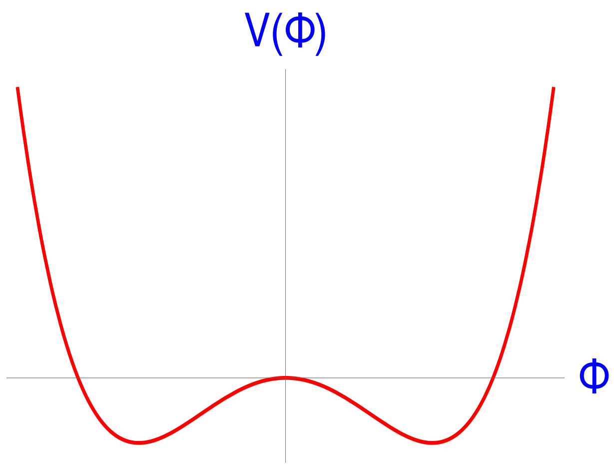

Figure 1.1: Higgs potential for $\mu_\Phi^2 > 0$ and $\lambda_\Phi > 0$.

with $\mu_H^2 > 0$ and $\lambda_H > 0$. The minimum of potential corresponds to

$$\langle H \rangle = \begin{pmatrix} 0 \\ v/\sqrt{2} \end{pmatrix} \tag{1.11}$$

where $\langle H \rangle$ is called the vacuum expectation value and $v = \mu_H/\sqrt{\lambda_H}$. Now the vacuum breaks the symmetry $SU(2)_L \times U(1)_Y$ down to $U(1)_{\text{em}}$, and it is known as spontaneous symmetry breaking. The Higgs field can be expressed in the Unitary gauge as

$$H = \begin{pmatrix} 0 \\ (v + h(x))/\sqrt{2} \end{pmatrix} \tag{1.12}$$

where $h(x)$ is the small perturbation around the minimum of the Higgs potential. The Higgs boson's mass can be calculated by using the Equation 1.10 and Equation 1.12

$$m_h = v\sqrt{2\lambda_H} \tag{1.13}$$

In the year 2012, the Higgs boson is discovered at LHC with the mass of 125 GeV. We know that the Fermi constant fixes the vev to be 246 GeV. Now, utilizing there values along with the Equation 1.13, one can obtain the quartic coupling $\lambda_\Phi = 0.3$.

1.1.4 Mass generation of the gauge bosons

The masses of the gauge boson, $W^\pm, Z$, can be obtained by inserting vev from Equation 1.9 in the kinetic term of the scalar potential.

$$|D_\mu H|^2 = \frac{1}{2}(\partial_\mu h)^2 + \frac{g^2 v^2}{4} W^+ W^- + \frac{v^2}{8}(gW_\mu^3 - g' B_\mu)^2 \tag{1.14}$$

Where $W^\pm = \frac{1}{\sqrt{2}}(W_\mu^1 \mp W_\mu^2)$ and the mass of the charged vector boson can be written as

$$m_W^2 = \frac{1}{4} g^2 v^2 \tag{1.15}$$

One can get the mass term for the neutral gauge boson after using the following relations

$$Z_\mu = \cos\theta_w W_\mu^3 - \sin\theta_w B_\mu \tag{1.16}$$

$$A_\mu = \cos\theta_w W_\mu^3 + \sin\theta_w B_\mu \tag{1.17}$$

Where θ_w represents the weak mixing angle widely known as the Weinberg angle and can be defined as

$$\tan\theta_w = \frac{g'}{g}, \quad \cos\theta_w = \frac{m_W}{m_Z} \tag{1.18}$$

Now, the masses of the neutral gauge boson are given by

$$m_Z^2 = \frac{1}{2}(g^2 + g')^2 v^2 \qquad\qquad m_A^2 = 0 \tag{1.19}$$

The gauge bosons obtain masses after eating up the three goldstone modes of the scalar doublet, while the photon respects the spontaneously broken symmetry by remaining massless. Here, the interaction of the gauge bosons with the Higgs comes from the kinetic terms in Equation 1.9 as

$$D_\mu \equiv \partial_\mu + ig_2\frac{\sigma^a}{2}W_\mu^a + ig_1\frac{I}{2}B_\mu \tag{1.20}$$

In addition, the relative strengths of the charged and the neutral current are encoded in the parameter ρ, which has the following form

$$\rho = \frac{m_W^2}{m_Z^2 \cos\theta_w^2} \tag{1.21}$$

In the SM, the parameter $\rho = 1$ at the tree level.

1.1.5 Yukawa interaction of fermions

SM is a chiral theory, and because of the chiral structure of the weak interaction, the bare mass term for the fermions is not allowed within this model. Here masses of the fermions are generated from the Yukawa interaction with the Higgs field after the Electroweak symmetry breaking (EWSB) when this scalar acquires vacuum expectation value and can be written as

$$-\mathcal{L}_{\text{Yukawa}} = y_u\bar{Q}_L H u_R + y_d\bar{Q}_L\tilde{H}d_R + y_e\bar{l}_L H e_R + h.c., \tag{1.22}$$

where $\tilde{H} = i\sigma^2 H^*$. Here y_u, y_d, and y_e are the Yukawa matrices of the up type quark, down type quark, and charged leptons. It is clear that the masses of the fermions are proportional to the strength of their Yukawa interaction with the Higgs fields and are given by $m_f = \frac{y_f v}{\sqrt{2}}$. It is to be noted that all the masses are given here at tree level.

1.2 Quest for Physics Beyond SM

Despite the remarkable success of the SM so far, it has several shortcomings. Among them, some significant ones include the inability to accommodate particle candidates of dark matter, the non-zero neutrino mass, and the matter-antimatter asymmetry. So the standard model is an effective theory describing the low energy phenomenon. So an extension is needed to accommodate additional new physics phenomena. In this thesis, we extend particle content or gauge group or both to address mainly dark matter along other BSM puzzles.

1.2.1 Dark Matter

One of the pressing puzzles of the standard model is the existence of dark matter. Dark matter can be found in a wide range of astronomical scales in different experiments, from a few kiloparsecs to a large scale, i.e., the whole size of the observable Universe. The observations that have played a vital role in supporting the dark matter presence are the rotation curve, bullet cluster, gravitational lensing, large-scale structure formation, cosmic microwave background (CMB), etc. Interestingly, the study of CMB makes the presence of dark matter very strong and gives some estimation. Dark matter has around twenty-six percent share of the total budget of the energy content of the Universe. In addition, observations establish that eighty percent of the total matter content of the present Universe is in the form of dark matter. The current bound on relic density of dark matter is $\Omega h^2 = 0.1121 \pm 0.0056$. Efforts to detect and probe dark matter from different directions have continued. Despite being the major matter component, we know very little about its composition, mass, interaction, and other properties except for the gravitational interaction, by which all celestial measurements have been made so far. As a result, dark matter remains one of the biggest mysteries of the Universe. If the DM is made of some (yet unknown) fundamental particles in Nature, then the properties of the dark matter are given by

- Dark matter has to be stable or at least have a decay time larger than the present age of the Universe.
- It does not carry any electric charge, i.e., neutral.
- Dark matter is non-interacting means dark matter interaction with itself or interaction with another particle should be very small.
- It is cold, i.e., it was non-relativistic at the time of radiation matter equality when structure formation starts. Non-relativistic matter dictates that the momentum of the dark matter is less than its mass. The velocity of propagation of DM is also very much smaller than the velocity of light.

Several dark matter paradigm exists in the literature depending on the production mechanism and the interaction of dark matter. Among them, the most popular and well-explored one is the Weakly interacting massive particle (WIMP) paradigm. There is also another exciting paradigm alternative to WIMP, which is a feebly interacting massive particle (FIMP) paradigm. The self-interacting dark matter picture has been paid attention to for a few years due to its ability to answer the small-scale problem in cosmology. The next chapter will provide a detailed description of several different aspects of DM.

1.2.2 Neutrino Mass

The neutrinos are the only neutral matter particles of the standard model interacting with matter through weak and gravitational interactions. It is essential to mention that the SM possesses the $B - L$ accidental symmetry where B and L stand for baryon and the lepton number, respectively. This accidental symmetry and the non-existence of a right-handed partner of neutrinos in the SM establish that the neutrinos are massless. There are several compelling neutrino oscillation experiments like KamLand [9], SuperKamiokande [10], K2K [11] etc., which have confirmed the existence of the tiny mass for neutrinos as well as a finite mixing among their different flavors.
Though the exact mass of the neutrinos is still unknown, the cosmological observations such as the study of cosmic microwave background have placed an upper bound on the sum of the masses of the relativistic spices(neutrinos), $\sum_i m_i < 0.12$ eV [12]. Both the oscillation experiment and cosmological observations suggest studying the tiny but non-zero mass of neutrinos. The smallness of Majorana mass of the neutrinos may arise from the higher dimensional effective operators. The most popular one is the dimension five operators of the form $HHl_{L_i}l_{L_j}/\Lambda$ proposed by Weinberg where H and l_{L_i} are the SM Higgs, and the lepton doublet and $i = 1, 2, 3$ is the family index. This non-renormalizable operator has coefficient f_{ij}/Λ suppressed by a mass scale Λ. The Weinberg operator may be realized with three types of tree level seesaw mechanism: type-I requiring the exchange of three RHNs; type-II involves the exchange of triplet scalar; and type-III with the fermion triplet exchange. In addition, there exist several loop mechanisms to achieve the Wienberg operator known as type IV, V, and VI. Since our study involves type-I seesaw and the radiative generation of neutrino mass so will briefly describe these two mechanisms here.

- **Type-I seesaw Mechanism**
  The Type-I seesaw mechanism [13–18] is the most well-known way of generating neutrino mass and addressing their experimentally observed mixing. The smallness of the neutrino mass can be described by the presence of a large energy scale. In this context, the fermion sector of the SM is extended by three right-handed neutrinos ($N_{R_i=1,2,3}$). The following Lagrangian can

describe the masses and interaction of these RHNs

$$-\mathcal{L}^{\text{Type-I}} = Y_{\alpha i}\bar{l}_{L_\alpha}\tilde{H}N_{R_i} + \frac{1}{2}M_{ij}\bar{N}^c_{R_i}N_{R_j} + h.c., \tag{1.23}$$

Where $Y_{\alpha i}$ denotes the matrix of Yukawa coupling for the neutrinos. Here, the bare Majorana mass terms for the RHNs are allowed by the SM gauge symmetry. After the EWSB, the neutrinos acquire Dirac mass (m_D), where $(m_D)_{\alpha i} = \frac{Y_{\alpha i v}}{\sqrt{2}}$. Now the mass matrix of all the neutrinos is given by

$$\mathcal{L}_{\text{mass}} = \begin{pmatrix} \bar{\nu}_L & \bar{N}^c_R \end{pmatrix} \begin{pmatrix} 0 & m_D \\ (m_D)^T & M \end{pmatrix} \begin{pmatrix} \nu^c_L \\ N_R \end{pmatrix} + h.c., \tag{1.24}$$

where ν_L represents the left-handed field of the SM neutrinos and m_D, M both are the 3×3 mass matrices, respectively. After the block diagonalization with the assumption that $m_D \ll M$, one gets the two mass eigenvalues as

$$m_\nu \simeq m_D M^{-1}(m_D)^T \tag{1.25}$$

$$m_{heavy} \simeq M \tag{1.26}$$

One can determine the mass eigenvalues and the mixing of the neutrino by diagonalizing the light neutrino mass matrix as

$$m_\nu = U^*_\nu m^{\text{diag}}_\nu U^\dagger_\nu \tag{1.27}$$

where $m^{\text{diag}}_\nu = diag(m_1, m_2, m_3)$ comprises of mass eigenvalues and U_ν is the PMNS matrix [19]. Here, we are in a basis where the mass and the flavor eigenstates of the charged leptons are identical which manifest that the diagonalizing matrix becomes an identity matrix.

Few other variants of the seesaw mechanism exist in the literature, including Type-II seesaw [18, 20–23], Type-III [23] and Inverse seesaw [24, 25] mechanisms though we are not going to discuss this mechanism in detail. Now we briefly describe the radiative generation of neutrino mass in the upcoming section.

- **Radiative Mass generation of neutrino**

  Several possibilities for the radiative generation of neutrino mass can be found in literature [26–30]. The most popular one is the mass generation in the context of an extended version of the inert Higgs Doublet (IHD) model [31, 32] which is the special case of the so-called two Higgs doublet model [33, 34]. In addition to the IHD, three right-handed neutrinos are added to the model, similar to the Type-I seesaw. In this scenario, an extra discrete symmetry $\mathcal{Z}_2$ is introduced under which all the newly added fields change their sign while all the SM fields transform trivially. Such a charge assignment forbids the usual Yukawa interaction of the heavy neutrinos with the SM leptons and the Higgs. Though the Yukawa interaction of RHNs with the leptons is allowed in the presence of the IHD. The most general renormalizable Lagrangian respecting SM as well as the additional discrete $\mathcal{Z}_2$ symmetry is given by

$$-\mathcal{L}^{\text{Type-I}} = Y_{\alpha i}\bar{l}_{L\alpha}\tilde{\eta}N_{R_i} + \frac{1}{2}M_i\bar{N}^c_{R_i}N_{R_i} + h.c., \tag{1.28}$$

where $\eta = [\eta^{\pm}, (\eta_0 + iA_0)/\sqrt{2}]^T$ refers to the newly introduced scalar $SU(2)$ doublet. The neutral component of this doublet does not acquire any vev since the imposed discrete symmetry is exact. As a result, the neutrinos remain massless at tree level through mass can be generated at one loop as shown in Figure 1.2. The light neutrino mass in this setup can be parametrized as

$$(m_\nu)_{\alpha\beta} = \sum_i \frac{Y_{i\alpha}Y_{i\beta}M_i}{32\pi^2}\left[\frac{m^2_{\eta_0}}{m^2_{\eta_0} - M_i^2}\ln\frac{m_{\eta_0}}{M_i} - \frac{m^2_{A_0}}{m^2_{A_0} - M_i^2}\ln\frac{m_{A_0}}{M_i}\right] \tag{1.29}$$

Where m_{η^0} and m_{A_0} refer to the CP even and CP odd components of the scalar doublet. In this framework, there is a light stable scalar due to the discrete symmetry. This stable particle could be the neutral component of IHD or the lightest RHN, depending on the different parameters present in this model. It is clear that dark matter is coming into the loop to generate neutrino mass radiatively, and because of such involvement of DM, this is popularly known as the scotogenic model [35].

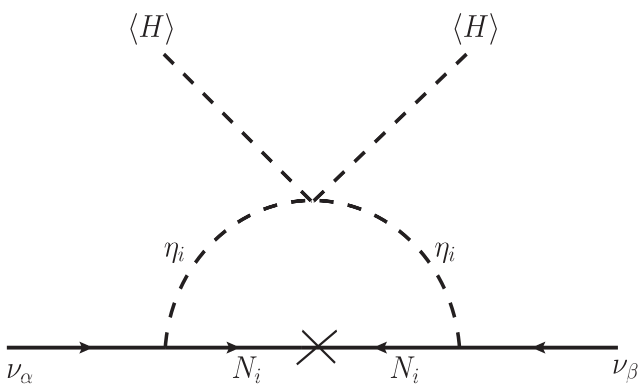

Figure 1.2: Neutrino mass generation at one loop.

1.2.3 Baryon Asymmetry

Now, we pay our attention to another striking puzzle that has bothered cosmologists for some time and whose solution is still speculative. This puzzle is the existence of excess matter over antimatter. It is conventional wisdom to think that the Universe should contain the same amount of baryons and anti-baryons just after the Big Bang. Assuming that they evolved identically, then there is no reason of existing of baryons with such a large amount, whereas the presence of anti-baryons in the Universe is so rare. Although, our standard model of particle physics is unable to give a plausible explanation for this asymmetry. This baryon asymmetry is parametrized by the baryon to photon ratio as,

$$\eta_B = \left.\frac{n_B - n_{\bar{B}}}{n\gamma}\right|_0 \tag{1.30}$$

where the subscripts $n_B, n_{\bar{B}}$ represent the number density of baryons and anti-baryons, respectively, n_γ the number density of photon, and the subscript 0 indicates the value of asymmetry at the present-day value. Due to the baryon-antibaryon annihilation, we do not observe any strong γ ray emission, which suggests the absence of anti-baryons. So one can reasonably consider, $n_{\bar{B}} \approx 0$. However, antimatter can be found in the accelerator and the cosmic ray.
The study of the processes of the big bang nucleosynthesis and cosmic microwave background's anisotropy from WMAP has given us the estimate of the baryon asymmetry of the Universe, and both of them occurred a long time after the production of the asymmetry. The abundance of ^{4}He, D, ^{3}He, and ^{7}Li have been measured from astrophysical observations. Theoretically, it is known how each abundance is crucially dependent on the value of the baryon asymmetry, i.e., the baryon to photon ratio. The 1σ range of this ratio after matching the predicted and the measured value is

$$\eta_{B\mathrm{BBN}} = (5.80 - 6.60) \times 10^{-10} \tag{1.31}$$

One possible way to explain such asymmetry is that the excess of baryon over anti-baryon was generated dynamically with time though the Universe has started as baryon symmetric. Despite the presence of all the ingredients to dynamically generate the asymmetry, the SM of particle physics fails to produce a large amount of asymmetry, as observed by the experiments. Hence, one needs to invoke physics beyond the SM to address the observed asymmetry. There are three necessary conditions for the successful generation of baryon asymmetry proposed by A. Sakharov in 1967 [36]. These conditions are the baryon number (B) violation, C and CP violation, and departure from the thermal equilibrium.

Several new physics possibilities exist in the literature [37–45] which try to explain the excess of matter over antimatter. However, the *Bariogenesis via Leptogenesis* mechanism is the most popular one among them. Here, the lepton asymmetry is generated first, and then this asymmetry is transformed partially to the baryon asymmetry via the non-perturbative sphelaron process.
Bariogenesis via Leptogenesis scenario can be realized in the Type-I seesaw model. Here, the bare mass of the RHNs violates the lepton number. In this context, the Yukawa interaction of neutrino works as a source of CP violation, and if the out-of-equilibrium decays of RHNs to the SM lepton doublet and the SM Higgs have occurred, then all the Sakharov conditions can be satisfied naturally.
The main idea behind the thermal leptogenesis [37, 46–51] is the following. Here, the heavy RHNs are produced thermally in the early Universe. Due to the Universe's expansion, when the temperature of the Universe falls below the mass of the RHNs, then the heavy RHNs decay out of equilibrium to generate asymmetry in the visible sector. The total decay width is given by

$$\Gamma_{N_i} \simeq \sum_\alpha \Gamma(N_i \to l_{L_\alpha} + H) + \sum_\alpha \Gamma(N_i \to \bar{l}_{L_\alpha} + \bar{H}) = \frac{(Y^\dagger Y)_{ii}}{8\pi} M_i \tag{1.32}$$

Where decay of particle, as well as decay of anti-particle, are considered. Now, the CP asymmetry ϵ_i can be expressed as

$$\epsilon_i = \sum_\alpha \frac{\Gamma(N_i \to l_{L_\alpha} + H) - \Gamma(N_i \to \bar{l}_{L_\alpha} + \bar{H})}{\Gamma(N_i \to l_{L_\alpha} + H) + \Gamma(N_i \to \bar{l}_{L_\alpha} + \bar{H})} \tag{1.33}$$

One needs to take the decay width of RHNs at tree and one-loop levels to produce CP asymmetry. The interference of the tree level and the loop level decay amplitudes generate the CP violation. The tree-level and one-loop level Feynman diagrams of the RHNs decay have been shown in Figure 1.3. However, the decays of all three RHNs can generate CP asymmetry. Here the asymmetry is only generated by the lightest RHN under the assumption that RHNs maintain the following mass hierarchy $M_1 < M_2 < M_3$. The rapid lepton number violating interaction of the lightest RHNs washes out the lepton asymmetry produced by the out-of-equilibrium decay of the other two heavier RHNs since the lightest RHN may remain in thermal equilibrium after the completion of the decay of heavier RHNs. So the production of asymmetry from the decay of the lightest RHN is relevant here. After that, the lepton asymmetry is converted to the baryon asymmetry via the sphaleron process. We have presented the derivation of the Boltzmann equation to calculate the baryon asymmetry in Appendix A.

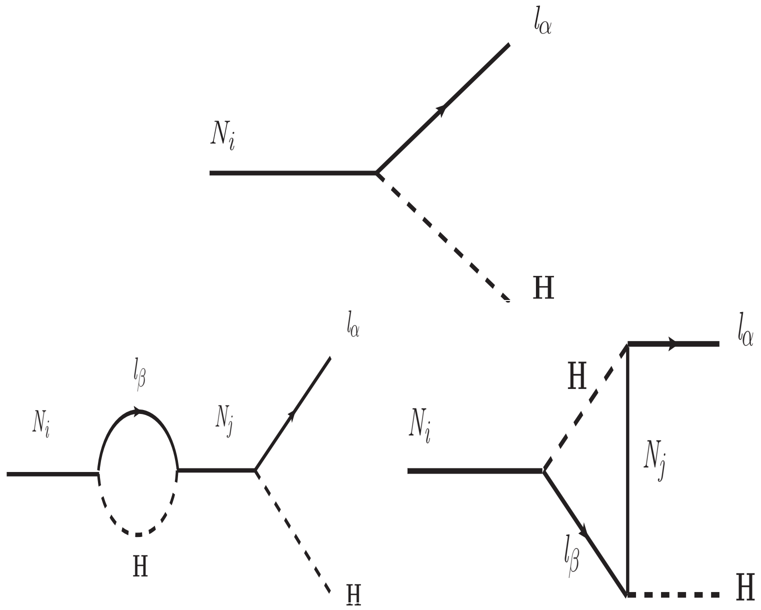

Figure 1.3: Feynman diagrams for the decay of the right-handed neutrinos at the tree and one-loop level.

1.3 Outline of Thesis

One of the interesting areas of research to address the puzzles of the SM is the model building, where the particle contents or/and gauge groups of the SM are extended. We have studied different models for dark matter, while in some contexts, we try to build connections with other BSM aspects like the neutrino mass, leptogenesis, etc., with DM. This compelled the particle physics community to reach a consensus that SM is an effective description of low-energy phenomena so that an embedding extended) theory accommodate additional new physics. In this thesis, we study the new physics associated with dark matter and beyond the Standard Model (BSM) scenario by either including extra particles within the SM gauge group, extending symmetry structure, or using both. Below, we point out the silent features and different aspects based on which the present thesis work was carried out.

- The first aspect explores the WIMP paradigm of dark matter, which is very popular and well studied in the literature. It assumes the thermal equilibrium between the dark matter and the SM particles. Here, the so-called freeze-out mechanism fixed the abundance of dark matter. The null results over the years in the direct detection severely constrain this picture. However, the feeble interaction of dark matter with the bath particles can naturally explain the non-observations of the signals in such experiments. Another exciting alternative to WIMP is FIMP, which assumes feeble interaction of dark matter such that it never gets thermalized with the bath. It gets produced from the decay or the scattering of the bath particle, and the freeze-in mechanism sets its abundance.

- The dark matter production depends on the early history of cosmology since it is occurring in the early Universe. Usually, we do dark matter phenomenology considering the standard cosmological scenario, which dictates that the early Universe was radiation dominated. However, there is no reason to believe that the energy budget of the pre-BBN era of the Universe was dominated by radiation. Interestingly, any deviation from the standard scenario significantly alters the dark matter production, where the final abundance may differ by a few orders. We explore one such possibility of non-standard cosmology where the energy budget is dominated by some other species having a larger redshift than radiation, called a fast-expanding Universe. In addition, Baryogenesis via leptogenesis scenario can also be affected by such modified cosmology since the lepton asymmetry production occurs in the early Universe.

- The primary assumption of the FIMP paradigm is the feeble interaction between the DM and SM particles. However, if present, it does not restrict DM from interacting strongly with other dark sector particles. In such cases, the dark matter abundance is fixed by the freeze-out of the conversion process occurring in the dark sector rather than freeze-in, termed reannihilation. The realization of such an exciting scenario is available in the literature, where the dark sector comprises a fermion dark matter along with a scalar or vector mediator or both. If the fermion dark matter has a significantly large interaction with the light mediator, it can generate considerably large velocity-dependent self-interaction, which can solve the small-scale problem of cosmology.

- So far, we have mentioned several times that dark matter production occurs at a very early time when the temperature is very high. So the consideration of thermal effects is crucial, though it is often overlooked. It has been recently encountered that the dark matter freeze-in production may proceed via a kinematically forbidden decay solely because of significant thermal correction to mass, dubbed as forbidden freeze-in.

Before going to the details of the study conducted, we discuss different observational evidence, different candidates, various search strategies, and the construction of Boltzmann equations to calculate the abundance of dark matter in Chapter 2. We will discuss different aspects of DM and other BSM scenarios in

the upcoming chapters.
The following three chapters explore different extended realizations of the singlet doublet scenario, a well-motivated new physics model accommodating different aspects of dark matters. In Chapter 3, we explore the WIMP scenario of DM in a minimally extended singlet doublet model, where we have found [52] that direct detection severely constrains the singlet doublet mixing angle. Then, we discuss that the small Majorana mass term for the singlet field not only helps in evading the direct detection bound but generating the Majorana mass radiatively in the presence of singlet scalars. The Yukawa interaction among the scalars, the lepton, and the BSM fermion doublet violates the lepton number. In the next chapter (Chapter 4), We discuss the realization of the Baryogenesis via leptogenesis in the same frame where the lepton asymmetry is generated via the decays of the heavy scalars. We have found [53] that the radiation-dominated Universe cannot produce the correct baryon asymmetry because of the huge washout of lepton asymmetry. In contrast, the non-standard cosmology offers to generate an ample amount of asymmetry by significantly reducing the washout.
Chapter 5 explores [54] the reannihilation of dark matter in a singlet scalar singlet-Doubet model where the reannihilation occurs because of the large interaction between the singlet doublet Dirac DM and the scalar mediator. The standard picture of cosmology fails in making the fermion dark matter the main component due to the huge conversion of DM to the scalar. As a result, the scalar dominantly contributes to the relic density as it is a stable particle. Adopting the kination and the faster than kination picture of the non-standard cosmology resolves these issues by suppressing the conversion process significantly. We further demonstrate that the realized parameter space can successfully generate the large velocity-dependent self-interaction in the presence of the MeV scalar mediator.
In our following investigations extended over the following two chapters, we probed the importance of thermal effects in dark matter production. In Chapter 6, we adopt the U_{B-L} model to study the FIMP dark matter where we incorporate thermal correction to the masses [55]. Here, the RHN(lightest one) dark matter and the $B-L$ gauge boson are produced from the decay of the $B-L$ scalar. Here, the $B-L$ scalar develops a sizeable thermal mass at high temperatures. When the mass of the $B-L$ scalar is smaller than both the DM and the $B-L$ gauge boson, both the particles produce via the kinematically forbidden channel because of the thermal effects. Finally, in Chapter 7, we discuss the impact of the thermal effects on the phenomenology of scalar dark matter in the context of the $U_{L_\mu-L_\tau}$ model [56]. Here, all the particles and the dark matter get significant thermal mass corrections. The dark matter production takes place before the

breaking of $L_\mu - L_\tau$ symmetry from the massless gauge boson associated with $U_{L_\mu - L_\tau}$. This framework can potentially address the $(g-2)$ anomaly, and we restrict ourselves to the parameter space for which the $(g-2)$ data is satisfied. It is found that if you want to explain the $(g-2)$ anomaly along with the dark matter where the scalar decays are inefficient, then the only option is the incorporation of thermal effects to produce dark matter, which makes this scenario attractive. Finally, in Chapter 8, we present the summary of this thesis and the future directions of our study.

Chapter 2

Early Universe and Dark Matter

There are unambiguous pieces of evidence pointing out the fact that the baryonic matter constitutes less than five percent of the total energy budget of the Universe, while around twenty-six percent of contribution comes from DM. In Chapter 1, we discuss the SM of fundamental particles, which can only describe a minute portion of the total matter content, and the rest of the part remains mysterious. Now, we try to shed some light on the DM puzzle. In order to carry out the task, it is necessary to discuss, what are the evidences of DM? What is the interaction they possess? What are the dark matter candidates? How to detect such elusive particles? etc. In the following, we will briefly discuss some of these features.

2.1 Observational evidences of dark matter

In this section, we demonstrate the observational evidences for dark matter existence on a wide variety of scales starting from the scale of the smallest galaxies to clusters of galaxies and cosmological scales.

2.1.1 Discovery of missing mass "Dark Matter"

In the early 1930s, the existence of the omnipresent DM was first realized when the Swiss astronomer Fritz Zwicky looked at the movement of several distant galaxies in the Coma cluster, 99 Mpc distance away from the Milky Way [57, 58]. He found that the magnitude of velocities of the galaxies with respect to each other is substantially greater than the velocity arising from the gravitational potential well made by the visible matter alone. This calculation is based on the very well-known theorem called Virial Theorem, which connects the average of total kinetic energy [59, 60], $\langle K \rangle$ to the average potential energy, $\langle V \rangle$ for the system in equilibrium. Assuming that the Coma cluster is comprised of N number of galaxies, the total kinetic energy takes the form

$$\langle K \rangle = \frac{1}{2}\sum_{i=1}^{N} m_i {v_i}^2 = \frac{1}{2}\bar{v}^2 \sum_{i=1}^{N} m_i = \frac{1}{2} M_{tot}\bar{v}^2 \tag{2.1}$$

where $\bar{v}$ is the average velocities of the galaxies, and M_{tot} dictates the total mass of the Coma cluster. Now suppose the fact that the cluster is spherical; the average potential energy can be approximated as

$$\langle V \rangle = -\frac{1}{2}\sum_{i}^{N}\sum_{j>i} \frac{G m_i m_j}{r_{ij}} = -\frac{3}{5}\frac{G M_{tot}^2}{R_{eff}} \tag{2.2}$$

where r_{ij} is the effective distance between any two galaxies and R_{eff} represents the total effective radius of the Coma cluster. Note that, here, the sum is considered for all possible pairs of galaxies. Now plugging the values of $\langle K \rangle$ and $\langle V \rangle$ from Equation 2.1 and Equation 2.2 to the Virial Theorem $2\langle K \rangle + \langle V \rangle = 0$, the expression for the average velocities can be obtained,

$$\bar{v}^2 = \frac{3}{5}\frac{G M_{tot}}{R_{eff}} \tag{2.3}$$

This relationship is a potent tool in estimating the cluster's total mass if the average velocity is known. The observation relied on the total luminosity mass of the Coma cluster is surprising, which shows that the average velocity is much larger than the expected one. This puzzling result can have two possible explanations. One is that the Coma cluster may not be a gravitationally bounded object, and the virial theorem may not be applicable here. According to the luminosity mass observation, this cluster is a system where the kinetic energy is dominated over the potential energy. As a result, all the individual galaxies should be able to escape from the cluster because of the high velocity, and the cluster should not survive. But this interpretation does not support the observations. Another possible solution is that the system maintains virial equilibrium with a much larger gravitational potential containing a considerable amount of different nonluminous matter. Therefore, Zwicky concluded that an enormous amount of invisible matter, which he named "Dark Matter," within the cluster is needed to hold the galaxy cluster together.

2.1.2 Rotation curves

The precise measurement of the rotation curves of spiral galaxies in the 1970s by the astronomers' Vera Cooper Rubin, Kent Ford, and Ken Freeman has played

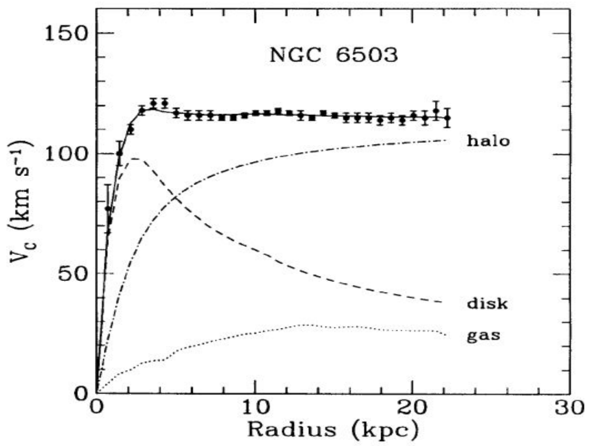

Figure 2.1: Rotation curve for the spiral galaxy NGC 6503 [61] where the solid line represents the observed behavior. Here the dashed, dotted, and dashed-dotted lines stand for the rotation curves for the visible component, gas, and the DM halo, respectively.

a vital role in establishing the existence of dark matter. The rotation curves display the variation of the radial velocity of the stars inside a galaxy with their distance from the galactic center, as shown in Figure 2.1. They have calculated the mass distribution of the Andromeda galaxy M31 with the help of the measured rotational velocities of the galaxies via redshifts. One can easily calculate the mass distribution by using Newton's law. Further, one can obtain the following expression for the rotational velocity,

$$v(r) = \sqrt{\frac{GM(r)}{r}} \tag{2.4}$$

where r is the distance from the center of the galaxy, $M(r)$ represents the mass contained within the distance r, and $v(r)$ is the rotational velocity. The spiral galaxy comprises a dense central bulge and a thin disc as the outer region where most of the visible mass is concentrated in the central part. If we assume that the density is almost constant, then the mass increases since the volume ($\propto r^3$) as we go far from the center for $r \ll R_c$. But for large distances, i.e., $r \gg R_c$ mass becomes independent of distance which one can realize using the Gauss law. Using this information, one can obtain the following velocity behavior with distance for large and small r.

$$v(r) \propto \begin{cases} r & r \ll R_c, \\ r^{-1/2} & r \gg R_c \end{cases} \tag{2.5}$$

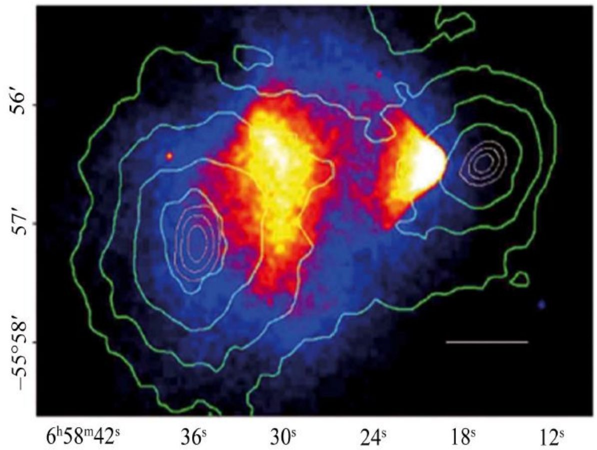

Figure 2.2: Gas distribution of bullet cluster. Image taken from [62].

So, the calculation predicts that the rotational velocity should increase with r as we go far from the center and reach a maximum value. After that, the velocity should fall off, as shown in Figure 2.1. But the observation indicates that the velocity remains almost constant after reaching the maximum. The existence of a considerable amount of invisible mass beyond the boundary of the visible galaxy naturally explains the flatness behavior of the rotation curve at a large distance. Today, hundreds of spiral galaxies have been observed, and all the observations established the exact flatness nature of the rotation curve. So the discrepancy between the observation and the prediction in the rotation curves plays a crucial role in making the dark matter problem much more prominent.

2.1.3 Bullet Cluster

The study of the bullet cluster, comprised of two colliding clusters of galaxies, provides direct evidence supporting the existence of dark matter. In the collision of two clusters, the baryonic matter of the clusters interacts and, as a result, slows down; in contrast, the dark matter passes without experiencing any interaction. The collision of galaxy clusters separates the ordinary and dark matter components. The comparison of the measurement of the total mass with the help of gravitational lensing and the X-ray image taken by Chandra X-ray Observatory marks the separation as shown in Figure 2.2. Using this method, one can also find the locations of both dark matter and ordinary matter. It is also clear from Figure 2.2 that the small clumps of ordinary matter move away from the collision center with smaller velocity than the large clump of dark matter, which manifests the collisionless behavior of the dark matter. If dark matter has any self-interaction, that must be very weak [63].

Figure 2.3: **Left:** Image of the galaxy cluster SDSS J0146-0929 is displaying Einstein's ring due to strong gravitational lensing. **Right:** Image of the galaxy cluster SDSS J1004+4112 showing multiple images of the same quasar around the center. Credit: ESA/Hubble and NASA.

2.1.4 Gravitational Lensing

Gravitational lensing is one very important outcome of the general theory of relativity. According to GTR, the path of the light rays gets deflected when they travel past a massive object, and one can measure the amount of mass of the lensing object. There are different kinds of gravitational lensing depending on the mass of the foreground(lensing) object.

- **Strong Lensing**
  In this context, a massive and dense object is present between the source and the observer, and the light emitted from the source follows several paths in reaching the observer. As a consequence, multiple images of the same physical object can be viewed, as illustrated in the right panel of Figure 2.3. An Einstein ring can be observed when the lensing object is exactly situated on the source-observer axis, and the Einstein radius of the ring is given by

$$\theta_{\mathrm{E}} \simeq \sqrt{\frac{4G_N d_{OS}}{d_O d_S}} \tag{2.6}$$

  Where d_O and d_S are the distance between the observer and the source from the lensing objects, respectively, and d_{OS}, represents the distance between the source and the observer. However, a series of arcs would be observed instead of rings when the location of the object is slightly shifted from the source-observer axis; see the left panel of the Figure 2.3. Since 1980's the strong lensing has been used as an essential tool to measure the masses of the galaxies.

- **Weak Lensing**
  The presence of the gravitational potential generated by some massive object situated near to the line of sight and located between the source and the observer distorts the apparent shape of the luminous source. This effect is termed the weak lensing effect. The source image gets distorted and magnified or sheared due to such effects. Although the average shape of the galaxy is circular, the galaxy looks like an ellipsoid on average due to the shearing effect of the weak lensing. Here, one can reconstruct the gravitational potential along the line of sight by combining the observation of many galaxies. The Sloan Lens ACS Survey utilizes this method to calculate the fraction of the baryonic as well as the DM from large sample galaxies [64]. They have noticed that in a sphere of radius around ~ 8 kpc from the galactic center, the dark matter fraction is almost 27%, which manifests that the baryonic matter dominates the core of the galaxy.
  There is another class of lensing which is called gravitational microlensing [65]. Though it is pretty similar to the strong lensing, the effect is weaker. This effect improves the lens's focus and thereby makes the source object more bright.

2.1.5 Cosmic Microwave Background

The Cosmic microwave background study is a vital tool to probe the cosmology of the early Universe, provides solid proof for the existence of dark matter, and helps determine the amount of dark matter present in the Universe. The CMB is radiation emitted in the early stage of the Universe at the redshifts $z \sim 1100$ around 380000 years after the big bang and travels in all directions. According to our present understanding of cosmology, just after the Big Bang, the Universe was a very hot and dense thermal soup of particles. At that moment, the photons were not free to propagate since Compton scatterings occurred between photons and the baryonic matter. As the Universe grows in size because of the Hubble expansion, it cools down. When the temperature reached the order of the energy needed to bind an electron with the hydrogen nucleus, the formation of Hydrogen atoms started. After that, the Universe became transparent to the photons as it decoupled from the baryon, and it could free stream, and this phenomenon is well known as recombination. Penzias and Wilson accidentally discovered these freely propagating photons for the first time in 1964 at Bell Labs. After the recombination, the range of photons is increased from very short to very large length scales due to the decoupling. The CMB spectrums can be described accurately by a black body distribution function at a temperature different from the tempera-

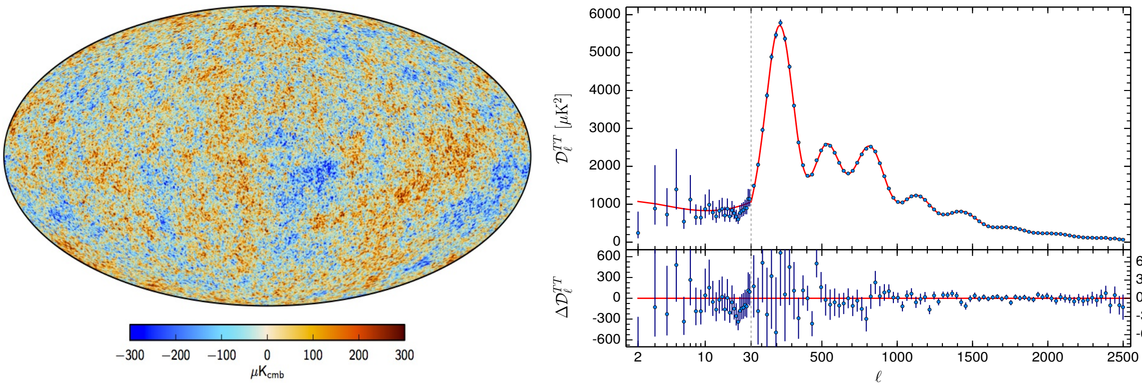

Figure 2.4: **Left Panel:** The full-sky map of the temperature anisotropies of the CMB. **Right Panel:** Blue points are the temperature power spectrum data where the red curve represents the best fit base ΛCDM theoretical spectrum. Images taken form [66]

ture of the matter as the decoupling took place. Though the Universe evolves, the CMB spectrum today can still be described by the black body radiation at a temperature lower than the recombination temperature. Here, the photon's energy is redshifted because of the expansion of the Universe, and we know that temperature is proportional to the energy of the photon. So these photons encode the information about the state of the Universe at the time of the recombination. Therefore, the study of CMB photons helps to obtain the general properties of matter.
CMB is a description of radiation with the perfect black body at temperature $T_0 = 2.725$ K. The anisotropies in the angular distribution of the temperature of the CMB sky have been measured precisely, which can map the presence of under-density and the overdensity in the primordial plasma before the recombination as displayed in the left panel of Figure 2.4. Therefore, one can extract information about the baryon and matter distribution of the Universe by studying the anisotropies in the CMB spectrum. The observed temperature of the CMB as a function of angular position in the sky deviates from the mean value by a tiny amount. So the anisotropies can be characterized by the difference in temperature as

$$\frac{\Delta T}{T}(\theta, \phi) = \frac{T(\theta, \phi) - \bar{T}}{\bar{T}} \tag{2.7}$$

Now one can express this temperature difference as a function of position using the Fourier series in the spherical coordinates, i.e., the spherical harmonics as follows

$$\frac{\delta T}{T}(\theta, \phi) = \sum_{l=1}^{\infty} \sum_{m=-l}^{l} a_{lm} Y_{lm}(\theta, \phi) \tag{2.8}$$

Where, $Y_{lm}(\theta, \phi)$ represents the spherical harmonics and a_{lm} refers to the multipole moments. Considering the fact that the sky is almost uniform on a large scale, the anisotropies are very small $\delta T/T \sim 10^{-5}$. Here, the variance C_l of a given moment can be expressed as

$$C_l = \langle |a_{lm}|^2 \rangle \equiv \frac{1}{2l+1} \sum_{m=-l}^{l} |a_{lm}|^2 \tag{2.9}$$

The spherical harmonics analysis becomes a simplified ordinary Fourier analysis in two dimensions since the Universe is relatively flat on small sections of the sky. In such a limit, l represents the Fourier wave number. Here, the angular wavelength is defined as $\theta = 2\pi/l$. So it is evident from this definition that the large multipole moments refer to small angular scale. One can reasonably approximate the temperature fluctuation as Gaussian supported by the observations; see the left panel of Figure 2.4. Interestingly, one can accurately express the information of the CMB as a function of the multipole moments. Now it is essential to understand the anisotropy properly since the acoustics peaks in the power spectrum originate due to it, as shown in the right panel of Figure 2.4. This power spectrum is the primary outcome of the competition between the baryon and photon. Here, the photon pressure tries to erase the anisotropy in temperature, whereas the non-relativistic matter forms large halos of matter, thereby creating local anisotropies. The acoustic waves in the baryon photon plasma are generated due to the effects of this competition. As a result, we observe the so-called acoustic oscillations.

The measurement of the CMB helps in constraining the cosmology as each peak of the distribution corresponds to one cosmological parameter. According to the most recent measurements of the Planck Collaboration, the energy content of the Universe consists of 68.3% dark energy, 26.8% dark matter, and 4.9% baryonic matter, as shown in the Figure 2.5.

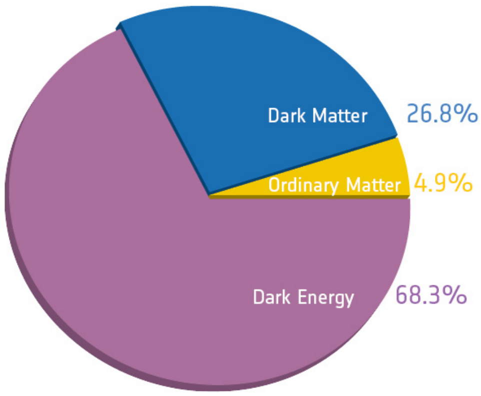

Figure 2.5: The energy content of the Universe from the recent results of the Planck Satellite experiment. Credit: ESA and the Planck Collaboration

2.2 Brief Review on the Early History of the Universe

Some of the important evidences behind the existence of the DM are already discussed. Although it is not yet wholly settled, in this thesis, we regard dark matter as a fundamental particle that is a part of the dark sector in the extended BSM family. In this chapter, we will examine different dark matter candidates who get produced in the early times of the Universe. To understand a clear description of dark matter production, it is very important to know the picture of the early Universe.

2.2.1 Standard Early History of the Universe

The Universe is spatially isotropic and homogeneous on a large scale, which was assumed initially and later verified with observation. This isotropy and homogeneity of the Universe can be described by the Friedmann-LemaÎtre-Robertson-Walker (FLRW) metric as

$$ds^2 = dt^2 - a^2(t)\left(\frac{dr^2}{1-kr^2} + r^2 d\theta^2 + r^2 \sin^2\theta d\phi^2\right) \tag{2.10}$$

where t represents the cosmic time, r, θ, ϕ are the spherical polar coordinates. Here $a(t)$ refers to the scale factor of the Universe, and the parameter k dictates the spatial curvature of the Universe where $k = 0, +1, -1$ stands for the flat, closed, and open space of the Universe, respectively. The FLRW metric has an implicit dependence on time appearing through the scale factor. The explicit time dependence can be obtained by solving the evolution of the scale factor by using the following Einstein equations

$$R_{\mu\nu} - \frac{1}{2}\mathcal{R}g_{\mu\nu} \equiv G_{\mu\nu} = 8\pi G T_{\mu\nu} + \Lambda g_{\mu\nu} \tag{2.11}$$

where $G_{\mu\nu}$ refers to the Einstein tensor, $T_{\mu\nu}$ represents the stress energy-momentum tensor, and Λ is the cosmological constant.
Now one can obtain the Friedmann equations describing the evolution of the Universe for any given energy component by solving the Einstein equations with the FLRW metric as

$$H^2 + \frac{k}{a^2} = \frac{1}{3M_P^2}\rho + \frac{\Lambda}{3} \tag{2.12}$$

$$\frac{\ddot{a}}{a} = -\frac{1}{6M_P^2}(\rho + 3p) \tag{2.13}$$

where $M_P = 2.4\times10^{18}$ GeV is the reduced Planck mass, ρ and p refer to the energy density and the local pressure of the fluid, respectively. The Λ term describes the dark energy density. Now we focus on the early Universe, and we know that the role of dark energy is negligible and so we can take $\Lambda = 0$. In Equation 2.12, a new variable H is introduced, which is known as the Hubble rate and is defined as

$$H = \frac{\dot{a}}{a} \tag{2.14}$$

where $\dot{a}$ represents the derivative of a with respect to time.
In the early Universe, there was more than one fluid present in theory. So one can define the total energy density and the pressure of the system as

$$\rho_{tot} = \sum_i \rho_i, \quad p_{tot} = \sum_i p_i \tag{2.15}$$

Where the index i represents the ith fluid and ρ_i and p_i are the energy density and the pressure of the fluid. This individual pressure and the energy density are not free parameters; rather, they are connected through the equation of the state of the fluid, which is given by

$$p_i = \omega_i \rho_i \tag{2.16}$$

where the parameter ω specifies the fluid such as $\omega = 1/3, 0, -1$ refer to radiation, pressureless non-relativistic matter, and dark energy, respectively.
Now one can define the critical density for the flat Universe ($k = 0$) by using the

first Friedmann equation

$$\rho_c = 3M_P^2 H^2 \tag{2.17}$$

One important parameter to study the early Universe is the density parameter which is a dimensionless quantity and defined as the ratio of the energy density of any fluid to the critical energy density of the Universe

$$\Omega_i = \frac{\rho_i}{\rho_c}, \qquad \Omega_{tot} = \frac{\rho_{tot}}{\rho_c} = \sum_i \Omega_i \tag{2.18}$$

There are several important cosmological parameters that have been measured by the Planck experiment. Here we have given the numerical values of some parameters today

$$\Omega_{\Lambda,0} \sim 0.69 \tag{2.19}$$

$$\Omega_{r,0} \sim 10^{-5} \tag{2.20}$$

$$\Omega_{m,0} \sim 0.31 \tag{2.21}$$

We know that non-relativistic matter comprises baryonic matter and dark matter, and their current contributions are given by

$$\Omega_{b,0} \sim 0.05, \qquad \Omega_{DM,0} \sim 0.26 \tag{2.22}$$

Here the index 0 in the subscript denotes the value of the parameters at the present day.

The SM of cosmology predicts that the space is critically flat, which is further confirmed by various experiments and simulations. Using the Equation 2.12 and considering the flatness of space, the Hubble rate can be expressed as

$$H^2 = \frac{1}{3M_P^2}\rho \tag{2.23}$$

One can derive the continuity equation with the help of the Friedmann equations Equation 2.12 and Equation 2.13. This equation dictates the evolution of the energy density in the expanding Universe and is written as

$$\dot{\rho} + 3H(p+\rho) = 0 \tag{2.24}$$

Now inserting the expressions of the pressure and the Hubble rate from the equations Equation 2.15 and Equation 2.23 into the continuity equation, one can express the evolution of number density as a function of the scale factor $a(t)$ as follows

$$\rho = \rho_0 \left(\frac{a_0}{a}\right)^{3(1+\omega)} \tag{2.25}$$

Now we shift our focus toward the thermal bath particles. In the early times when the Universe was radiation dominated, at that point in time, all the species were relativistic. The energy density of those particles is given by

$$\rho(T) = g_*(T)\frac{\pi^2 T^4}{30} \tag{2.26}$$

where g_* denotes the number of relativistic degrees of freedom. Now the relativistic degrees of freedom at any temperature T are defined by

$$g_* = \sum_{\text{bosons}} g_i^b \left(\frac{T_i}{T}\right)^4 + \frac{7}{8}\sum_{\text{fermions}} g_i^f \left(\frac{T_i}{T}\right)^4 \tag{2.27}$$

Where g_* stands for species i, which decouples from the thermal bath at temperature T_i, g_i^b and g_i^f represent the internal degrees of freedom for ith the boson and fermion, respectively. The evolution of the relativistic degrees of freedom has been displayed in Figure 2.6. For $T > 1$ TeV, all the SM species are relativistic and maintain equilibrium and $g_* = 106.75$. For $T < 1$ MeV $g_* = 3.36$ since the only relativistic species are the photons and neutrinos in such temperature. In

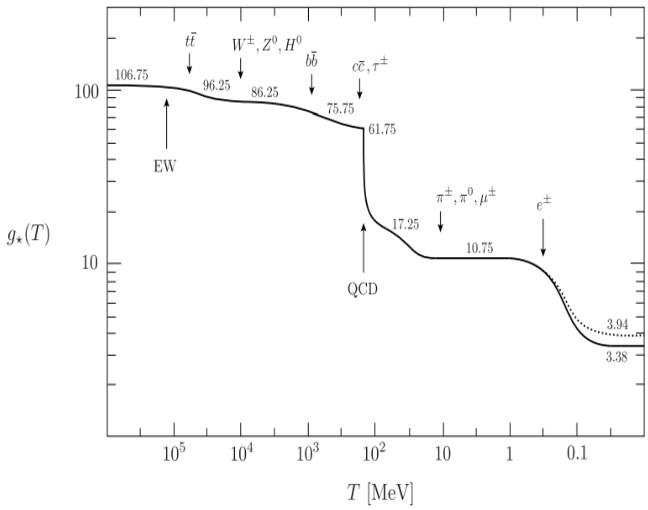

Figure 2.6: Evolution of the standard model degrees of freedom with the temperature. Image credit: Cosmology notes by Baumann

addition, the Universe evolved adiabatically in the early times; as a result, the entropy of the system remains conserved.

$$\frac{d}{dt}(sa^3) = 0 \tag{2.28}$$

where s characterizes the entropy density and is defined as

$$s = \frac{\rho + p}{T} = \frac{2\pi^2}{45} g_{*s}(T) T^3 \tag{2.29}$$

where g_{*s} represents the relativistic degrees of freedom contributed to the entropy and defined by

$$g_{*s} = \sum_{\text{bosons}} g_i^b \left(\frac{T_i}{T}\right)^3 + \frac{7}{8} \sum_{\text{fermions}} g_i^f \left(\frac{T_i}{T}\right)^3 \tag{2.30}$$

Finally, the Hubble rate of the early Universe when the Universe was radiation dominated is given by*

$$H(T) = \sqrt{\frac{\pi^2 g_*}{90}} \frac{T^2}{M_P} \tag{2.31}$$

We know that the Big Bang Nucleosynthesis occurred when the energy budget of the Universe was radiation dominated. Still, we do not have any information about the Universe's energy budget before BBN. So potentially, there is a possibility that some other species rather than radiation may dominate the energy budget in such early times of the Universe. There are many alternative cosmological scenarios present in the literature. One such non-standard cosmological aspect we will discuss here.

2.2.2 Non-Standard History of the Early Universe

We consider a species ϕ whose energy density redshifts with the scale factor as

$$\rho_\phi \propto a^{-(4+n)} \tag{2.32}$$

The standard cosmological scenario can be revived by setting $n = 0$. Here we always take $n > 0$, which specifies the picture that the energy density dominated over the radiation in the early enough times. The energy density of ϕ and the radiation must equal at a temperature greater than the BBN temperature to keep intact the remarkable success of BBN.

- **A Faster Expansion**

*Another commonly used form of Hubble rate is, $H = 1.66 * \sqrt{g_*} T^2/M_{Pl}$, where $M_{Pl}(= 1.22 \times 10^{19}\ GeV)$ represents the Planck mass.

We have already discussed how the expansion rate of the Universe, i.e., the Hubble rate, is controlled by the energy density through the Friedmann equations. Here we consider a picture of a cosmological history where both the species ϕ and radiation are present in the early Universe and contribute to the energy density. In this context, the energy density reads as

$$\rho = \rho_\phi + \rho_r \tag{2.33}$$

where ρ_ϕ and ρ_r correspond to the energy density of the species ϕ and radiation, respectively.

In the case of standard cosmological history, radiation is the only component that was present and contributed to the energy density. This energy density is expressed already in terms of temperature and the effective relativistic degrees of freedom and given in the Equation 2.26. It is advantageous to express the ρ_ϕ as a function of the radiation temperature. However, we have already expressed ρ_ϕ as a function of the scale factor in Equation 2.32. We have to find out the relation between the scale factor and radiation temperature. Then we will be able to parametrize the energy density of ϕ as a function of T. One can obtain that $g_{*s}(T)^{1/3}Ta$ = constant by exploiting Equation 2.28 and Equation 2.29. One can write the following equation for any reference temperature T_r using Equation 2.32.

$$\frac{\rho_\phi(T)}{\rho_\phi(T_r)} = \left(\frac{a(T)}{a(T_r)}\right)^{-(4+n)} \tag{2.34}$$

Here T_r denotes a temperature where the energy density of ϕ equals with the radiation energy density i.e. $\rho_\phi(T_r) = \rho_r(T_r)$. Now using this relation along with $g_{*s}(T)^{1/3}Ta$ = constant, one can re-express the energy density ϕ as

$$\rho_\phi(T) = \rho_r(T_r)\left(\frac{g_{*s}(T)}{g_{*s}(T_r)}\right)^{(4+n)/3}\left(\frac{T}{T_r}\right)^{(4+n)} \tag{2.35}$$

In this context, the full energy density of the Universe reads as

$$\rho(T) = \rho_\phi(T) + \rho_r(T) \tag{2.36}$$

$$= \rho_r(T)\left[1 + \left(\frac{g_*(T_r)}{g_*(T)}\right)\left(\frac{g_{*s}(T)}{g_{*s}(T_r)}\right)^{(4+n)/3}\left(\frac{T}{T_r}\right)^{n}\right] \tag{2.37}$$

From the above equation, it is clear that the energy budget of the Universe is dominated by ϕ for $T \geq T_r$. Now, using the Friedmann equation, we can evaluate the Hubble expansion rate with Equation 2.37 in hand. Assuming $g_{*s} \simeq g_*$, the Hubble rate for temperature larger than T_r is approximately given by

$$H(T) = \sqrt{\frac{\pi^2 g_*}{90}} \frac{T^2}{M_P} \left(\frac{T}{T_r}\right)^{n/2}, \quad T \gg T_r \tag{2.38}$$

$$= H_R(T) \left(\frac{T}{T_r}\right)^{n/2} \tag{2.39}$$

Where, $H_R(T)$ denotes the Hubble rate for the radiation dominated Universe. The above expressions show that the Hubble rate for a given temperature is always larger than the rate corresponding to the standard history of cosmology. So the Universe expands faster than the usual standard picture. Although these non-standard parameters are not free and we will discuss the constraints on it.

2.2.3 BBN Constraints on Non-Standard parameters

BBN occurred when the Universe was a few seconds old, i.e., the temperature of the Universe was few MeV. We do not want to spoil the striking agreement between the theoretical prediction on the abundance of light elements considering the radiation-dominated Universe at the time of BBN and the observations. So the reference temperature should be larger than the BBN temperature to ensure the success of the theoretical prediction.

A serious problem with the BBN can emerge if T_r is less than a few MeV when the formation of light elements begins. In such cases, the Universe expands faster than the standard scenario, which may alter the predicted abundance of the light elements.

The effects of the fluid ϕ are taken into account by the effective number of relativistic degrees of freedom

$$\rho(T) = g_*^{\text{eff}}(T) \frac{\pi^2 T^4}{30} \tag{2.40}$$

where we define

$$g_*^{\text{eff}}(T) = g_*(T) + \Delta g_*^{\phi}(T) \tag{2.41}$$

Here, $g_*(T)$ describes the standard contributions coming from radiation, and $\Delta g_*^{\phi}(T)$ stands for the energy density of the field ϕ. The presence of ϕ can be described as the number of effective neutrinos. Thus the number of relativistic degrees of freedom in the Equation 2.40 becomes

$$g_*^{\rm eff} = 2 + \frac{7}{8} \times 4 + \frac{7}{8} \times 2 \times N_\nu \tag{2.42}$$

Here we consider the effects of photons, positrons along with neutrinos. In the Standard model, number of flavours of the neutrinos for $T > 1$ MeV is $N_\nu^{\rm SM} = 3$. Now comparing these two expressions of g_* with and without BSM, one can obtain

$$\Delta N_\nu = \frac{4}{7}\Delta g_*^\phi \tag{2.43}$$

Here, the temperature-dependent additional contributions coming from the extra neutrinos have the following expressions

$$\Delta N_\nu = \frac{4}{7}\Delta g_*^\phi(T_r)\left(\frac{g_{*s}(T)}{g_{*s}(T_r)}\right)^{(4+n)/3}\left(\frac{T}{T_r}\right)^n \tag{2.44}$$

The above equation can be simplified further by considering T_r around the BBN temperature as

$$\Delta N_\nu \simeq \frac{4}{7}\frac{43}{4}\left(\frac{T}{T_r}\right)^n \tag{2.45}$$

BBN bounds on N_ν can be found in the Ref, which put constraints on the non-standard parameters as

$$T_r \geq (15.4)^{1/n}{\rm MeV} \tag{2.46}$$

2.3 Thermodynamics and The Evolution of the Universe

2.3.1 Boltzmann Equation

The evolution of the number density of the particle describes by the evolution of the phase space distribution function $f(p^\mu, x^\mu)$. Consider a system where a particle χ interacts with the rest of the particles of the thermal bath, and the following equation demonstrates this picture very well

$$\hat{L}[f] = \hat{C}[f] \tag{2.47}$$

where this equation is familiar with the name of the Boltzmann equation and governs the evolution of the distribution function$f(p^\mu, x^\mu)$ of any spices. Here $\hat{L}$

is the Liouville operator, and $\hat{C}$ represents the collision operator. The general covariant form of the Liouville operator is

$$\hat{L} = p^{\alpha}\frac{\partial}{\partial x^{\alpha}} - \Gamma^{\alpha}_{\beta\gamma}p^{\beta}p^{\gamma}\frac{\partial}{\partial p^{\alpha}} \tag{2.48}$$

All the gravitational effects of the problem enter the equation via the affine connection of the metric. For the FLRW model, the phase space density of the Universe is spatially homogeneous and isotropic, i.e., $f = f(|\vec{p}|, t)$ (or equivalently $f = f(E, t)$). In this model, the Liouville operator takes the form

$$\hat{L}[f(E,t)] = E\frac{\partial f}{\partial t} - \frac{\dot{a}}{a}|\vec{p}|^2\frac{\partial f}{\partial E} \tag{2.49}$$

where $a(t)$ represents the scale factor of the metric. One can define the number density in terms of the phase space density in the following way

$$n(t) = \frac{g}{(2\pi)^3}\int d^3p f(E,t) \tag{2.50}$$

where g is the internal degree of freedoms. Using Equation 2.49 and Equation 2.50 and doing integration by parts, the Boltzmann equation can be rewritten as

$$\frac{dn}{dt} + 3\frac{\dot{a}}{a}n = \frac{g}{(2\pi)^3}\int \hat{C}(f)\frac{d^3p}{E} \tag{2.51}$$

The collision term for the process $\chi + a + b + ... \longleftrightarrow i + j + ...$ is given by

$$\begin{aligned}\frac{g}{(2\pi)^3}\int \hat{C}(f)\frac{d^3p}{E} = -\int & d\Pi_\chi d\Pi_a d\Pi_b ....d\Pi_i d\Pi_j ....\\ &\times (2\pi)^4\delta^4(p_\chi + p_a + p_b.... - p_i - p_j....)\\ &\times \big[|\mathcal{M}|^2_{\chi+a+b+....\longrightarrow i+j+....} f_a f_b....f_\chi (1\pm f_i)(1\pm f_j)....\\ &- |\mathcal{M}|^2_{i+j+....\longrightarrow \chi+a+b+....+....} f_i f_j....(1\pm f_a)(1\pm f_b)....(1\pm f_\chi)\big]\end{aligned} \tag{2.52}$$

where $f_i, f_j, f_a, f_b, ...$ are the phase space densities of the spices $i, j, a, b, ...$ respectively. f_χ refers to the phase space density of χ (the spices whose evolution we are studying); $(+)$ stands for bosons and $(-)$ stands for fermions; and

$$d\Pi \equiv g\frac{1}{(2\pi)^3}\frac{d^3p}{2E} \tag{2.53}$$

where g refers to the internal degrees of freedom. The four-dimensional delta function dictates the energy-momentum conservation. For the calculation of the matrix element squared($|\mathcal{M}|^2$), an average over initial and final spins are considered, while the appropriate symmetry factors for the identical particles in the initial and final states are also taken into account. Here a very simple process$\chi + a + b \leftrightarrow i + j$ is taken for the analysis. The first assumption is the CP(or T) invariance, which simplifies the Equation 2.52 and implies that

$$|\mathcal{M}|^2_{i+j\rightarrow\chi+a+b} = |\mathcal{M}|^2_{\chi+a+b\rightarrow i+j} \equiv |\mathcal{M}|^2 \tag{2.54}$$

Here the second approximation considers the Maxwell-Boltzmann statistics for the spices instead of taking the Fermi-Dirac distribution for fermions and Bose-Einstein distribution for bosons. In the absence of Bose condensation or Fermi degeneracy one can approximate $1 + f \sim 1$, and $f_i(E_i) = exp[-(E_i - \mu_i)/T]$ for all the spices which are maintaining kinetic equilibrium. Now the Boltzmann equation takes the following simplified form after taking these approximations

$$\begin{aligned} \dot{n_\chi} + 3Hn_\chi = -\int d\Pi_\chi d\Pi_a d\Pi_b d\Pi_i d\Pi_j (2\pi)^4 |\mathcal{M}|^2 \\ \times \delta^4(p_i + p_j - p_\chi - p_a - p_b)[f_a f_b f_\chi - f_i f_j] \end{aligned} \tag{2.55}$$

where $H(\equiv \dot{a}/a)$ is the Hubble rate. It is very important to know the significance of the individual terms in Equation 2.55. The term $3Hn_\chi$ is responsible for the dilution effect due to the expansion of the Universe, whereas the term on the right-hand side represents the variation in the number density of χ because of its interaction with the rest of the particles in the thermal plasma.
It is customary to translate number density (n_χ) to yield (Y) for the analysis of the Boltzmann equation

$$Y \equiv \frac{n_\chi}{s} \tag{2.56}$$

Here the effect of the expansion of the Universe is absorbed; the yield will change if there is interaction. As a result, the yield will vary with the collision term. The temperature is a better variable than time to study the evolution of the Universe. So it is common to define a dimensionless quantity

$$x = \frac{m_\chi}{T} \tag{2.57}$$

where m_χ refers to the mass of the χ spices. Assuming that the number of relativistic degrees of freedom (g_*) and the entropy degrees of freedom (g_{*s}) do not vary with time and the time and the variable x maintains the relation $dt/dx =$

$1/Hx$ in the radiation dominated era. Now one can express the Hubble rate as

$$\begin{aligned} H =& \sqrt{\frac{4\pi^3}{45}}\sqrt{g_*}\frac{T^2}{M_P} \\ =& \sqrt{\frac{4\pi^3}{45}}\sqrt{g_*}\frac{m_\chi^2}{M_P}\frac{1}{x^2} \end{aligned} \tag{2.58}$$

After using the newly defined variable and the above definition, one can parametrize the Boltzmann equation in a more simplified form

$$\begin{aligned} \frac{dY}{dx} =& -\frac{1}{Hsx}\int d\Pi_\chi d\Pi_a d\Pi_b d\Pi_i d\Pi_j (2\pi)^4 |\mathcal{M}|^2 \\ & \times \delta^4(p_i + p_j - p_\chi - p_a - p_b)[f_a f_b f_\chi - f_i f_j] \end{aligned} \tag{2.59}$$

2.3.2 Abundance analysis of the out of equilibrium species

So far, we have discussed the general Boltzmann equation in the above section. Here we study the relic abundance produced by the stable or longlived particle, which is the main focus of the thesis. For stable particles, $2 \leftrightarrow 2$ processes are essential, but if the particle is unstable, other processes must be considered for the analysis. Now we consider the process $\chi\bar{\chi} \leftrightarrow \psi\bar{\psi}$ where ψ and $\bar{\psi}$ is any SM particles in thermal equilibrium. So these bath particles obey the following equilibrium distribution

$$\begin{cases} f_\psi = e^{\frac{E_\psi}{T}} \\ f_{\bar{\psi}} = e^{\frac{E_{\bar{\psi}}}{T}} \end{cases} \tag{2.60}$$

The delta function in Equation 2.59 implies the conservation of energy.

$$E_\chi + E_{\bar{\chi}} = E_\psi + E_{\bar{\psi}} \tag{2.61}$$

Utilizing the above information, one obtains

$$f_\psi f_{\bar{\psi}} = e^{-(E_\psi + E_{\bar{\psi}})/T} = e^{-(E_\chi + E_{\bar{\chi}})/T} = f_\chi^{\text{eq}} f_{\bar{\chi}}^{\text{eq}} \tag{2.62}$$

Now, the Equation 2.59 can be simplified further by defining the thermally average cross-section for $2 \to 2$ process after obtaining $[f_\chi f_{\bar{\chi}} - f_\psi f_{\bar{\psi}}] = [f_\chi f_{\bar{\chi}} - f_\chi^{\text{eq}} f_{\bar{\chi}}^{\text{eq}}]$

$$\langle \sigma v \rangle \equiv \int d\Pi_\chi d\Pi_{\bar{\chi}} d\Pi_\psi d\Pi_{\bar{\psi}} (2\pi)^4 \tag{2.63}$$

$$\times \delta^4(p_\chi + p_{\bar{\chi}} - p_\psi - p_{\bar{\psi}}) |\mathcal{M}|^2 e^{-E_\psi/T} e^{-E_{\bar{\psi}}/T} \tag{2.64}$$

Now the simplified version of the Boltzmann equation becomes

$$\frac{dY}{dx} = -\frac{\langle \sigma v \rangle s}{Hx}\left(Y^2 - Y_{\rm eq}^2\right) \tag{2.65}$$

where $Y = n_\chi/s = n_{\bar{\chi}}/s$ is the yield of the particle χ as well as the anti-particle $\bar{\chi}$. When the production of χ involves multiple processes, it is crucial to consider the contribution of all the processes to calculate the abundance of the particle χ. In addition, it is also necessary to know the equilibrium abundance of all the species to compute the evolution of the yield where the equilibrium abundance is given

$$Y_{\rm eq}(x) = \frac{45}{4\pi^4}\frac{x^2}{g_{*s}}K_2(x) \tag{2.66}$$

where $K_2(x)$ is the second modified Bessel function of the second kind.
For a scenario where $1 \to 2$ decay is relevant for the evolution of the yield, then one has to solve the following Boltzmann equation

$$\frac{dY}{dx} = -\frac{\langle \Gamma \rangle}{Hx}\left(Y - Y_{\rm eq}\right) \tag{2.67}$$

Now, the most general Boltzmann equation where both the $1 \to 2$ and $2 \to 2$ processes are relevant has the following form

$$\frac{dY}{dx} = -\frac{\langle \sigma v \rangle s}{Hx}\left(Y^2 - Y_{\rm eq}^2\right) - \frac{\langle \Gamma \rangle}{Hx}\left(Y - Y_{\rm eq}\right) \tag{2.68}$$

Where the thermally averaged annihilation cross-section for any $2 \to 2$ process can be expressed as

$$\langle \sigma v \rangle = \frac{1}{8m_\chi^4 T K_2^2(m_\chi/T)}\int_{4m_\chi^2}^{\infty} ds(s - 4m_\chi^2)\sigma\sqrt{s}K_1(\sqrt{s}/T) \tag{2.69}$$

Here $K_1(x)$ and $K_2(x)$ are the modified Bessel functions of the second kind. Moreover, the thermally average decay rate can be written as

$$\langle \Gamma \rangle = \Gamma\frac{K_1(x)}{K_2(x)} \tag{2.70}$$

2.3.3 WIMP Dark Matter: Freeze-Out

WIMP paradigm assumes that the DM maintains thermal equilibrium with the rest of the thermal bath particles in the early Universe. Such kind of scenario is first explored by the authors' Benjamin W. Lee and Steven Weinberg. The main focus of this section is to understand how dark matter production occurs with the help of Equation 2.65. Now plugging the expressions of the Hubble rate and the entropy density in the Equation 2.65, one obtains

$$\frac{dY}{dx} = -\frac{\lambda}{x^2}\langle\sigma v\rangle\left(Y^2 - Y_{\rm eq}^2\right) \tag{2.71}$$

where

$$\lambda = \frac{2\pi\sqrt{90}}{45}\frac{g_{*s}}{\sqrt{g_*}}m_\chi M_P \tag{2.72}$$

The assumption of WIMP scenario implies at $x = 0$, $Y_\chi = Y_\chi^{\rm eq}$. The rate of interaction for any $2 \to 2$ process is given by

$$\Gamma_{\rm an} = n_{\rm eq}\langle\sigma v\rangle \tag{2.73}$$

The rate of interaction decreases as the Universe expands and when $\Gamma \simeq H$, the DM decouples from the thermal plasma. This mechanism is called freeze-out, and this point is characterized by $x = x_{\rm fo}$. Using the criterion of freeze-out, one obtains the approximated value of the $x_{\rm fo}$ as

$$x_{\rm fo} \simeq \log\left[\sqrt{\frac{45}{4\pi^5}}M_P m_\chi g\sqrt{\frac{x_{\rm fo}}{g_*}}\langle\sigma v\rangle_{\rm fo}\right] \tag{2.74}$$

Here g_* and $\langle\sigma v\rangle$ both are calculated at freeze-out where $\langle\sigma v\rangle_{\rm fo} = \langle\sigma v\rangle|_{x=x_{\rm fo}}$. The parameter g represents the internal degrees of freedom of the DM. In addition, the usual range of $x_{\rm fo}$ for the WIMP DM is $x_{\rm fo} \sim 20-25$ irrespective of the DM mass when the DM mass lies between GeV to TeV.

After the decoupling from the thermal bath, the interaction of DM becomes insignificant, and the abundance of DM freezes. Looking at the evolution of the DM yield, one can separate two distinct regimes and obtain an approximated form of the yield for those regimes. We have already discussed that the DM was a part of the thermal plasma before the freeze-out. So the DM yield refers to the equilibrium yield for $x \le x_{\rm fo}$.

$$Y(x) = Y_{\rm eq} \tag{2.75}$$

In contrast, the DM interaction rate becomes very negligible means the yield remains almost unchanged after the decoupling. Here the yield can be approximated as the yield at the freeze-out for $x > x_{\rm fo}$

$$Y(x) = Y(x_{\rm fo}) \tag{2.76}$$

The temperature of the Universe today is $T_\infty = 2.725 \pm 0.001$ K where the observed abundance of the DM is $Y_\infty = Y_{x\to\infty} \simeq Y(x \gg x_{\rm fo})$. The relic density of the dark matter can be evaluated by using the following relation for any DM mass after calculating the yield numerically

$$\Omega_\chi h^2 = 2.744 \times 10^8 \frac{m_\chi}{\rm GeV} Y_\infty \tag{2.77}$$

The Planck experiment already puts a limit on the relic abundance of dark matter, which is $\Omega_\chi h^2 = 0.1121 \pm 0.0056$.

Now the Equation 2.71 can be solved by using different numerical techniques. Though it is challenging to obtain an analytical solution since there are complications in dealing with the annihilation cross-section. However, one can get an analytical solution by imposing some special conditions on the evolution of the yield. In addition, one can see from Figure 2.7 that the DM yield does not change after the freeze-out, whereas the equilibrium yield falls rapidly. So one can neglect $Y_{\rm eq}$ compare to Y in Equation 2.71. Note that the condition is not valid before freeze-out since DM matter yield follows the equilibrium distribution in this regime. Now considering both the assumptions, one derives

$$\frac{1}{Y_\infty} = \frac{1}{Y_{\rm fo}} + \int_{x_{\rm fo}}^{\infty} \frac{dx}{x^2} \lambda \langle \sigma v \rangle \tag{2.78}$$

Here, the λ varies with x as both g_{*s} and g_* are temprature dependent. In order to calculate Y_∞, the value of g_{*s} and g_* at $T_{\rm fo}$ are used. After neglecting $\frac{1}{Y_{\rm fo}}$, one can approximate Y_∞ as

$$Y_\infty = \left(\lambda_{\rm fo} \int_{x_{\rm fo}}^{\infty} \frac{dx}{x^2} \langle \sigma v \rangle \right)^{-1} \tag{2.79}$$

with $\lambda_{\rm fo} \equiv \lambda|_{x=x_{\rm fo}}$.

Now we will discuss a few interesting points about the annihilation cross-section. In the WIMP scenario, the relative velocity between two annihilating DM particles is very small. So one can express the annihilation cross-section in terms of relative velocity. Under this assumption, we can write the cross-section in a power series of v as

$$\sigma v \simeq a + b v^2 + c v^4 + \mathcal{O}(v^6) \tag{2.80}$$

with $v \simeq \sqrt{s/4m_\chi^2 - 4}$. Here the first three terms refer to the s-wave, p-wave, and d-wave contribution, respectively. Now the thermally averaged annihilation cross-section is given by

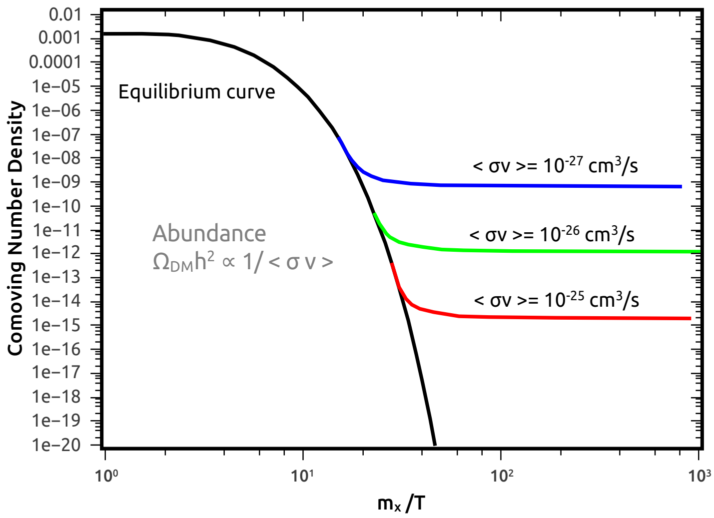

Figure 2.7: Freeze-out case: Evolution of the DM yield with the dimensionless parameter $x(= m_\chi/T)$. Image taken from [67]

$$\langle \sigma v \rangle = \frac{x^{3/2}}{2\sqrt{\pi}} \int_0^\infty dv v^2 (\sigma v) e^{-xv^2/4} \simeq a + \frac{6b}{x} + \frac{15c}{x^2} + \mathcal{O}(1/x^3) \tag{2.81}$$

When the DM annihilation occurs through the s-wave, then we can obtain a trivial solution for the DM yield as the thermally averaged cross-section is independent of temperature, i.e., constant, and we can write the following by using the Equation 2.81

$$Y_\infty = \frac{x_{\rm fo}}{\lambda_{\rm fo}\langle \sigma v \rangle} \tag{2.82}$$

Now we can easily calculate the relic density of the DM by using the following relation

$$\Omega h^2 = \frac{1.09 \times 10^9 x_{\rm fo}}{\sqrt{g_*} M_P \langle \sigma v \rangle} {\rm GeV}^{-1} \tag{2.83}$$

Where we assume that the number of relativistic degrees of freedom for energy and entropy is almost equal at the freeze-out and the typical value for the WIMP picture is $g_{*s} = g_* \sim 80 - 100$. The values of $x_{\rm fo}$ lies between $20 - 30$ while the exact value of $x_{\rm fo}$ depends on the mass of the DM. Therefore, the value of the relic abundance depends on the annihilation cross-section while there is no direct dependency on mass.

Generally, for the DM mass range $\sim (10^{-1} - 10^4)$ GeV, one needs $\langle \sigma v \rangle \sim 2 \times 10^{26} {\rm cm}^3/{\rm s}$ to satisfy the correct relic density. In this mass range, the variation of

annihilation cross-section with mass is very mild .
Figure 2.7 displays, the numerical solutions of the Equation 2.71 for different values of thermally averaged annihilation cross-section. As we mentioned earlier that $\langle\sigma v\rangle \sim 2\times 10^{26}\text{cm}^3/\text{s} \sim 1$ pb regardless of the DM mass. Interestingly, this value matches the typical order of the electroweak interaction. That is the reason it is called the WIMP *miracle*.

2.3.4 FIMP Dark Matter: Freeze-In

Already, we have discussed the WIMP paradigm, where the primary assumption is that in the early Universe, the DM was in thermal equilibrium. However, when the coupling of interaction between the DM and the visible sector is tiny $\sim \mathcal{O}(10^{-7})$, then the DM never gets thermalized with the thermal plasma. In such a scenario, the abundance of dark matter in the early times was negligibly small.

$$Y(x_0) \simeq 0 \tag{2.84}$$

In the early Universe, DM production occurred via the annihilation of dark matter when the temperature was very high. As the Universe expands, the possibility of collision between the standard model particles decreases; as a result, production reduces. When the Universe expands further, and the temperature becomes low enough, the production becomes insignificant. So the abundance of dark matter freezes in, and it remains constant till today. This kind of DM is well-known as FIMP.
The initial abundance of dark matter for the freeze-in scenario is negligible, so one can safely neglect the Y^2 term compared to the equilibrium one in Equation 2.71. As a result, the DM abundance before the freeze-in is much smaller than the equilibrium abundance. So the simplified version of the Boltzmann equation for the $2 \to 2$ process is given by

$$\frac{dY}{dx} = \frac{\lambda}{x^2}\langle\sigma v\rangle\left(Y^2 - Y_{\text{eq}}^2\right) \simeq -\frac{\lambda}{x^2}\langle\sigma v\rangle Y_{\text{eq}}^2 \tag{2.85}$$

Contrary to the freeze-out mechanism, the FIMP type DM yield increases with the temperature until the yield freezes in. Figure 2.8 shows the solution of the Boltzmann equation for the freeze-in scenario with different thermally averaged annihilation rates. Here, it is clear that the larger annihilation rate demands a larger abundance of dark matter.
It is not true that DM production always takes place through the annihilation of the bath particles. The DM may get produced from the decay of a heavy particle.

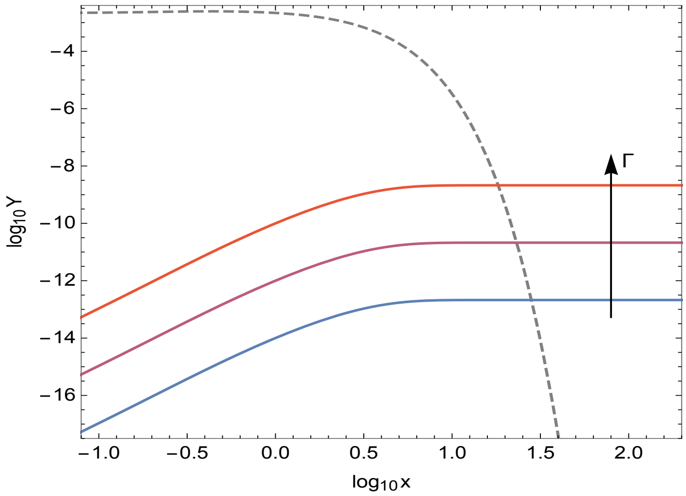

Figure 2.8: Freeze-in case: Evolution of the DM yield with the dimensionless parameter x. Image is taken from [68].

Now the Boltzmann equation for the $1 \to 2$ process reads as

$$\frac{dY}{dx} = -\frac{\langle \Gamma \rangle}{Hx}\left(Y - Y_{\text{eq}}\right) \simeq \frac{\langle \Gamma \rangle}{Hx} Y_{\text{eq}} \tag{2.86}$$

An interesting scenario occurs when the DM has sufficiently large interaction with the other dark sector particles. In this scenario, initially, the dark matter produced from the bath when the population of DM becomes significant. The DM will start to produce other dark sector particles and get thermalized due to their large interaction. Here, the DM final yield is not fixed by freeze-in; rather, the final abundance is set by the freeze-out of the processes in the dark sector. Since this freeze-out takes place in the dark sector, it is termed a dark freeze-out. This kind of scenario receives the name of annihilation of dark matter. We have studied such an exciting picture in detail in Chapter 5.

We know that dark matter production takes place at a high temperature. So the consideration of temperature effects may become necessary in some cases. Suppose the dark matter is getting produced from decays provided that the mass of the decaying particle is larger than the total mass of the final state particles. The dark matter may produce from a lighter particle than the dark matter if that particle develops a sizeable thermal mass compared to dark matter. Any particle can acquire a large thermal mass in the early Universe when the temperature was very high. So the incorporation of the thermal mass opens up a new paradigm where the dark matter produces from a kinematically forbidden channel. The dark matter produced via a forbidden process is called the forbidden freeze-in dark matter. Chapter 6 involves a study of FFI dark matter.

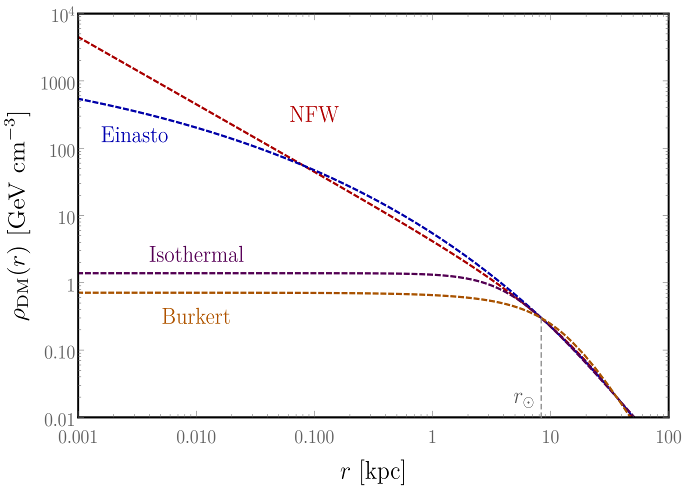

Figure 2.9: The display of NFW, Einasto, Isothermal and Burkert galactic Dark Matter density profile where $\alpha = 0.17$ with $r_s = \{24.4, 28.4, 4.3, 12.6\}$ kpc respectively. Image is taken from [69].

2.3.5 DM Halo profile

Dark matter follows a distribution within the dark matter halo, where the phase space distribution of DM comprises the spatial and velocity distribution. This distribution has a crucial impact on direct and indirect detections since this method considers the DM halo the source of dark matter.

2.3.5.1 DM density profile

In literature, there exist several spherically symmetric halo profiles to demonstrate the DM halo. Among those profiles, the Navarro-Frenk-White profile is the most popular one and is given by

$$\rho_{\rm NFW}(r) = \frac{\rho_c}{\left(\frac{r}{r_s}\right)\left[1+\left(\frac{r}{r_s}\right)^2\right]} \tag{2.87}$$

where ρ_c and r_s represent the characteristic density and radius, respectively. Actually, it is a fit to the density profile, which is guided by the N body simulation. It is also constructed so that it can mimic the particular behaviour of density profile as $\rho(r) \sim r^{-1}$ for $r < r_s$ and $\rho(r) \sim r^{-3}$ for $r > r_s$. Note that this profile has a divergence for $r \to 0$. The recent simulations suggest that the Einasto profile can describe the halo densities more accurately. This profile is introduced by Einasto and has the following shape

$$\rho_{\rm Einasto}(r) = \rho_c\left(-\frac{2}{\alpha}\left[\left(\frac{r}{r_s}\right)^\alpha - 1\right]\right) \tag{2.88}$$

where r_s is the radius within which half of the total halo mass is enclosed, and ρ_s describes the DM density at this radius. The free parameter α can be calibrated to interpret the variousness in the simulated halos.
In addition, One of the commonly used profiles is the Burkert profile. This profile is inspired by the rotational curve measurement of the dwarf galaxies and parametrizes as

$$\rho_{\text{Burkert}}(r) = \frac{\rho_c}{\left(1+\frac{r}{r_s}\right)\left[1+\left(\frac{r}{r_s}\right)^2\right]} \tag{2.89}$$

ρ_s is the central dark matter density, and r_s is the core radius. In the inner part of the halo, it reconstructs the flat density profile while falls rapidly ($\rho(r \gg r_s) \propto r^{-3}$) in the outer region.
There is also another notable profile, the so-called isothermal profile. This profile is more pertinent for phenomenology rather than describing the dark matter distribution. it has the potential to reproduce the flat rotation curve and has the following expression

$$\rho_{\text{Isothermal}}(r) = \frac{\rho_c}{a^2 + r^2} \tag{2.90}$$

where ρ_0 and a are the constants. The isothermal density profile remains almost constant in small values of radius($r < r_s$) and falls less sharply $\rho(r) \propto r^{-2}$ for $r \gg r_s$. All the distributions discussed above are shown in the Figure 2.9 for the case of the Milky Way.
It is essential to know the dark matter density along with the DM distribution in the galactic neighborhood of the Sun. for the DD and ID experiments. The attempt to calculate this quantity has been determined not only by using the density profile but also by several other studies with the help of different methods. This result indicates that the DM density lies between

$$\rho_{\text{DM}} = 0.3 - 0.4 \ \text{GeV/cm}^{-3} \tag{2.91}$$

2.3.6 Problems in small scales structures

The prediction of the ΛCDM model matches beautifully with the observation at large scales, while it clearly shows the difficulty of explaining the astrophysical observations on small scales. There are several issues, commonly known as small-scale structure problems, and among them, three prominent problems will be discussed here.

• **Cups-Core problem:** This problem is associated with the discrepancy in the behavior of the density of the dark matter in the central part of smaller galaxies. According to the prediction of N body simulation, the DM density profile is cuspy, where the dark matter density follows . In contrast, the actual behavior of the dark matter density can be deduced by using the observations of smaller systems. It is encountered that the smaller halos have the core, where the dark matter density remains constant at a small radius.

• **Missing satellite problem:** This is related to the mismatch between the predicted number of subhalos in N-body simulation and the observed number of satellite galaxies.

• **Too big to fail problem:** It is expected that the Milky way satellites with the largest stellar velocity would inhabit the most massive subhalos of the Milky Way. But the circular velocity profile of the most massive halos in CDM simulation does not match the observation. The less massive subhalos host these observed satellite galaxies where the most massive one fails. The question is why the less massive subhalo successfully forms the luminous counterparts while the most massive subhalo does not. In short, the too big to fail problem demonstrates that the center of the most massive subhalo by CDM simulation is too dense to host the observed satellite of the Milky Way.

• **Diversity problem:** Observations point out that the density profile in the inner region of a Halo posses many different behaviours while the cosmological simulations suggest a small scatter in density profile in the case of Halos with similar mass and size. Such variety in the slope in the inner part of the density profile is known as the diversity problem.

2.3.7 Self-interaction of dark matter: Solution to the small scale problem

There are very few solutions for small-scale problems like the baryonic feedback effects etc. However, an alternative and exciting way to solve this problem is by invoking the self-interaction of the dark matter.
The same principles used to place-bound on the dark matter self-interaction have been applied to solve the small-scale structure problems. The core can be generated by reducing the number of particles in the subhalos of the galaxies, which can solve both the issues of the cups-core problem and the missing satellite problem. Since the generation of the core necessarily reduces the rotational velocity of the

core and the dwarf galaxy host the largest subhalo. There are enormous studies that consider different self-interacting dark matter models when the evolution of the halo is simulated . To support the creation of the core in the dwarf galaxies suggest that the following order of self-interaction of dark matter is needed.

$$\sigma_{\rm SI}/m \sim 1 \text{ cm}^2/\text{g} \tag{2.92}$$

One needs a velocity-dependent cross-section to solve the small-scale problem with the help of dark matter self-interaction while satisfying the bound at the cluster halo size, i.e., recovering the collisionless behavior at a large scale . Here, it is mentioned that the cross-section's velocity dependence comes naturally when the dark matter self-interaction occurs via a Yukawa-type potential. It is shown that this yields a large cross-section at a small velocity while the cross-section falls very fast as velocity increases. This behavior perfectly matches the requirement that the dark matter self-interaction needs to be large at the velocity of 10 km/s, which is the actual velocities range to resolve the small-scale puzzle while becoming small at the velocities of 1000 km/s, which is the natural velocity range where the bound from the DM cluster halo lies. It has been verified further in the numerical simulation that the incorporation of self-interaction of dark matter generated by the Yukawa type of interaction does replicate the expected behavior for the dwarf galaxy halo . Light mediator extended version of the SM naturally mimics the appearance of the Yukawa potential in non-relativistic limit .

It is tough to harmonize cosmology with the models where light mediators are present in the article content. When the freeze-out mechanism fixes a dark matter relic in the presence of a light mediator, then that mediator must be thermalized. This mediator must be unstable because if this is stable, then it becomes the dominant dark matter component, and it over closes the Universe. To resolve this issue, the mediator has to decay, and it must decay before the Big Bang Nucleosynthesis since its decay after BBN may alter the primordial abundance of the light elements. When the DM is connected with the visible sector by kinetic mixing or Higgs portal interaction, it is also challenging to explain the short lifetime of the mediator while satisfying the strong bound coming from direct detection experiments.

2.4 Dark Matter Searches

In Chapter 1, we have discussed the DM properties. In this chapter, we already demonstrate the WIMP and FIMP scenarios and the procedure to calculate the relic density. Now, we are going to describe how DM can be detected. The

DM experimental detections can be grouped into three categories: Direct detection of DM-nucleus scattering process in underground experiment [70]; Indirect detection, i.e., detection of SM particles produced from the DM annihilation process [71] and eventually, the production of DM at collider such as the LHC [72]. The FIMP can have similar properties as the WIMP; its feeble interaction with the SM particles makes the detection more challenging. However, the detection techniques are the same for both cases.
Several current experiments are trying to detect dark matter and unravel its nature and interaction apart from the gravitational interaction. In this section, we explore the current prospect of dark matter detection.

2.4.1 Direct Detection

Direct detection experiments of DM use the most promising detection techniques. The basic idea behind DM detection is to measure the recoil energy of the DM nucleus scattering happening in the DM halo. E. Witten and M. Goodman came up first with such an interesting idea in the 1980's [73]. Unfortunately, electromagnetic techniques can not be used to detect the DM since it is an electrically neutral particle. However, the elastic scattering between the DM and the nucleus provides the possibility to detect it. So, the knowledge of different astrophysical properties helps us in predicting the DM interaction rate with the underground detector.

- **Event Rate**

  The differential event rate is the most important quantity in the direct detection experiments, which is usually referred to as the differential rate unit (dru) [74–76]. The differential event rate is calculated per count, kg, day, and keV and expressed as

$$\frac{dR}{dE_{\rm NR}} = \frac{\rho_0}{m_N m_\chi} \int_{v>v_{min}} v f(v) \frac{d\sigma}{dE_{\rm NR}}(v, E_{\rm NR}) dv \tag{2.93}$$

  where m_N and m_χ are the masses of the nucleon and the dark matter, respectively, $E_{\rm NR}$ represents the nuclear recoil energy, and σ refers to the DM-nucleon scattering cross-section.

  Generally, the direct detection experiments consider the assumption that DM follows an isotropic distribution in a singular isothermal sphere, $\rho(r) \sim r^{-2}$. The DM local density is $\rho_\odot = \rho|_{r=R_\odot}$ with $R_\odot = 8.0 \pm 0.5$ kpc [77] represents the distance between the Sun and the galactic centre. The commonly used dark matter local density in the direct detection experiments is $\rho_\odot = 0.3\ \text{GeV/cm}^3$ [78].

DD commonly uses the isotropic and Gaussian velocity distribution

$$f(\vec{v}) = \frac{1}{\sqrt{2\pi}\sigma_v} e^{-|\vec{v}|^2/2\sigma_v^2} \tag{2.94}$$

where σ_v represents the velocity dispersion of the DM gas cloud. Here, this N-body simulation [79] supported approximation is known as the *Standard Halo Profile*. The velocity dispersion can be written in terms of the circular velocity of the galaxy as $\sigma_v = \sqrt{3/2}v_c$, with $v_c = 220 \pm 20$ km/s [80].
The integral integrates over all possible velocities above a certain minimum velocity which is fixed by the requirement to induce the nuclear recoil. One can obtain this minimum velocity by using simple kinematics as

$$v_{min} = \sqrt{\frac{m_N E_{\rm NR}}{2\mu_{\chi N}^2}} \tag{2.95}$$

where $\mu_{\chi N} = \frac{m_\chi m_N}{m_\chi + m_N}$ is the reduced mass of the dark matter and nucleon system. The DM escapes from the the DM halo when the velocity of DM is larger than the escape velocity, $v > v_{\rm esc} = 544$ km/s [81].
The total event rate per kilogram per day can be estimated by integrating the Equation 2.93 in the range of possible energies of the nuclear recoil as follows

$$R = \int_{E_{\rm NR,low}}^{E_{\rm NR,high}} dE_{\rm NR}\ \epsilon(E_{\rm NR})\ \frac{dR}{dE_{\rm NR}} \tag{2.96}$$

Where $\epsilon(E_{\rm NR})$ is the efficiency of the detector and $E_{\rm NR,low}$ refers to the threshold of the detector. Here the value of the $E_{\rm NR,high}$ fixes by the kinematics as

$$E_{\rm NR,high} = \frac{2\mu_{\chi N} v_{\rm esc}^2}{m_N} \tag{2.97}$$

- **DM Nucleus Cross-Section**
  Equation 2.97 gives the rate of the interaction of DM with the Nucleus with the detector per day and per kilogram. All the information about the DM-Nucleus interaction is encoded in the DM-Nucleus cross-section.

$$\frac{d\sigma}{dE_{\rm NR}} = \left(\frac{d\sigma}{dE_{\rm NR}}\right)_{\rm SI} + \left(\frac{d\sigma}{dE_{\rm NR}}\right)_{\rm SD} \tag{2.98}$$

  This cross-section is comprised of two contributions; one is the spin-independent contribution which arises from the DM coupling with the scalar as well as

Nucleon	Δ_u	Δ_d	Δ_s
Protons	0.80(3)	-0.46(4)	-0.12(8)
Neutrons	-0.46(4)	0.80(3)	-0.12(8)

Table 2.1: Displays the matrix element of the axial-vector current in a nucleon. The first row shows Δ_q^p where the second row shows Δ_q^n [86].

the vector, and the other is the spin-dependent contribution that comes because of the axial-vector interaction of the DM.
The DM-nucleus cross-section relies on the DM-nucleon cross-section, where the microscopic information of the collision is encoded. In the case of a small momentum transfer from dark matter to the nucleus, one can obtain an expression relating to the microscopic and macroscopic cross-sections.

(a) **Spin-Dependent Cross-Section**

The spin-dependent cross-section depends on the spin of the dark matter and the angular momentum of the system. The expression takes the following form for the fermionic dark matter [75]

$$\left(\frac{d\sigma}{dE_{\rm NR}}\right)_{\rm SD} = \frac{16G_F^2 m_N}{\pi v^2}\frac{J+1}{J}(a_p\langle S_p\rangle + a_p\langle S_p\rangle)^2\frac{S(E_{\rm NR})}{S(0)} \tag{2.99}$$

Where $S(E_{\rm NR})$ and $S(0)$ represent the form factors, $\langle S_{p,n}\rangle$ refer to the expectation values of the spin content of the nucleus and J represents the total angular momentum of the nucleus. Here the coefficients a_p and a_n can be expressed as

$$\begin{cases} a_p = \sum_{q=u,d,s} \frac{\alpha_q^A}{\sqrt{2}G_F}\Delta_q^p \\ a_n = \sum_{q=u,d,s} \frac{\alpha_q^A}{\sqrt{2}G_F}\Delta_q^n \end{cases} \tag{2.100}$$

The different α^A couplings arise from the dark matter axial-vector interaction with the quarks, which are model dependent. In addition, the information about the quark spin content of the nucleon are encoded in $\Delta_q^{n,p}$ which are proportional to $\langle N|\bar{q}\gamma_\mu\gamma_5 q|N\rangle$. Generally, the lattice QCD [82] and the experimental nuclear physics techniques [83–85] both strategies are used to determine these coefficients. The values of $\Delta_q^{n,p}$ are shown in Table 2.1.

(b) **Spin-Independent Cross-Section**

The cross-section is independent of the spin of the dark matter and the nucleus angular momentum in the limit of zero momentum trans-

Nucleon	f_{TG}	f_{Tu}	f_{Td}	f_{Ts}
Protons	0.917(19)	0.018(5)	0.027(7)	-0.037(17)
Neutrons	0.910(20)	0.013(3)	0.040(10)	0.037(17)

Table 2.2: Displays the light quarks contribution to the mass of the proton and neutron where the numbers in the parentheses represent the one sigma uncertainity [91].

fer [87]. The expression can be written as

$$\left(\frac{d\sigma}{dE_{\rm NR}}\right)_{\rm SI} = \frac{2m_N}{\pi v^2}\left([Zf^p + (A-Z)f^n]^2 + \frac{B_N^2}{256}\right)F^2(E_{\rm NR}) \quad (2.101)$$

Where $B_N \equiv \alpha_u^V(A+Z) + \alpha_d^V(2A-Z)$ refers contribution due to the vector vector interaction and $\alpha_{u,d}^V$ represents the vector vector coupling between the DM and the u and d quarks. Here (A, Z) are the number of neutrons and protons of the nucleus and $F^2(E_{\rm NR})$ is the experimental form factor [88, 89].

Ultimately, the quantity $f^{p,n}$ has the following structure

$$\frac{f^{p,n}}{m_{p,n}} = \sum_{q=u,d,s}\frac{\alpha_q^S}{m_q}f_{Tq}^p + \frac{2}{27}f_{T,G}^p\sum_{q=u,d,s}\frac{\alpha_q^S}{m_q} \quad (2.102)$$

Where α_q^S represents the scalar-scalar coupling of the DM with the quarks. The nucleon matrix elements are encoded in the coefficients $f_{T,q}^{p,n}$, which gives the contribution of the light quarks of the nucleus. These coefficients have the following definitions

$$f_{T,q}^{p,n} = \frac{m_q}{m_{p,n}}\langle N|\bar{q}q|N\rangle \quad (2.103)$$

These quantities are calculated using the Lattice QCD or experimentally or precisely using the measurements of the pion-nucleon sigma term [90]. Here $f_{T,G}^{p,n}$ denotes the contribution of the gluons to the mass of the nucleon and can be defined as

$$f_{T,G}^{p,n} = 1 - \sum_{q=u,d,s} f_{T,q}^{p,n} \quad (2.104)$$

All the constants discussed here are summarized in Table 2.2.

- **Current Status of Direct Detection Landscape**

  The search for dark matter becomes one of the tough challenges of the High energy physics. Many experimental groups have been trying their best to

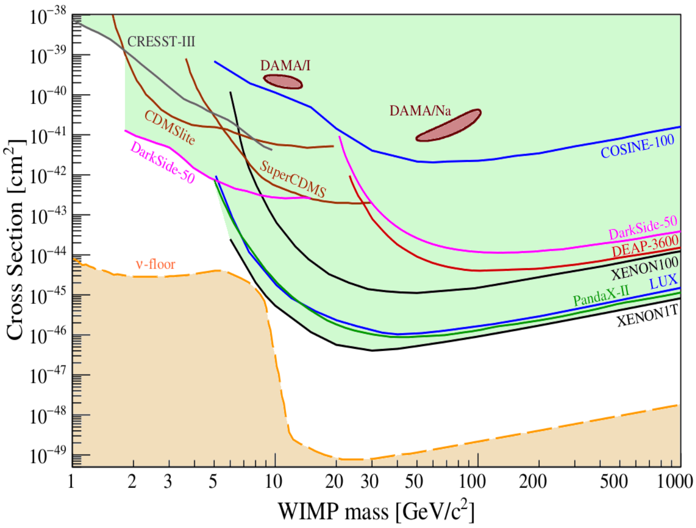

Figure 2.10: Bounds from SI direct detection experiments of dark matter. The excluded region is the space above the different lines. The two contours filled with red colors display the DM observation from DAMA/LIBRA, and the yellow region refers to the neutrino floor [92]. Image taken from [70]

detect the DM over several years, though they do not found any signature of WIMP dark matter or other forms of dark matter. So, we only have experimental bounds on the theoretical model of dark matter.

The first experiment of direct detection started in 1987 when 0.72 kg of high purity germanium crystal was used as a target. After that, several DD experiments were performed, which further improved the experimental bound on the dark matter. Nowadays, the landscape of DM searches consists of several DD experiments where the present experiments use novel gas like Xenon, argon, etc., as targets.

Among different search strategies, the DD experiments play a very important role in placing a very strong bound on DM. As we discussed, there are two kinds of cross-section of dark matter one is spin-dependent, and another is spin-independent; between strongest bounds come from the spin-independent cross-section for most of the models. Some of the current limits on dark matter have been shown in Figure 2.10. The signature of the direct detection experiments for the WIMP dark matters occurs due to the single scatter nuclear recoils. Interestingly, the coherent neutrino-nucleus scattering (CNNS) also produces the same kind of signal (in any detector), which generates irreducible background for the WIMP search. The limits in parameter space from the such background are shown in Figure 2.10 by the yellow dashed line, known as the "neutrino-floor," where it limits the parameter space from below.

2.4.2 Indirect Detection

The dark matter indirect detection is based on the search for the anomalous component in the cosmic rays as a result of the annihilation of the DM pair. Generally, there are three kinds of detectable fluxes which are charged particles, like electrons and positrons, protons and antiprotons, photons, and, finally, neutrino fluxes. Several works have appeared which have tried to find the DM signature since the 1970s. Some of the initial publications have looked at γ ray fluxes [93, 94], positron fluxes [95, 96], antiproton fluxes [97, 98] etc.
One can constrain the DM models by studying these fluxes of the stable particles that reached the Earth. Normally, in most of the BSM models, the annihilation of the DM particles produces the SM particles resulting in the final states with the stable particles. If such processes exist, then the signature of dark matter can be found in the cosmic rays detected on the Earth. The indirect detection aims to track the footprints of the dark matter in the stable particle fluxes detected in the experiments. However, it is not always true that DM annihilations should produce detectable signatures all the time. When the DM annihilation cross-section possesses dependency on the relative velocity of the dark matter, then the contribution of these processes to the flux of the stable particles is negligibly small as the velocity of DM today is very small. Though the study of all kinds of fluxes is interesting and important, here we are interested in the flux of uncharged particles or, more specifically, the photons.

- **Propagation of Uncharged Particles**
  There are two fluxes of uncharged particles arriving at Erath: the neutrinos flux and the photons flux. The most significant flux of the neutrinos is the solar neutrino flux generated in the Sun, and the other is the atmospheric neutrino flux produced in the atmosphere. These neutrinos can propagate easily because of their weak interaction with other particles, making their mean path larger. In the propagation, the neutrinos encounter several different effects; for a complete description of to deal with such subtilities, see the Ref [99].
  The other neutral particle on which our primary interest lies is the γ rays. The differential fluxes of photons produced due to the DM annihilation that reaches the Earth from a window of size $\Delta\Omega$ can be parametrized as [100]

$$\frac{d\Phi_\gamma}{dE}(E) = \frac{J}{8\pi m_\chi^2}\sum_f \langle\sigma v\rangle_f \frac{N_\gamma^f}{dE}(E), \tag{2.105}$$

with

$$J = \int_{\Delta\Omega} d\Omega \int \rho^2(s) ds \tag{2.106}$$

is called the J-factor, and it has all the astrophysical information. More precisely, the J-factor represents the integration of the DM profile along the line of sight. When the γ rays are produced via the decay of DM, the flux is given by

$$\frac{d\Phi_\gamma}{dE}(E) = \frac{J}{4\pi m_\chi} \sum_f \Gamma_f \frac{N_\gamma^f}{dE}(E), \tag{2.107}$$

where

$$J = \int_{\Delta\Omega} d\Omega \int \rho^2(s) ds \tag{2.108}$$

- **Experimental status of indirect detection**
  The current prospect of indirect detection plays a vital role in providing constraints on the BSM models having dark matter candidates. Here, we will give a current status for the γ ray searches.
  In indirect detection, the γ-ray search experiments are the most promising source in placing bounds. The dwarf spheroidal galaxies are DM-dominated objects, and it emits low diffuse γ rays. One can set limits on different BSM models by using the observation of the photons coming from dwarf spheroidal galaxies.
  A few years back, the photon flux of 15 different dSphs was analyzed by the Fermi-LAT experiment. Generally, the Fermi collaboration has studied photons with energy range 500 MeV to 500 GeV [101, 102].
  Though the dSphs are providing the strongest bounds as a γ ray source, different advancements have been made to study the γ rays coming from the galactic center and other sources [103, 104].

2.4.3 Collider searches

We have already discussed different techniques of direct detection and indirect detection. So, it is necessary to talk about the production of dark matter at colliders for the completion of the DM search strategies. The LHC searches give the current strongest bound on the dark matter. Since the dark matter does not have any electromagnetic and strong interaction, so it remains undetected at the collider, leaving the signature of missing energy or the missing momentum. Now, we discuss some DM searches at collider .

1. **Invisible decay of the SM-Higgs**
   ATLAS and CMS impose bounds on the invisible decay of the Higgs, and the current bound can be found in the Ref [105]. One can constrain the DM model when the DM couples to the Higgs for the DM mass $m_{DM} \leq m_h/2$.

2. **Invisible decay of the SM Z-boson**
   In some scenarios, the DM directly couples to the Z boson, where the precise measurements of Z at LEP contain the DM. Here also, the mass of the dark matter has to satisfy the criterion $m_{DM} \leq m_Z/2$ like the Higgs case.

3. **Mono-X searches**
   In some cases, the DM does not interact directly with the SM particles. Here, the DM can be produced along with some standard model particles at the collider. In such cases, one can talk about the DM by studying the SM particles which have been produced along with the dark matter. Here this X stands for these SM particles, which can be Higgs, Z boson, QCD jets, etc

   .

Chapter 3

Pseudo-Dirac dark matter and radiative neutrino mass in a singlet doublet scenario

3.1 Introduction

In this chapter, we study a simple extension of Standard Model, which offers a common origin for pseudo-Dirac dark matter interaction with the visible sector and radiative generation of neutrino mass. The singlet doublet fermionic dark matter scenario is studied extensively [106–112, 112–117, 117–123, 123, 123–136], and it falls within the WIMP paradigm. There are two neutral fermion states in this set up which mix with each other and the lightest one is identified as the DM candidate. The mixing angle depends on the coupling strength of the singlet and doublet fermion with the SM Higgs. The magnitude of this mixing angle determines whether the DM is singlet like or doublet dominated. In singlet doublet model DM candidate can be probed at direct search experiments through its interaction with nucleon mediated by the SM Higgs and the neutral gauge boson. However, the null results at direct search experiments restrict the range of the mixing angle below $\lesssim 0.06$ [106], making the DM almost purely singlet dominated. Considering a setup where SM is extended with a singlet fermion, Ref. [137] (subsequently in Ref. [138]) demonstrated that inclusion of a small Majorana mass term for the singlet fermion in the Lagrangian splits the DM eigenstate into two nearly-degenerate Majorana states with a tiny mass difference. In the small Majorana mass limit, the splitting does not make any difference to the relic abundance analysis, however, making a vital portal to direct detection of the pseudo-Dirac DM candidate [137]. We apply this interesting feature in the singlet doublet dark matter model by allowing a small Majorana mass term for the singlet fermion in addition to the Dirac terms for both the singlet and doublet. This inclusion brings a significant relaxation on the singlet doublet mixing angle, which is otherwise severely constrained, as discussed before. Present model may also provide exciting implications in collider searches with rich phenomenology. However, it is even more appealing to note the implication in yet another sector, seemingly unrelated so far.

We make use of the same Majorana mass term for the singlet fermion in generating the low energy neutrino mass radiatively [30, 139]. The present mechanism of neutrino mass generation is also familiar as the scotogenic inverse seesaw scheme. In the process, we extend the minimal version of the singlet doublet DM framework with multiple copies of a real scalar singlet fields *. These additional scalar fields can couple with the SM leptons and the doublet fermion through lepton number violating vertices. Thus in the radiative one-loop level DM particles and the singlet scalars take part in the generation of neutrino masses. As a result, the eigenvalues of the SM neutrinos are determined by the masses of DM sector particles, scalar singlets and the Majorana mass parameter of the singlet fermion. More importantly, the Majorana nature of the SM neutrino is solely determined by the introduced Majorana mass term for the singlet fermion, which also helps in successfully evading the spin-independent (SI) constraints in dark matter. Thus the DM sector and the neutrino mass parameters are strongly correlated in the present set up which we are going to explore in detail.

The chapter is organized as follows. In Section 3.2, we present the structure of our model, which is primarily an extended form of the singlet doublet model. We describe the field content, their interactions and insertion of additional Majorana term. In Section 3.3, we discuss the consequence of our model in dark matter phenomenology. We examine the properties of our pseudo-Dirac dark matter candidate and how it extends its model parameter space evading the spin-independent direct detection limits. In Section 3.4, we explain the mechanism of radiative generation of neutrino mass and look at the parameter space where oscillation data can be satisfied simultaneously along with the dark matter constraints and relic. Finally, we conclude highlighting features of our study in Section 3.5.

3.2 The Model

We extend the SM particle sector by one $SU(2)_L$ doublet fermion (Ψ) and one gauge singlet fermion (χ). In addition, we also include three copies of a real

*A similar exercise on the radiative generation of neutrino mass within the singlet doublet DM framework is performed in Ref. [129] except having a pure Majorana type DM.

BSM and SM Fields	$SU(3)_C \times SU(2)_L \times U(1)_Y \equiv \mathcal{G}$			$U(1)_L$	Spin	$\mathcal{Z}_2$
$\Psi \equiv \begin{pmatrix} \psi^0 \\ \psi^- \end{pmatrix}$	1	2	$-\frac{1}{2}$	0	$\frac{1}{2}$	$-$
χ	1	1	0	0	$\frac{1}{2}$	$-$
$\phi_i\ (i = 1, 2, 3)$	1	1	0	0	0	$-$
$\ell_L \equiv \begin{pmatrix} \nu_\ell \\ \ell \end{pmatrix}$	1	2	$-\frac{1}{2}$	1	$\frac{1}{2}$	$+$
$H \equiv \begin{pmatrix} w^+ \\ \frac{1}{\sqrt{2}}(v + h + iz) \end{pmatrix}$	1	2	$\frac{1}{2}$	0	0	$+$

Table 3.1: Field contents and charge assignments under the SM gauge symmetry, Lepton number, Spin and additional $\mathcal{Z}_2$.

scalar singlet field ($\phi_{1,2,3}$). The BSM fields are charged under an additional $\mathcal{Z}_2$ symmetry while SM fields transform trivially under this additionally imposed $\mathcal{Z}_2$ (see Table 3.1). The BSM fields do not carry any lepton numbers. The Lagrangian of the scalar sector is given by

$$\mathcal{L}_{scalar} = |D^\mu H|^2 + \frac{1}{2}(\partial_\mu \phi)^2 - V(H, \phi), \tag{3.1}$$

where,

$$D^\mu = \partial^\mu - ig\frac{\sigma^a}{2}W^{a\mu} - ig'\frac{Y}{2}B^\mu, \tag{3.2}$$

with g and g' being the $SU(2)_L$ and the $U(1)_Y$ gauge couplings respectively. The scalar potential $V(H, \phi)$ takes the following form

$$V(H, \phi_i) = -\mu_H^2\,(H^\dagger H) + \lambda_H\,(H^\dagger H)^2 + \frac{\mu_{ij}^2}{2}\,\phi_i\phi_j + \lambda_{ijk}\phi_i^2\phi_j\phi_k + \frac{\lambda_{ij}}{2}\,\phi_i\phi_j(H^\dagger H). \tag{3.3}$$

We consider μ_H^2, μ_{ij}^2 and the quartic coupling coefficients λ_{ij} and λ_{ijk} are real and positive. In general the mass term for scalars (μ_{ij}^2), the quartic coupling coefficients (λ_{ij}, λ_{ijk}) are non diagonal. The vacuum expectation values (vev) of all the scalars H and $\phi_{1,2,3}$'s after minimising the scalar potential in the limit $\mu_H^2, \mu_{ij}^2 > 0$ are obtained as,

$$\langle H \rangle = v, \quad \langle \phi_{1,2,3} \rangle = 0. \tag{3.4}$$

Since all the quartic couplings are positive, the scalar potential is bounded from below in any field direction with the set of stable vacuum in Equation 3.4 [140, 141]. For sake of simplicity † we assume that μ_{ij}^2, λ_{ij}, λ_{ijk} are diagonal with the masses of the scalar fields parametrised as $(M_{\phi_1}^2, M_{\phi_2}^2, M_{\phi_3}^2)$. The discrete symmetry $\mathcal{Z}_2$ remains unbroken since $\langle \phi_{1,2,3} \rangle = 0$. The Lagrangian for the fermionic sector (consistent with the charge assignments) is written as:

$$\mathcal{L} = \mathcal{L}_f + \mathcal{L}_Y, \tag{3.5}$$

where,

$$\begin{aligned}\mathcal{L}_f &= i\overline{\Psi}_L\gamma_\mu D^\mu\Psi_L + i\overline{\Psi}_R\gamma_\mu D^\mu\Psi_R + i\overline{\chi}_L\gamma_\mu\partial^\mu\chi_L + i\overline{\chi}_R\gamma_\mu\partial^\mu\chi_R \\ &- M_\Psi\overline{\Psi}_L\Psi_R - M_\Psi\overline{\Psi}_R\Psi_L - M_\chi\overline{\chi}_L\chi_R - \frac{m_{\chi_L}}{2}\overline{\chi_L^c}\chi_L - \frac{m_{\chi_R}}{2}\overline{\chi_R^c}\chi_R,\end{aligned} \tag{3.6}$$

and

$$\mathcal{L}_Y = Y\overline{\Psi}_L\tilde{H}\chi_R + h_{ij}\overline{\ell_i}\Psi_R\phi_j + h.c.. \tag{3.7}$$

We keep a small Majorana mass ($m_{\chi_{L,R}} \ll M_\chi$) term for the χ field in Equation 3.6. In this particular set up the lightest neutral fermion is a viable dark matter candidate which has a pseudo-Dirac nature provided a tiny $m_{\chi_{L,R}}$ exists. The choice of this non-vanishing $m_{\chi_{L,R}}$ is kept from the necessity of evading strong spin-independent dark matter direct detection bound. As we will see later that this term is also helpful in generating light neutrino mass radiatively. The first term in Equation 3.7 provides the interaction of DM with the SM particles mediated through the Higgs. While the second term in Equation 3.7 violates the lepton number explicitly ‡. This kind of lepton number violation could trigger a thermal or non-thermal leptogenesis (baryogenesis) in the early Universe, provided sufficient CP asymmetry is generated [53].

3.3 Dark Matter

The different variants of singlet doublet fermion dark matter are extensively studied in the literature [106–129] over the years. Here we go through the DM phenomenology in brief. In the present study, we consider $M_\phi \gg M_\psi, m_{\chi_{L,R}}$ such that the role ϕ fields in DM phenomenology is minimal §. The Dirac mass matrix

†In the present analysis the quartic couplings for the singlet scalars have negligible role and can take any arbitrary positive value within their respective perturbativity bounds [142, 143].

‡Consideration of complex scalar singlets instead of real ones would lead to the conservation of the lepton number [129].

§In principle, scalars could take part in DM phenomenology through coannihilation processes. However, considering the mass pattern, we have chosen for simplicity, their contributions turn out to be negligible.

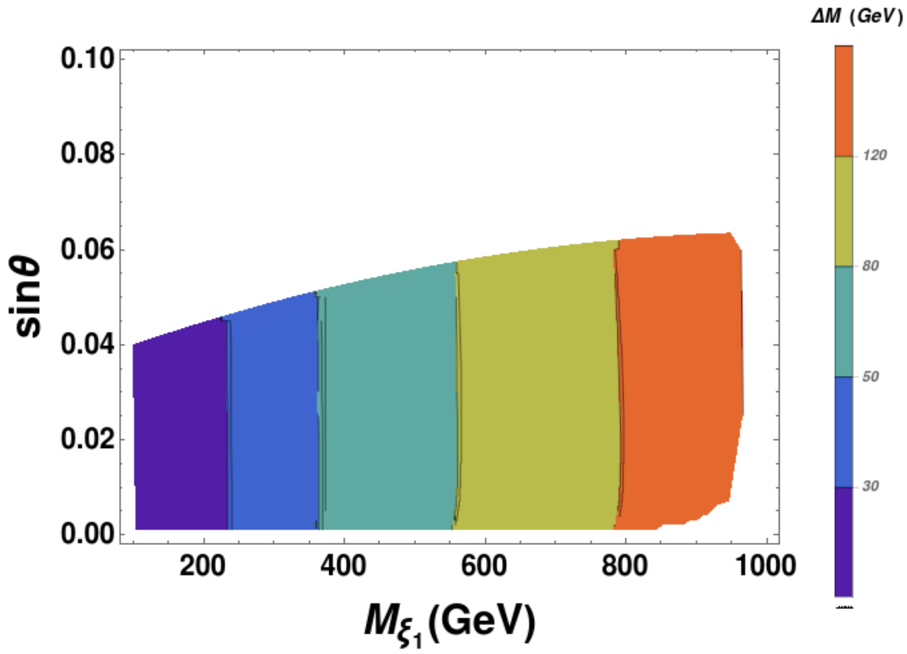

Figure 3.1: Region of parameter space allowed from both the relic density and direct detection bounds are shown in a plane of dark matter mass M_{ξ_1} and mixing angle $\sin\theta$, in the limit Majorana mass $m_{\chi_{L,R}} = 0$. Different colors are for different values of mass gap $\Delta M = (M_{\xi_2} - M_{\xi_1})$ allowed here. In this scenario, upper limit in $\sin\theta$ is strongly constrained from direct detection bounds which gradually relaxed with higher dark matter mass and thus a lower cross section.

for the neutral DM sector after the spontaneous breakdown of the electroweak symmetry is obtained as (in $m_{\chi_{L,R}} \to 0$ limit),

$$\mathcal{M}_D = \begin{pmatrix} M_\Psi & M_D \\ M_D & M_\chi \end{pmatrix}, \tag{3.8}$$

where we define $M_D = \frac{Yv}{\sqrt{2}}$. Therefore, we are left with two neutral Dirac particles which we identify as (ξ_1, ξ_2). The mass eigenvalues of (ξ_1, ξ_2) are given by,

$$M_{\xi_1} \approx M_\chi - \frac{M_D^2}{M_\Psi - M_\chi} \tag{3.9}$$

$$M_{\xi_2} \approx M_\Psi + \frac{M_D^2}{M_\Psi - M_\chi} \tag{3.10}$$

Therefore, the lightest state is ξ_1, which we identify as our DM candidate. The DM stability is achieved by the unbroken $\mathcal{Z}_2$ symmetry. The mixing between two flavor states, *i.e.* neutral part of the doublet (ψ^0) and the singlet field (χ) is parameterised by θ as

$$\sin 2\theta \simeq \frac{2Yv}{\Delta M}, \tag{3.11}$$

where $\Delta M = M_{\xi_2} - M_{\xi_1} \approx M_\Psi - M_\chi$ in the small Y limit. In small mixing case, ξ_1 can be identified with the singlet χ. The DM phenomenology is mainly controlled by the following independent parameters.

$$\{M_\Psi,\ M_\chi,\ \theta\}. \tag{3.12}$$

The DM would have both annihilation and coannihilation channels to SM particles, including the gauge bosons [118, 122] as shown in Figure D.1 of Appendix D. It turns out that the coannihilation channels play the dominant role in determining the relic abundance for pure singlet doublet fermion DM since the annihilation processes are proportional to the square of mixing angle and hence suppressed in the small mixing limit. The DM can be searched directly through its spin-independent scattering with nucleon mediated by both SM Higgs and Z boson as depicted in Figure D.2 of Appendix D. In Figure 3.1 we show the observed relic abundance by Planck 2018 [144] and spin-independent direct detection bounds (from XENON 1T [145]) satisfied region in $\sin\theta - M_{\xi_1}$ plane for different values of M_{ξ_2} in the absence of the Majorana mass term ($m_{\chi_{L,R}}$). We have used Micromega 4.3.5 [146] package for the numerical analysis. It is observed that the relic abundance is satisfied for a particular M_{ξ_1} when $\Delta M = M_{\xi_2} - M_{\xi_1}$ is small. This means the coannihilation processes are dominant compared to the annihilation processes in determining the observed relic abundance. One important point to note is that the required amount of ΔM increases with the DM mass for any fixed value of $\sin\theta$. Figure 3.1 also evinces strong constraint on $\sin\theta \lesssim 0.06$ primarily from the direct detection bounds, which gradually relaxed with higher dark matter masses because of a lower cross section. Finally, it keeps the DM framework alive from spin-independent direct detection bound.

The strong upper bound on $\sin\theta$ can be alleviated by taking the presence of $m_{\chi_{L,R}}$ into account. The tiny nature of $m_{\chi_{L,R}}$ makes ξ_1 pseudo-Dirac. In the limit $m \to 0$ where we define $m = (m_{\chi_L} + m_{\chi_R})/2$, the Majorana eigenstates of ξ_1 (*i.e.* $\zeta_1,\ \zeta_2$) become degenerate. The presence of a non-zero $m_{\chi_{L,R}}$ breaks this degeneracy, and we can still write

$$\zeta_1 \simeq \frac{i}{\sqrt{2}}(\xi_1 - \xi_1^c), \tag{3.13}$$

$$\zeta_2 \simeq \frac{1}{\sqrt{2}}(\xi_1 + \xi_1^c). \tag{3.14}$$

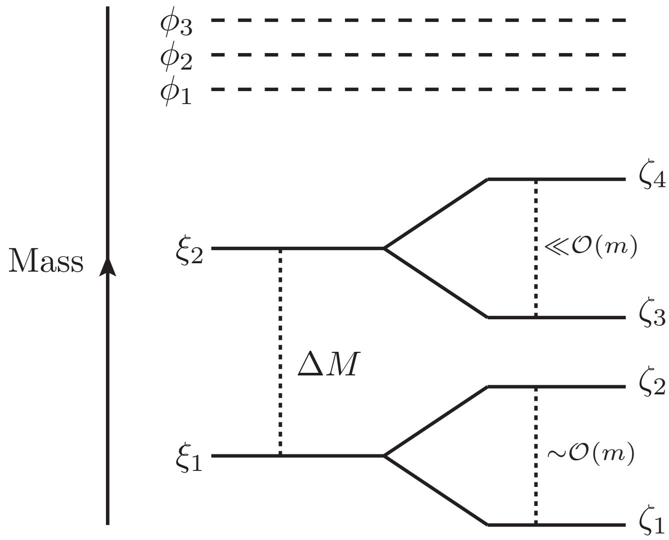

Figure 3.2: Mass spectrum of the dark sector, showing the lightest pseudo-Dirac mode as dark matter and other heavy BSM fermions and scalars. Generation of large mass difference (ΔM) and small mass gap (m) discussed at the text expressed at the zeroth order of δ_r. Scalars are assumed to be heavier in this study.

in the pseudo-Dirac limit $m \ll M_{\zeta_1}, M_{\zeta_2}$ where $M_{\zeta_1,\zeta_2} \simeq M_{\xi_1} \mp m$. Similarly, the state ξ_2 is spilt into ζ_3 and ζ_4. Hence we will have four neutral pseudo-Dirac mass eigenstates in the DM sector. The complete mass spectrum of the neutral dark sector particles is displayed in Figure 3.2. The mass of the charged fermion ψ^- lies in between ζ_3 and ζ_2 as followed from Equation 3.9. The pseudo-Dirac nature of the eigenstates forbid the interaction of DM (ζ_1) with the neutral current mediated by SM Z boson at zeroth order of $\delta_r \simeq (m_{\chi_L} - m_{\chi_R})/m_{\xi_1}$. Thus the pseudo-Dirac DM could have the potential to escape the SI direct search bound. Although at next to leading order, the DM still possesses non-vanishing interaction with Z boson depending on the magnitude of δ_r. This is analyzed in the next paragraph. It is important to note that the m can not be arbitrarily small since there exists a possibility of the lighter state ζ_1 to scatter inelastically with the nucleon to produce heavier state ζ_2 [147–149]. It imposes some sort of lower bound on $m \gtrsim \mathcal{O}(1)$ KeV [147–149] in order to switch off such kind of interaction. However, the presence of a vertex like $\bar{\zeta_1}\gamma^\mu\zeta_2$ can give rise to huge Z mediated s-channel coannihilation cross section of the DM with the next to lightest state (NLSP) [148] in the above mentioned limiting value of m. This cross section would have a suppression factor of $\sin^4\theta$. In spite of this, for moderate values of $\sin\theta$, the cross section can turn huge. We have examined and found that keeping $m \sim \mathcal{O}(1)$ GeV effectively prevents the Z mediated s-channel coannihilation of the DM with the NLSP [149] even with moderate values of $\sin\theta$. A similar result

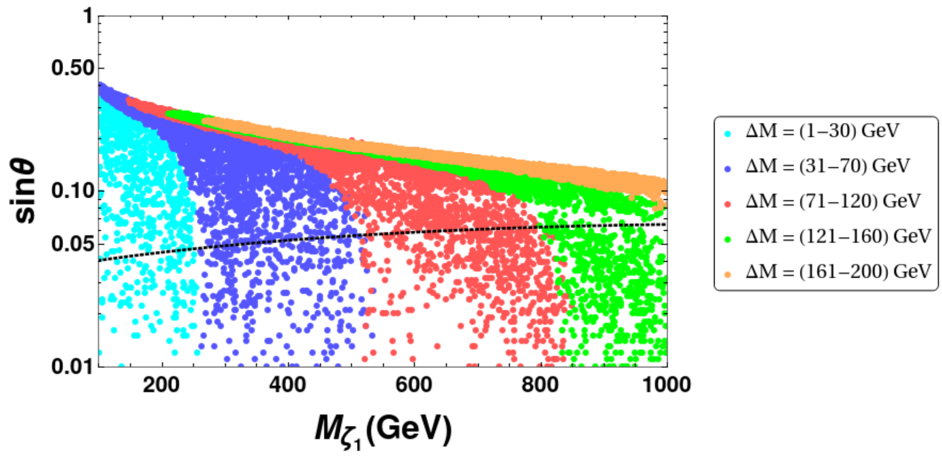

Figure 3.3: Region of parameter space allowed from both the relic density and direct detection bounds are shown in a plane of dark matter mass M_{ζ_1} and mixing angle $\sin\theta$, in case of a nonzero but small Majorana mass $m_{\chi_{L,R}}$ insertion. Different colors are for different values of mass gap $\Delta M = (M_{\xi_2} - M_{\xi_1})$ allowed here. It is instructive to compare this present plot with Figure 3.1. Unlike the previous $m_{\chi_{L,R}} = 0$ case (denoted by black dotted line here), upper limit from direct detection is much relaxed and barely constrained in this scenario. The present upper limit in $\sin\theta$ is primarily constrained from the relic density criteria and (unlike the previous case) constrain is being stronger at higher dark matter mass.

is obtained in Ref. [137,150]. At linear order in δ_r, a direct search of pseudo-Dirac dark matter through Z-mediation is still possible which we discuss below.

The vector operator for the SI direct search process mediated by Z boson will be modified to

$$\mathcal{L} \supset \alpha(\bar{\zeta_1}\gamma^\mu\zeta_1)(\bar{q}\gamma_\mu q), \tag{3.15}$$

with $\alpha = \frac{4g^2\delta_r \sin^2\theta}{m_Z^2\cos^2\theta_W}C_V^q = \alpha' C_V^q$ and g as the $SU(2)_L$ gauge coupling constant. Note that, at zeroth order in δ_r, vector boson interaction of dark matter would vanish, and only the Higgs mediated processes would contribute to the direct search. Considering DM mass larger than the nucleon mass, the spin-independent direct detection cross section per nucleon is obtained as [106,108]

$$\sigma^{\rm SI} \simeq \frac{a}{\pi}\frac{M_{\zeta_1}^2 m_N^2 \alpha'^2}{(M_{\xi_1}+m_N)^2 A^2}\left[ZC_V^p + (A-Z)C_V^n\right]^2, \tag{3.16}$$

where $m_N = 940$ MeV, the nucleon mass, θ_W is the Weinberg angle and $C_V^p = \frac{1}{2}(1-4\sin^2\theta_W)$, $C_V^n = -\frac{1}{2}$. It is clear from the smallness of the term $(1-4\sin^2\theta_W)$ that, the DM particle rarely talks to protons, and hence the SI cross section mainly depends on the DM interaction with neutrons. For Dirac fermion $a =$

1 [151], while for Majorana $a = \frac{1}{4}$ [151]. From the above relation, one can extract δ_r as follows,

$$\delta_r = 1.07 \times 10^{19} \left(\frac{\sigma^{\rm SI}}{\rm cm^2}\right)^{1/2} \left(\frac{1}{\sin^2\theta}\right). \tag{3.17}$$

Now to evade direct search constraints for the DM mass $\gtrsim 100$ GeV, it is sufficient to have $\sigma^{\rm SI} \lesssim 10^{-47}$ cm^2. Imposing this bound in Equation 3.17, we can report an upper bound on the difference of Majorana mass parameters $m_{\chi_L} - m_{\chi_R}$ which is,

$$m_{\chi_L} - m_{\chi_R} \lesssim 3.4 \times 10^{-5} \frac{M_{\zeta_1}}{\sin^2\theta}. \tag{3.18}$$

The above bound turns out to be strongest for smaller M_{ζ_1} and larger $\sin\theta$. For the present analysis, where we accommodate a WIMP like candidate with mass $\mathcal{O}(100)$ GeV and $\sin\theta \lesssim 0.3$. This automatically sets the bound as follows

$$m_{\chi_L} - m_{\chi_R} \lesssim 13.5 \text{ MeV}. \tag{3.19}$$

Taking the contribution of the Z mediated interaction of the DM with nucleon of the order of $\mathcal{O}(10^{-47})$ cm^2 and considering $m_{\chi_L} \simeq m_{\chi_R} = 1$ GeV, we have plotted the relic abundance and direct search allowed points on $\sin\theta - M_{\zeta_1}$ plane in Figure 3.3. Different colors are presented for different values of mass gap $\Delta M = (M_{\xi_2} - M_{\xi_1})$ allowed here. It is instructive to compare this present plot with Figure 3.1. Unlike the previous $m_{\chi_{L,R}} = 0$ case (upper constraint limit of which is illustrated by a black dotted line in current plot), here upper limit from direct detection is much relaxed and barely constrains this scenario. In fact, the present upper limit in $\sin\theta$ is primarily constrained from the relic density criteria, and unlike the previous case, the constraint is being stronger at higher dark matter mass. From this analysis, it is clear that the earlier obtained limit on $\sin\theta$ got relaxed at a considerably good amount. Another notable feature of Figure 3.3 is that for lighter DM, large mass splitting is allowed for higher values of $\sin\theta$. This follows from the fact that the annihilation cross section starts to play an equivalent role as coannihilation at large $\sin\theta$. The above values of Majorana mass parameters would be used to evaluate the neutrino mass.

The allowed parameter space of DM in Figure 3.3 is also subject to indirect detection constraints. The indirect search for dark matter experiments aims to detect the SM particles produced through DM annihilation in a different region of our observable universe where DM is possibly present abundantly, such as the center of our galaxy or satellite galaxies. Among the many final states, photon and

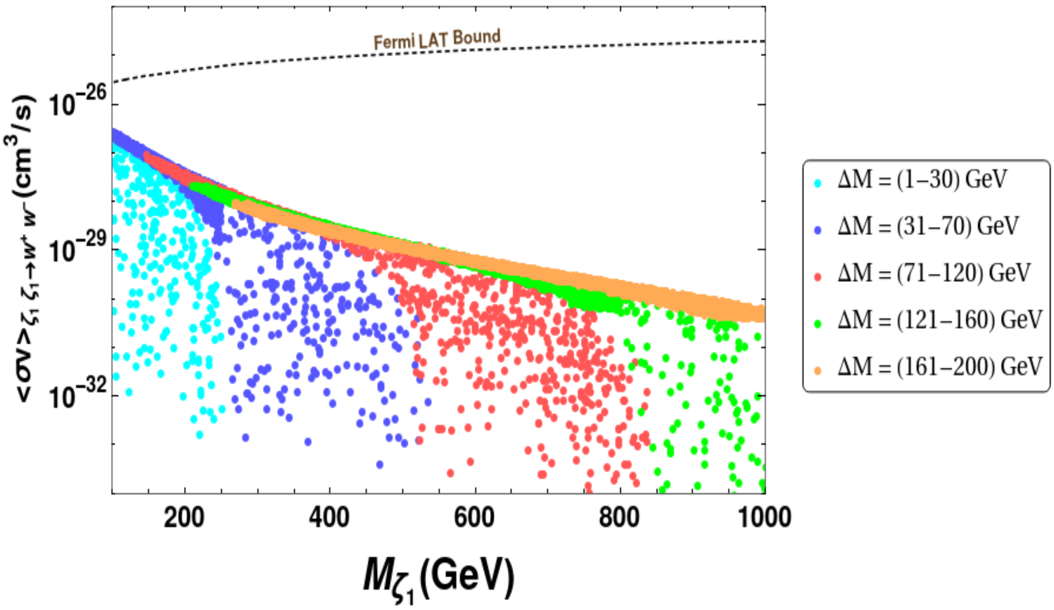

Figure 3.4: Annihilation cross sections for relic and direct search satisfied points of DM (see Figure 3.3) to W^+W^- final states for different sets of ΔM. The bound from Fermi LAT+MAGIC [152] is also included for comparison purpose.

neutrinos, being neutral and stable can reach the indirect detection experiments without significant deviation in the intermediate regions. Strong constraint is deduced from the measured photons at space based telescopes like the Fermi-LAT or ground based telescopes like MAGIC [152]. The photon flux in a specific energy range is written as

$$\Phi_F = \frac{1}{4\pi} \frac{\langle \sigma v \rangle_{\rm ann}}{2m_{DM}^2} \int_{E_{\rm min}}^{E_{\rm max}} \frac{dN_\gamma}{dE_\gamma} dE_\gamma \times J, \tag{3.20}$$

where $J = \int dx \rho^2(r(b,l,x))$ encapsulate the cosmological factors, conventionally known as $J-$factor, representing the integrated DM density within the observable solid angle along the line of sight (LOS) of the location. $r(b,l,x)$ is the distance of the DM halo in coordinate represented by b, l and $\rho(r)$ is the DM density profile. From the observed Gamma ray flux produced by DM annihilations, one can restrict the relevant parameters which contribute to the DM annihilation into different charged final states like $\mu^+\mu^-$, $\tau^+\tau^-$, W^+W^- and b^+b^-.

Let us recall that the relic satisfied region in Figure 3.3 is mostly due to the coannihilation effects provided the DM annihilations remain subdominant. Although for larger $\sin\theta$, DM annihilations start to contribute to the relic density at a decent amount. Among the many final states of DM annihilation in our scenario, $\langle \sigma v \rangle_{\zeta_1\zeta_1}$ is the dominant one with contributions from both s and t channels mediated by $\psi^\pm$ and the SM Higgs. In particular, the annihilation channels having $W^{\pm}$ in the final states involve $SU(2)_L$ gauge coupling. Therefore, to check the consistency of our framework against the indirect detection bounds, we focus on DM annihilation into W-pair $\zeta_1\zeta_1 \to W^+W^-$ as shown in Figure D.3 of Appendix D. In Figure 3.4, we exhibit the magnitude of $\langle\sigma v\rangle_{\zeta_1\zeta_1\to W^+W^-}$ for all the relic satisfied points in Figure 3.3 and compare it with the existing experimental bound from Fermi-Lat [152]. We see that all the relic satisfied points lie well below the experimental limit. We also confirm that the model precisely satisfies the indirect search bounds on other relevant final state charged particles.

Before we end this section, it is pertinent to note that in this analysis, our focus was on the DM having mass in between hundred GeV to one TeV. Naturally, a question emerges that what happens for the higher DM masses. Since we have two independent parameters, namely ΔM and $\sin\theta$, it is possible to account for the correct order of relic abundance for any arbitrary DM mass by tuning one of these. Besides, stringent direct search bound can also be escaped easily with a vanishing tree level neutral current (due to pseudo-Dirac nature of DM) unless $\sin\theta$ turns extremely large. We have numerically checked that even for DM as massive as 50 TeV, both relic density and direct search constraints can be satisfied in the present framework. However, a model independent conservative upper-bound on WIMP DM mass can be drawn using partial-wave unitarity criteria. The analysis performed in [153] points out that a stable elementary particle produced from thermal bath in the early Universe can not be arbitrarily massive ($\lesssim 34$ TeV) corresponding to $\Omega h^2 \sim 0.1$. Since it is a model independent bound, it applies in our case too.

3.4 Neutrino Mass

In the presence of the small Majorana mass term ($m_{\chi_{L,R}}$) of χ field and the lepton number violating operator in Equation 3.7, it is possible to generate active neutrino mass radiatively at one loop as displayed in Figure 3.5. It is worth mentioning that this type of mass generation scheme is known as one loop generation of inverse seesaw neutrino mass [154].

The neutrino mass takes the form as provided below [30, 139, 154],

$$m_{\nu_{ij}} = h^T_{ki}\Lambda_{kk}h_{jk}, \tag{3.21}$$

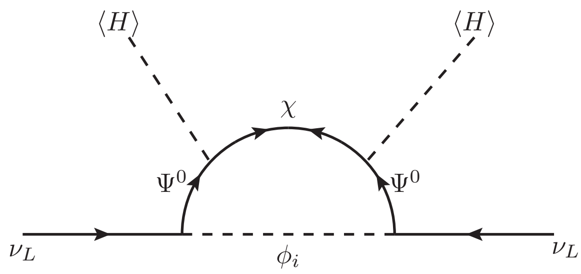

Figure 3.5: Generation of neutrino mass radiatively at one loop level getting contributions from tiny Majorana mass term inserted in the dark sector along with the heavy singlet scalars.

where, $\Lambda_{kk} = \Lambda^L_{kk} + \Lambda^R_{kk}$ with

$$\Lambda^L_{kk} = m_{\chi_L} \cos^2\theta \sin^2\theta \Big[\int \frac{d^4q}{(2\pi)^4} \frac{M^2_{\xi_1}}{(q^2 - M^2_{\phi_k})(q^2 - M^2_{\xi_1})^2} + \int \frac{d^4q}{(2\pi)^4} \frac{M^2_{\xi_2}}{(q^2 - M^2_{\phi_k})(q^2 - M^2_{\xi_2})^2} - \int \frac{d^4q}{(2\pi)^4} \frac{2M_{\xi_1}M_{\xi_2}}{(q^2 - M^2_{\phi_k})(q^2 - M^2_{\xi_1})(q^2 - M^2_{\xi_2})} \Big], \tag{3.22}$$

and

$$\Lambda^R_{kk} = m_{\chi_R} \cos^2\theta \sin^2\theta \Big[\int \frac{d^4q}{(2\pi)^4} \frac{q^2}{(q^2 - M^2_{\phi_k})(q^2 - M^2_{\xi_1})^2} + \int \frac{d^4q}{(2\pi)^4} \frac{q^2}{(q^2 - M^2_{\phi_k})(q^2 - M^2_{\xi_2})^2} - \int \frac{d^4q}{(2\pi)^4} \frac{2q^2}{(q^2 - M^2_{\phi_k})(q^2 - M^2_{\xi_1})(q^2 - M^2_{\xi_2})} \Big] \tag{3.23}$$

The h_{ij} is the Yukawa coupling as defined in Equation 3.7. Each integral of the above two expressions for Λ_{kk} can be decomposed as two 2-point Passarino-

Veltman functions [155, 156] as provided below:

$$\Lambda^L_{kk} = \frac{1}{16\pi^2} m_{\chi_L} \cos^2\theta \sin^2\theta \Big[\frac{M^2_{\xi_1}}{M^2_{\phi_k} - M^2_{\xi_1}} \{B(0, M_{\xi_1}, M_{\phi_k}) - B(0, M_{\xi_1}, M_{\xi_1})\}$$
$$+ \frac{M^2_{\xi_2}}{M^2_{\phi_k} - M^2_{\xi_2}} \{B(0, M_{\xi_2}, M_{\phi_k}) - B(0, M_{\xi_2}, M_{\xi_2})\}$$
$$- \frac{2M_{\xi_1} M_{\xi_2}}{M^2_{\xi_2} - M^2_{\xi_1}} \{B(0, M_{\xi_2}, M_{\phi_k}) - B(0, M_{\xi_1}, M_{\phi_k})\} \Big], \tag{3.24}$$

$$\Lambda^R_{kk} = \frac{1}{16\pi^2} m_{\chi_R} \cos^2\theta \sin^2\theta \Bigg[\{B(0, M_{\xi_1}, M_{\phi_k}) - B(0, M_{\xi_2}, M_{\phi_k})\}$$
$$\Bigg\{ 1 + \frac{2M_{\xi_1}}{M^2_{\xi_2} - M^2_{\xi_1}} (M_{\xi_1} - \frac{m_{\chi_L}}{m_{\chi_R}} M_{\xi_2}) \Bigg\} \Bigg] + \frac{m_{\chi_L}}{m_{\chi_R}} \Lambda^L_{kk}, \tag{3.25}$$

where $B(p, m_1, m_2)$ is defined as [157],

$$B(p, m_1, m_2) = \int_0^1 dx \Big[\frac{2}{\tilde{\epsilon}} + \log\Big(\frac{\mu^2}{m_1^2\, x + m_2^2\, (1-x) - p^2\, x\, (1-x)} \Big) \Big], \tag{3.26}$$

with, $\frac{2}{\tilde{\epsilon}} = \frac{2}{\epsilon} - \gamma_E + \log(4\pi)$, $\epsilon = n - 4$ and γ_E is the Euler-Mascheroni constant.

The mass scale Λ_{kk} is a function of DM mass, mixing angle θ and the masses of the scalar fields. The pseudo Dirac DM phenomenology restricts $\sin\theta$ for a particluar DM mass in order to satisfy both relic and direct detection bound. Using that information one can estimate Λ_{kk} for both higher and lower values of $\sin\theta$ for a particular DM mass. We use QCDloop [156] to evaluate Λ_{kk} numerically and which is found to be consistent with the analytical estimation of Λ_{kk}.

In Figure 3.6 (upper plots), we present the contours for $\Lambda_{11} = 10^5$ eV (left panel), $\Lambda_{11} = 10^{5.5}$ eV (right panel) considering several values of ΔM in the $\sin\theta -$ M_{ζ_1} plane. For this purpose, we fix $m_{\chi_{L,R}} = 1$ GeV and M_{ϕ_1} at 1.2×10^3 GeV. It is evident from this figure that, for a necessity of higher values of Λ_{11} one has to go for larger $\sin\theta$ values. In Figure 3.6 (lower plots), we present the contours for $\Lambda_{22} = 10^6$ eV (left panel), $\Lambda_{22} = 10^{6.5}$ eV (right panel) considering the set of earlier values of ΔM in the $\sin\theta - M_{\zeta_1}$ plane. Here also we take $m_{\chi_{L,R}} = 1$ GeV and fix M_{ϕ_2} at 10^4 GeV. One can draw a similar conclusion on the contours of Λ_{22} as we get for Λ_{11}.

It is to note that, in order to make the three SM neutrinos massive one needs to take the presence of three scalars, although it is sufficient to have two scalars only for a scenario where one of the active neutrinos remains massless. In the presence of a third copy of the scalar, we would have evaluated the corresponding

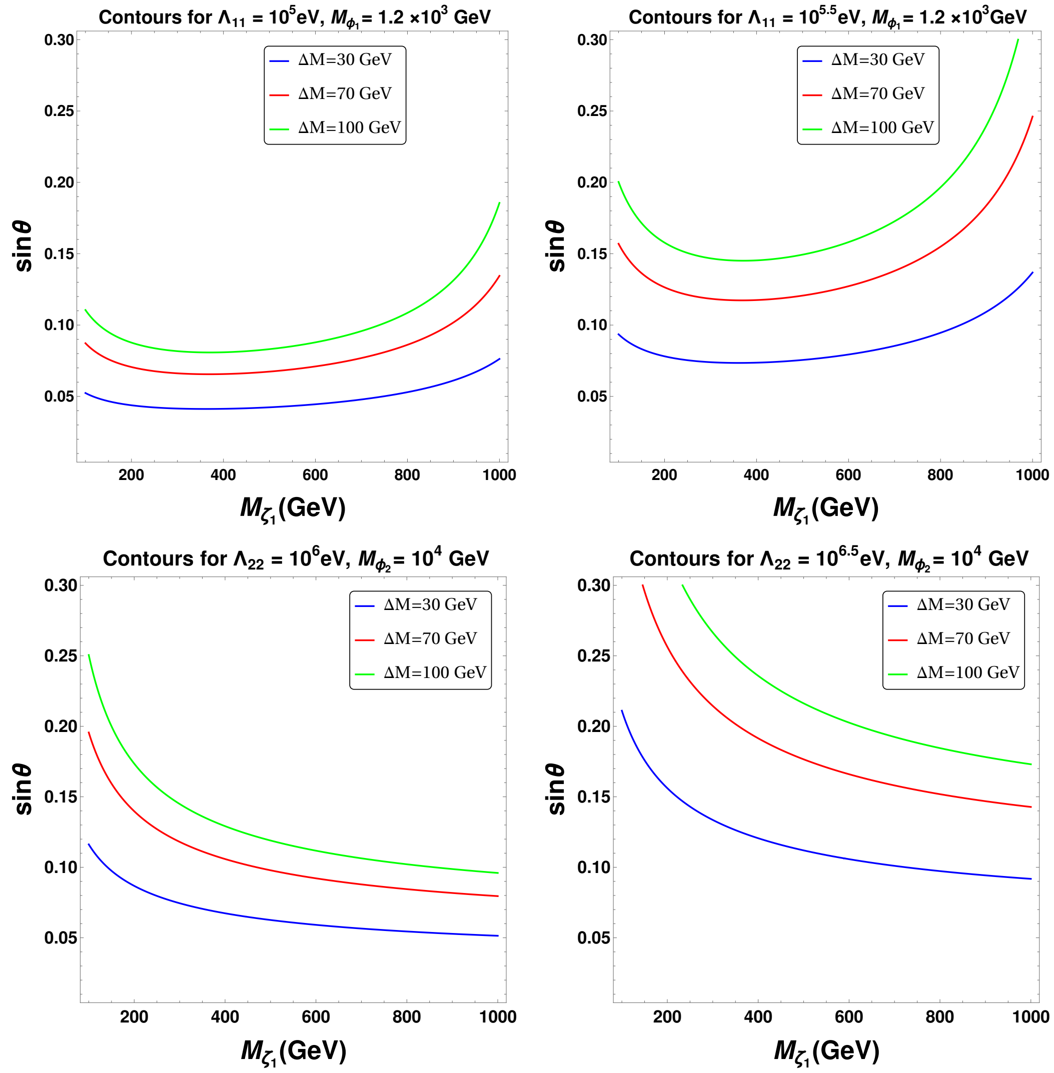

Figure 3.6: (Upper plots) demonstrate the contours for Λ_{11} for different values of ΔM in $\sin\theta - M_{\zeta_1}$ plane. Similarly, (lower plots) demonstrate Contours for Λ_{22}.

Λ in a similar manner.

Once we construct the light neutrino mass matrix with the help of different Λ_{ij}s we can study the properties associated with neutrino mass. The obtained low energy neutrino mass matrix $m_{\nu_{ij}}$ thus constructed is diagonalized by the unitary matrix $U_\nu(U)$.

$$m_\nu^{\text{diag}} = U^T m_\nu U, \tag{3.27}$$

We consider the charged lepton matrix to be diagonal in this model. In that case, we can identify U as the standard U_{PMNS} matrix [19] for lepton mixing.

To start with Equation 3.21, one can get the light neutrino mass in terms of the Yukawa couplings h_{ij} and the mass scale Λ_{kk}. The h_{ij} which is present in Equation 3.21 can be connected to the oscillation parameters with the help of

SL no.	M_{ζ_1} (GeV)	ΔM (GeV)	$\sin\theta$	Ωh^2	$\text{Log}_{10}\left[\frac{\sigma^{\text{SI}}}{\text{cm}^2}\right]$	Λ_{11} (eV)	Λ_{22} (eV)	Λ_{33} (eV)
I	200	47	0.256	0.12	-46.71	1.95×10^6	5.04×10^6	8.44×10^6
II	800	123	0.066	0.12	-48.26	2.79×10^5	3.38×10^5	7.18×10^5

Table 3.2: Two sets of relic and direct search satisfied points and corresponding values of Λ considering $m_{\chi_{L,R}} \sim 1$ GeV, scalar field masses, $M_{\phi_i} \sim \{1.2 \times 10^3,\ 10^4, 10^5\}$ (GeV) and the lightest active neutrino mass $m_\nu^{\text{lightest}} \sim 0.01$ eV. The points are also tested to satisfy $\text{Br}(\mu \to e\gamma)$ bound.

Casas-Ibarra parameterization [158], which allows us to use a random complex orthogonal rotation matrix $\mathcal{R}$. Using this parameterization, we can express the Yukawa coupling by the following equation [158].

$$h^T = D_{\sqrt{\Lambda^{-1}}}\,\mathcal{R}\,D_{\sqrt{m_\nu^{\text{diag}}}}\,U^\dagger, \tag{3.28}$$

where, $D_{\sqrt{m_\nu^{\text{diag}}}} = \text{Diag}(\sqrt{m_{\nu 1}},\ \sqrt{m_{\nu_2}},\ \sqrt{m_{\nu 3}}),\ D_{\sqrt{\Lambda^{-1}}} = \text{Diag}(\sqrt{\Lambda_{11}^{-1}},\ \sqrt{\Lambda_{22}^{-1}},\ \sqrt{\Lambda_{33}^{-1}})$. The $\mathcal{R}$ can be parameterised through three arbitrary mixing angles which we choose to be $(\frac{\pi}{4}, \frac{\pi}{3},$ and $\frac{\pi}{6})$. Now to have a numerical estimate of the Yukawa couplings h_{ij}, as stated earlier we consider $m_{\chi_{L,R}}$ at 1 GeV and scalar field masses at $\{1.2 \times 10^3,\ 10^4, 10^5\}$ GeV and make use of two sets of relic density and direct search satisfied points as tabulated in Table 3.2. At the same time, we use best fit central values of the oscillation parameters to construct the U_{PMNS} matrix and choose the normal hierarchy mass pattern [159] with the lightest active neutrino mass eigenvalue as 0.01 eV. In Table 3.3 we represent the Yukawa coupling matrices (h) using the above sets of benchmark points. So far, the analysis of neutrino part has been carried out by keeping m_χ fixed at 1 GeV. One can go for an even higher choice of $m_{\chi_{L,R}}$ values (competent with the pseudo-Dirac limit), however, in such a scenario the order of the elements of the h matrix will be reduced further as evident from Equation 3.21. One can choose arbitrary masses for the scalars for generating the active neutrino mass radiatively at one loop order as described before. However corresponding Yukawas h_{ij} would be suitably modified such that higher values in M_{ϕ_i}s would suppress them further than our benchmark scenario, represented in Table 3.3.

It is expected that constraint on the model parameter, specifically h_{ij} may arise from the lepton flavour–violating (LFV) decays of ϕ fields. The most stringent limit comes from the $\mu \to e\gamma$ decay process [160–162]. However, the Yukawa couplings being very small $\sim \mathcal{O}(10^{-5})$ as tabulated in Table 3.3 easily overcome the present experimental bound [163]. The pseudo-Dirac nature of dark matter is testable at colliders through displaced vertices [150]. A detailed study is required whether a relaxed $\sin\theta$ has some role to play in this regard.

SL no.	h_{ij}
I	$10^{-5} \times \begin{pmatrix} -4.26+2.29i & 2.38-1.01i & -2.03-0.75i \\ 2.67-2.09i & 3.10-4.42i & 3.51-2.60i \\ 7.44-7.15i & 3.29-2.30i & -0.076-1.03i \end{pmatrix}$
II	$10^{-4} \times \begin{pmatrix} -1.13+0.60i & 0.92-0.39i & -0.70-0.26i \\ 0.71-0.55i & 1.20-1.70i & 1.20-0.90i \\ 1.97-1.90i & 1.27-0.89i & -0.026-0.35i \end{pmatrix}$

Table 3.3: Numerical estimate of the two Yukawa coupling matrices which are built for the sets of benchmark points tabulated in Table 3.2.

3.5 Conclusion

In this work, we study a simple extension of the standard model, including a singlet doublet dark sector in the presence of a small Majorana mass term. As a consequence generated eigenstates deviate from Dirac nature, owing to a small mass splitting between pair of two pseudo-Dirac states. Lightest of these pseudo-Dirac fermionic states, considered as dark matter, can evade the strong spin-independent direct detection constrain by suppressing the scattering of dark matter with nucleon through the Z-boson mediation. We explicitly demonstrate this significant weakening of the direct detection constraint on the singlet doublet mixing parameter while ensuring that such dark matter is still capable of satisfying the thermal relic fully.

The same Majorana mass term provides an elegant scope to generate neutrino mass radiatively at one loop, which requires an extension of the dark sector model with copies of real scalar singlet fields. Introduction of these additional scalars is also motivated by stabilizing the electroweak vacuum even in the presence of a large mixing angle. They also provide a source of lepton number violation, generating light Majorana neutrinos satisfying oscillation data fully. Hence this present scenario offers the potential existence of a pseudo-Dirac type dark matter in the same frame with light Majorana neutrinos. We obtain two different bounds on the left and right component of the newly introduced Majorana mass parameter, *i.e.* $(m_{\chi_L} + m_{\chi_R}) \gtrsim \mathcal{O}(1)$ GeV and $(m_{\chi_L} - m_{\chi_R}) \lesssim \mathcal{O}(1)$ MeV, accounting for the correct order of active neutrino masses and oscillation data. We further demonstrate the dependence of these model parameters and reference benchmark points satisfying best fit central values of the oscillation parameters and consistent with the pseudo-Dirac dark matter constraints.

Chapter 4

A dark clue to seesaw and leptogenesis in a pseudo-Dirac singlet doublet scenario with (non)standard cosmology

4.1 Introduction

In this work, our endeavor is to establish a comprehensive connection between the dark sector and the observed baryon asymmetry of the Universe in a non-standard cosmological scenario. The dark sector involves an extended version of the singlet doublet Dirac dark matter [106] framework with the dark matter weakly interacting with the thermal bath. The analysis is in continuation from our previous work in Chapter 3, where it is shown by us [52] that the presence of a small Majorana mass for the singlet fermion in addition to the Dirac mass makes the DM (admixture of singlet and doublet) of pseudo-Dirac nature *. The pseudo-Dirac dark matter is known to leave imprints at the collider in the form of a displaced vertex which can be traced. The pseudo Dirac nature also assists the DM to escape from the direct search experiments by preventing its interaction with the neutral current at the tree level [137]. We have shown that eventually the absence of a neutral current at the tree level leads to a substantial improvement for the allowed range of the mixing angle between the singlet and doublet fermion which was otherwise strongly constrained. In [52] we also extend the minimal singlet dark matter set up by inclusion of copies of a dark singlet scalar field to

* In view of the rich phenomenology associated with a pseudo-Dirac DM, we deform the pure Dirac version of the singlet doublet DM model. One can find the Majorana version of the singlet doublet dark matter in [120]. For other related works and associated phenomenology based on a similar kind of setup, one can refer to [107–119, 121–123, 125–136].

yield light active neutrino masses radiatively. We particularly have emphasized that the Majorana mass term which is related to non observation of DM at direct search experiments can yield the correct order of light neutrino masses. In the present work we explore the DM phenomenology in an identical set up by making an important assumption of presence of a non-standard thermal history of the Universe. In particular we consider the presence of a popular non-standard scenario before the BBN dubbed as fast expanding Universe [164].

As previously mentioned we also offer a slightly different approach for realizing leptogenesis, where the lepton asymmetry originates from the lepton number and CP violating decay of singlet dark scalar fields into SM leptons and one of the dark sector fermion. The produced lepton asymmetry further can account for the observed baryon asymmetry of the Universe through the usual sphaleron process. We specifically have shown that the presence of a non-standard era in the form of a fast expanding Universe is slightly preferred in order to generate the observed amount of matter-antimatter asymmetry in this particular set up.

This work is organised as follows. In Section 4.2 we present the structure and contents of the model, which is primarily an extended version of the singlet doublet model. Theoretical as well as experimental constraints of the model parameters are debated in Section 4.3. Section 4.4 is kept for explaining the cosmology of fast expanding universe where working mathematical forms are provided to utilise them in following sections. We detail the DM phenomenology in presence of non-standard cosmology in the Section 4.5. Different aspects of parameter dependance and related constraints are discussed quantifying the effect of non-standard scenario. In Section 4.6, we present the neutrino mass generation technique. Then Section 4.7 is dedicated for the baryogenesis through leptogenesis and the required analytical formula realizing the same. Results and analysis for neutrino mass and BAU are shown in Section 4.8. Finally we summarize our findings and conclude in Section 4.9.

4.2 Structure of the model

We propose a pseudo-Dirac singlet doublet *fermionic dark matter* model and extend it minimally to accommodate *neutrino mass* and *baryon asymmetry of the Universe*. The fermion sector in the set up includes one vector fermion singlet ($\chi = \chi_L + \chi_R$) and another $SU(2)_L$ vector fermion doublet ($\Psi = \Psi_L + \Psi_R$). The BSM scalar sector is enriched by three copies of a real scalar singlet field ($\phi_{1,2,3}$). We consider the SM fields to transform trivially under a imposed $\mathcal{Z}_2$ symmetry while all the BSM fields are assigned odd $\mathcal{Z}_2$ charges (see Table 4.1). The BSM fields are non-leptonic in nature. The Lagrangian of the scalar sector is given by

BSM and SM Fields	$SU(3)_C \times SU(2)_L \times U(1)_Y \equiv \mathcal{G}$			$U(1)_L$	$\mathcal{Z}_2$
$\Psi_{L,R}$	1	2	-$\frac{1}{2}$	0	$-$
$\chi_{L,R}$	1	1	0	0	$-$
ϕ_i $(i = 1, 2, 3)$	1	1	0	0	$-$
$\ell_L \equiv \begin{pmatrix} \nu_\ell \\ \ell \end{pmatrix}$	1	2	-$\frac{1}{2}$	1	$+$
$H \equiv \begin{pmatrix} w^+ \\ \frac{1}{\sqrt{2}}(v + h + iz) \end{pmatrix}$	1	2	$\frac{1}{2}$	0	$+$

Table 4.1: Fields and their quantum numbers under the SM gauge symmetry, lepton number and additional $\mathcal{Z}_2$.

$$\mathcal{L}_{\text{scalar}} = |D^\mu H|^2 + \frac{1}{2}(\partial_\mu \phi)^2 - V(H, \phi), \tag{4.1}$$

where,

$$D^\mu = \partial^\mu - ig\frac{\sigma^a}{2}W^{a\mu} - ig'YB^\mu, \tag{4.2}$$

with g and g' stand for the $SU(2)_L$ and the $U(1)_Y$ gauge couplings respectively. Below we write the general form of the scalar sector potential $V(H, \phi)$ consistent with the charge assignment in Table 4.1:

$$V(H, \phi_i) = -\mu_H^2\,(H^\dagger H) + \lambda_H\,(H^\dagger H)^2 + \frac{\mu_{ij}^2}{2}\,\phi_i\phi_j + \frac{\lambda_{ijk}}{2}\,\phi_i^2\phi_j\phi_k + \frac{\lambda_{ij}}{2}\,\phi_i\phi_j(H^\dagger H). \tag{4.3}$$

After minimization of the scalar potential in the limit $\mu_H^2, \mu_{ij}^2 > 0$ the vacuum expectation values (vev) for both the scalars H and ϕ_i's can be obtained as given below,

$$\langle H \rangle = v, \quad \langle \phi_i \rangle = 0. \tag{4.4}$$

For simplification, we consider $\lambda_{ij}, \lambda_{ijk}$ as diagonal in addition to mass matrix for the scalars, parameterized as Diag$(M_{\phi_1}^2, M_{\phi_2}^2, M_{\phi_3}^2)$. Since $\langle \phi_i \rangle = 0$, $\mathcal{Z}_2$ remains unbroken which stabilizes the DM candidate.

The Lagrangian for the fermionic sector at tree level is written as:

$$\mathcal{L} = \mathcal{L}_f + \mathcal{L}_Y, \tag{4.5}$$

where,

$$\mathcal{L}_f = i\bar{\Psi}\gamma_\mu D^\mu\Psi + i\bar{\chi}\gamma_\mu\partial^\mu\chi - M_\Psi\bar{\Psi}\Psi - M_\chi\bar{\chi}\chi - \frac{m_{\chi_L}}{2}\overline{\chi^c}P_L\chi - h.c. - \frac{m_{\chi_R}}{2}\overline{\chi^c}P_R\chi - h.c., \tag{4.6}$$

and

$$\mathcal{L}_Y = Y_1\bar{\Psi}_L\tilde{H}\chi_R + Y_2\bar{\Psi}_R\tilde{H}\chi_L + h_{\alpha i}\bar{\ell}_{L_\alpha}\Psi_R\phi_i + h.c.. \tag{4.7}$$

In the $\mathcal{L}_f$, the doublet has a Dirac like mass term $M_\Psi\bar{\Psi}\Psi$ which can be expanded as $M_\Psi(\overline{\Psi_L}\Psi_R + \overline{\Psi_R}\Psi_L)$. While for χ field both the Dirac $M_\chi(\overline{\chi_L}\chi_R + \overline{\chi_R}\chi_L)$ and Majorana type masses ($m_{\chi_{L,R}}$) appear in Equation 4.6, which is perfectly allowed by the imposed Z_2 symmetry. In a similar line the Equation 4.7 shows the Yukawa like interaction pattern of $\psi_{L,R}$ and $\chi_{L,R}$ with the SM Higgs and ϕ. Hereafter we work with a generic choice $Y_1 = Y_2 \equiv Y$ in order to reduce the number of free parameters in the model (see [165,166] for such an example). This particular choice of equality helps us to evade the spin dependent direct detection bound (please refer to footnote ¶). With this equality the first two Yukawa terms can be written in a compact form like $Y\bar{\Psi}\tilde{H}\chi$. We specifically assume that the Majorana mass for χ field is much smaller than the Dirac one *i.e.* $m_{\chi_{L,R}} \ll M_\chi$. In the present framework the lightest neutral fermion is a viable dark matter candidate which is of pseudo-Dirac nature in the limit $m_{\chi_{L,R}} \ll M_\chi$. As we see in [52] that this non-vanishing $m_{\chi_{L,R}}$ assists in evading strong spin-independent dark matter direct detection bound. In addition, it is also found [52] to be crucial in generating light neutrino mass radiatively.

The presence of a non-vanishing $m_{\chi_{L,R}}$ and and M_χ along with ϕ being a real scalar field and non-vanishing coupling coefficient Y result in symbolizing the Yukawa like interaction (h) involving SM leptons and the doublet ψ as a lepton number violating vertex at tree level. The interaction of DM with the SM particles mediated through the Higgs is realized by the first term in Equation 4.7, whereas the second term which is also responsible for active neutrino mass generation through radiative loop [52] manifests the explicit violation of the lepton number [†].

In the present study, we consider $M_{\phi_i} \gg M_\psi, m_{\chi_{L,R}}$ such that the role of ϕ fields in DM phenomenology is minimal [‡]. After the spontaneous EW symmetry breaking, the Dirac [§] mass matrix for the neutral DM fermions is given by (in

[†]The purpose of choosing the dark sector scalar fields as real is justified to pave the way for explicit lepton number violation [129] in Equation 4.7.

[‡]Ideally the scalars, being a part of the dark sector can engage in DM phenomenology through coannhilation processes however considering the mass pattern in Figure 4.1 their contributions turn out to be minimal.

[§] The Majorana version of the singlet doublet dark matter accommodates one pair of Weyl

$m_{\chi L,R} \to 0$ limit),

$$\mathcal{M}_D = \begin{pmatrix} M_\Psi & M_D \\ M_D & M_\chi \end{pmatrix}, \tag{4.8}$$

where we define $M_D = \frac{Yv}{\sqrt{2}}$. After diagonalisation of $\mathcal{M}_D$ the mass eigenvalues are computed as,

$$M_{\xi_1} = \frac{M_\chi + M_\Psi}{2} - \frac{1}{2}\sqrt{4M_D^2 + M_\chi^2 - 2M_\chi M_\Psi + M_\Psi^2}, \tag{4.9}$$

$$M_{\xi_2} = \frac{M_\chi + M_\Psi}{2} + \frac{1}{2}\sqrt{4M_D^2 + M_\chi^2 - 2M_\chi M_\Psi + M_\Psi^2}, \tag{4.10}$$

where the Dirac mass eigenstates are represented as (ξ_1, ξ_2). It is evident from Equation 4.9 that ξ_1 is the lightest eigenstate. The mixing between two flavor states, *i.e.* neutral part of the doublet (ψ^0) and the singlet field (χ) is parameterised by θ as

$$\sin 2\theta = \frac{\sqrt{2}\, Yv}{\Delta M}, \tag{4.11}$$

where $\Delta M = M_{\xi_2} - M_{\xi_1}$ which turns out to be of the similar order of $M_\Psi - M_\chi$ in the small θ limit. Also, in small mixing case, ξ_1 can be identified with the singlet χ. In the limit $m \to 0$ where we define

$$m = (m_{\chi_L} + m_{\chi_R})/2, \tag{4.12}$$

the Majorana eigenstates of ξ_1 (*i.e.* ζ_1, ζ_2) are degenerate. A small amount of non-zero $m_{\chi_{L,R}}$ breaks this degeneracy , and we can still write

$$\zeta_1 \simeq \frac{i}{\sqrt{2}}(\xi_1 - \xi_1^c), \tag{4.13}$$

$$\zeta_2 \simeq \frac{1}{\sqrt{2}}(\xi_1 + \xi_1^c). \tag{4.14}$$

in the pseudo-Dirac limit $m \ll M_{\zeta_1}, M_{\zeta_2}$ where $M_{\zeta_1,\zeta_2} \simeq M_{\xi_1} \mp m$. In a similar fashion, the state ξ_2 would be splitted into ζ_3 and ζ_4. Hence we will have four neutral mass eigenstates in the DM sector with the lightest state (ζ_1) being the DM candidate. Since all of the mass eigenstates have pseudo-Dirac origin, we mark them as "pseudo-Dirac" states. For a formal understanding on the construction of pseudo Dirac fermion in terms of the Weyl spinors, we refer the readers to Appendix B .

$SU(2)_L$ doublet fermions and one Weyl singlet fermion. Thus the number of neutral Weyl degrees of freedom is three. While in our case there exist four neutral Weyl degrees of freedom.

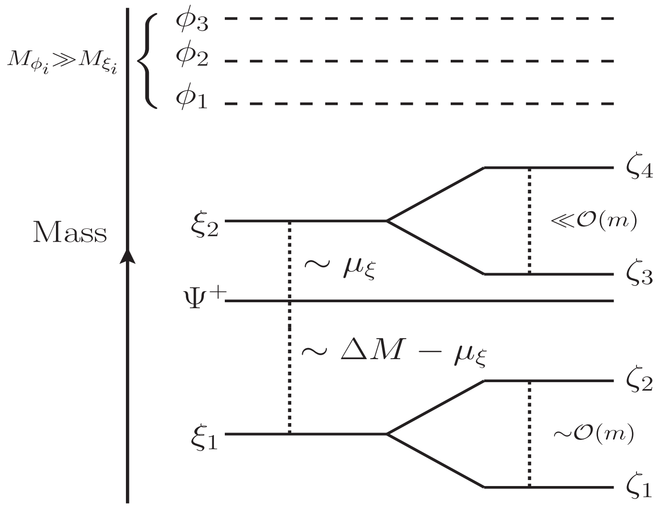

Figure 4.1: Mass spectrum of the dark sector, showing the lightest pseudo-Dirac mode as the dark matter and other heavy BSM fermions and scalars. The mass of the charged fermion is M_Ψ and it lies somewhere in between ξ_1 and ξ_2 with $\mu_\xi = \frac{\Delta M \sin^2(2\theta)}{4}$ in the limit of small $\sin\theta$. The mass ordering is subject to change depending on the numerical values of m, ΔM and $\sin\theta$.

For a representative mass spectrum of the dark sector, please follow Figure 4.1, showing the lightest pseudo-Dirac mode as the dark matter candidate together with other heavy BSM fermions and scalars. In the following section we look into the possible constraints before emphasizing cosmological predictions of the model.

4.3 Model Constraints

In this section we summarize the possible constraints on the model parameters arising from different theoretical and experimental bounds.

- **Perturbativity and stability bounds:** Any new theory is expected to obey the perturbativity limit which imposes strong upper bounds on the model parameters:

$$\lambda_{ij},\ \lambda_{ijk} < 4\pi, \quad \text{and} \quad Y,\ h_{ij} < \sqrt{4\pi}. \tag{4.15}$$

It is also essential to ensure the stability of the scalar potential in any field direction. The stable vacuum of a scalar potential in various field directions are determined by the co-positivity conditions [140,141] where all the scalar quartic couplings are involved. Here we are considering all the scalar quartic couplings as real and positive and thus automatically satisfy the necessary

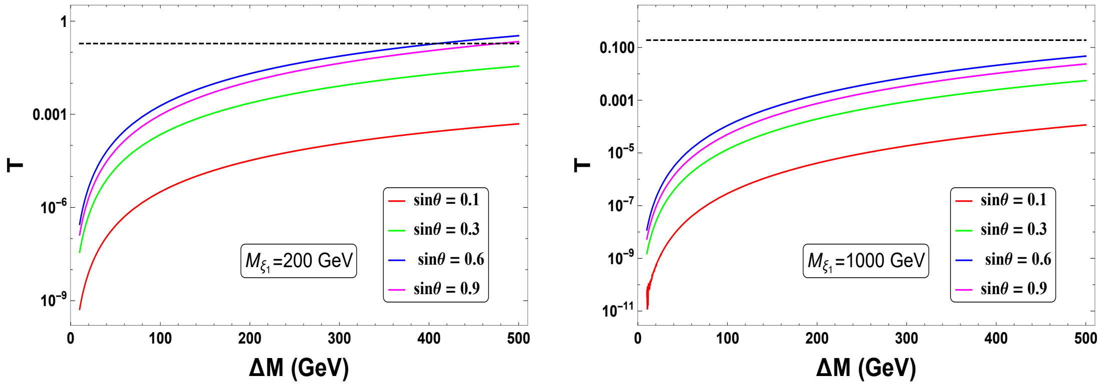

Figure 4.2: Sketch of T parameter using Equation 4.16 as a function of ΔM for two different values of M_{ξ_1}= 200 GeV (left) and 1000 GeV (right). Each line indicates constant magnitude of $\sin\theta$. The black dashed line stands for the observed upper limit of T parameter.

co-positivity conditions.

- **Bound on Majorana mass parameter:** In the presence of a small Majorana mass, the ξ_1 state gets splitted into two non degenerate Majorana eigenstates. This triggers the possibility of inelastic scattering of ξ_1 with nucleon to produce ξ_2. Such inelastic scattering would give rise to non zero excess of nucleon recoil into direct detection experiments (*e.g.* XENON 1T) which is strongly disfavored. Hence, it is recommended to forbid such kind of inelastic processes. This poses some upper limit on the Majorana mass parameter $m_{\chi_L} + m_{\chi_R} \gtrsim 240$ KeV for DM having mass $\mathcal{O}(1)$ TeV considering Xenon detector [148, 149].

- **Electroweak precision observables:** Owing to the presence of an additional $SU(2)_L$ doublet fermion, the electroweak precision parameters put some restrictions on the model parameters. It turns out that in the small Majorana mass limit the S and U parameters do not pose any significant constraint [166]. However one needs to inspect the magnitude of T parameter originating from the BSM sources. Considering the small Majorana mass limit, the analytical expression for T parameter in our framework carries the following form [166]:

$$T \simeq \frac{g^2}{16\pi^2 M_W^2 \alpha}\Bigg[\tilde{\Pi}(M_\Psi, M_\Psi, 0) + \cos^4\theta\,\tilde{\Pi}(M_{\xi_2}, M_{\xi_2}, 0) + \sin^4\theta\,\tilde{\Pi}(M_{\xi_1}, M_{\xi_1}, 0)$$
$$+ 2\sin^2\theta\cos^2\theta\,\tilde{\Pi}(M_{\xi_1}, M_{\xi_2}, 0) - 2\cos^2\theta\,\tilde{\Pi}(M_\Psi, M_{\xi_2}, 0) - 2\sin^2\theta\,\tilde{\Pi}(M_\psi, M_{\xi_1}, 0)\Bigg] \tag{4.16}$$

where α being the fine structure constant. The vacuum polarization functions ($\tilde{\Pi}$) are defined as

$$\tilde{\Pi}(M_a, M_b) = -\frac{1}{2}(M_a^2 + M_b^2)\left\{\text{Div} + \text{Ln}\left(\frac{\mu^2}{M_a M_b}\right) - \frac{1}{2}\right\} - \frac{(M_a^4 + M_b^4)}{4(M_a^2 - M_b^2)}\text{Ln}\left(\frac{M_a^2}{M_b^2}\right) + M_a M_b\left\{\text{Div} + \text{Ln}\left(\frac{\mu^2}{M_a M_b}\right) + 1 + \frac{M_a^2 + M_b^2}{2(M_a^2 - M_b^2)}\text{Ln}\left(\frac{M_b^2}{M_a^2}\right)\right\}. \tag{4.17}$$

The present experimental bounds on T is given by [159]:

$$\Delta T = 0.07 \pm 0.12, \tag{4.18}$$

In Figure 4.2, we demonstrate the functional dependence of T parameter on M_{ξ_1}, ΔM and $\sin\theta$. Two notable features come out: (i) for a constant M_{ξ_1} and $\sin\theta$, one can observe the rise of T parameter with ΔM and thus at some point crosses the allowed experimental upper limit, (ii) for higher DM mass, the constraints on the model variables from T parameter turn weaker.

- **Relic density bound and direct search constraints:** The observed amount of relic abundance of the dark matter is obtained by the Planck experiment [144]

$$0.1166 \lesssim \Omega_{\rm DM}h^2 \lesssim 0.1206. \tag{4.19}$$

Along with this, the dark matter relic density parameter space is constrained significantly by the direct detection experiments such as LUX [167], PandaX-II [168] and XENON 1T [169]. In our analysis, we will follow the Xenon-1T result in order to validate our model parameter space through direct search bound.

Here we would like to reinforce the view that although the Z-boson mediated spin independent (SI) direct search process can be suppressed at tree level (as commented in the introduction section), the SM Higgs mediated SI direct search process still survives providing loose constraints. Thus the bound on the SI direct search cross section from experiments like Xenon-1T is still applicable. The spin dependent direct search cross section is negligible in our working limit $Y_1 \sim Y_2$ (see footnote ¶ for more details).

- **Bounds from invisible decay of Higgs and Z boson:** In case the

DM mass is lighter than half of Higgs or Z Boson mass, decays of Higgs and Z boson to DM are possible. Invisible decay widths of both H and Z are severely restricted at the LHC [159, 170], and thus could constrain the relevant parameter space. Since, in the present study our focus would be on the mass range 100 GeV – 1 TeV for DM, the constraints from H and Z bosons does not stand pertinent.

In the upcoming discussions we will strictly ensure the validity of the above mentioned constraints on the model parameters while specifying the the benchmark/reference points that satisfy the other relevant bounds arising from DM phenomenology and leptogenesis.

4.4 Fast expanding Universe

As mentioned earlier, the presence of a new species in the early Universe before the radiation domination epoch can significantly escalate the expansion rate of the universe, which in turn has a large impact on the evolution of the particle species present in that epoch. In this section we brief the quantitative justification of the effect of a new species on the expansion rate of the universe. Hubble parameter H delineates the expansion rate of the Universe. At temperature, higher than T_r with the condition $g_*(T) = \bar{g}_*$ (some *constant*), with the help of Equation 2.39 the Hubble rate can be written as

$$H(T) = H_R(T)\left(\frac{T}{T_r}\right)^{n/2}, \qquad (\text{with} \;\; T \gg T_r) \tag{4.20}$$

where $H_R(T) \sim 1.66\, \bar{g}_*^{1/2} \frac{T^2}{M_{\rm Pl}}$, the Hubble rate for radiation dominated Universe. In case of SM, $\bar{g}_*$ can be identified with the total SM degrees of freedom $g_*(\text{SM}) = 106.75$. It is important to note from Equation 4.20 that the expansion rate is larger than what it is supposed to be in the standard cosmological background provided, $T > T_r$ and $n > 0$. Hence it can be stated that if the DM freezes out during η domination, the situation will alter consequently with respect to the one in the standard cosmology.
With positive scalar potential for the field responsible for fast expansion, value of $0 < n \leq 2$ can be realized. The candidate for $n = 2$ species could be the quintessence fluids [171] where in the kination regime $\rho_\eta \propto a(t)^{-6}$ can be attained. However for $n > 2$, one needs to consider negative potential. A specific structure of $n > 2$ potential can be found in Ref. [164] which is asymptotically free.

4.5 Revisiting dark matter phenomenology

The comoving number density of the DM (ζ_1) is governed by the Boltzmann's equation (in a radiation dominated Universe) [172]:

$$\frac{dY_{\zeta_1}}{dz_D} = -\frac{\langle\sigma v\rangle s}{H_R(T) z_D}(Y_{\zeta_1}^2 - Y_{\zeta_1}^{\mathrm{eq}^2}), \tag{4.21}$$

where, $z_D = \frac{M_{\zeta_1}}{T}$ and $\langle\sigma v\rangle$ stands for the thermally averaged annihilation cross section with v being the relative velocity of the annihilating particles. The equilibrium number density of the DM component is represented by $Y_{\zeta_1}^{\mathrm{eq}}$ in Equation 4.21. The relic abundance of the DM is obtained by using [172]:

$$\Omega_{\mathrm{DM}} h^2 = 2.744 \times 10^8 \; M_{\zeta_1} Y_{z_D=\infty} \tag{4.22}$$

In the WIMP paradigm, it is presumed that DM stays in thermal equilibrium in the early Universe. Considering the DM freezes out in the RD Universe, the required order of thermally averaged interaction strength of the DM to account for correct relic abundance is found to be,

$$\langle\sigma v\rangle \approx 3 \times 10^{-26} \mathrm{cm}^3 \; \mathrm{sec}^{-1}, \tag{4.23}$$

The Equation 4.23 quantifies an important benchmark for WIMP search, which bargains on a major assumption that the universe was radiation dominated at the time of DM freeze out. However, in an alternative cosmological history, depending on the decoupling point of DM from the thermal bath this number is expected to change by order of magnitudes, which in turn, brings out significant changes in the relic satisfied parameter space of a particular framework.

In the current framework, the DM ζ_1 can (co-)annihilate with the other heavier neutral and charged fermions into SM particles through Z or Higgs mediation. Furthermore, co-annihilation processes like $\psi^+\psi^- \to$ SM, SM ($\psi^\pm$ are the charged counterpart of the vector fermion doublet Ψ) also supply their individual contributions to total $\langle\sigma v\rangle$. The relevant Feynman diagrams contributing to the possible annihilation and co-annihilation channels of the DM can be found in [124]. For the model implementation we have used Feynrules [173] and subsequently Micromega [174] to carry out the DM phenomenology.

As mentioned in the previous section for the fast expanding Universe the Hubble parameter $H_R(T)$ in Equation 4.21 in presence of the new species η, need to be replaced with $H(T)$ of Equation 4.20 with $n > 0$. This recent temperature dependence of the expansion rate of the Universe provide some new degrees of freedom as we also observe here. For the standard cosmological background, in pseudo Dirac singlet doublet dark matter model there are three independent parameters for a particular DM mass namely: ΔM, $\sin\theta$ and the Majorana mass m[¶]. For simplicity of our analysis we keep the Majorana mass m small by fixing it at 1 GeV. Then the relevant set of parameters which participate in the DM phenomenology in presence of the modified cosmology are the following :

$$\Big\{\Delta M,\ \ \sin\theta,\ T_r,\ n\Big\}, \tag{4.24}$$

for a certain DM mass.

4.5.1 Spin independent direct search

The part of the Lagrangian relevant for spin independent direct search of the DM within the Dirac limit ($m \to 0$) is given by,

$$\mathcal{L} \supset \frac{g}{2\cos\theta_W}\sin^2\theta\ \overline{\xi_1}\gamma^\mu Z_\mu \xi_1 + \frac{Y}{\sqrt{2}}\sin\theta\cos\theta\ h\ \bar{\xi_1}\xi_1, \tag{4.25}$$

However switching the parameter m on, leads to the pseudo-Dirac limit in which the neutral current interaction of the DM ζ_1, i.e., first term of Equation 4.25 vanishes at zeroth order in $\delta_r = \frac{m_{\chi_L}-m_{\chi_R}}{M_{\zeta_1}}$. Although a small residual vector-vector interaction of the DM to the quarks, due to the non-pure Majorana nature of the mass eigenstates still exists at leading order in δ_r. This brings about the Z mediated effective interactions of the DM with nucleon which is given by,

$$\mathcal{L} \supset \alpha\ \delta_r\ (\bar{\zeta_1}\gamma^\mu\zeta_1)(\bar{q}\gamma_\mu q), \tag{4.26}$$

with $\alpha = \left(\frac{4g^2\sin^2\theta}{m_Z^2\cos^2\theta_W}\right)C_V^q = \alpha' C_V^q$ and g as the $SU(2)_L$ gauge coupling constant. In addition, the SM Higgs mediated process of DM-nucleon scattering will be present at the tree level as evident from Equation 4.25. The relevant Feynman diagrams are shown in Figure 4.3. It is pertinent to comment that in the vanishing δ_r limit only Higgs mediated diagram in Figure 4.3 contribute to the SI direct

[¶]It is worth mentioning that for a general case where the two Yukawas are not equal, one has to deal with two mixing angles, namely θ_L and θ_R rather considering only one (θ). In the pseudo Dirac case with $\theta_L \neq \theta_R$ (or $Y_1 \neq Y_2$), a few extra axial type interactions for DM (ζ_1) appear in the Lagrangian which vanish in the $\theta_L \sim \theta_R$ (or $Y_1 \sim Y_2$) limit. These axial couplings have negligible contribution to the DM relic abundance as we have checked. Having said that, one of the axial interactions of DM $\sim \overline{\zeta_1}\gamma_\mu\gamma_5\zeta_1 Z^\mu$ (with coupling coefficient proportional to $\sin^2\theta_R - \sin^2\theta_L$) can yield non zero spin dependent nucleon cross section for $\theta_L \neq \theta_R$ which can provide signal in the spin dependent direct search experiments. Since, one of our major aims of the present study is to hide the DM at both spin independent and spin dependent direct search experiments, we work with the pseudo-Dirac and $\theta_L \sim \theta_R$ limits respectively. This further simplifies the scenario, with a single Yukawa like coupling in the set up which is sufficient to portray the novel features of the proposed scenario.

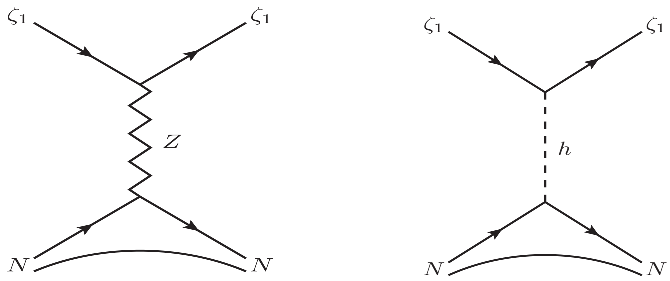

Figure 4.3: Feynman diagrams contributing to the spin independent direct search of the DM.

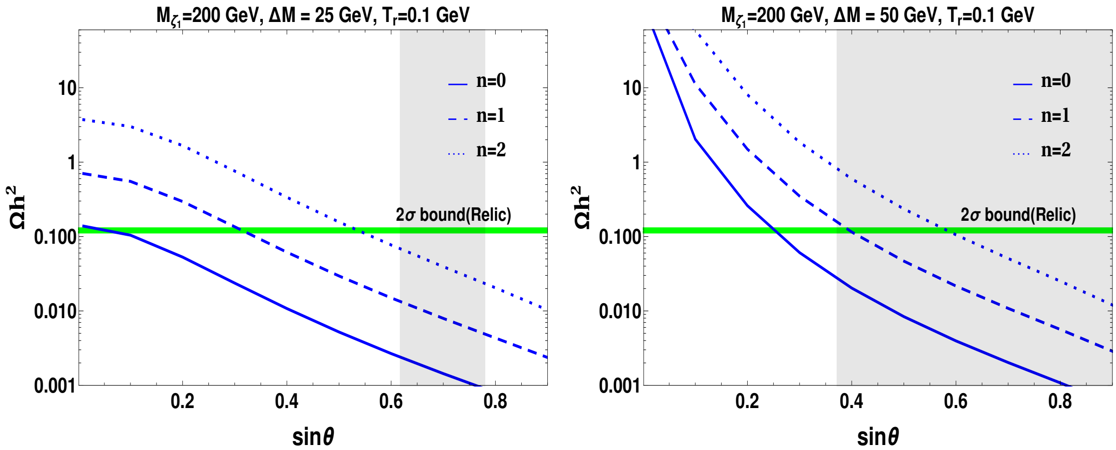

Figure 4.4: Relic abundance of the DM as a function of the mixing angle between the singlet and doublet is shown considering both standard (solid line) and non-standard (dashed and dotted lines) thermal history of the Universe, for $M_{\zeta_1} = 200$ GeV with (left) $\Delta M = 25$ GeV and (right) $\Delta M = 50$ GeV. The disfavored region from the spin independent direct detection constraints are denoted by respective shaded region. Here we have considered $T_r = 0.1$ GeV.

search of DM.

4.5.2 Dark matter in presence of (non)standard thermal history

In case of a faster expansion of the Universe, the DM freezing takes place quite earlier than what it does in the standard scenario, resulting into an overabundance. Hence, to account for the observed relic abundance, an increase of the total annihilation cross section of DM is required. This in turn necessitates the rise of the associated coupling coefficients.

This fact can be realized from Figures 4.4-4.5, where the DM relic abundance is plotted against $\sin\theta$ by considering $T_r = 0.1$ GeV. We choose two different DM masses for the analysis, one at a comparatively lower range with $M_{\zeta_1} = 200$ GeV shown in Figure 4.4 while the other one in a higher mass regime at $M_{\zeta_1} = 1000$

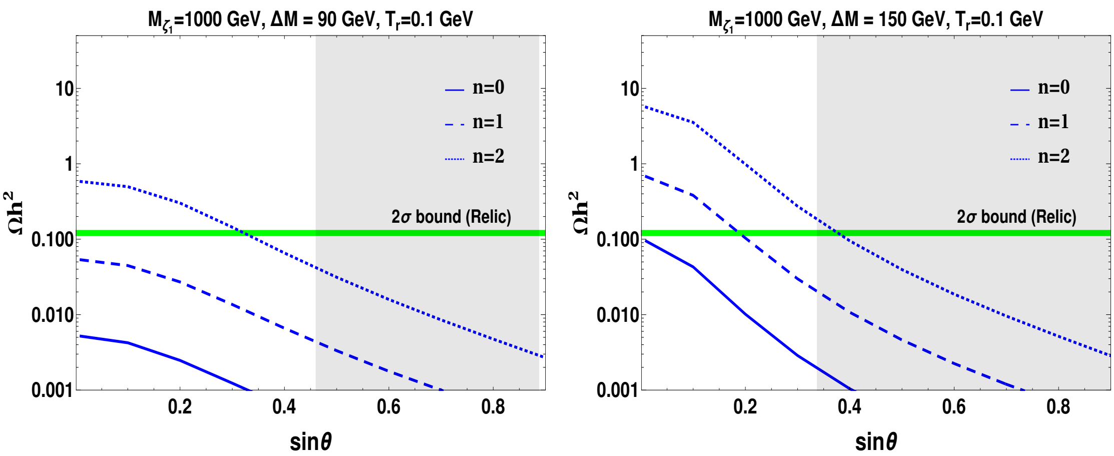

Figure 4.5: The same as Figure 4.4 but for a choice of higher DM mass, for $M_{\zeta_1} = 1000$ GeV with (left) $\Delta M = 90$ GeV and (right) $\Delta M = 150$ GeV. Here we have fixed $T_r = 0.1$ GeV.

GeV as in Figure 4.5. We also take different values of n and ΔM to have a clear comprehension of how the new degrees of freedom changes the relic density. It is prominent that a larger value of $\sin\theta$ is required in order to satisfy the observed density limit (green color band representing 2σ range of the observed relic density) for $n \gtrsim 1$ compared to the $n = 0$ (standard) case. We also display the SI direct search constraints on the same plot. The contribution to spin independent direct detection cross section comes solely from the Higgs mediated diagrams (right panel of Figure 4.3) since we are working in the $\delta_r = 0$ limit. The direct detection cross section seemingly restricts the value of $\sin\theta$ in an intermediate range. For example, such a constraint of $0.62 \lesssim \sin\theta \lesssim 0.76$ is indicated as shaded region in left panel of Figure 4.4. This is because the SI direct search cross section is proportional to the factor: $\sin^2\theta\cos^2\theta$, as evident from Equation 4.25. In the right panel of the Figures 4.4-4.5, this intermediate range (specifically the upper limit) of $\sin\theta$ is not apparently visible since it exceeds the plotting range.

A few important aspects of the analysis can be drawn from Figures 4.4-4.5. It is seen that for a particular DM mass, non-standard cosmology ($n > 0$) requires larger $\sin\theta$ to be consistent with the observed relic abundance as mentioned earlier. For a specific value of n, relic density increases with ΔM thus at some point can be ruled out from SI direct search bound for a specific DM mass. For example, in the left panel of Figure 4.4, fixing $n = 2$ can satisfy the correct relic and which is also allowed by the SI direct search bound. However once ΔM is increased up to a substantial amount it enters into the disfavored region, as seen in the right panel of Figure 4.4.

So far the DM phenomenology has been studied by assuming $T_r = 0.1$ GeV. Nonetheless one can look for the DM parameter space considering a higher value

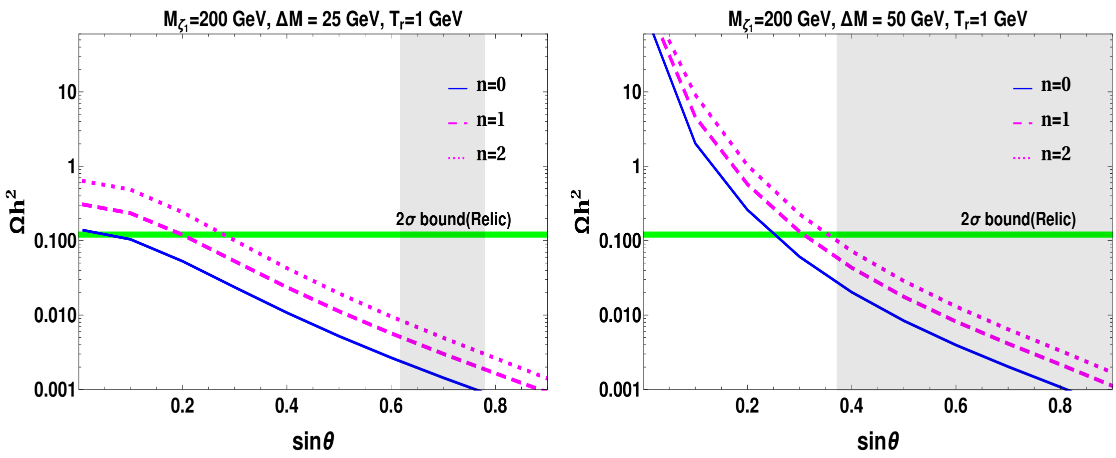

Figure 4.6: The same as Figure 4.4 but for a choice of larger $T_r = 1$ GeV.

of T_r. In Figure 4.6, we use a slightly larger value of $T_r = 1$ GeV and present the relic contours for different values of n in $\Omega h^2 - \sin\theta$ plane. It is observed that increase of T_r reduces the relic density for a particular n. As an example, in the left panel of Figure 4.4, the required value of $\sin\theta$ was 0.53 to satisfy the relic abundance criteria considering $n = 2$ and $T_r = 0.1$ GeV. Now for $T_r = 1$ GeV, this value got shifted to 0.25. Enhancement of T_r is also preferred in the view of SI direct search constraints as can be seen by comparing the right panel of Figure 4.4 and Figure 4.6 where the $n = 2$ relic contour turns out to be favored in the later case. This leads to a realization that, lowering the required value of $\sin\theta$ to account for the expected relic density further reduces the SI direct search cross section. One can assign a further higher value to $T_r > 1$, however the scenario will approach towards the standard case which is prominent in comparing Figure 4.4 and Figure 4.6. We end this section by tabulating two sets of relic satisfied points for $n = 2$ in Table 4.2 which have relevance in the study of neutrino mass and leptogenesis.

BP	n	T_r (GeV)	M_{ζ_1} (GeV)	ΔM (GeV)	$\sin\theta$	Ωh^2	$\mathrm{Log}_{10}\left[\frac{\sigma^{\mathrm{SI}}}{\mathrm{cm}^2}\right]$
I	2	0.1	200	25	0.53	0.12	-46.71
II	2	0.1	1000	90	0.325	0.12	-46.8

Table 4.2: Two sets of relic and SI direct search satisfied points collected from Figures 4.4-4.5

.

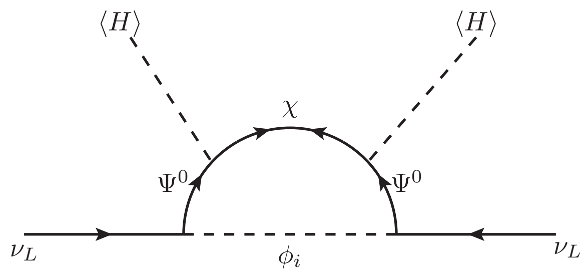

Figure 4.7: Schematic diagram of radiative neutrino mass generation.

4.6 Neutrino mass generation

This model renders a mechanism which explains the radiative generation of light neutrino mass. The relevant one loop process is shown in Figure 4.7 which establishes the fact that the presence of the heavy scalars are essential in order to make the Majorana light neutrinos massive. The light neutrino mass matrix can be expressed by the following equation [30, 139, 154]:

$$m_{\nu_{\alpha\beta}} = h^T_{i\alpha} \Lambda_{ii} h_{\beta i}, \tag{4.27}$$

where, $\Lambda_{ii} = \Lambda^L_{ii} + \Lambda^R_{ii}$. The Λ^L_{ii} and Λ^R_{ii} include the contribution from m_{χ_L} and m_{χ_R} respectively. For the full analytical expressions representing Λ^L_{ii}, Λ^R_{ii} we refer to our earlier work [52]. We use Casas-Ibarra parameterization [158] in order to connect the mixing parameters with neutrino Yukawa coupling. Using this parameterization, one can write [158]:

$$h^T = D_{\sqrt{\Lambda^{-1}}}\, \mathcal{R}\, D_{\sqrt{m_\nu^{\rm diag}}}\, U^\dagger, \tag{4.28}$$

where, $\mathcal{R}$ is a complex orthogonal matrix. Any complex orthogonal matrix can be manifested by $\mathcal{R} = O\ e^{iA}$ where O and A represent any arbitrary real orthogonal and real anti-symmetric matrices respectively [175]. The exponential of the anti-symmetric matrix A can be simplified to

$$e^{iA} = 1 - \frac{\cosh r - 1}{r^2} A^2 + i \frac{\sinh r}{r} A \tag{4.29}$$

with $r = \sqrt{a^2 + b^2 + c^2}$ and

$$A = \begin{pmatrix} 0 & a & b \\ -a & 0 & c \\ -b & -c & 0 \end{pmatrix} \tag{4.30}$$

For our purpose, we consider O as an identity matrix and also for simplicity of the anti-symmetric matrix A we have chosen the equality $a = b = c \equiv a$. It is important to note that, this particular parameterization for the $\mathcal{R}$ matrix helps us to achieve a desired order of Yukawa coupling by keeping the neutrino mixing parameters intact. We denote, $D_{\sqrt{m_\nu^{\rm diag}}} = \text{Diag}(\sqrt{m_{\nu 1}},\ \sqrt{m_{\nu_2}},\ \sqrt{m_{\nu 3}}),\quad D_{\sqrt{\Lambda^{-1}}} = \text{Diag}(\sqrt{\Lambda_{11}^{-1}},\ \sqrt{\Lambda_{22}^{-1}},\ \sqrt{\Lambda_{33}^{-1}})$. It is also worth mentioning that this special kind of Casas-Ibarra parametrization for the neutrino Yukawa coupling is found to be facilitating to produce the parameter space responsible for generating the observed BAU in the present framework. Authors in [176] have shown the explicit roles of the anti-symmetric matrix A and its elements a, b, c in order to achieve sufficient amount of lepton asymmetry. In our case too, the usefulness of this particular parametrization can be observed in Section 4.8 where we tune a such that one can acquire the observed BAU. As obtained from the recent bayesian analysis [177], the mild preference for the normal mass hierarchy (NH) of the neutrinos, allows us to chose the NH as the true hierarchy among the three light neutrino masses. It is also found that the latest global fit of neutrino oscillation data [178] seems to favor the second octant of the atmospheric mixing angle for both the mass hierarchies. The recent announcement made by the experiment prefers the Dirac CP phase to be $-\pi/2$ with 3σ confidence level (for detail one may refer to [179]). Keeping all these in mind for the numerical analysis section we fix all the neutrino parameters to their 3σ central values including the maximal values for the Dirac CP phase. It is also noted that, a random scan of all the neutrino parameters in their entire 3σ range would not affect our present analysis much. The resulting Yukawa coupling in the neutrino sector governs the CP violating decay of the BSM scalar leading to an expected amount of lepton asymmetry which we discuss in the next section.

4.7 Baryogenesis via Leptogenesis from scalar decay

In this section, we describe the production mechanism of lepton asymmetry driven by the decay of the scalar belonging to the dark sector. Our proposal for leptogenesis differs from the usual scenario of leptogenesis in the type I seesaw framework in the sense that, in such a scheme the production of lepton asymmetry is guided by the decay of the heavy Majorana RHN. The present set up, on account of the presence of lepton number violating vertex involving ϕ and the SM leptons, motivates us to investigate the process of lepton asymmetry creation from the singlet scalar (ϕ) decay which has also served a key role in generating the light

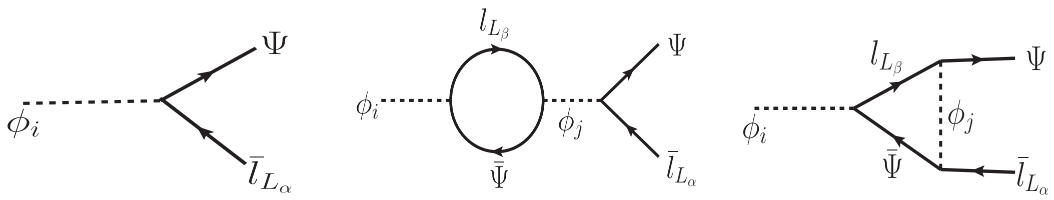

Figure 4.8: Possible feynman diagrams for lepton asymmetry production from singlet scalar decay

neutrino mass. We will also see that presence of a non-standard history of the early Universe provides indisputable contribution in order to yield correct order of baryon asymmetry by suppressing the washout factor significantly.

In the present framework the dark sector scalar (ϕ) can undergo a CP violating decay to SM leptons and the additional BSM fermion doublet which leads to lepton number violation by one unit. This particular decay process can naturally create lepton number asymmetry provided out-of-equilibrium criteria is satisfied. Earlier we have commented on the choice of the mass spectrum of dark sector scalars *i.e.* $M_{\phi_1} < M_{\phi_2} < M_{\phi_3}$ (see Figure 4.1), which however do not play any decisive role in favoring the true hierarchy of neutrino mass. All these scalars can potentially contribute to generate the final $B-L$ asymmetry. The CP asymmetry factor is defined as the ratio of the difference between the decay rates of ϕ into the final state particles with lepton number +1 and -1 to the sum of all the decay rates, quantified as,

$$\epsilon_i^\alpha = \frac{\Gamma(\phi_i \to \bar{L}_\alpha \Psi) - \Gamma(\phi_i \to L_\alpha \bar{\Psi})}{\Gamma(\phi_i \to \bar{L}_\alpha \Psi) + \Gamma(\phi_i \to L_\alpha \bar{\Psi})}, \tag{4.31}$$

The total lepton asymmetry receives contributions from two kind of subprocesses: (i) superposition of tree level and vertex diagram and (ii) superposition between tree level and self energy diagram as shown in Figure 4.8. This allows us to write $\epsilon_T = \epsilon_{\text{vertex}} + \epsilon_{\text{self energy}}$. Driven by Equation 4.31, we can obtain the analytical form of ϵ_{vertex} which is given by (see Appendix C for the detail):

$$\epsilon^i_{\text{vertex}} = \frac{1}{4\pi} \sum_{j \neq i} \frac{\text{Im}\left[(h^\dagger h)_{ij} h_{\alpha j} h^*_{\alpha i}\right]}{(h^\dagger h)_{ii}} x_{ij} \log\left(\frac{x_{ij}}{x_{ij}+1}\right) \tag{4.32}$$

where, $h_{\alpha i}$ is the Yukawa matrix governing the lepton number violating interaction in this set up and $x_{ij} = \frac{M^2_{\phi_j}}{M^2_{\phi_i}}$. In computing Equation 4.32 we have considered the massless limit for the SM leptons. We also have figured out that the $\epsilon^i_{\text{self energy}}$ exactly vanishes in this limit. A more detailed analytical understanding of this asymmetry parameter is provided in the Appendix C. The obtained amount of lepton asymmetry can estimate the observed BAU in presence of a rapid expansion of the Universe for a particular domain of scalar mass. The effect of this unorthodox cosmology is crucial especially in bringing down the leptogenesis scale and can be realized from the modifications brought out in the Boltzmann's Equations which we are going to discuss in the following subsection.

4.7.1 Boltzmann's equations and final baryon asymmetry

The evolutions of number densities of ϕ and $B-L$ asymmetry can be obtained by solving the following set of coupled Boltzmann's equations (BEQs) [48, 50]:

$$\frac{dN_{\phi_i}}{dz} = -D_i(N_{\phi_i} - N_{\phi_i}^{eq}), \quad \text{with} \quad i = 1, 2, 3 \tag{4.33}$$

$$\frac{dN_{B-L}}{dz} = -\sum_{i=1}^{3} \epsilon_i D_i(N_{\phi_i} - N_{\phi_i}^{eq}) - \sum_{i=1}^{3} W_i N_{B-L}, \tag{4.34}$$

with $z = M_{\phi_1}/T$ when the decaying scalar is the ϕ_1. For convenience in numerical evaluation in case all the three scalars are actively involved in the generation of the final lepton asymmetry (which is true here) one can redefine a generalized temperature-function (z), writing $z = \frac{z_i}{\sqrt{x_{1i}}}$ with $i = 1, 2, 3$. Note that N_{ϕ_i}'s are the comoving number densities normalised by the photon density at temperature larger than M_{ϕ_i}. The first one of the above set of coupled equations tells us about the evolution of the scalar number density whereas the second determines the evolution of the amount of the lepton asymmetry which survives in the interplay of the production from parent particle (first term) and washout (second term), as a function of temperature.

To properly deal with the wash out of the produced lepton asymmetry one must take into account all the possible processes which can potentially erase a previously created asymmetry. Ideally there exist four kinds of processes which contribute to the different terms in the above BEQs: decays, inverse decays, $\Delta L = 1$ and $\Delta L = 2$ scatterings mediated by the decaying particle. In the weak washout regime, the later two processes contribute negligibly to the washout. Hence in our present analysis, considering an initial equilibrium abundance[‖] of N_1, the inverse decay offers the principal contribution.

The Hubble expansion rate in the standard cosmology is estimated to be $H_R(T) \approx \sqrt{\frac{8\pi^3 g_*}{90}} \frac{M_{\phi_1}^2}{M_{\rm Pl}} \frac{1}{z^2} \approx 1.66 g_* \frac{M_{\phi_1}^2}{M_{\rm Pl}} \frac{1}{z^2}$ with $g_* = 106.75$, being the effective relativistic degrees of freedom. The D_i in Equation 4.33 denotes the decay term

[‖]In the case of vanishing initial abundance of N_1, the $\Delta L = 1$ scatterings can enhance the abundance of N_1 and increase the efficiency factor [180, 181] which can be expressed as,

$$D_i = \frac{\Gamma_{D,i}}{Hz} = K_i x_{1i} z \langle 1/\gamma_i \rangle, \tag{4.35}$$

considering $H = H_R$ and one can write $\Gamma_{D,i} = \bar{\Gamma}_i + \Gamma_i = \tilde{\Gamma}_{D,i}\langle 1/\gamma_i \rangle$ with $\langle 1/\gamma_i \rangle$, the ratio of the modified Bessel functions $\mathcal{K}_1$ and $\mathcal{K}_2$ quantifying the thermally averaged dilution factor as $\langle 1/\gamma_i \rangle = \frac{\mathcal{K}_1(z_i)}{\mathcal{K}_2(z_i)}$. Note that Γ_i represents the thermally averaged decay width of ϕ_i to SM lepton and the BSM fermion doublet whereas $\bar{\Gamma}_i$ stands for the conjugate process of the former. The wash out factor K_i in Equation 4.35 is related to the decay width and the Hubble expansion rate as

$$K_i \equiv \frac{\tilde{\Gamma}_{D,i}}{H(T = M_{\phi_i})}. \tag{4.36}$$

The decay and inverse decay processes automatically take the resonant part of the $\Delta L = 2$ scatterings into account. Thus to avoid double counting it is a mandatory task to properly subtract the real intermediate states (RIS) contribution where the decaying particle can go on-shell in the s-channel scattering. For a detailed analytical understanding of RIS subtraction one may look into [48]. At the same time, it is to note that at a higher temperature the non-resonant parts of $\Delta L = 2$ scatterings become important when the mediating particle (here the scalar ϕ) is exchanged through u-channel. An in-depth study of such high temperature affect on the $\Delta L = 2$ scatterings mediated by heavy RHNs can be found in [50, 182]. Now the inverse decay (ID) width $\Gamma_{\rm ID}$ is connected to Γ_D as:

$$\Gamma_{\rm ID}(z_i) = \Gamma_D(z_i)\frac{N^{\rm eq}_{\phi_i}(z_i)}{N^{\rm eq}_l}, \tag{4.37}$$

where $N^{\rm eq}_{\phi_i} = \frac{3}{8} z_i^2 \mathcal{K}_2(z_i)$ and $N^{\rm eq}_l = \frac{3}{4}$. Then it follows that the relevant wash out term in the present scenario will take the following form:

$$W_i \approx W_i^{\rm ID} = \frac{1}{2}\frac{\Gamma_{\rm ID}(z_i)}{Hz}, \tag{4.38}$$

$$= \frac{1}{4} K_i x_{1i}^2\, \mathcal{K}_1(z_i) z^3, \tag{4.39}$$

for standard Universe. We would like to mention once again that in the BEQs of Equation 4.33 N_{ϕ_i} and N_{B-L} denote the respective abundances with respect to photon number density in highly relativistic thermal equilibrium.

The influence of non-standard cosmology as briefed in Section 4.4, is observed in the form of a new set of modified BEQs where the Hubble rate of expansion obeys the form as shown in Equation 4.20. Hence in the alternative cosmological

BP	Λ_{11} (eV)	Λ_{22} (eV)	Λ_{33} (eV)	a	$h_{\alpha i} \times 10^4$
I	9.94×10^7	1.02×10^8	1.04×10^8	2.9	$\begin{pmatrix} -10.08 - 3.17i & 4.02 - 7.94i & -0.31 - 6.58i \\ -1.54 - 10.38i & 8.92\,0.26i & 5.71 - 3.1i \\ 1.05 - 6.88i & 5.65 + 1.81i & 4.13 - 0.83i \end{pmatrix}$
II	5.54×10^7	5.69×10^7	5.83×10^6	2.7	$\begin{pmatrix} -9.55 - 3.0i & 3.97 - 7.5i & -0.29 - 6.22i \\ -1.46 - 9.84i & 8.44 + 0.24i & 5.39 - 2.91i \\ 0.96 - 6.53i & 5.36 + 1.69i & 3.86 - 0.75i \end{pmatrix}$

Table 4.3: Numerical estimation of the two Yukawa coupling matrices which are obtained for the sets of benchmark points (BP) tabulated in Table 4.2. Reference scalar masses are considered as $M_{\phi_i} = \{10^7, 10^{7.1}, 10^{7.2}\}$ GeV.

scenario with $n > 0$ the Hubble parameter in the present section will be modified according to Equation 4.20 wherever applicable. For example with the new Hubble expansion rate, the decay term looks like,

$$D_i = \frac{\Gamma_{D,i}}{Hz} = K_i z^{n/2+1} x_{1i}^{n/4+1} \frac{\mathcal{K}_1(z_i)}{\mathcal{K}_2(z_i)}. \tag{4.40}$$

Similarly, the washout parameter K_i and $W_{\rm ID}$ will be modified to

$$K_i = \frac{\tilde{\Gamma}_{D,i}}{H_R(T = M_{\phi_i})} \left(\frac{T_r}{M_{\phi_i}}\right)^{n/2}, \tag{4.41}$$

$$W_i = \frac{1}{4} K_i x_{1i}^{n/4+2}\, \mathcal{K}_1(z_i) z^{n/2+3} \tag{4.42}$$

With all these inputs, the final baryon asymmetry of the Universe can be obtained by using,

$$\eta_B = a_{\rm sph} \frac{N_{\text{B-L}}}{N_\gamma^{\rm rec}} = 0.0126\ N_{\text{B-L}}^f, \tag{4.43}$$

where $a_{\rm sph}$ indicates standard sphaleron factor and $N_{\text{B-L}}^f$ being the final B-L asymmetry.

4.8 Results for neutrino mass and leptogenesis

It is clear from the above discussion that the Yukawa couplings and the masses of BSM scalar and fermionic fields enter into both one loop diagrams responisble for neutrino mass and lepton asymmetry calculation respectively. Here we present some numerical estimates of the relevant parameters which offer correct order of neutrino mass and lepton asymmetry in this set up.

For numerical computation we choose the lightest active neutrino mass to be 0.001 eV, abiding by the cosmological bound on the sum of neutrino masses as reported by Planck ($\sum_i m_{\nu_i} < 0.12$ eV) [144, 183, 184]. We also prefer to choose the maximal value for Dirac CP phase $\delta_{CP} = -\frac{\pi}{2}$ and the best fit central values for rest of the oscillation parameters. Using these values, it is trivial to obtain the

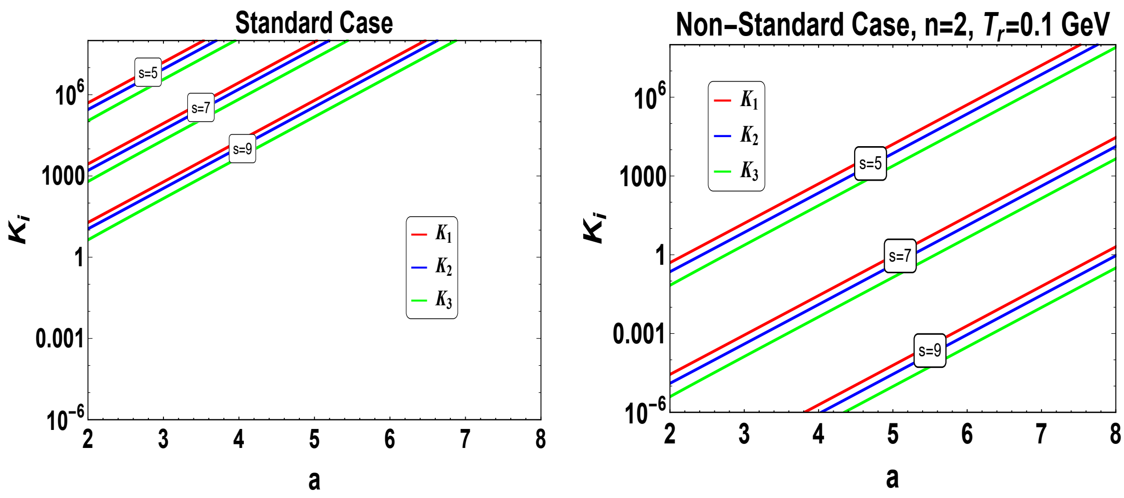

Figure 4.9: Washout factors as a function of a for (left) standard and (right) non-standard case. We consider here $M_{\phi_i} = \{10^s, 10^{s+0.1}, 10^{s+0.2}\}$ GeV with $s = \{7, 8, 9\}$ for the benchmark point I in Table 4.2.

Yukawa couplings ($h_{\alpha i}$) with the help of Equation 4.28 once the mass scales of the BSM fields are known. In Table 4.3, we provide the numerical estimate of the Yukawa couplings matrix (h) for the two reference points as noted in Table 4.2, considering scalar masses as $\{10^7, 10^{7.1}, 10^{7.2}\}$ GeV. This estimation is essential for the calculation of baryon asymmetry as well.

As emphasized earlier, one of the primary aims of this study is to investigate the dynamical generation of baryon asymmetry considering the presence of non-standard cosmology ($H \neq H_R$) instead of the standard one ($H = H_R$). The Figures 4.9-4.10 illustrate the reason behind this preference. In Figure 4.9, we show the variation of the washout factor K_i as a function of the parameter a present in Equation 4.28 considering both standard (left) and non-standard (right) cases. In Figure 4.10, we exhibit the variation of ϵ_i with respect to the parameter a. For clarity we have chosen different domains for the scalar mass, considering $M_{\phi_i} : \{10^s, 10^{s+0.1}, 10^{s+0.2}\}$ GeV where s can take the values as $s = 5, 7, 9$. Using this set of M_{ϕ_i} values and the reference point I in Table 4.2 we prepare these figures. These figures give a clear insight on the fact that both the washout factor K_i and ϵ_i are increasing functions of a. Moreover, for lower M_{ϕ_i} the wash out becomes stronger ($K_i \gg 1$). The Figure 4.10 reveals that the order of the asymmetry parameter remains to be more or less unaltered irrespective of the choice of M_ϕ scales. This can be understood from Equation 4.32, where the term involving the functional dependence of M_{ϕ_i} takes a constant value close to unity for any arbitrary choice of M_{ϕ_i}.

In contrast to the standard case, the right panel of Figure 4.9 shows that the

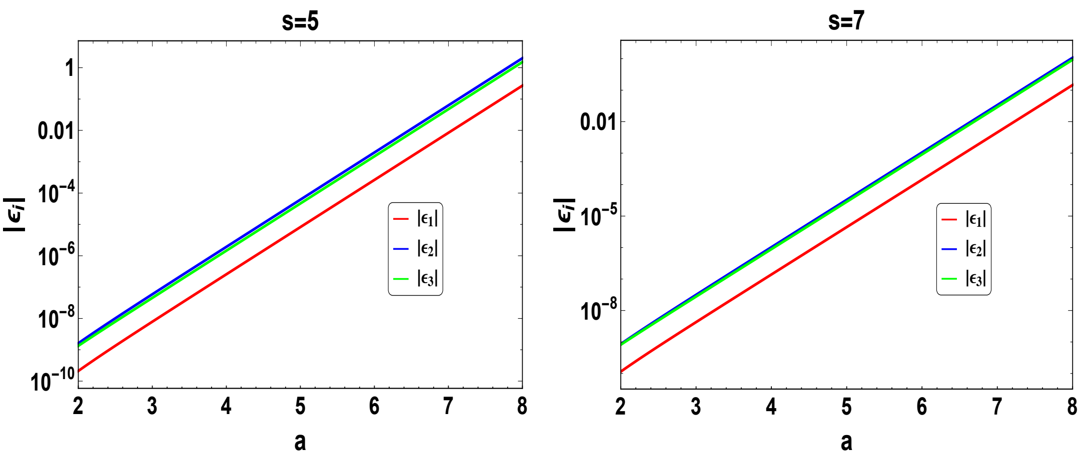

Figure 4.10: Order of lepton asymmetry parameter ϵ_i as a function of a in Equation 4.28 for considering scalar masses $M_{\phi_i} = \{10^5, 10^{5.1}, 10^{5.2}\}$ GeV (left) and $M_{\phi_i} = \{10^7, 10^{7.1}, 10^{7.2}\}$ GeV (right) for the benchmark point I in Table 4.2.

order of K_i's can be substantially suppressed in case the Universe expands faster where we have chosen T_r and n to be 0.1 GeV and 2 respectively. Although in the standard case it may be possible to generate the correct order of baryon asymmetry with superheavy scalar fields ($M_{\Phi_i} \gg 10^9$ GeV), we prefer the non-standard option since it opens up the possibility of relaxing the lower bound on M_ϕ's to meet the weak washout criteria ($K_i < 1$).

We numerically solve the BEQs of Equation 4.33 with the initial conditions that the scalars are in thermal equilibrium at $T > M_{\phi_i}$ and also assume that the initial B-L asymmetry $N^{\rm ini}_{B-L} = 0$. We have performed this analysis by assuming the lightest scalar $M_{\phi_1} \sim \mathcal{O}(10^7)$ GeV and which is enforced to obey two kinds of hierarchies with the other two heavier scalars. First we consider a compressed pattern of mass hierarchy among the scalars and in the later part we speculate on the case with a relatively larger mass hierarchy. This two hierarchy patterns lead to distinct evolutionary dynamics of the scalars as understood from Figures 4.11-4.12.

In Figure 4.11, we show the evolution of $N_{\phi_{1,2,3}}$ (left) and N_{B-L} (right) by considering the compressed mass pattern with $n = 2$, $M_{\phi_i} = \{10^7, 10^{7.1}, 10^{7.2}\}$ GeV. As it is seen that, number density of the scalars drops from their equilibrium abundances and $N_{\rm B-L}$ rises with decreasing temperature and finally $N_{\rm B-L}$ gets saturated at some finite value. In Table 4.4, we list the required values of the parameter a to attain the observed amount of η_B for the reference points of Table 4.2 considering $n = 2$ and $T_r = 0.1$ GeV. We also include the order of the lepton asymmetry parameter and the η_B values for $n = 1$. It is clearly understood that a smaller value of n, reduces the amount of η_B for a fixed T_r and a.

Next we consider a representative uncompressed mass hierarchies among the

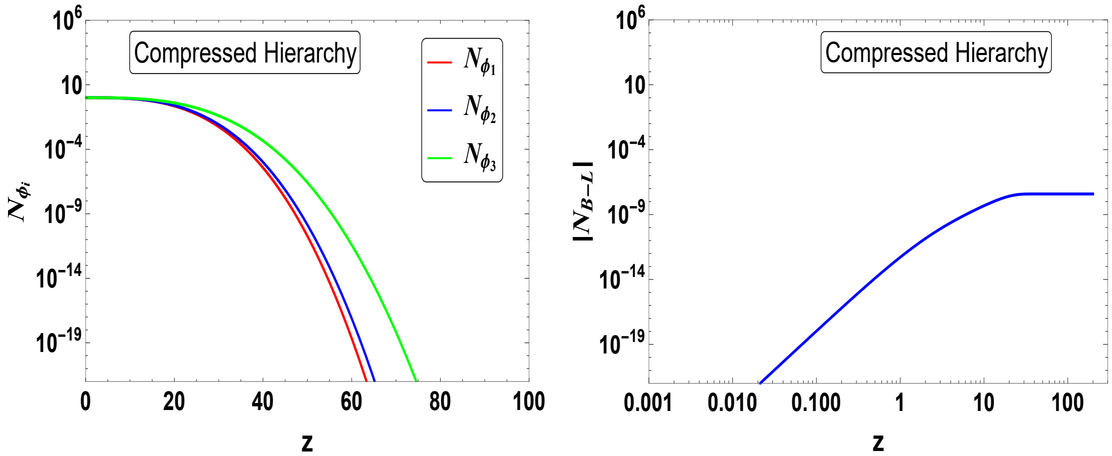

Figure 4.11: Evolution of N_{ϕ_i} (left) and $N_{\mathrm{B-L}}$ (right) as a function of temperature T considering compressed mass hierarchy among the scalars with $\{M_{\phi_i} \to 10^7, 10^{7.1}, 10^{7.2}\}$ GeV and $T_r = 0.1$ GeV for the benchmark point I in Table 4.2.

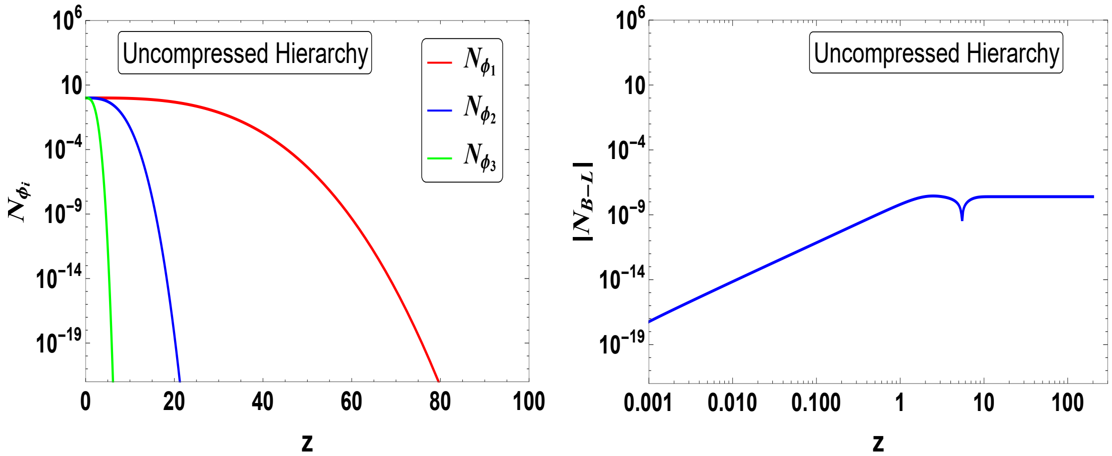

Figure 4.12: Evolution of N_{ϕ_i} (left) and $N_{\mathrm{B-L}}$ (right) as a function of temperature T considering uncompressed mass hierarchy among the scalars with $\{M_{\phi_i} \to 10^7, 10^9, 10^{11}\}$ GeV and $T_r = 0.1$ GeV for the benchmark points I in Table 4.2.

scalars (not shown in the Tables) and fix $M_{\phi_i} = \{10^7, 10^9, 10^{11}\}$ GeV. In Figure 4.12, we show the evolution of $N_{\phi_{1,2,3}}$ and N_{B-L} as a function of temperature T. Since $M_{\phi_{2,3}}$ are quite heavier as compared to M_{ϕ_1}, their number densities fall sharply at a very early stage of evolution. Hence, in the evolution, first N_{B-L} gets created from ϕ_3 decay. Then when ϕ_2 starts decaying, N_{B-L} changes its sign which is observed in form of a kink in right of Figure 4.12 is observed. Finally the decay of the lighter scalar ϕ_1 helps in keeping the remnant asymmetry upto the expected amount successfully. Similar to the earlier case, in Table 4.5, we tabulate the findings: the value of a, order of $\epsilon_{1,2,3}$ and $\eta_B(n = 1)$ to attain the correct order of η_B.

The present analysis appears to be suitable for any mass window for the

BP	a	$\|\epsilon_1\|$	$\|\epsilon_2\|$	$\|\epsilon_3\|$	$\eta_B(n=1)$	$\eta_B(n=2)$
I	2.9	3.01×10^{-9}	2.21×10^{-8}	1.95×10^{-8}	5.07×10^{-13}	3.71×10^{-10}
II	2.7	2.68×10^{-9}	1.98×10^{-8}	1.7×10^{-8}	5.69×10^{-13}	3.28×10^{-10}

Table 4.4: Estimating baryon asymmetry considering compressed mass hierarchy with $M_{\phi_i}=\{10^7,10^{7.1},10^{7.2}\}$ GeV for the two benchmark points in Table 4.2.

.

BP	a	$\|\epsilon_1\|$	$\|\epsilon_2\|$	$\|\epsilon_3\|$	$\eta_B(n=1)$	$\eta_B(n=2)$
I	2.75	8.99×10^{-13}	7.03×10^{-8}	4.05×10^{-8}	1.30×10^{-13}	2.86×10^{-10}
II	2.75	1.52×10^{-12}	1.26×10^{-7}	8.16×10^{-8}	2.10×10^{-16}	4.30×10^{-10}

Table 4.5: Estimation of baryon asymmetry considering uncompressed mass hierarchy with $M_{\phi_i}=\{10^7,10^9,10^{11}\}$ GeV for the two benchmark points in Table 4.2.

.

scalars provided the validity of the analytical expressions for $\epsilon_{1,2,3}$ in Equation 4.32 holds. It is to note here that, as of now we have explored this scenario only for unflavored regime of leptogenesis, but it would be intriguing to examine this framework including flavor effects where the charged lepton Yukawa interactions are fast enough. In analogy with the scenario where lepton asymmetry originates from the decay of a heavy RHN, a different magnitude of a would be required to describe the evolution of such processes, consistent with the observations. Since, we are already in the weak wash out regime, apparently it can be claimed that the contribution from the individual flavor asymmetries would be minimum [50].

4.9 Summary and Conclusion

We have constructed an attractive framework deciphering baryogenesis from leptogenesis along with a pseudo-Dirac dark matter candidate and neutrino mass in a scalar extended singlet doublet scenario. Successful accomplishment of all the three entities at the same time is conspired by a mere Majorana mass term for the singlet fermion present in the Lagrangian. We have considered both standard and non-standard cosmology and furnished a comparative analysis between the two. Since the thermal history of the Universe is largely unknown prior to the big bang nucleosynthesis, we conceive the idea of fast-expanding Universe and analyze the singlet doublet DM phenomenology in detail. In one of our earlier works, we have investigated pseudo-Dirac singlet doublet DM phenomenology in view of spin independent DM SI direct search experiments. Here we extend that idea and find that the impact of this rapid expansion of the Universe turns significant especially the relevant parameter space to be consistent with the direct detection bound receives huge deviation compared to the standard one. First, we estimate the interaction strength for the singlet doublet dark matter with the visible sector for two specific DM masses ($\lesssim 1$ TeV) considering the various kinds of the fast expansion of the Universe (with different temperature dependences) which turns out to be higher than in the usual scenario. This looks consistent with the earlier model independent works in this direction. In the later part, we discuss the radiative generation of neutrino mass which require an extension of the minimal framework with additional singlet scalars. We further calculate the baryon asymmetry of the Universe from the decay of these dark scalars by using the Yukawa couplings which get constrained from the neutrino oscillation data. The proposed mechanism of lepton asymmetry generation is slightly different from the ones available in the existing literature where the decay of heavy right-handed neutrino generates the asymmetry in the lepton sector. We conclude with an important notion that the non-standard Universe is perhaps preferred over the standard one in the present scenario to yield the observed amount of baryon asymmetry in the Universe.

Chapter 5

Self-interacting freeze-in dark matter in a singlet doublet scenario

5.1 Introduction

We focus on working in a scenario where the GeV scale fermion dark matter predominantly contribute to the total relic abundance. Stronger interaction strength between the fermionic dark matter and the mediator scalar is desired for producing large self-interaction [185–189]. On the other hand, a strongly coupled dark sector generally leads to the formation of internal dark thermal equilibrium with a separate dark sector temperature T_D [189–194]. In our present scenario, after the freeze-in production of χ, they start annihilating into a pair of ϕ and vice versa, maintaining the dark sector equilibrium before a freeze-out mechanism triggers for χ. In literature, such rich dynamics inside a hidden dark sector is familiarly known as the reannihilation effect [190, 191]. Considering radiation dominated Universe (RD), we find that after the dark sector freezes out, ϕ shares a sizeable contribution to the total relic abundance. Thus, a χ dominated scenario is very unlikely.

Since our aim is to provide a χ dominated scenario which may also give rise to velocity-dependent fermionic self-interacting dark matter (see [189] for a similar exercise in a different framework), the proposed set up as discussed above in the radiation dominated Universe does not work. In the present study, we apprehend that the presence of a non-standard epoch in the early Universe could be useful to alleviate this. A faster expansion of the Universe can prevent the dark sector from reaching thermal equilibrium or slow down the dark sector interaction rate. These assist in suppressing the $\chi\chi \to \phi\phi$ conversion rate to obtain a χ dominated dark matter scenario. We have employed two particular kinds of modified cosmology [53, 164, 195] namely kination domination and faster than kination domination. We have found that such non-standard epochs in the early Universe can work remarkably to reach our defined aim of obtaining $\Omega_\chi h^2 \sim 0.12$ [12] which has the potential to resolve the cosmological problems as earlier stated. Additionally, the presence of a non-standard epoch helps to provide a complementary probe of the GeV scale dark matter in the singlet doublet framework via displaced vertices which is not possible in a radiation dominated scenario as shown in [111, 196]. The chapter is organised as follows. In Section 5.2, we furnish the model structure and the corresponding Lagrangians. Next, in Section 5.3, we discuss the dark matter phenomenology considering the standard cosmology and two different forms of non-standard cosmology. We describe the discovery prospects of the proposed model at collider experiments in Section 5.4. Estimate of the self-interaction cross section for the singlet doublet dark matter are presented in Section 5.5. Finally, we summarise by pointing out the new findings of our analysis and draw the conclusion in Section 5.7.

5.2 The Model

We extend the SM particle content by one $SU(2)_L$ vector doublet fermion (Ψ) with hypercharge $Y = -\frac{1}{2}$ and one hyperchargeless gauge singlet vector fermion (χ). In addition, we also include a real scalar singlet field (ϕ) which assists the DM to yield strong dark matter self-interaction. We impose a discrete Z_2 symmetry under which the SM particles and the ϕ field transform trivially while the BSM fermions are assigned odd Z_2 charges. The Lagrangian of the scalar sector is read as

$$\mathcal{L}_{\rm scalar} = |D^\mu H|^2 + \frac{1}{2}(\partial^\mu \phi)(\partial_\mu \phi) - V \ , \tag{5.1}$$

where the covariant derivative is defined as,

$$D^\mu = \partial^\mu - ig\frac{\sigma^a}{2}W^{a\mu} - ig'\frac{Y}{2}B^\mu, \tag{5.2}$$

with g and g' being the $SU(2)_L$ and the $U(1)_Y$ gauge couplings respectively. The scalar potential $V = V(H) + V(\phi) + V(\phi, H)$ takes the following form,

$$V(H) = -\mu_H^2\,(H^\dagger H) + \lambda_H\,(H^\dagger H)^2, \tag{5.3}$$

$$V(\phi) = \frac{m_\phi^2}{2}\phi^2 + \frac{\lambda_\phi}{4!}\phi^4 + \frac{b_3}{3!}\phi^3, \tag{5.4}$$

$$V(\phi, H) = \frac{\lambda_{\phi H}}{2}\phi^2(H^\dagger H) + a_3\ \phi(H^\dagger H). \tag{5.5}$$

Note that we do not write the liner term for ϕ in $V(\phi)$ since it can always be absorbed through the redefinition of the other parameters. We assume that all the mass scales and the coupling coefficients are real and positive. In this limit, the vacuum expectation values (vev) of the scalars H and ϕ after minimising the potential V are obtained as,

$$\langle H \rangle = v \;, \quad \langle \phi \rangle = 0. \tag{5.6}$$

The Lagrangian for the fermionic sector is written as,

$$\mathcal{L} = \mathcal{L}_f + \mathcal{L}_Y, \tag{5.7}$$

where,

$$\mathcal{L}_f = i\overline{\Psi}\gamma_\mu D^\mu \Psi + i\overline{\chi}\gamma_\mu \partial^\mu \chi - m_\Psi \overline{\Psi}\Psi - m_\chi \overline{\chi}\chi \tag{5.8}$$

$$\mathcal{L}_Y = \; - Y\overline{\Psi}\tilde{H}\chi + h.c. - \lambda\phi\overline{\chi}\chi - \delta\phi\overline{\Psi}\Psi, \tag{5.9}$$

where we have defined $\Psi^T = (\psi^+ \;\; \psi^0)$.

The Dirac mass matrix for the neutral fermions after the spontaneous breakdown of the electroweak symmetry is obtained as,

$$\mathcal{M}_D = \begin{pmatrix} m_\Psi & M_D \\ M_D & m_\chi \end{pmatrix}, \tag{5.10}$$

where we define $M_D = \frac{Yv}{\sqrt{2}}$. After diagonalisation of Equation 5.10, we are left with two neutral Dirac particles which we identify as ξ_1 and ξ_2. The mass eigenvalues of ξ_1 and ξ_2 are given by,

$$m_{\xi_1} \approx m_\chi - \frac{M_D^2}{m_\Psi - m_\chi} \tag{5.11}$$

$$m_{\xi_2} \approx m_\Psi + \frac{M_D^2}{m_\Psi - m_\chi} \tag{5.12}$$

Therefore, the lightest eigenstate is ξ_1, which is the stable DM candidate of our framework. The stability of the DM is ensured by the unbroken $\mathcal{Z}_2$ symmetry. The mixing between two flavor states, *i.e.* neutral part of the doublet (ψ^0) and the singlet field (χ) is parameterised by,

$$\sin 2\theta \simeq \frac{2Yv}{\Delta M}, \tag{5.13}$$

where $\Delta M = m_{\xi_2} - m_{\xi_1} \approx m_\Psi - m_\chi$ in the small Y limit. Here, ξ_1 can be identified with the singlet χ. Since the present analysis involves freeze-in dark matter production, the mixing between the singlet and doublet fermions is always very tiny. Therefore, henceforward we identify the dark matter candidate as χ.

5.3 Dark matter relic

The present set-up has two stable particles ϕ and χ, and both can contribute to total DM relic abundance. The relative contribution of each component to the DM relic is dependent on early Universe history, as we discuss below. We have worked with $m_\phi \ll m_\chi$. We also set the interaction strength between the lighter scalar and our fermion DM candidate (χ) relatively large $\lambda \sim \mathcal{O}(10^{-1})$ with an aim to obtain a large amount of self-interaction for χ that can address the problems associated with small scale structures of the Universe. We assume the parameters $a_3, \lambda_{\phi H}$, which mix ϕ with SM Higgs sector and δ which couples ϕ with ψ to be extremely tiny or negligibly small such that both ϕ and χ can never equilibrate with the SM bath. On the other hand, the Yukawa coupling $Y(\ll 1)$ connecting the dark matter with SM bath is another important parameter for present study. It determines the production rate of fermion dark matter from SM bath by via freeze in process. We make a specific choice $a_3, \delta, \lambda_{\phi H} \ll Y$ which implies ϕ can only be populated at a non-negligible rate from the $\chi\chi \to \phi\phi$ process, depending on the expansion rate of the Universe. The Yukawa coupling Y along with the self interacting coupling λ would decisively determine the dynamics of our model and we would specify their strength during benchmark selection.

5.3.1 Radiation dominated Universe

In the standard description of Big bang cosmology, the Universe is radiation dominated prior to BBN. Initially both the components begin with zero number density and first χ gets produced from the SM bath. Below we list the relevant processes that populate the DS particles before and after EW symmetry breaking.

- **Before EW symmetry breaking:** The DM production takes place from the $\Psi\Psi \to \chi\chi$ (H mediated), $HH \to \chi\chi$ (Ψ mediated) and $\Psi \to H\chi$ processes. If $Y \ll 1$, the scattering processes are expected to be suppressed due to Y^4 dependence and the decay channel of Ψ (with decay width $\propto Y^2$) will dominantly contribute to the non-thermal yield of DM relic density.

- **After spontaneous EW symmetry breaking:** The singlet doublet mixing occurs which triggers additional production processes for the DM. In this regime, the DM production channels are the (i) scatterings: SM SM $\to \chi\chi$, SM SM $\to \chi\xi_2$ and (ii) decays: $\xi_2 \to \chi h,\ \chi Z;\ \psi^\pm \to \chi W^\pm$. Both the scattering processes could be mediated by Higgs and $SU(2)_L$ gauge bosons. In the limit $Y \ll 1$, the scattering process SM,SM$\to \chi\chi$ would have sub-dominant impact on the production of DM.

Considering the decays to play dominant role in the non-thermal production of χ at early Universe* we define $\langle\Gamma_\Psi\rangle^T = \langle\Gamma_\Psi\rangle\, \Theta(T-T_{\rm EW})+\langle\Gamma_{\Psi^\pm}+\Gamma_{\xi_2}\rangle\, \Theta(T_{\rm EW}-T)$ where $T_{\rm EW}\sim 160$ GeV indicates the EW symmetry breaking temperature. The $\langle\Gamma_\Psi\rangle^T$ is the thermally averaged decay width where T is the SM temperature. The subsequent process $\chi\chi\to\phi\phi$ process† yields ϕ and when the number density of ϕ is sufficient, it can further annihilate to χ and form a local dark sector thermal equilibrium with an uniform temperature T_D provided [194, 197]

$$r \equiv \frac{n_\chi\langle\sigma v\rangle_{\chi\chi\to\phi\phi}}{\mathcal{H}} \gg 1. \tag{5.14}$$

Finally χ freezes out and both contribute non-negligibly to the total relic abundance. The set of Boltzman equations that governs such dynamics with $z(=\frac{m_\chi}{T})$ are given by [189–194],

$$\frac{dY_\phi}{dz} = \frac{s}{\mathcal{H}z}\langle\sigma v\rangle^{T_D}_{\chi\chi\to\phi\phi}\left[Y_\chi^2 - \left(\frac{Y_\chi^{\rm eq}(T_D)}{Y_\phi^{\rm eq}(T_D)}\right)^2 Y_\phi^2\right] \tag{5.15}$$

$$\frac{dY_\chi}{dz} = -\frac{s}{\mathcal{H}z}\langle\sigma v\rangle^{T_D}_{\chi\chi\to\phi\phi}\left[Y_\chi^2 - \left(\frac{Y_\chi^{\rm eq}(T_D)}{Y_\phi^{\rm eq}(T_D)}\right)^2 Y_\phi^2\right] + \frac{45z^2}{2\pi^2 m_\chi^3}\frac{s\langle\Gamma_\Psi\rangle^T}{\mathcal{H}}\left(Y_\Psi^{\rm eq}(T)-Y_\chi\right), \tag{5.16}$$

where Y_i represents the comoving number density of $i^{\rm th}$ component. The final relic abundance of $i^{\rm th}$ component can be determined by $\Omega_i h^2 = 2.744\times10^8\times m_i\times Y_i(z=\infty)$.

Note that each of the dark sector particles could follow thermal distribution having its own temperature provided sufficient self interaction exists. Now if the conversion procees $\chi\chi\to\phi\phi$ is efficent enough, the DS particles reach thermal equilibrium quickly after the initial production with a common temperature. In that case we can safely use the thermal distribution anstaz for the DS particles. Two possible methods to estimate the dark sector are prevalent in literature. The first one is to obatin the energy density of the DS as function of temperature and subsequently estimating the dark temperature [189–191, 198, 199]. The other one

*This will be justified in a while.

†It is simple to ensure that the dominant production of ϕ occurs from $\chi\chi\to\phi\phi$ process by tuning the other relevant parameters $\{a_3, b_3, \lambda_{\phi H}, \delta\}$ at sufficiently smaller value.

	λ	m_Ψ	m_χ	m_ϕ	Y	$\Omega_\chi h^2$	$\Omega_\phi h^2$
RD-I	0.145	1.5 TeV	20 GeV	10 MeV	5.45×10^{-10}	0.0075	0.111
RD-II	0.095	1.5 TeV	10 GeV	10 MeV	5.48×10^{-10}	0.0085	0.110
RD-III	0.085	1.5 TeV	5 GeV	10 MeV	5.65×10^{-10}	0.0035	0.116

Table 5.1: Three representative benchmark points that describe the reannihilation scenario in the present framework considering radiation dominated Universe.

is calculating the DS temperature using the second moment approximation [200–202]. In both the methodlogy it is generally assumed that the DS particles follow a distribution which is close to the thermal one with the underlying assumption of sufficent self-interaction of DS particles. In the present work we have utilized the first prescription following [189, 191] in order to compute the dark sector temperature. We have presumed that DS reaches thermal equilibrium and share a common temperature T_D since we consider λ to be considerably larger having magnitude $\sim \mathcal{O}(0.1)$ with $m_\Psi \gg m_\chi$. Later we numerically verify this after obtaining the solutions of the relevant Boltzman equations to make our analysis self-consistent.

We solve the Boltzman equation for the total dark sector energy density ($\rho_D = \rho_\chi + \rho_\phi$) where ρ_i indicates the energy density for an individual component [187, 189–191, 194, 198, 202].

$$\frac{d\rho_D}{dt} + 3H(\rho_D + p_D) = \mathcal{P}_\Psi n_\Psi^{\rm eq}, \tag{5.17}$$

where the quantity $\mathcal{P}_\Psi$ represents the thermally averaged energy transfer rate from the SM to dark sector. The notation $p_D = p_\chi + p_\phi$ stands for the sum of the pressures for individual components. The standard form of p_D is given by,

$$p_D = \frac{g_\chi}{6\pi^2}\int_{m_\chi}^{\infty}\frac{(E_\chi^2 - m_\chi^2)^{3/2}}{e^{E_\chi/T_D}+1}dE_\chi + \frac{g_\chi}{6\pi^2}\int_{m_\phi}^{\infty}\frac{(E_\phi^2 - m_\phi^2)^{3/2}}{e^{E_\phi/T_D}-1}dE_\phi, \tag{5.18}$$

The symbols g_χ and g_ϕ imply the internal degrees of freedom for χ and ϕ species. Additionally, one can write the energy density of the dark sector as,

$$\rho_D = \frac{g_\chi}{2\pi^2}\int\frac{(E_\chi^2 - m_\chi^2)^{1/2}E_\chi^2 dE_\chi}{e^{\frac{E_\chi}{T_D}}+1} + \frac{g_\phi}{2\pi^2}\int\frac{(E_\phi^2 - m_\phi^2)^{1/2}E_\phi^2 dE_\phi}{e^{\frac{E_\phi}{T_D}}-1}. \tag{5.19}$$

Analytical computation of the integrations in RHS of Equations 5.18-5.19 in presence of Fermi-Dirac distribution function looks complicated. Instead one can

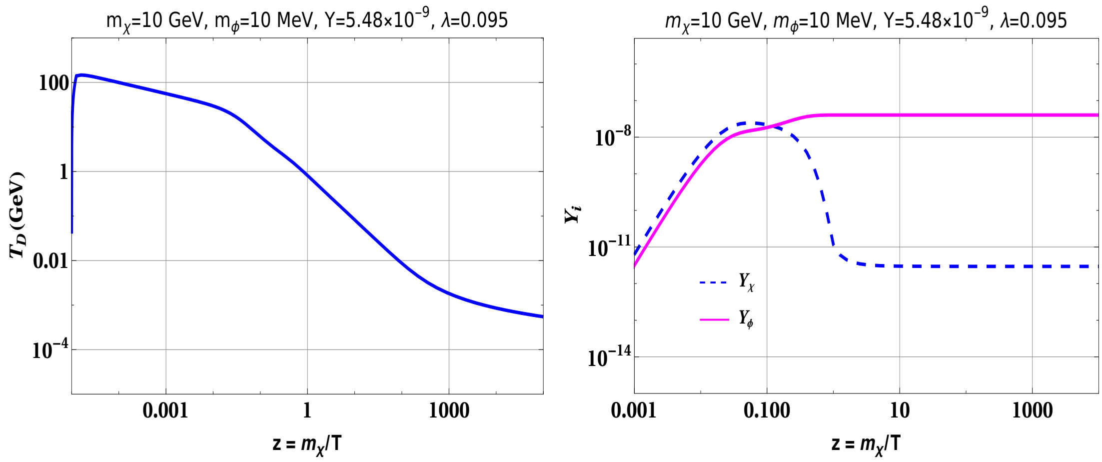

Figure 5.1: The left plot shows the variation of dark sector temperature T_D as a function of inverse temperature z. Corresponding evolutions for the number densities of dark sector particles are shown in the right plot. Here, after initial non-thermal production of χ strong self-interaction generates a dark sector thermal equilibrium. Further, freeze-out produces the ϕ abundance. The Figures are computed considering the benchmark point RD-II in Table 5.1.

compute the same in the Maxwell Boltzman-approximation. We find [‡],

$$p_D = \frac{g_\chi}{2\pi^2} m_\chi^2 T_D^2 K_2\left(\frac{m_\chi}{T_D}\right) + \frac{g_\phi}{2\pi^2} m_\phi^2 T_D^2 K_2\left(\frac{m_\phi}{T_D}\right) \tag{5.20}$$

$$\begin{aligned}\rho_D =& \frac{g_\chi m_\chi^2}{2\pi^2} T_D \left[m_\chi K_1\left(\frac{m_\chi}{T_D}\right) + 3T_D K_2\left(\frac{m_\chi}{T_D}\right)\right] \\ &+ \frac{g_\phi m_\phi^2}{2\pi^2} T_D \left[m_\phi K_1\left(\frac{m_\phi}{T_D}\right) + 3T_D K_2\left(\frac{m_\phi}{T_D}\right)\right].\end{aligned} \tag{5.21}$$

Replacing Equation 5.20 and Equation 5.21 in Equation 5.17, it is simple to obtain the evolution equation for T_D as function of SM temperature.

In Table 5.1, we provide three reference points that instigate dark freeze out of χ after the non-thermal production from the SM bath for three choices of dark matter masses having magnitude 5 GeV, 10 GeV and 20 GeV, respectively. For all benchmark points, we have fixed m_Ψ at 1.5 TeV. This particular choice is motivated to evade the current LHC bound (see Fig. 5.8). In case of non-thermal dark matter production one requires to ensure that the DM remains out of equilibrium with the SM thermal bath. In the present set up with $m_\Psi = 1.5$ TeV, the scattering process SM SM$\to$ $\chi\xi_2$ after the EW symmetry breaking is inefficient (or kinematically forbidden) to thermalize the DM with the SM due to large mass hierarchy between the top quark mass and ξ_2. The other scattering process SM SM$\to$ $\chi\chi$ can be still active however is suppressed by the Y^4

[‡]We verified a close match between the numerical estimation from the standard expression with this approximation for our calculation.

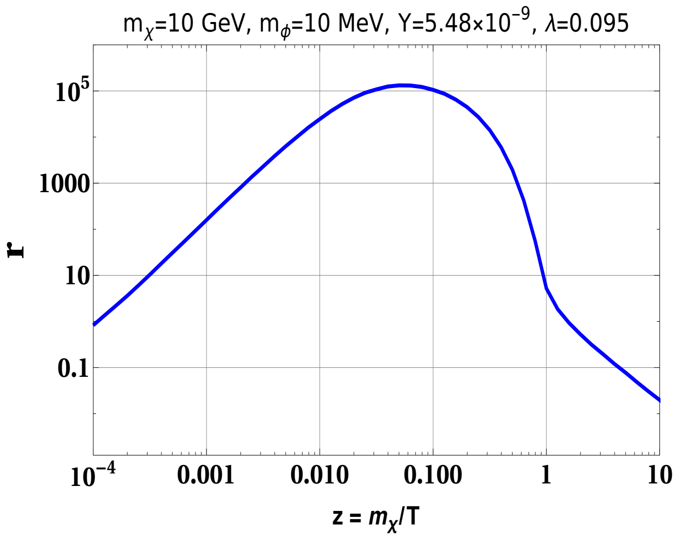

Figure 5.2: The ratio of the interaction rate among the dark sector particles and Hubble parameter of the Universe following Equation 5.14 as function of temperature for for the benchmark point RD-II in Table 5.1.

dependence. Before EW symmetry breaking all the relevant scattering processes have Y^4 dependence as mentioned earlier. We find $Y \lesssim \mathcal{O}(10^{-3})$ keeps the DM out of thermal equilibrium from the SM bath at any temperature considering a DM mass $\sim \mathcal{O}(10)$ GeV in standard RD Universe.

In the present study, we focus on a secluded kind of mechanism where DM χ gets produced from SM bath and conversion of χ yields ϕ. However as seen from the Lagrangian, we may have a few other sources for the production of ϕ from the SM particles. This includes processes like $\Psi\Psi \to \phi\phi$, $HH \to \phi\phi$ with their combined efficacy is function of the coupling parameters $\{a_3, b_3, \lambda_{\phi H}, \delta\}$. We fix them at sufficiently small values as mentioned earlier such that the aforementioned production processes of ϕ are effectively switched of with negligible contribution. We have considered $\delta = 10^{-12}$, $\frac{a_3}{m_\phi} = \frac{b_3}{m_\phi} = 10^{-12}$ and $\lambda_{\phi H} = 10^{-15}$ throughout our analysis.
The evolutions of dark sector temperature and χ and ϕ abundances for the benchmark point RD-II (with DM mass 10 GeV) are shown in Figure 5.1. To generate these Figures, we solve the set of coupled Boltzmann equations as described in Equations 5.16-5.19 and also used Equations 5.20-5.21 with the initial conditions $(Y_\chi,\ Y_\phi,\ T_D) = 0$ and $Y_\Psi = Y_\Psi^{\rm eq}(T)$. In Figure 5.2, we display the ratio r as defined in Equation 5.14 to measure the strength of dark sector interaction rate as a function of SM temperature for the same benchmark point. This figure confirms the formation of dark sector equilibrium after the non-thermal production of both the components with $r \gg 1$ for a finite period. In the left of Figure 5.1, we see the evolution pattern of the dark temperature as a function of SM bath

temperature. Since the dark matter annihilation to SM particles is negligible, it turns out that $T_D \ll T$ always. Initially, the dark temperature increases from zero due to constant entropy injection from the SM bath and reaches a maximum value. Then, due to the expansion of the Universe, it keeps decreasing. Till $T \sim m_\Psi$, the production of χ continues from Ψ decay, and hence we see a slower decreasing rate of T_D initially, and after that, it becomes steep.

The most intriguing part is, here, due to large λ, the χ keeps annihilating to ϕ till the decoupling and ends with suppressed abundance (see right of Figure 5.1). Hence for the chosen benchmark points in the reannihilating scenario, we notice $\Omega_\chi \ll \Omega_\phi$. An enhancement of λ for a fixed m_χ may slightly increase the relic of ϕ further, while it will be reduced further in the opposite limit. However, a small λ is not desirable in view of generating sufficient self-interaction of χ to solve the small scale structure problems of the Universe. It is to note that for all three reference points in Table 5.1, the total relic abundance $\Omega_T h^2 = \Omega_\phi h^2 + \Omega_\chi h^2 \sim 0.12$ [12] remains within the observed limit by Planck requiring a similar order of Y value.

Thus, radiation dominated Universe with a large λ fails to provide a pure χ dominated scenario due to the late time annihilation of the dark matter χ to mediator ϕ. We anticipate that a non-standard Universe in the form of kination or faster than kination domination could enforce significant suppression of ϕ production rate from $\chi\chi \to \phi\phi$ process even in the presence of large λ. This may occur if the ratio in Equation 5.14 remains comparatively suppressed till late time. Note that such faster expansion of the Universe may also slow down the production rate of χ from the SM bath. However, that can be increased by adjusting Y.

5.3.2 Non-standard Universe

In standard description of cosmology, we generally assume that the Universe is radiation dominated in the pre big bang nucleosynthesis (BBN) era. However, due to lack of evidences, possibilities remain open that before BBN, the Universe could have been occupied by a nonstandard fluid, redshifting faster or slower than the radiation component. Earlier works have emphasised that consideration of such modified cosmology poses non-trivial impact on the dark matter phenomenlogy.

A non-standard Universe can be sketched by assuming the presence of an additional species (η) along with the radiation component in the Universe. We consider the equation of parameter (ω) of the nonstandard fluid is larger than that of radiation. We parameterize this by $\rho_\eta \propto a^{-3(1+\omega)}$ which can be converted to $\rho_\eta \propto a^{-(4+n)}$ with $\omega = \frac{1}{3}(n+1)$ and $n > 0$. The modified description of the Universe leads to the redefinition of the Hubble parameter ($\mathcal{H}$) as given

	λ	m_Ψ	m_χ	m_ϕ	Y	n	T_r	$\Omega_\chi h^2$
FKD-I	0.145	1.5 TeV	20 GeV	10 MeV	1.86×10^{-8}	3	19.7 MeV	0.120
FKD-II	0.095	1.5 TeV	10 GeV	10 MeV	2.6×10^{-8}	3	20 MeV	0.119
FKD-III	0.085	1.5 TeV	5 GeV	10 MeV	1.24×10^{-7}	3	4 MeV	0.119

Table 5.2: Three representative benchmark points that demonstrate *pure freeze-in* non-standard cosmology with faster than kination domination.

by [53, 164, 195],

$$\mathcal{H}^2 = \frac{\rho_R + \rho_\eta}{3M_P^2}, \tag{5.22}$$

where M_P refers the reduced Planck scale, ρ_R and ρ_η correspond to the energy densities of radiation and η component. The total energy density of the Universe in presence of η as function of temperature can be expressed as,

$$\rho(T) = \rho_{\rm rad}(T) + \rho_\eta(T) \tag{5.23}$$

$$= \rho_{\rm rad}(T)\left[1 + \frac{g_*(T_r)}{g_*(T)}\left(\frac{g_{*s}(T)}{g_{*s}(T_r)}\right)^{(4+n)/3}\left(\frac{T}{T_r}\right)^n\right], \tag{5.24}$$

where $\rho_R = \frac{\pi^2}{30} g_*(T)T^4$ with g_* stands for the number of relativistic degrees of freedom. The relativistic entropy degrees of freedom is denoted by g_{*s}. Thus a faster expanding Universe is simply parameterised by the set of (n, T_r). A larger n or smaller T_r prompts the energy density of the Universe to redshift more faster. The temperature T_r implies the end of modified expansion rate and we get back the radiation dominated phase. In case of standard radiation dominated Universe, η field would be absent and we simply consider $\rho = \rho_{\rm rad}$. The BBN observation on the number of relativistic degrees of freedom imposes a lower bound on T_r ($\gtrsim (15.4)^{1/n}$ MeV). A special case $n = 2$ (or $\omega = 1$) is familiar as kination domination phase. For $n > 2$, one has to consider scenarios faster than quintessence with negative potential. We refer the readers to [164], for a detailed description of a fast-expanding Universe. Below we separately discuss the cases for kination domination and faster than kination domination.

5.3.2.1 Faster than kination phase

As earlier mentioned a faster than kination phase is realised for $n > 2$. Here we consider $n = 3$. A faster expansion implies enhanced Hubble rate which can suppress the interaction rate among the dark sector particles. If the interaction rate among the dark sector particles gets heavily suppressed (*i.e.* $r \ll 1$), that leads to the production of χ by pure freeze-in. In that case the governing Boltzman

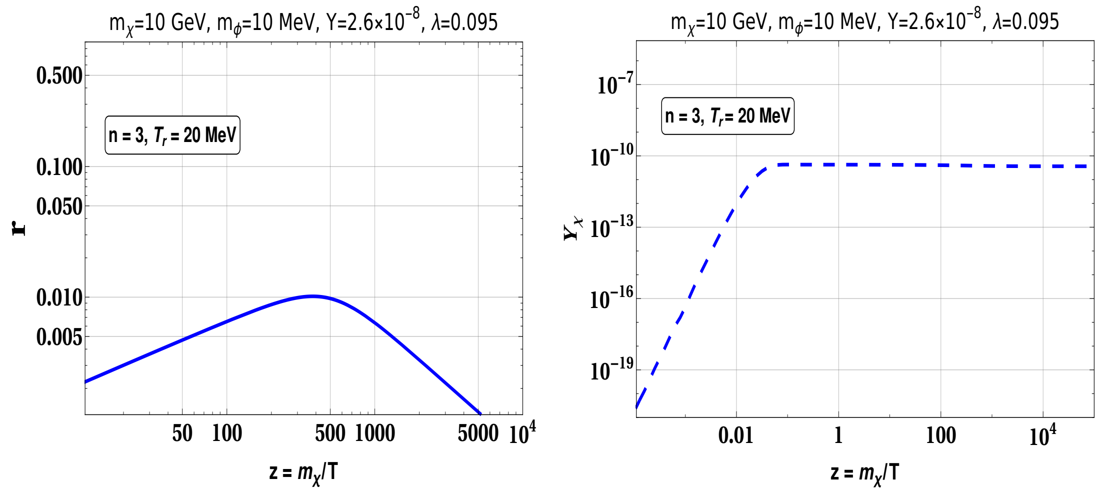

Figure 5.3: Left: The ratio of the interaction rate among the dark sector particles and Hubble paramter of the Universe as function of temperature for the benchmark point FKD-II in Table 5.2. Right: The evolution of DM comoving number density is shown with temperature for the same reference point.

equation for χ looks very simple as given by [55, 203],

$$\frac{dY_\chi}{dz} = \frac{45z^2}{2\pi^2 m_\chi^3}\frac{s\langle\Gamma_\Psi\rangle^T}{\mathcal{H}}\big(Y_\Psi^{\rm eq}(T) - Y_\chi\big). \tag{5.25}$$

Since the rate of the conversion process $\chi\chi \to \phi\phi$ is negligibly low in case of pure freeze-in, we do not estimate the relic of ϕ here, which is expected to be barely abundant in the present Universe. For the same reason, the computation of dark temperature is not essential here.

In Table 5.2, we note down three benchmark points with BSM model inputs $\{\lambda, m_\Psi, m_\chi, m_\phi\}$ are same as used in Section 5.3.1. We have considered zero initial abundance of χ since it remains out of equilibrium in the early Universe. We fix $n = 3$ for this case and vary the T_r and Y in order to obtain correct relic abundance (by pure freeze-in) as allowed by Planck. Recall that these three reference points have portrayed reannihilation patterns with $\Omega_\chi h^2 \ll \Omega_\phi h^2$ for a radiation dominated Universe. In the right of Figure 5.3, we have depicted the evolution of comoving abundance of χ with temperature considering the reference point FKD-II. We have used $n = 3$ and fixed the parameters T_r and Y such that correct relic abundance for χ is attained. In left of Figure 5.3, we estimate the parameter r as earlier defined and found it to be order of $\sim \mathcal{O}(10^{-2})$. This indeed ensures the validity of labelling the present scenario as *pure freeze-in*. Here we do not mention the abundance of the ϕ field. Owing to the faster expansion of the Universe, the produced χ never creates its own bath, and it is expected that the contribution of $\chi\chi \to \phi\phi$ would be negligible in yielding ϕ. Nevertheless, a conservative test can always be performed by solving the Boltzmann equations for Y_ϕ and Y_χ while considering the maximum [§] possible value of $\langle\sigma v\rangle_{\chi\chi\to\phi\phi}$. By utilising this conservative method, we have found similar results (maximum uncertainty is 2%) with Y_ϕ remaining much lower than Y_χ. We also notice from Table 5.2, that the required order of the Yukawa coupling is relatively larger than the one shown in Section 5.3.1 considering standard RD Universe. The reason is obvious as a faster expanding Universe not only suppresses the rate of $\chi\chi\to\phi\phi$ process but also slows down the production process of χ and therefore, one needs to raise BSM Yukawa coupling parameter Y appropriately. To investigate the T_r dependence on Y further, in Figure 5.4, we show the relic density satisfied contours in the $T_r - Y$ plane for $m_\chi = 10$ GeV and 20 GeV considering $n = 3$. We keep the corresponding values of λ and m_Ψ in accordance with Table 5.2. For a fixed DM mass, a smaller T_r requires larger Y. This occurs since a smaller T_r implies an enhanced Hubble rate, and it requires a larger Y to obey the relic abundance bound. Moreover, a smaller DM mass also requires larger Y to obey the relic bound. It is to note that in Figure 5.4, we have kept T_r below 25 MeV. Beyond this value of T_r, the ratio r would turn larger than $\mathcal{O}(10^{-2})$ and therefore, the contribution of $\chi\chi\to\phi\phi$ conversion in the final DM relic may turn important at some extent.

In summary, the above discussion reveals that a faster than kination dominated early Universe ($n = 3$) is able to provide a pure freeze-in yield for χ with absolutely dominant share to the total relic abundance even in the presence of $\lambda \sim \mathcal{O}(10^{-1})$. This is in sharp contrast to the RD Universe where we found $\Omega_\chi h^2 \ll \Omega_\phi h^2$ with the same values of λ and mass scales of the dark sector particles. In the upcoming section, we discuss how the scenario evolves in the case of kination dominated ($n = 2$) early Universe.

5.3.2.2 Kination phase

Earlier, we have seen, faster than kination domination has led to pure freeze-in for the parameters that show reannihilation in the case of an RD Universe by suppressing the interaction rate among dark sector particles. Now, we consider the kination domination case ($n = 2$), which leads to a relatively slower expansion rate of the Universe than $n = 3$ and hence may enhance the interaction rate a bit inside the dark sector. Thus to realise pure freeze-in with kination domination era, a relatively smaller value of Y for a fixed T_r is expected to obey the relic bound compared to the $n = 3$ case. Indeed such prediction emerges to be correct as

[§]Maximum possible value of a thermally averaged cross section can be found by equating the temperature of the corresponding bath with the heavier mass scale approximately associated with the interaction.

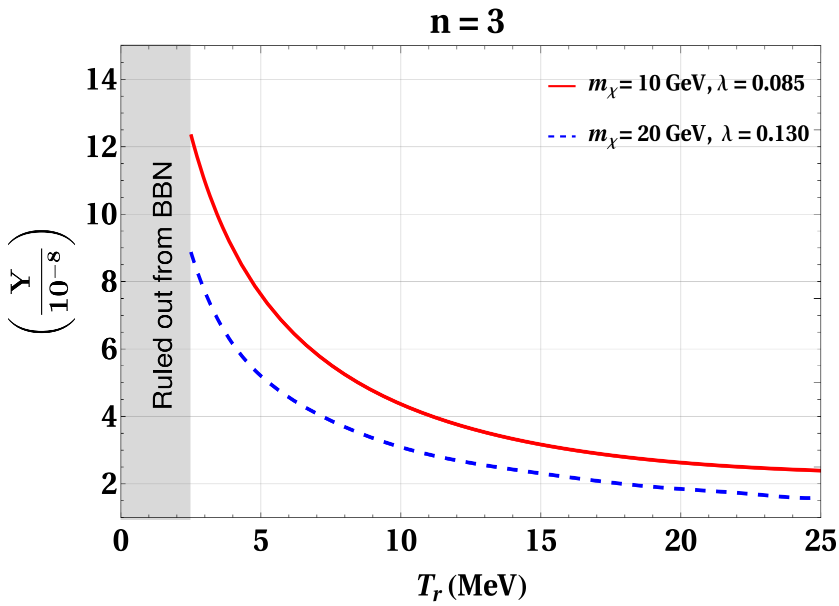

Figure 5.4: Relic satisfied contours in $T_r - Y$ plane considering $n = 3$ for $m_\chi = 10$ GeV and 20 GeV.

evident from Figure 5.5 where we show the estimate of the order of Y for m_χ=10 GeV and 20 GeV as function of T_r considering $n = 2$. Using the approximate method as commented earlier, we have found that for the respective ranges for Y and T_r in Figure 5.5, the ratio r always remains $\lesssim \mathcal{O}(10^{-2})$ and thus relic ϕ is always suppressed with an uncertainity 5% atmost.

One may also wonder whether a reannihilating scenario for the dark matter χ with final correct relic abundance is possible in non-standard cosmological models. To investigate this, let us stick to the $n = 2$ case. This would obviously require a larger T_r compared to the pure freeze-in case with $n = 2$. Assuming internal equilibrium of dark sector is established for some period in the early Universe, the set of Boltzman equations remain same as in Equations 5.15-5.17. We would like to reuse the same three set of benchmark values for $(\lambda, m_\Psi, m_\chi, m_\phi)$ as originally introduced in Section 5.3.1. We would like to emphasise that, these points depict a reannihilation pattern in the radiation dominated Universe, while the presence of a kination or faster than kination dominated epoch transform it to pure freeze-in with almost full χ occupancy in the total relic abundance provided suitable choices for T_r are made. Here, we find out the estimates of (Y, T_r) such that it shows a reannihilation pattern with $\Omega_\chi h^2 \gg \Omega_\phi h^2$. We consider zero initial abundance for the dark sector particles as well as $T_D^{\rm ini} = 0$. In Table 5.3, we note down the required order of T_r and the Yukawa coupling that predicts such scenario considering the same set of $(\lambda, m_\Psi, m_\chi, m_\phi)$ as used in Section 5.3.1.

The evolution patterns of T_D, Y_χ and Y_ϕ for the benchmark point KD-II in

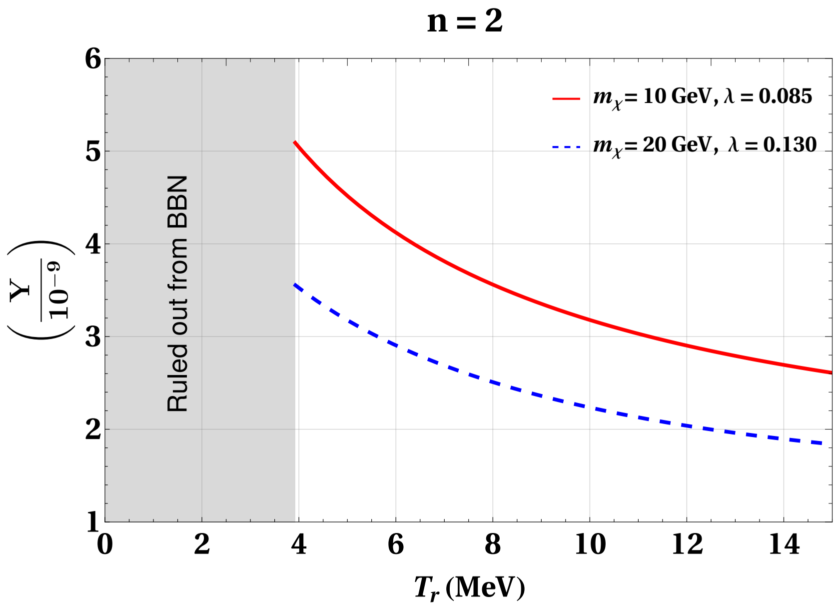

Figure 5.5: Relic satisfied contours in $T_r - Y$ plane for $m_\chi = 10$ GeV and 20 GeV considering $n = 2$.

	λ	m_Ψ	m_χ	m_ϕ	Y	n	T_r	$\Omega_\chi h^2$	$\Omega_\phi h^2$
KD-I	0.145	1.5 TeV	20 GeV	10 MeV	3.5×10^{-9}	2	205 MeV	0.115	0.003
KD-II	0.095	1.5 TeV	10 GeV	10 MeV	4.5×10^{-9}	2	110 MeV	0.117	0.002
KD-III	0.085	1.5 TeV	5 GeV	10 MeV	1.3×10^{-8}	2	20 MeV	0.118	0.002

Table 5.3: The representative benchmark points that lead to reannhilation after freeze-in production of χ in presence of kination dominated epoch with $n = 2$.

Table 5.3 are shown in Figures 5.6-5.7. In the left of Figure 5.6, the ratio r is plotted as a function of the temperature of the SM bath. This figure shows r crosses unity for a brief period and dark sector equilibrates. This feature enables χ to annihilate at a late time to ϕ after production from the standard model bath. However, the annihilation rate is suppressed due to faster expansion of the Universe, which results in reduced relic for ϕ as compared to the one in RD Universe. We also notice such an enhanced expansion rate of the Hubble parameter slows down the χ production process itself, but that can be adjusted by tuning the Yukawa coupling Y appropriately (see Table 5.3). In right of Figure 5.6, the temperature T_D is plotted as a function of SM temperature T. We see a nontrivial pattern for the temperature evolution of the dark sector here. The T_D remains constant up to $z \sim 0.01$ then reduces with z. This has occurred specifically due to an accidental cancellation between the second term of LHS in Equation 5.17 and the term in RHS while solving the Boltzman equation for dark sector energy density. Such cancellation is triggered by the same temperature dependence of

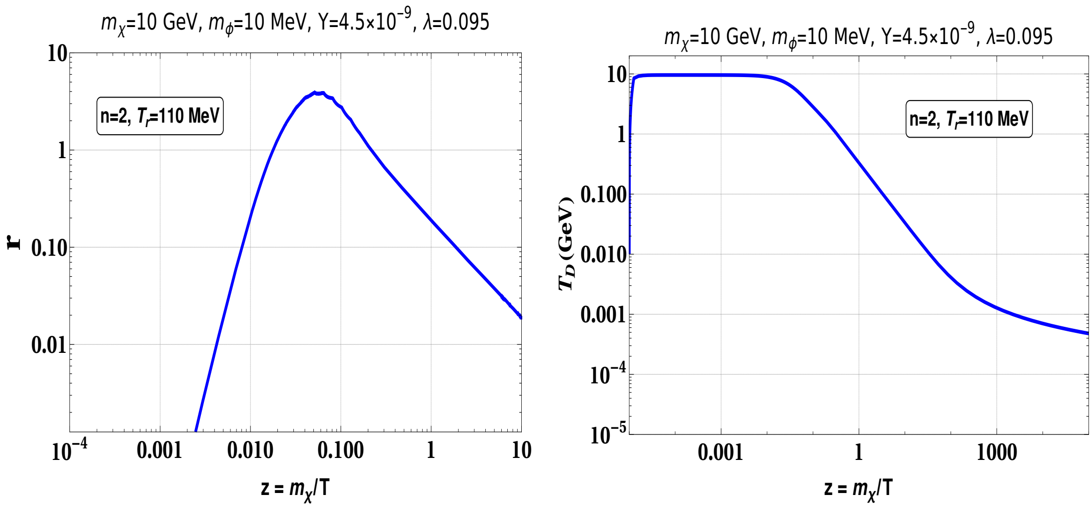

Figure 5.6: Left: The variation of parameter r is shown against the SM temperature for the reference point KD-II. Right: The variation of T_D on SM temperature T is shown for the same reference point.

the Hubble parameter and $n_\Psi^{\rm eq}$ when Ψ is relativistic. In Figure 5.7 the evolution patterns for the number densities of χ and ϕ considering the benchmark point KD-II are shown as function of SM temperature. The obtained patterns are similar as in case of RD Universe. The comoving number density of χ drops from its freeze-in value due to late time dark freeze out. Similar reannihilation patterns for m_χ = 20 GeV and 5 GeV can be obtained as well with the proper assignments of other relevant parameters as pointed out in Table 5.3. For all three the benchmark points of Table 5.3, χ occupies the maximum share of total relic abundance, whereas ϕ can contribute up to 2% of the total relic.

Before we close this section, let us draw a clear comparison between the impacts of standard and non-standard cosmology within the present setup. We begin by fixing the mediator mass m_ϕ = 10 MeV and dark matter mass at 5 GeV, 10 GeV and 20 GeV, respectively. In an RD Universe, a larger value of λ (motivated from generating velocity dependent large self interaction) leads to the annihilation of χ to ϕ after its production by forming dark sector equilibrium. Consequently, we obtain ϕ as a dominant DM component rather than χ. We then anticipate that presence of a non-standard epoch (kination or faster than kination) in the early Universe can assist in realising a dominant share of χ in total DM relic abundance with or without reaching dark sector thermal equilibrium for the same dark sector parameters as used in the RD scenario. We have utilised the same benchmark points as used in the RD case and show that, indeed, a fast-expanding Universe changes the DM dynamics completely and helps in realizing χ as the main dark matter component. This occurs since the presence of a modified cosmology enhance the expansion rate of the Universe and suppresses

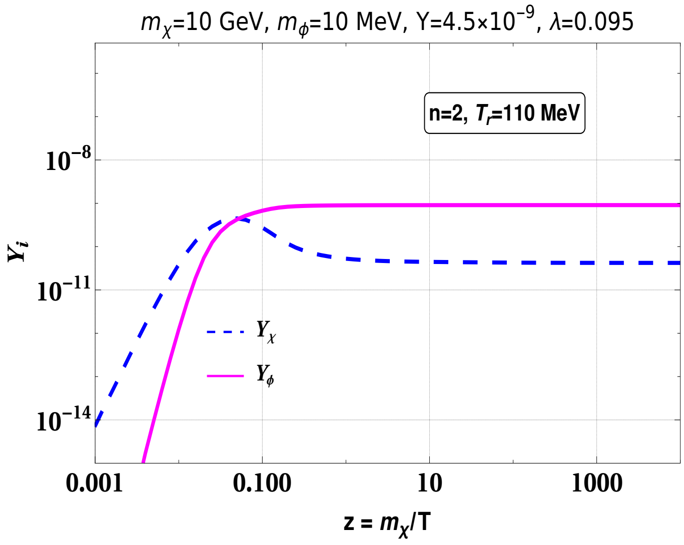

Figure 5.7: The evolution of χ and ϕ number densities are shown with SM temperature for the benchmark point KD-II.

the conversion rate of the $\chi\chi \to \phi\phi$ process. One can also spot that it requires a larger amount of Yukawa coupling Y to obey the relic density bound in a non-standard era compared to the case in RD Universe. This, in turn, improves the collider search prospects of the present set up as we will talk about shortly.

5.4 Discussion on Collider searches

We shall now briefly discuss the detection prospects of the proposed singlet scalar extended singlet doublet freeze-in DM at colliders. The possible collider signatures of the singlet doublet fermion DM model have been discussed in detail in the context of WIMP [?,125] and FIMP [111,196] DM scenarios. The collider sensitivity of the singlet doublet dark matter model is mainly based on the $Y\overline{\Psi}\tilde{H}\chi$ vertex. Note that the same vertex determines the production efficiency of the dark matter in the early Universe. Depending on the cosmological history and dark sector dynamics, we found that the value of Y keeps changing for fixed DM mass and m_Ψ or m_{ξ_2}. For example, a fast expanding Universe prefers larger Y as compared to the RD Universe in each of the pure freeze-in or reannihilation scenarios to obtain a constant dark matter relic. Therefore in the present framework, the colliders can perhaps be utilised to test the cosmological history at the early Universe and the hidden dark sector dynamics in the context of the singlet doublet model.

One of the possible signatures at LHC could be the disappearing charge track signature induced by $\psi^\pm \to \pi^\pm \xi_2$ decay with decay length $c\tau_{\psi^\pm} \sim \mathcal{O}(1)$ cm.

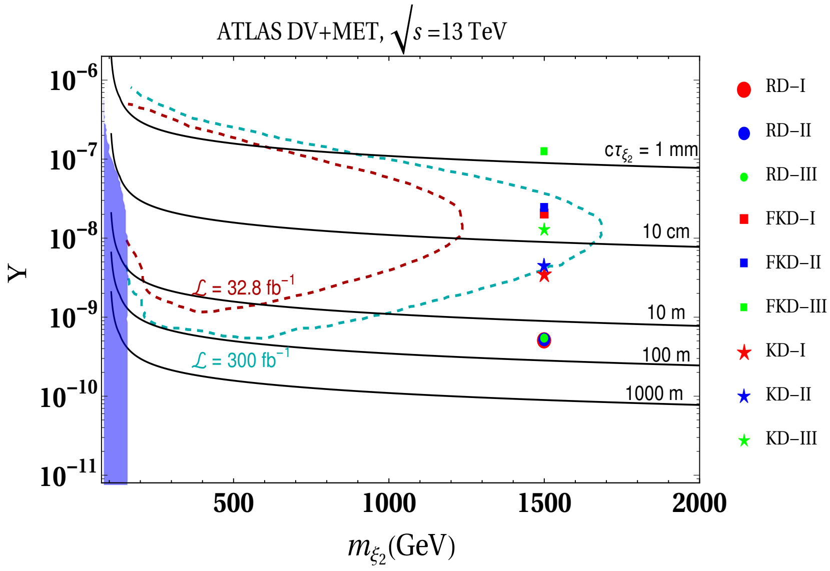

Figure 5.8: Discovery prospects of the chosen benchmark points (both in standard and non standard cosmology) in $Y - m_{\xi_2}$ plane. The blue region is disfavored by the search of disappearing charge track signature. We have also shown the present and proposed LHC exclusion sensitivities by the dashed red and green contours respectively as taken from [111].

Independent analyses by ATLAS and CMS collaborations [204,205] have inferred strong restriction on the chargino mass considering a supersymmetric framework as a benchmark model. Since the decay $\psi^\pm \to \pi^\pm \xi_2$ is equivalent to chargino to Higgsino production, in the present analysis, the bounds provided by ATLAS and CMS can be employed in our analysis as well. In Figure 5.8, the purple shaded region is disfavored due to non-observation of disappearing charge track assuming $\text{Br}(\psi^\pm \to \pi^\pm \xi_2) \simeq 1$. In our analysis, we have considered m_Ψ to be of the TeV scale. Thus the bound arising from the disappearing charge track signature is not important for our case.

On the other hand, due to gauge mediated interactions, the heavy charged ($\psi^\pm$) and neutral (approximately ξ_2) components of dark fermion doublet in this model can be produced at a hadronic collider. The relevant processes are $p\, p \to \psi^+\, \psi^-$, $\xi_2\, \xi_2$ and $\psi^\pm\, \xi_2$ which further decay to DM (χ or ξ_1) along with jets in final states via hh, hZ, ZZ, W^+W^- modes. The presence of feeble interaction between heavy doublet and the DM ($Y\overline{\Psi}\tilde{H}\chi$), which is the one of requirements of freeze-in scenario makes the heavy neutral state ξ_2 longlived ($c\tau_{\xi_2} > 1$ mm) at the typical scale of detector length. The heavy charged state, $\psi^\pm$ promptly decays to a heavier neutral state, ξ_2 with a soft pion which is difficult to probe. The charge fermion, $\psi^\pm$ can also decay directly into DM with W ($\psi^\pm \to W^\pm\chi$), which is suppressed when the singlet doublet mixing is small. In the limit of small singlet doublet mixing, the direct and associate productions of $\xi_2\,\xi_2$ are one of the promising modes for our analysis which can give rise to displaced vertices with jets plus missing energy signature (DV+MET) before reaching the end of the tracker. Similar kind of search has been performed by ATLAS with $\sqrt{s}$ = 13 TeV and $\mathcal{L}$ = 32.8 fb^{-1} in the context of split supersymmetric models (i.e. gluino-neutralino) [206]. Such events are analysed by looking at the individual jet tracks which are originating from a displaced vertex. The ATLAS DV+$\not{E}_T$ search estimates the final events targeting at least one displaced vertex with jets and large missing transverse energy. So the signal processes which can give rise to the DV+$\not{E}_T$ signature at LHC in this framework are given as:

$$\begin{aligned} pp \rightarrow \quad & \left(\psi^+\psi^-\right) \rightarrow \bar{\xi}_2\,\xi_2 + \text{ soft pions} \rightarrow hh/hZ/ZZ + \overline{\chi}\chi \rightarrow \text{jets} + \overline{\chi}\chi; \\ \rightarrow \quad & \left(\psi^\pm\xi_2\right) \rightarrow \bar{\xi}_2\,\xi_2 + \text{ soft pion} \rightarrow hh/hZ/ZZ + \overline{\chi}\chi \rightarrow \text{jets} + \overline{\chi}\chi; \\ \rightarrow \quad & \bar{\xi}_2\,\xi_2 \rightarrow hh/hZ/ZZ + \overline{\chi}\chi \rightarrow \text{jets} + \overline{\chi}\chi. \end{aligned} \tag{5.26}$$

Note that here we have only considered hadronic decay channels of h and Z, since large hadronic branching yields a sizeable cross-section of the $pp \rightarrow$ jets $+\,\overline{\chi}\chi$. The above signal cross-section mainly depends on the long-lived particle mass, $m_{\xi_2}(\simeq m_\Psi)$ and the Yukawa coupling, Y. The heavy neutral state, ξ_2 can decay inside (1 mm $-$ 100 m) or outside the detector that crucially depends on the strength of Y.

An accurate prediction of discovery prospects of our proposed scenario requires proper recasting with the exact limits from CMS and ATLAS. One needs to perform a careful reconstruction and selection of events employing suitable cuts and considering the generator-level efficiency and background estimation. The details of the recasting strategy of this singlet doublet model have been performed in Ref. [111]. In Figure 5.8 we extract the present and proposed exclusion bounds obtained on $m_{\xi_2}-Y$ plane from [111] and check the sensitivities of the benchmark points we used so far, implying different kinds of dark matter dynamics both in standard and non-standard cosmology. The benchmark points FKD-I and FKD-II with n = 3, which signify pure freeze-in in non-standard cosmology, are inside the 300 fb^{-1} exclusion limit and can be traced in the future runs of ATLAS. Two of the three benchmark points (KD-II and KD-III) with n = 2 are also likely to be probed in the next run of ATLAS. If tested, these would probably indicate the presence of modified cosmology with the values of non-standard cosmological parameters as listed in Table 5.2 and Table 5.3. The benchmark points labelled as RD-I, RD-II and RD-III are far outside the reach of ATLAS 300 fb^{-1} run. For these reference points, the decay lengths of ξ_2 turns out to be very large with $c\tau_{\xi_2} \sim \mathcal{O}(1)$ km. Thus it is challenging to search ξ_2 with

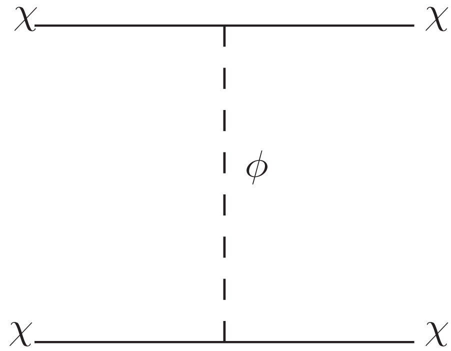

Figure 5.9: Feynman diagram for dark matter self interaction

such long lifetimes at ATLAS and CMS with current and future sensitivities. The proposed MATHUSLA surface detector experiment [207,208] could be capable of probing such a long-lived particle. We do not discuss this in detail and refer the readers to [196].

5.5 Dark matter self-interaction

The present set-up resembles a two-component dark matter framework. We have seen in Sections 5.3.2.1 and 5.3.2.2, that χ could be the main component with almost 100% relic share owing to the presence of modified cosmology. Hence χ, being adequately abundant in the present Universe, can be an ideal candidate for self-interacting dark matter. Figure 5.9 displays the Feynman diagram of DM self interaction. As earlier mentioned, few long-standing tensions between astrophysical observations and N-body simulations for cold DM suggests the DM to be self-interacting with 0.1 cm^2/gm $\lesssim \sigma/m_\chi \lesssim$ 10 cm^2/gm for DM relative velocity ($30 \lesssim v_d \lesssim 200$) km/s [209] and $\sigma/m_\chi \sim 0.1$ cm^2/gm at galaxy cluster scale [209]. In the present framework, the self interaction can take place through ϕ mediation. We assume the χ to be symmetric in nature. The DM self-interaction processes are $\chi\chi \to \chi\chi$, $\overline{\chi\chi} \to \overline{\chi\chi}$ and $\overline{\chi}\chi \to \overline{\chi}\chi$. The nonrelativistic self-scattering in DM halos is conventionally described by a Yukawa potential,

$$V(r) = \pm\frac{\alpha_D^2}{4\pi r}e^{-m_\phi r}, \tag{5.27}$$

where "±" stands for repulsive and attractive potentials. The parameter α_D is the analog of fine structure constant defined by $\alpha_D = \frac{\lambda^2}{4\pi}$. In general, a fermion dark matter can self-interacts via both scalar and vector portal. Note that the scalar interactions are purely attractive, while a vector interaction could be both attractive or repulsive [209]. In literature, uses of two kind of cross sections can be noticed namely (i) transfer cross section (σ_T) and (ii) viscosity cross section (σ_V), which are defined as follows [209–214]:

$$\sigma_T = \int d\Omega(1-\cos\theta)\frac{d\sigma}{d\Omega}\,, \qquad \sigma_V = \int d\Omega \sin^2\theta \frac{d\sigma}{d\Omega}\,, \tag{5.28}$$

where θ is the scattering angle. The viscosity cross section has certain merits over the transfer one. For example, the σ_V takes care of the divergences in both forward and backward scatterings in the DM halo. In addition, for self-interaction between identical particles, transfer cross sector fails. In view of this, we calculate the σ_V in the present set up.

The description of the self-scattering could be of different natures (classical, semi-classical or quantum), parameterized by two dimensionless parameters,

$$\kappa = \frac{m_\chi v_d}{m_\phi} \quad \text{and} \quad \beta = \frac{2\alpha_\chi m_\phi}{m_\chi v_d^2}, \tag{5.29}$$

which are correlated to the momentum and strength of the potential relative to the kinetic energy. The system is known to be in the classical, semi-classical, and quantum regime for $\kappa \gg 1$, $\kappa \gtrsim 1$ and $\kappa \lesssim 1$ respectively. The analytical form of σ_V in classical and semi-classical regimes can be found in Ref. [215].

For the quantum case (excluding the Born approximation for $2\beta\kappa^2 \ll 1$), in principle one needs to solve the Schrodinger equation by partial wave analysis in order to compute the differential cross section. The differential scattering cross section can be computed by,

$$\frac{d\sigma}{d\Omega} = \frac{1}{k^2}\left|(2l+1)e^{i\delta_l}P_l(\cos\theta)\sin\delta_l\right|^2. \tag{5.30}$$

where the phase shift for the partial wave is indicated by δ_l. The Schrodinger equation for the radial wave function $R_l(r)$ of the reduced DM two-particle system is written as,

$$\frac{1}{r^2}\frac{\partial}{\partial r}\left(r^2\frac{dR_l}{dr}\right) + \left(k^2 - \frac{l(l+1)}{r^2} - 2\mu V(r)\right)R_l = 0, \tag{5.31}$$

where $\mu = m_\chi/2$ is the reduced mass and $k = \mu v_d$. Then by obtaining δ_l from the asymptotic form of the radial function $R_l(r)$, one can reach at the approximated expression for the viscosity cross section:

$$\sigma_V m_\phi^2 \simeq \frac{4\pi}{\kappa^2}\int_0^\infty dl \frac{(l+\frac{1}{2})(l+\frac{3}{2})}{2l+2}\ \sin^2 2\delta'\left(l+\frac{1}{2}\right), \tag{5.32}$$

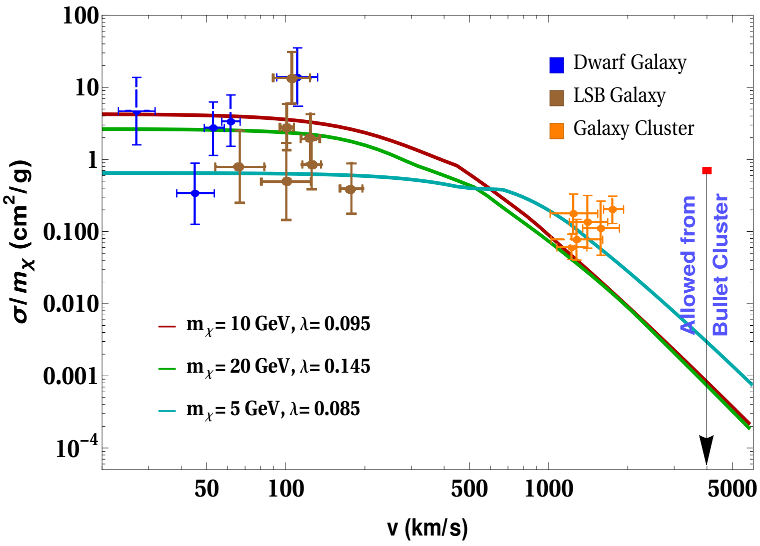

Figure 5.10: Self-interaction cross section as function of velocity for the two different sets of (m_χ, λ) that have been used to describe the dark matter phenomenology in Sections 5.3.2.1 and 5.3.2.2. The black arrow indicates the constraint from the Bullet Cluster which is $\frac{\sigma}{m_\chi} < 0.7\ \mathrm{cm}^2/\mathrm{g}$ for $v = 4000$ km/s [63, 210]. We fix m_ϕ at 10 MeV. We also show the observational data from dwarfs (blue), low surface brightness (LSB) galaxies (brown), and galaxy clusters (orange) as taken from [216].

where $\delta'(l + 1/2) \simeq \delta_{l+1} - \delta_l$. The analytical computation of σ_V looks unlikely in the above case, where both quantum and non-resonant effects are important. However, for $\kappa \ll 1$, the S-wave scattering dominates, and the Hulthen potential can be implemented to find the σ_V analytically as indicated in [215].

In Figure 5.10, we estimate the velocity dependence of the viscosity cross section σ_V considering three sets of (m_χ, λ) as used for the DM analysis earlier in Section 5.3.2.1 and Section 5.3.2.2 with m_ϕ= 10 MeV. Note that for all three benchmark points, we could obtain nearly same percent relic abundance for the dark matter candidate χ in considering non-standard cosmology namely kination domination or faster than kination domination. For all three (m_χ, λ) sets, the parameter $\frac{\sigma_v}{m_\chi}$ remains in the range (0.1-10) cm^2/g at $v_d = (30-200)$ km/s. Notably, these three reference points also yield strong self interaction at galaxy cluster scale as prefered by the observational data. We also found that these points satisfy the bound $\frac{\sigma_v}{m_\chi} < 0.7\ \mathrm{cm}^2/\mathrm{g}$ at $v_d = 4000$ km/s, arising from the observations in Bullet Cluster galaxies [209]. In the case of RD dominated Universe, for the three benchmark points under our discussion, χ is not adequately abundant in the present scenario, and hence the solution of small structure anomalies remains unlikely. However, the assumption of a modified cosmology before BBN turns instrumental in the simultaneous realisation of adequately abundant χ component dark matter and sufficient self-interaction to alleviate the small scale anomalies of the Universe.

5.6 Brief comment on DM direct detection

In our framework, the DM-neucleon scattering processes which are responsible for the direct detection search are mediated via Z-boson and Higgs boson with the corresponding Feynman amplitudes are proportional to $\sin^2\theta$ and $\sin^4\theta$ respectively. Since we require very small order of Y in our scenario, it is expected that the spin independent direct-detection cross-section to be extremely supressed and and lie well below current experimental bounds. For example, with $m_\chi = 10,\ \Delta M = 1.49$ TeV and $Y = 2.6 \times 10^{-8}$ (FKD-II in table 2), the DM-neucleon spin dependent scattering cross-section is $\sigma^{\rm SI} \simeq 10^{-36}$ **pb** as calculated using micrOMEGAs 4.3 [146]. It is far below the current spin independent direct search bound $\sim 10^{-9}$ **pb** from XENON 1T. This observation holds true for the other benchmark points as well having similar or smaller order of Y.

5.7 Summary and Conclusion

The singlet doublet model is a simple particle extension of SM, providing a viable dark matter candidate from mixing of doublet and singlet fermions after the electroweak symmetry breaking. Different variants of this scenario are extensively studied for its enriched dark sector and collider signatures. In this work, we have examined whether a non-thermally produced and adequately abundant GeV scale fermion doublet dark matter candidate has the potential to be probed at colliders. We also discuss the prospect of alleviating the small scale structure anomalies of the Universe.

We have minimally extended the singlet doublet dark matter model with a MeV scale singlet scalar, which mediates the dark matter self-interaction. The singlet scalar is stable in Universe lifetime since it has no decay mode. The fermion dark matter has a non-thermal origin and can be produced adequately in the early phase of the Universe. A strong self-interaction, in general, prefers a sizable non-gravitational interaction strength between the dark matter and the mediator particle. With such a notion, our computation indicates the formation of internal dark thermal equilibrium when the conversion process from the fermion dark matter to scalar mediator turns so efficient that it significantly suppresses relic abundance for our dark matter candidate. In fact, the mediator particle emerges to be way more abundant in the present Universe. The process as mentioned above is prominent in a standard radiation-dominated Universe, and we remain unsuccessful in obtaining the singlet doublet fermion dark matter as the main component.

We adopt two specific non-standard cosmological scenarios such as kination and faster than kination-dominated early Universe to circumvent this issue. The motivation for such choices is to suppress the conversion process inside the dark sector. We have found that proper tunings of non-standard cosmological parameters completely alter the evolution patterns of the number densities for the dark sector particles. In fact, the benchmark points which had earlier manifested a reannihilating pattern in the RD dominated Universe depict a pure freeze-in scenario in the non-standard Universe with negligible mediator abundance in the present Universe. In addition, for some choices of the non-standard cosmological parameters, the dark sector still goes through internal thermal equilibrium. However, that does not cause colossal depletion to the dark matter relic, unlike the case considering radiation domination.

In short, the presence of a modified cosmology helps realise the fermion-dark matter as the main component that is adequately abundant in the present Universe. An exciting consequence comes in terms of collider constraints, where we found that the displaced Vertex signature can provide the robust exclusion bound on the GeV scale DM parameter space. Some of our benchmark points are already within the projected exclusion limit that can be tested by LHC in the next run. We have further demonstrated that the realised parameter space can indeed generate velocity-dependent sufficient self-interactions (consistent with the bounds from observations at bullet cluster galaxies) with a MeV scale mediator.

We conclude with the comment that, in general, a freeze-in dark matter being feebly coupled to the visible sector is extremely hard to track at experiments. Interestingly, the proposed framework of singlet doublet freeze-in GeV scale DM has ample scopes to be indirectly probed *e.g.* in the astrophysical experiments at galaxy scales due to the strong self-interaction of the fermion dark matter as well as in the collider experiments by virtue of modified cosmological theory.

Chapter 6

Freeze-in Dark Matter Through Forbidden Channel in $U(1)_{B-L}$

6.1 Introduction

In this work, we focus on DM production, where it has renormalizable interactions with the thermal bath (IR freeze-in). From here onwards, we will refer to the freeze-in scenario where the DM production dominantly takes place at a temperature near about the mass of the decaying* bath particle as a *standard freeze-in* or SFI. Deviating from this scenario, in the present analysis, we consider the production of DM in a parameter regime where its production remains kinematically forbidden in the SFI framework. Darmé et al. studied such a mechanism recently for DM production in Ref. [217]. The interesting feature of this particular production mechanism is the involvement of thermally corrected masses [217–223] of the particles participating in the DM production. Here, one considers that the mediator is not only a part of the hot thermal plasma, but it may also acquire a sizable thermal mass. In the early Universe, when the temperature was extremely high, the thermal mass of the mediator can have differed substantially from its mass at vacuum, i.e., the thermal effects must have dominated the mediator's mass. Analogous to the SFI, here, the initial population of dark matter is assumed to be zero or negligibly small, and it is produced gradually from the mediator's decay. At a sufficiently high temperature, the mediator can acquire large thermal mass, and the condition: $M_{\text{mediator}}(T) > 2M_{\text{DM}}$ can easily be achieved. The dark matter then can be copiously produced from this decay, even if such a process remains kinematically forbidden at low temperatures. This alternative approach of DM production can be indexed as *forbidden freeze-in* (FFI). This new FFI scenario

*Assuming the production of the DM through the scattering of the bath particles remains sub-dominant in comparison the production via decay.

can open up an exciting and new paradigm of dark matter phenomenology.

This work aims to explore the FFI scenario in a minimal $U(1)_{B-L}$ extension [224–230] of the SM. As is well known, the $B-L$ extension necessitates the introduction of three right-handed neutrinos (RHN) to make the model free from the triangular anomaly. Unlike the Type-I seesaw [13, 16, 17, 231–234], here, the bare mass term for the RHNs are not allowed at tree level. Hence, in order to make the RHNs massive, they are required to couple to an SM gauge singlet (complex) scalar appropriately charged under the $U(1)_{B-L}$ symmetry. These RHNs become massive once the $B-L$ scalar acquires a non-zero vacuum expectation value (vev) and spontaneously breaks the $U(1)_{B-L}$ symmetry. In addition, the $B-L$ gauge boson also becomes massive after the breaking of $B-L$ symmetry. It is interesting to point out that the $B-L$ setup can provide a common solution to three of the most important issues of present-day particle physics and cosmology, *i.e.*, the non-zero neutrino mass [53, 234–238], baryogenesis via leptogenesis [37,46,47,53,180,239,240] from the decay of heavier RHNs and dark matter (WIMP/FIMP). The WIMP type DM in the context of the $B-L$ extension has been thoroughly studied [241–243]. Here, the lightest RHN (non-trivially charged under a Z_2 symmetry) plays the role of a DM [244]. Even though such extension can explain all three outstanding issues under the same umbrella, the DM phenomenology still remains highly constrained. The RHN dark matter relic density can only satisfy the Planck limit [12] near the resonance regimes [241, 242]. An interesting alternative is to consider the lightest RHN as FIMP type DM (SFI). This possibility is also vastly explored in the literature [227–229, 243, 245, 246] and unlike the WIMP scenario, here a sizable mass range is allowed[†] for DM. Contrary to this, in the present setup, we follow the FFI approach to study the freeze-in production of dark matter from the kinematically disallowed decay of the scalar that gets a significant thermal mass correction while maintaining equilibrium with the hot thermal plasma in the early Universe. This chapter is organized as follows. In Section 6.2, we introduce the model part while Section 6.3 describes in detail the thermal mass correction of the mediator. Different theoretical and experimental constraints deemed relevant here are described in Section 6.4. Next, we present the forbidden freeze-in production of dark matter and the estimation of numerical results in Section 6.5 and finally, we summarize our findings in Section 6.6.

[†]We would like to point out that in a recent study [247], the authors have shown that Lyman$-\alpha$ bound can also exclude DM mass $\lesssim \mathcal{O}(15 \text{ keV})$ if produced through a freeze-in mechanism.

Field	$SU(2)_L \times U(1)_Y$	Y_{BL}	$\mathbb{Z}_2$
N_1	(1, 0)	-1	$-$
N_2, N_3	(1, 0)	-1	$+$
S	(1, 0)	2	$+$

Table 6.1: The additional fields and their quantum numbers under different symmetry groups. Here, Y_{BL} refers to the $U(1)_{B-L}$ charge.

6.2 The scenario

The present scenario explores the possibility of a $U(1)_{B-L}$ extension of the SM gauge symmetry. Here, the particle content is extended by adding three right-handed neutrinos N_i $(i = 1, 2, 3)$ together with a complex scalar S, all of them charged under the $U(1)_{B-L}$ symmetry. In addition, the SM leptons and quarks also carry $U(1)_{B-L}$ charges of -1 and $+\frac{1}{3}$, respectively. Further, invoking an additional unbroken discrete Z_2 symmetry and making one of the RHN (say, N_1) non-trivially charged under it ensures its stability by forbidding its interactions with the SM leptons and Higgs. Being stable, N_1 contributes as a suitable DM candidate in the present setup. On the other hand, the remaining BSM particles and SM particles carry a positive charge under this Z_2. In Table 6.1, we present the charges of all the BSM fields under the different symmetry groups.

These $B-L$ charge assignments also eliminate the possibility of triangular $B-L$ gauge anomalies in our model [248]. With the given particle spectrum and the gauge symmetries, the most general renormalizable and gauge invariant Lagrangian for the present setup can be written as,

$$\mathcal{L} = \mathcal{L}_{KE} + \mathcal{L}_y - V(\phi, S) \tag{6.1}$$

where kinetic terms $\mathcal{L}_{KE}$ for the BSM fields are given as,

$$\mathcal{L}_{KE} = |D_\mu S|^2 + \sum_{i=1,2,3} \bar{N}_i i\gamma^\mu D_\mu N_i - \frac{1}{4} Z_{\mu\nu} Z^{\mu\nu}, \tag{6.2}$$

with $Z^{\mu\nu} = \partial^\mu Z^\nu_{BL} - \partial^\nu Z^\mu_{BL}$, and $D_\mu = \partial_\mu + i\,[Y g' + Y_{BL}\, g_{BL}]\,(Z_{BL})_\mu$. Here, we work in the pure $U(1)_{B-L}$ model, where g' is considered to be zero. This choice of $g' = 0$ forbids Z-Z_{BL} mixing at the tree level[‡]. Finally, g_{BL} denotes the $U(1)_{B-L}$ gauge coupling.

Moving on to the scalar part of the Lagrangian, the most general renormalizable scalar potential for this setup is given by

[‡]The gauge kinetic mixing is highly constrained by electroweak precision measurements demands it to be $\lesssim 10^{-4}$ [249].

$$V(\phi,S) = -\mu_\phi^2\phi^\dagger\phi - \mu_S^2|S|^2 + \frac{\lambda_\phi}{2}(\phi^\dagger\phi)^2 + \lambda_{\phi S}(\phi^\dagger\phi)|S|^2 + \lambda_S|S|^4. \tag{6.3}$$

For $\mu_S^2 > 0$, the CP even component of $B-L$ scalar $S = \frac{1}{\sqrt{2}}(v_{BL}+\phi_S)$ develops a non-zero vacuum expectation value v_{BL} and breaks the $U(1)_{B-L}$ symmetry. This breaking ensures Majorana masses for the RHNs (discussed latter) together with an additional massive $B-L$ gauge boson Z_{BL}. The masses of the $B-L$ scalar (ϕ_S) and gauge boson after the $B-L$ symmetry breaking is expressed as §,

$$m_S^2 = 2\,\lambda_S\,v_{BL}^2, \tag{6.4}$$
$$M_{Z_{BL}} = 2\,g_{BL}\,v_{BL}. \tag{6.5}$$

On the other hand, Electroweak Symmetry Breaking (EWSB) is triggered for μ_ϕ^2 when the CP-even components of ϕ receive a vev v. The minimization conditions for the potential in Equation 6.3 are given below:

$$\mu_\phi^2 = \frac{\lambda_\phi}{2}v^2 + \frac{\lambda_{\phi S}}{2}v_{BL}^2, \tag{6.6}$$
$$\mu_S^2 = \frac{\lambda_{\phi S}}{2}v^2 + \lambda_S\,v_{BL}^2. \tag{6.7}$$

After the EWSB, scalar doublet in the present setup can be parametrized as

$$\phi = \begin{pmatrix} 0 \\ \frac{1}{\sqrt{2}}(v+\phi_h) \end{pmatrix}. \tag{6.8}$$

Subsequent to the EWSB, a non-zero $\phi_h - \phi_S$ mixing leads to the following mass terms

$$V \supset \frac{1}{2}\begin{pmatrix}\phi_h & \phi_S\end{pmatrix}\begin{pmatrix}\lambda_\phi\,v^2 & \lambda_{\phi S}\,v\,v_{BL} \\ \lambda_{\phi S}\,v\,v_{BL} & 2\lambda_S\,v_{BL}^2\end{pmatrix}\begin{pmatrix}\phi_h \\ \phi_S\end{pmatrix}. \tag{6.9}$$

The mass matrix is diagonalised using

$$\begin{pmatrix}\phi_h \\ \phi_S\end{pmatrix} = \begin{pmatrix}c_\theta & s_\theta \\ -s_\theta & c_\theta\end{pmatrix}\begin{pmatrix}h \\ s\end{pmatrix} \tag{6.10}$$

§After the breaking of $B-L$ symmetry, ϕ also obtains mass due to the presence of $\lambda_{\phi S}$ interaction. We do not write that mass term explicitly as its presence does not alter the present analysis.

with

$$\tan 2\theta = \frac{-2\,\lambda_{\phi S}\,v\,v_{BL}}{\lambda_\phi\,v^2 - 2\,\lambda_S\,v_{BL}^2}. \tag{6.11}$$

The mass eigenstates (h, s) then have masses

$$m_{h,s}^2 = \frac{1}{2}\Big[\big(\lambda_\phi v^2 + 2\lambda_S v_{BL}^2\big) \pm \sqrt{\big(\lambda_\phi v^2 - 2\lambda_S v_{BL}^2\big)^2 + 4\lambda_{\phi S}^2 v^2 v_{BL}^2}\Big]. \tag{6.12}$$

Here we consider physical scalar h as the SM like Higgs boson with mass $m_h = 125.09$ GeV [250]. The various model parameters are expressible in terms of the physical quantities as follows:

$$\lambda_\phi = \frac{(m_h^2 c_\theta^2 + m_s^2 s_\theta^2)}{v^2}, \tag{6.13}$$

$$\lambda_{\phi S} = \frac{(m_s^2 - m_h^2) s_\theta c_\theta}{v\,v_{BL}}, \tag{6.14}$$

$$\lambda_S = \frac{(m_h^2 s_\theta^2 + m_s^2 c_\theta^2)}{2v_{BL}^2}. \tag{6.15}$$

The $\phi_S - \phi_h$ mixing angle is highly constrained, and the current experiments demand it to be small (see Section 6.4). As this mixing angle does not play any significant role in the present context, we have kept s_θ fixed at 10^{-3} throughout this work, such that it satisfies the experimental constraints. In the limit of sufficiently small $\phi_S - \phi_h$ mixing, one obtains $\phi_S \simeq s$, and $m_S \simeq m_s$.

Next, the Yukawa interactions for the present scenario is expressed as,

$$-\mathcal{L}_y \supset y_{11}\bar{N}_1^c N_1 S + y_{\alpha\beta}\bar{N}_\alpha^c N_\beta S + h_{i\alpha}\overline{l_L}\tilde{\phi} N_\alpha + h.c., \tag{6.16}$$

with $\alpha,\ \beta = 2,\ 3$ and $i = e, \mu, \tau$. As discussed earlier, N_1 being Z_2 odd remains stable, unlike the other two RHNs N_2 and N_3, which can decay into the scalar and the SM leptons (l) through the third term of Equation 6.16 if kinematically allowed. The existence of N_2 and N_3 in the present setup can also explain the origin of non-zero neutrino masses together with baryogenesis via leptogenesis. In addition, EWSB gives rise to the following mass matrix for $N_{1,2,3}$.

$$M_N = \sqrt{2}\,v_{BL}\begin{pmatrix} y_{11} & 0 & 0 \\ 0 & y_{22} & y_{23} \\ 0 & y_{23} & y_{33} \end{pmatrix}. \tag{6.17}$$

To demonstrate our point without losing the generality, we consider $y_{23} = 0$ for simplicity in the rest of the analysis, in which case M_N is diagonal with masses

$$M_i = \sqrt{2}\, y_{ii}\, v_{BL}. \tag{6.18}$$

For simplicity, we assume the other two RHNs to be nearly mass degenerate for the rest of the analysis and consider $y_{22} \simeq y_{33} = y$. Finally, for our analysis purpose, we choose the following sets of independent parameters:

$$\{m_s, M_1, y, v_{BL}, g_{BL}, s_\theta\}.$$

6.3 Thermal corrections

This section briefly comments on the thermal corrections to the masses of relevant particles. These corrections play a non-trivial role in understanding the DM phenomenology of the present setup. In the early Universe, when the temperature of the thermal soup was very high, the thermal corrections [182, 222, 251] to the masses of the particles in the bath must have been very large. In general, any particle that couples in the thermal bath with the primordial plasma is expected to obtain a mass proportional to the temperature of the Universe provided the condition $T > m_i$ is satisfied, here m_i denotes various mass scales involved in the theory [252].

SM particles are expected to be in equilibrium with the thermal plasma at high temperatures. In the present set up we also assume that the particles like the scalar S and the heavier RHNs $N_{2,3}$ remained in equilibrium with the thermal plasma due to their sizable interaction strengths in the early Universe. Hence, their masses are expected to obtain thermal corrections at high temperature. On the other hand, DM candidate N_1 in this model interacts very feebly with the thermal bath and never enters thermal equilibrium. Due to this reason, the thermal correction to its mass remains negligible even at high temperatures. For example, considering $U(1)_{B-L}$ breaking scale $v_{BL} \sim \mathcal{O}(10^{10}$ GeV) with a fixed DM mass $M_1 \sim 500$ GeV, one obtains $y_{11} \sim 3 \times 10^{-8}$ GeV, following Equation 6.18. With such a feeble interaction, the thermal corrections to N_1 mass at a temperature $T >> M_1$ remains negligible *i.e.* $M_1(T) = \sqrt{M_1^2 + (y_{11}^2/16)T^2} \simeq M_1$. Finally, the setup also demands a very feeble $g_{BL} \sim \mathcal{O}(10^{-8})$. Such a small g_{BL} also prevents Z_{BL} from entering into the equlibrium and hence its thermal mass can also be negelected. These choices of couplings will be further clarified in Section 6.5.

Now we discuss the thermal corrections to the mass of s as it plays a crucial role in the DM phenomenology of the present construct. Note that several pro-

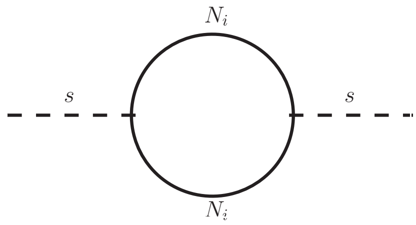

Figure 6.1: One-loop diagram contributing dominantly towards thermally corrected mass of scalar s.

cesses can provide thermal contributions to the mass of s. For example, one can have self-energy corrections with s, H, Z_{BL} and N_i coming in the loop, which can contribute to the thermally corrected mass of s. These contributions can be denoted as $\Pi_s^2(T)$, $\Pi_H^2(T)$, $\Pi_{Z_{Bl}}^2(T)$ and $\Pi_{N_i}^2(T)$ respectively. The present work demands a very large v_{BL} to ensure the feeble interaction of the DM with s. This, in turn, also makes the couplings like λ_S and $\lambda_{\phi S}$ negligibly small (see Equation 6.2, with $v_{BL} \sim \mathcal{O}(10^{10}$ GeV$)$, $\lambda_S \sim 10^{-13}$ and $\lambda_{\phi S} \sim 10^{-10}$). The smallness of these couplings guarantees that Π_s^2, Π_H^2 remains significantly small in comparison to $\Pi_{N_i}^2(T)$ (Note that the $N_i - N_i - S$ coupling (y) can be quite large) and can be ignored. Next, the set up also demands a very small g_{BL} and hence the contributions of $\Pi_{Z_{BL}}^2(T)$ can also be safely ignored. The thermal contribution to the mass of s from the diagram shown in Figure 6.1 is given as [222, 251]:

$$\Pi_{N_i}^2(T) = \frac{y_{ii}^2}{6} T^2. \tag{6.19}$$

Finally, the effective mass of the scalar can be expressed as,

$$M_s(T) = \sqrt{m_s^2 + \Pi_s^2(T) + \Pi_H^2(T) + \Pi_{Z_{BL}}^2(T) + \Pi_{N_i}^2(T)}. \tag{6.20}$$

One can similarly calculate the masses of $N_{2,3}$ in terms of temperature by incorporating all relevant contributions. In Section 6.5, we describe the importance of the thermal corrections in the context of the DM phenomenology.

6.4 Theoretical and experimental constraints

6.4.1 Theoretical constraints

The scalar potential discussed in Equation 6.3 must remain bounded from below in various directions in the field space. Stability of vacuum can be ensured if the quartic couplings satisfy the following conditions:

$$\lambda_\phi > 0,\ \lambda_S > 0,\ \lambda_{\phi S} + \sqrt{2\lambda_\phi \lambda_S} > 0. \tag{6.21}$$

On the other hand, to keep the model parameters perturbative, the parameters must obey:

$$|\lambda_i| < 4\pi,\ |g_i| < \sqrt{4\pi},\ |y_i| < \sqrt{4\pi}, \tag{6.22}$$

Where g_i and y_i denote the gauge, and the Yukawa couplings and λ_i represent the scalar quartic couplings involved in the calculation.

6.4.2 Experimental Constraints

I. **Relic density and direct detection**: Due to the presence of a DM, the model is subjected to the constraints coming from the Planck experiment [12]:

$$\Omega_{\rm DM} h^2 = 0.120 \pm 0.001. \tag{6.23}$$

Additionally, the model is also exposed to the constraints imposed by the direct detection experiments like LUX [167], PandaX-II [253] and Xenon-1T [169]. Elaborated discussions on the dark matter phenomenology are presented in Section 6.5.

II. **LHC diphoton searches**: In presence of the mixing between h and s, the tree level interactions of the SM Higgs with the SM fermion and gauge bosons get modified. In such a scenario, the signal strength in the di-photon channel then takes a form:

$$\mu_{\gamma\gamma} = c_\theta^2 \frac{BR_{h\to\gamma\gamma}}{BR^{\rm SM}_{h\to\gamma\gamma}} \simeq c_\theta^2 \frac{\Gamma_{h\to\gamma\gamma}}{\Gamma^{\rm SM}_{h\to\gamma\gamma}}. \tag{6.24}$$

LHC sets a limit on this new mixing angle as $|\sin\theta| \leq 0.36$ [254].

III. **LEP bound and opposite sign di-lepton search at LHC**: Since the SM fermions are charged under $U(1)_{B-L}$ symmetry and interact directly with the $U(1)_{B-L}$ gauge boson Z_{BL}, the footprints of Z_{BL} can be obtained in the collider searches. The null detection of such signature severely constrains the ratio $M_{Z_{BL}}/g_{BL}$. The exclusion limit from LEP-II [255, 256] on this ratio is:

$$\frac{M_{Z_{BL}}}{g_{BL}} \geq 7 \text{ TeV}. \tag{6.25}$$

On the other hand, one should also observe the constraints coming from opposite-sign di-lepton searches at LHC, which primarily excludes the model for 150 GeV $< M_{Z_{BL}} <$ 3 TeV [241, 257], depending on the size of g_{BL}. In this work, the $B-L$ gauge boson is treated as a FIMP which in turn demands g_{BL} to be very small, and hence the stringent constraints, as discussed above, can easily be evaded.

IV. **Invisible Higgs decay**: In this model, SM Higgs can also decay to the RHNs, Z_{BL} and also to the BSM scalar, if kinematically allowed. These extra decay modes can contribute towards invisible Higgs decay. In such a situation, we need to employ the bound on the invisible Higgs decay width as [105]:

$$Br(h \to \text{Invisible}) < 0.11, \tag{6.26}$$

$$\frac{\Gamma(h \to \text{Invisible})}{\Gamma(h \to SM) + \Gamma(h \to \text{Invisible})} < 0.11. \tag{6.27}$$

where $\Gamma(h \to \text{Invisible}) = \Gamma(\text{h} \to \text{BSM})$ when $m_i < \frac{m_h}{2}$ with $i = N_1, N_2, N_3, Z_{BL}, s$ and $\Gamma(h \to SM) = 4.2$ MeV. However, in our present analysis, we primarily focus on the parameter space where $m_i > \frac{m_h}{2}$. So the above constraint is not applicable.

6.5 Dark Matter Phenomenology

Null detection of WIMP dark matter in the direct [167, 169, 253] and indirect search experiments [258] has motivated the community to explore the various exotic realization of DM. Among such possibilities, the popular one is the FIMP-type DM, where the DM never comes in equilibrium with the thermal soup. Here, the initial abundance of the DM is assumed to be zero (or negligible). As the Universe cools down, its feeble interaction with the bath helps in its gradual production from decays or scatterings of the bath particles. Such a weaker strength of coupling ensures that the DM interaction rate invariably remains smaller than the Hubble expansion rate (H), *i.e.* $\Gamma_{int} < H$. Studies of such a FIMP type DM establish a condition where the maximum DM production takes place when the temperature of the thermal bath is of the order or below the

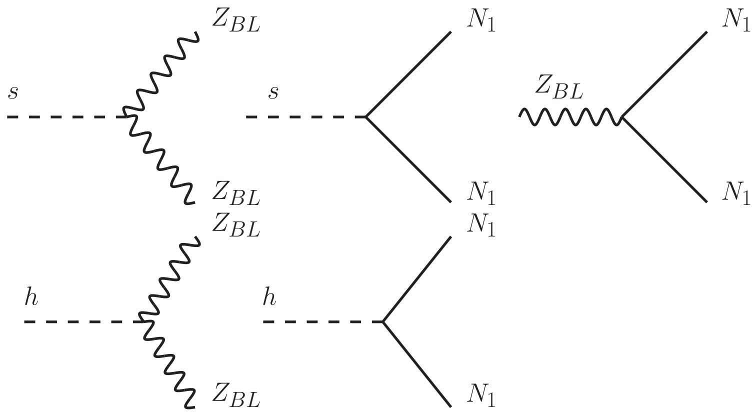

Figure 6.2: Possible production channels of Z_{BL} and the DM candidate N_1.

mass of the mother particle responsible for the production of the DM. Unlike the standard freeze-in scenario, in the present up, DM production can be enhanced at early times if thermal corrections to the mass of the mother particle are included. This mechanism of DM production can be dubbed as the *forbidden freeze-in*. Here, the DM production channel, which was otherwise forbidden or kinematically disallowed in the standard freeze-in (SFI), now becomes allowed once the thermal correction to the mass of the mother particle is incorporated.

The present setup explores the $U(1)_{B-L}$ extension of the SM where the lightest RHN (N_1), which is odd under a Z_2 symmetry, plays the role of FIMP dark matter. Here, the production of N_1 can take place from the decay of s, h (physical scalars obtained after the mixing between ϕ_S and ϕ_h after the EWSB) and Z_{BL}. All such relevant production channels of Z_{BL} and N_1 are depicted in Figure 6.2. The feeble interaction of N_1 is assured by choosing a relatively large v_{BL} ($\Gamma_{s\to N_1 N_1} \propto y_{11}^2 c_\theta^2 \propto M_1^2 c_\theta^2 / v_{BL}^2$) and a relatively smaller g_{BL} ($\Gamma_{Z_{BL}\to N_1 N_1} \propto g_{BL}^2$).

Note that, due to the smallness of g_{BL}, the $B-L$ gauge boson Z_{BL} also never thermalizes with bath and is produced feebly from the decay of s and h. Hence, in order to study the evolution of dark matter with the expansion of the Universe, one needs to solve a set of coupled Boltzmann equations while taking into account the evolution of Z_{BL} as well. The coupled Boltzmann equations are expressed as,

$$\frac{dY_{Z_{BL}}}{dx} = \frac{1}{Hx}\Bigg[\theta(M_s(m_s/x) - 2M_{Z_{BL}})\ \langle\Gamma_{s\to Z_{BL}Z_{BL}}\rangle Y_s^{EQ} - \langle\Gamma_{Z_{BL}\to\ all}\rangle Y_{Z_{BL}}\Bigg], \tag{6.28}$$

$$\frac{dY_{N_1}}{dx} = \frac{1}{Hx}\Bigg[\langle\Gamma_{Z_{BL}\to N_1N_1}\rangle Y_{Z_{BL}} + \theta(M_s(m_s/x) - 2M_1)\ \langle\Gamma_{s\to N_1N_1}\rangle Y_s^{EQ}\Bigg], \tag{6.29}$$

Here $x = m_s/T$, where T and $H = 1.67\sqrt{g_*}\frac{T^2}{M_{Pl}}$ denotes the temperature and expansion rate of the Universe respectively. Whereas $Y_j = n_j/\mathfrak{s}$ denotes the comoving number density of the different species ($j = s, Z_{BL}, N_1$) involved with $\mathfrak{s}$ being the entropy density. Y_s^{EQ} signifies the equlibrium density of s. Next, $\langle\Gamma_i\rangle$ with $i = s, Z_{BL}$ represents the thermally averaged¶ decay widths [228] where

$$\Gamma_{s\longrightarrow Z_{BL}Z_{BL}} = \frac{g_{BL}^2 c_\theta^2}{8\pi}\frac{M_s^3(T)}{M_{Z_{BL}}^2}\left(1 - \frac{4M_{Z_{BL}}^2}{M_s^2(T)}\right)^{1/2}\left(1 - \frac{4M_{Z_{BL}}^2}{M_s^2(T)} + \frac{12M_{Z_{BL}}^4}{M_s^4(T)}\right), \tag{6.30}$$

$$\Gamma_{s\longrightarrow N_1N_1} = \frac{M_s(T)}{32\pi}\ y_{11}^2 c_\theta^2\left(1 - \frac{4M_1^2}{M_s^2(T)}\right)^{3/2}, \tag{6.31}$$

$$\Gamma_{Z_{BL}\longrightarrow N_1N_1} = \frac{M_{Z_{BL}}}{24\pi}\ g_{BL}^2\left(1 - \frac{4M_1^2}{M_{Z_{BL}}^2}\right)^{3/2}, \tag{6.32}$$

$$\Gamma_{Z_{BL}\longrightarrow f\bar{f}} = \frac{M_{Z_{BL}}}{12\pi}\ g_{BL}^2\left(1 + \frac{2M_f^2}{M_{Z_{BL}}^2}\right)\left(1 - \frac{4M_f^2}{M_{Z_{BL}}^2}\right)^{1/2}. \tag{6.33}$$

Note that, due to the large $B - L$ breaking scale, BSM particles gain their masses in the early Universe, and hence the Z_{BL} is mainly produced through the decay of s. At this stage, we would also like to mention that due to the feeble interaction (y_{11}) of the DM with s and large value of both s and N_i masses at high temperature the production of N_1 is dominated by the decay of s, while its production from scattering processes like $N_iN_i \to N_1N_1$ or $hh(ss) \to N_1N_1$ remains subdominant and can be neglected. Finally, we have also ensured that rate of the scattering processes like $N_1N_i \to N_1N_i$ and $N_1h(s) \to N_1h(s)$ remains several orders of magnitude smaller than the Hubble expansion rate. For example we found that $\Gamma_{N_1N_i\to N_1N_i}/H(T) \sim 10^{-20}$ at $T \simeq 10^8$ GeV which shows that the

¶Since Z_{BL} never thermalizes with the plasma, one should properly consider the non-thermal distribution function ($f_{Z_{BL}}$) for Z_{BL} in order to calculate its thermally averaged decay width [228]. In such a scenario $\langle\Gamma_{Z_{BL}}\rangle = \frac{\int(\frac{M_{Z_{BL}}}{E_{Z_{BL}}})\Gamma_{Z_{BL}\to AA} f_{Z_{BL}}(p,T)d^3p}{\int f_{Z_{BL}}(p,T)d^3p}$.

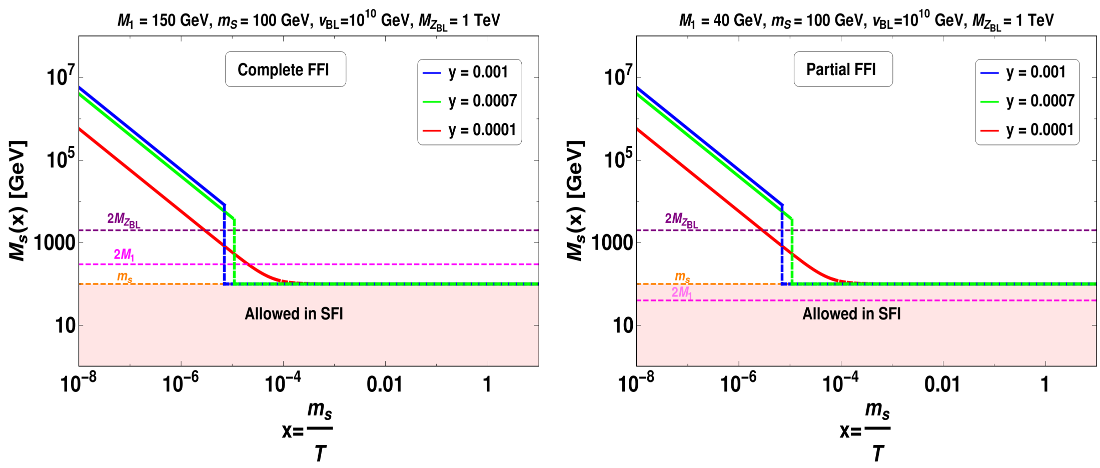

Figure 6.3: Variation of thermally corrected mass $M_s(x)$ of second scalar with a dimensionless quantity $x = \frac{m_s}{T}$ for three different values Yukawa coupling y. In the left panel, we demonstrate a scenario where the $B-L$ gauge boson Z_{BL} and the DM candidate N_1 can only be produced via the FFI mechanism. In contrast, the right panel depicts a picture where the Z_{BL} can only be produced via the FFI mechanism, but N_1 can be produced through both FFI and SFI.

N_1 never enters thermal equilibrium even at high temperatures.

In the present setup, we are interested in exploring the production of both Z_{BL} and N_1 through the forbidden channels. These channels become effective once thermal corrections to the mass of s are incorporated and remain active only till the point these decays are kinematically allowed, this is ensured by the use of $\theta-$function in Equation 6.5. Once the asymptotic yield of the DM $Y_{N_1}(x_\infty)$ is obtained after solving the Boltzmann equation, we can use it to calculate the relic density of the DM as,

$$\Omega_{N_1} h^2 = 2.744 \times 10^8 \left(\frac{M_1}{\text{GeV}}\right) Y_{N_1}(x_\infty), \tag{6.34}$$

where x_∞ indicates the asymptotic value of x after the DM freeze-in.

To understand the DM phenomenology more evidently, we categorize our study into two cases in terms of possible mass hierarchies: (A) $M_{Z_{BL}} > M_1 > m_s$, and (B) $M_{Z_{BL}} > m_s > M_1$ so that the effect of FFI and its benefits over SFI becomes visible. We demonstrate the importance of these two cases in Figure 6.3. Here, we show the variation of thermally corrected scalar mass $M_s(x)$ in terms of dimensionless parameter $x = m_s/T$ for three different choices of Yukawa couplings y. Note that, while generating Figure 6.3 we followed a conservative limit where it is assumed that the thermal correction to the mass of s remains significant till the temperature $T \sim M_{2,3} \sim y v_{BL}$. Below this temperature, the thermally corrected mass of s coincides with the bare mass value [252]. We follow the

Decay-Channels	SFI	FFI
$s \to Z_{BL} Z_{BL}$	X	✓
$s \to N_1 N_1$	X	✓
$Z_{BL} \to N_1 N_1$	X	✓

Table 6.2: List of processes contributing to dark matter and Z_{BL} production in a standard freeze-in (SFI) and forbidden freeze-in (FFI) scenario for a mass hierarchy $M_{Z_{BL}} > M_1 > m_s$. $s \to Z_{BL} Z_{BL}$ remains forbidden within this mass hierarchy for the SFI scenario, which in turn suggests that $Z_{BL} \to N_1 N_1$ is also forbidden even though this decay remains kinematically allowed.

same principle in presenting the rest of our analysis. In Figure 6.3 the dashed horizontal line represents the fixed values of different mass parameters, $2M_{Z_{BL}}$ (in purple), $2M_1$ (in magenta), and m_s (in orange) which helps to understand the mass hierarchy. The pink shaded region shows the parameter space where the FIMP type particles can also be produced if allowed in the SFI scenario. It is evident from the left panel of Figure 6.3 that the production of the FIMP type particles (Z_{BL} and N_1) can only take place through the mechanism of FFI if one considers the mass hierarchy $M_{Z_{BL}} > M_1 > m_s$. On contrary to this, in the right panel of Figure 6.3, we consider a situation where the mass of the dark matter *i.e.* M_1 lies below $M_s(T) = m_s$. Primary condition on scalar mass $M_s(T) = 2M_1$ ensures the production of the dark matter both from the decay of s and Z_{BL} in the forbidden freeze-in scenario and only through s in a standard freeze-in scenario. $s \to Z_{BL} Z_{BL}$ remains forbidden in this case due to the choice of mass hierarchy considered. This case also provides a clear distinction between the FFI and SFI scenarios. Next, we solve the set of coupled Boltzmann equations (Equation 6.5) numerically to study the evolution of Z_{BL} and N_1 with the expansion of the Universe for these two cases.

6.5.1 Case A: Complete FFI region when $M_{Z_{BL}} > M_1 > m_s$

In this mass hierarchy, s being the lightest BSM particle, it neither decays to Z_{BL} nor to N_1 in a typical SFI scenario. Once the thermally corrected mass of s is taken into account, the left panel of Figure 6.3 demonstrates that s can be heavy enough to produce both Z_{BL} and N_1 through the FFI mechanism. We also provide Table 6.2 for a better understanding of this picture.

To facilitate our discussion, in Figure 6.4a, we show the variation of $Y_{Z_{BL}}$ and Y_{N_1} with a dimensionless quantity $x = \frac{m_s}{T}$. The values of different parameters controlling the DM phenomenology are mentioned at the top of each plot. One notices that the production of the Z_{BL} which can occur through the decay of the second scalar s is kinematically forbidden with the given choices of m_s and $M_{Z_{BL}}$

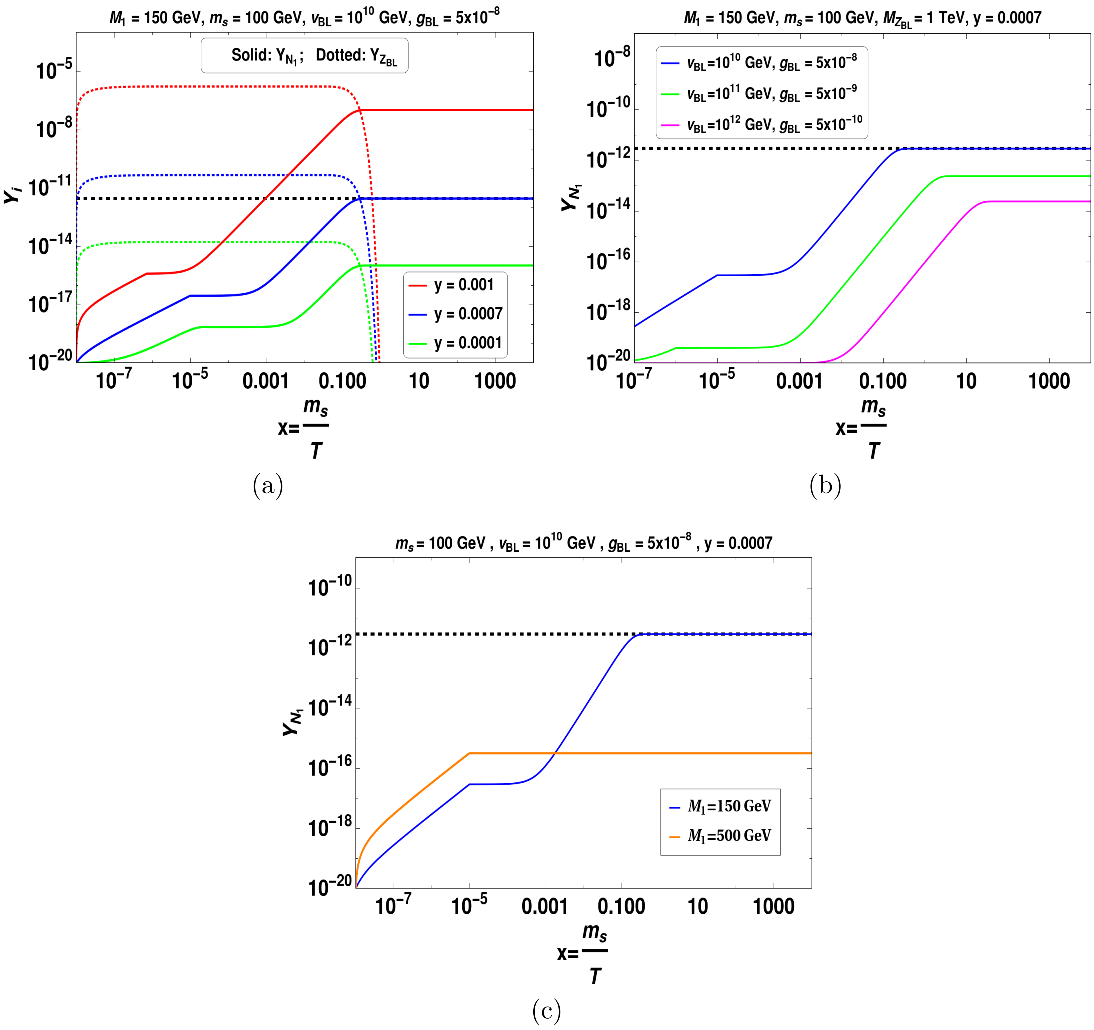

Figure 6.4: Evolution of generated yield of Z_{BL} (dotted lines) and dark matter N_1 (solid lines) with respect to a dimensionless parameter $x = \frac{m_s}{T}$. The values of different parameters controlling the DM phenomenology are mentioned at the top of each plot in a case study for complete FFI region, observed for mass hierarchy $M_{Z_{BL}} > M_1 > m_s$. Thick black dashed line represents the yield of the DM corresponding to the observed relic density.

if the thermal corrections are not incorporated. Looking at the Equation 6.2, one finds that for a large v_{BL} as required in this setup, the couplings λ_ϕ and $\lambda_{\phi S}$ remains significantly small, on the other hand, the setup also demands a very small g_{BL}; hence the contribution of $\Pi_s^2(T), \Pi_H^2(T)$ and $\Pi_{Z_{BL}}^2(T)$ in Equation 6.20 remains almost negligible. On the other hand, the scalar field can acquire a sizeable thermal mass depending on the choices of BSM Yukawa couplings ($y_{22} \propto M_2/v_{BL}$ and $y_{33} \propto M_3/v_{BL}$). This is also consistent with our expectation that the masses of the other two RHNs must be quite heavy to explain the non-zero neutrino masses and leptogenesis through Type-I seesaw. It is expected that, with an adequate choice of the y (with $y_{22} \simeq y_{33} = y$), one can easily obtain a scenario: $M_s(T) > 2M_{Z_{BL}}, 2M_1$ and thereafter, the decay of s can produce Z_{BL} and N_1. This can also be seen in Figure 6.4a. Next, with the choices of parameters considered, the production of N_1 can also proceed via the decay of Z_{BL}. In Figure 6.4a, the evolution of Z_{BL} (dotted) and N_1 (solid) are shown for three different choices of y, *i.e.* $y = 10^{-3}$ (red), $y = 7\times10^{-4}$ (blue), $y = 10^{-4}$ (green). With $y = 10^{-3}$, the thermally corrected mass of s is expected to be large. The larger mass leads to a relatively larger decay widths for the processes $s \to Z_{BL}Z_{BL}$ and $s \to N_1N_1$ (in comparison to smaller y values) which in turn generates relatively larger yields of Z_{BL} and N_1 in Figure 6.4a. One notices that the abundance of Z_{BL} gradually increases due to its production from the decay of s, then saturates (plateau) once its production rate becomes comparable to its decay rate. Finally, it falls as its decay to the SM fermions, and the DM overtakes its production. However, the abundance of N_1 increases slowly till the time (first bend) when the temperature of the Universe becomes of the order of the heavier RHN masses *i.e.* $T \simeq M_i$ (*i.e.* $x \simeq 7 \times 10^{-6}$ for $y = 0.001$), after which its production from the decay of s becomes kinematically forbidden, and its yield saturates. This is because, at this point, the dominant contribution to the thermally corrected mass of s becomes insignificant (as also discussed in Section 6.3), and $M_s(T)$ falls back to the bare mass value m_s. Subsequently, a relatively sharper rise is observed in its yield due to its production from Z_{BL}, and finally, its abundance saturates (at around $T \simeq M_{Z_{BL}}$ *i.e.* $x \simeq 10^{-1}$) once the decay of Z_{BL} is completed. It is interesting to point out that the production of Z_{BL} from the decay of s starts much earlier in comparison to the production of N_1. This happen because the s decays dominantly to Z_{BL} and sub-dominantly to N_1 (see Equation 6.5). Similar behavior is observed in the evolution of Z_{BL} for smaller y, but with a relatively smaller yield. With a small y, the thermal correction to the mass of s also remains small. This, in turn, reduces the decay width of s. Unlike the scenario with a relatively larger y, now N_1 production ceases when the decay $s \to N_1N_1$ becomes kinematically disallowed at a relatively later time (as a smaller y corresponds to a smaller value of $M_{2,3}$, hence a larger x). It again starts getting produced as the $Z_{BL} \to N_1N_1$ becomes operational. Finally, DM abundance freezes in once the decay of Z_{BL} is complete. The thick dashed horizontal black line (in each plot) indicates the abundance of dark matter for which the relic density satisfies the Planck experimental limit.

Next, in Figure 6.4b we show the evolution of the dark matter for three different combinations of v_{BL} and g_{BL} while keeping $M_{Z_{BL}}$ fixed at 1 TeV. Here, one finds that for a choice of smaller v_{BL} (and a larger g_{BL}), both the FFI production channels get enhanced, leading to an overabundant N_1 (as $\Gamma(s \to N_1N_1) \propto \frac{1}{v_{BL}^2}$ and $\Gamma(Z_{BL} \to N_1N_1) \propto g_{BL}^2$). Hence, one can accommodate the

Decay-Channels	SFI	FFI
$s \to Z_{BL} Z_{BL}$	X	✓
$s \to N_1 N_1$	✓	✓
$Z_{BL} \to N_1 N_1$	X	✓

Table 6.3: List of processes contributing to dark matter production in a standard freeze-in (SFI) and forbidden freeze-in (FFI) scenario for a mass hierarchy $M_{Z_{BL}} > m_s > M_1$. $s \to Z_{BL} Z_{BL}$ remains forbidden within this mass hierarchy for the SFI scenario, which in turn suggests that $Z_{BL} \to N_1 N_1$ is also forbidden even though this decay remains kinematically allowed.

correct yield of the DM by tuning these two parameters appropriately, as seen from the blue curve. Lastly, Figure 6.4c shows the effect of different DM masses on its evolution. For a choice with $M_1 = 500$ GeV, the only source of its production is the decay of s. The moment this decay stops, the DM yield becomes constant. In such a case, it is difficult for the DM to satisfy the measured relic at the Planck experiment.

6.5.2 Case B: Partial FFI region when $M_{Z_{BL}} > m_s > M_1$

We now aim to study the DM phenomenology with the above mass hierarchy where FFI decay modes are open partially, as also shown in the right panel of Figure 6.3. Hence evolution process of the DM indicates a distinct direction in the FFI scenario compared to SFI. Unlike the previous case, DM can now be produced directly from the decay of s, even if $M_s(T) \simeq m_s$ is satisfied. However, the production of the Z_{BL} can only be possible through the forbidden freeze-in mechanism from the decay of s[‖]. For a better understanding, in Table 6.3 we provide all the relevant decay channels required for the production of Z_{BL} and N_1 for FFI and SFI. Next, we demonstrate the importance of forbidden freeze-in (FFI) over the standard freeze-in (SSI) in Figure 6.5.

This figure shows a comparison between the production of the DM in the SFI scenario (dashed blue line) and the FFI scenario (solid blue line). Here, with the given choice of parameters, the Z_{BL} can never be produced from the decay of s in the SFI scenario. Hence its abundance remains almost negligible (as it can also be produced through scatterings). With such an insignificant yield, Z_{BL} contribution in producing the DM will always remain sub-dominant in comparison to the DM production coming from the s decay. Hence, the DM yield saturates as soon as its production from the s decay stops. In this situation, it may become difficult for the DM to satisfy the correct order of relic density. On the other hand, with

[‖] Although the production of Z_{BL} can proceed through $2 \to 2$ scatterings, its abundance remains almost negligible as the production cross-section depends on g_{BL}^4.

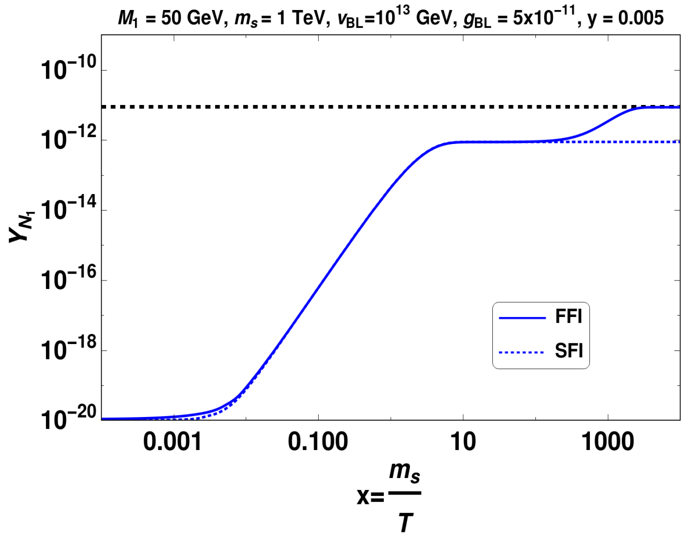

Figure 6.5: Evolution of generated yield of N_1 with respect to a dimensionless parameter $x = \frac{m_s}{T}$. The solid blue line depicts the production of N_1 in an FFI scenario which can satisfy the Planck experimental limit on the relic density for the given choice of parameters. With the same choice of parameters, the DM remains under-abundant for an SFI scenario, as shown by the dashed blue line. The values of different parameters controlling the DM phenomenology are mentioned at the top of each plot in a case study for partial FFI region, observed for mass hierarchy $M_{Z_{BL}} > m_s > M_1$. The thick black dashed line represents the abundance of the DM corresponding to the observed relic density.

the incorporation of FFI, DM can be further produced from the decay of both s and Z_{BL} in an adequate amount to satisfy the correct relic density with the given choice of parameters.

Finally, we also like to comment on the detection prospect of the model under consideration. The spontaneous breaking of the $U(1)_{B-L}$ symmetry at a high energy scale leads to the formation of Nambu-Goto *cosmic strings* [259]. Once formed, the collisions and self-interactions of strings produce non-self-interacting string loops, which further oscillates and radiates their energy in the form of gravitational wave (GW). The incoherent superposition of such continuous emission results in stochastic GW signals. This GW signal can be detected at the present and future GW detectors like pulsar timing arrays (PTAs), NANOGrav [260], PPTA [261], EPTA [262], IPTA [263], LISA [264], LIGO [265] etc. The searches of GWs can increase the predictability of the present setup. The detailed study of GWs is beyond the scope of the present work, and we plan to take it as a future endeavor.

6.6 Summary and conclusions

In this work, we study the phenomenology of feebly interacting massive particles as dark matter in a minimal $U(1)_{B-L}$ extension of the SM. The role of DM is played by the lightest of the three right-handed neutrinos, which in turn are introduced to make the model free from the triangular anomaly. The other two heavier RHNs can generate non-zero neutrino masses and matter-antimatter asymmetry of the Universe through Type-I seesaw. Here, an unbroken Z_2 symmetry ensures the stability of the DM. The setup also requires a complex $SU(2)_L$ singlet scalar charged under the $B-L$ symmetry. After obtaining a non-zero vev, the scalar breaks the $U(1)_{B-L}$ spontaneously and simultaneously makes the RHNs together with a $B-L$ gauge boson massive.

Due to their feeble interactions with the bath particles, both the DM candidate (N_1) and $B-L$ gauge boson (Z_{BL}) never comes in equilibrium with the thermal bath. Contrary to this, the complex scalar mediator remains in the thermal equilibrium with the bath due to its not-so-small interactions with the bath particles and contributes to the gradual freeze-in production of N_1 and Z_{BL}. Moreover, if kinematically allowed, the DM production is further dominated by the Z_{BL} decay.

Although FIMP-type DM is studied in the $B-L$ framework, the thermal corrections to the mediator masses were never taken into account. Incorporating such corrections to the mediator mass at high temperature opens up a new paradigm for a FIMP-type DM phenomenology. Simultaneously, it also opens up an attractive possibility of producing the DM in a kinematically forbidden region of the standard freeze-in (SFI) picture. In this work, we explore this exciting possibility. With this in mind, we categorized our study into two cases depending on the mass hierarchy of these particles. All other likely mass hierarchies can be summed up within these two possibilities.

The first illustration depicts a forbidden freeze-in (FFI) picture where gauge boson and dark matter are heavier than the complex scalar residing in the thermal bath. Hence, the decay is kinematically disallowed, and consequently, such a picture is utterly missing in the SFI framework. The appealing feature here is that the production of the DM can take place in two steps: first from the decay of the scalar due to the thermal corrections to its mass and then subsequently from the late time decay of the gauge boson. Our example explores the synergy between these two processes depending upon parameters in the model.

For further clarity, in our second case study, we choose a particular mass hierarchy ($M_{Z_{BL}} > m_s > M_1$) to mark the role of FFI over SFI scenarios. Here the production of Z_{BL} is kinematically forbidden in the SFI case, while the dark matter is produced only from $B-L$ scalar's decay. Unlike the standard scenario, with the help of a large thermally corrected mass in FFI, the scalar can produce the gauge boson together with the dark matter in the early Universe. Similar to the first scenario, the DM production again happens in two steps which makes the distinction of FFI with SFI noticeable. Finally, due to the involvement of a large $B-L$ breaking scale, the model can be tested indirectly in the GW search experiments. Such a scale leads to the formation of cosmic string, which further oscillates and radiates its energy in the form of gravitational waves.

Chapter 7

Thermally corrected masses and freeze-in dark matter: A case study with $U(1)_{L_\mu - L_\tau}$

7.1 Introduction

In this chapter, we further elucidate the idea of the thermally corrected masses of the various species and their effect on the freeze-in production of the DM in the minimal $U(1)_{L_\mu-L_\tau}$ [266] framework. Unlike the standard $U(1)_{B-L}$ model [55, 243, 267] which offers a stable DM in the form of right-handed neutrino (RHN), the $U(1)_{L_\mu-L_\tau}$ scenario requires an additional scalar (singlet under the SM gauge symmetry) with a non-trivial $U(1)_{L_\mu-L_\tau}$ charge to explain the presence of the DM in the universe. Assuming the DM interacts feebly with the bath particles, it can be produced from the decay of (i) the scalar responsible for the breaking of $U(1)_{L_\mu-L_\tau}$ symmetry, (ii) SM Higgs and, (iii) the massive gauge boson of $U(1)_{L_\mu-L_\tau}$ symmetry in the SFI scenario * if kinematically allowed as was also discussed in [266]. We demonstrate in this work that the DM being a scalar, can also obtain a thermally corrected mass at a high temperature due to its self-interaction. Such a possibility was not explored in [55, 217]. In this work, we aim to explore the deviation that can be observed from the SFI scenario once the thermal masses of the bath particle together with the DM are taken into account. Besides explaining the dark matter, an $U(1)_{L_\mu-L_\tau}$ framework can simultaneously explain the discrepancy in the anomalous magnetic moment of muon $(g-2)$ from its SM prediction [268] and non-zero neutrino masses [268]. Keeping this in mind, we show that the present setup can accommodate a DM that can be produced via

*The production of DM from the scatterings can safely be ignored, as it remains suppressed in comparison to the decay.

both SFI and FFI channels while also providing the solution for the discrepancy in the anomalous magnetic moment of muon $(g-2)$ results.

The chapter is organized as follows. The model is introduced in section 7.2, and the various constraints deemed relevant are detailed in section 7.3. We compute the relevant thermal masses in section 7.4. And the same section also elaborates on the ensuing freeze-in phenomenology. Finally, the study is concluded in section 7.5.

7.2 The model

We extend the SM gauge symmetry by an $U(1)_{L_\mu - L_\tau}$ symmetry where L_μ and L_τ represent the muon and tau lepton numbers respectively. The fermionic content of the model includes the SM leptons and quarks together with three additional right-handed neutrinos $(N_R^e, N_R^\mu, N_R^\tau)$. As suggested by the symmetry of the present scenario, the muon and tau carry a non-trivial charge under the $U(1)_{L_\mu - L_\tau}$. The newly introduced RHNs are singlet under the SM gauge symmetry, while two of them carry 1 and -1 unit of $U(1)_{L_\mu - L_\tau}$ the third remains uncharged. The scalar sector of the setup is enhanced with a complex scalar (S) which is a singlet under the SM gauge symmetry but carries 1 unit of $U(1)_{L_\mu - L_\tau}$ charge. We also introduce an additional scalar (ϕ), a SM gauge singlet that plays the role of the DM. The stability of the DM is guaranteed by its non-trivial charge assignment under $U(1)_{L_\mu - L_\tau}$ symmetry. The fermion and scalar content of the model inclusive of the SM ones and their respective charges are shown in Table 7.1 and Table 7.2.

Gauge Group	Baryon Fields			Lepton Fields			Scalar Fields		
	$Q_L^i = (u_L^i, d_L^i)^T$	u_R^i	d_R^i	$L_L^i = (\nu_L^i, e_L^i)^T$	e_R^i	N_R^i	H	S	ϕ
$\mathrm{SU(2)_L}$	2	1	1	2	1	1	2	1	1
$\mathrm{U(1)_Y}$	1/6	2/3	$-1/3$	$-1/2$	-1	0	1/2	0	0

Table 7.1: Particle contents and their charge assignments under SM gauge group.

Gauge Group	Baryon Fields	Lepton Fields			Scalar Fields		
	(Q_L^i, u_R^i, d_R^i)	(L_L^e, e_R, N_R^e)	$(L_L^\mu, \mu_R, N_R^\mu)$	$(L_L^\tau, \tau_R, N_R^\tau)$	H	S	ϕ
$U(1)_{L_\mu - L_\tau}$	0	0	1	-1	0	1	$n_{\mu\tau}$

Table 7.2: Particle contents and their charge assignments under $U(1)_{L_\mu - L_\tau}$.

With an idea of particle content and their charges under the different symmetry groups we now proceed to write their interactions. To begin with, we first write the kinetic terms for the additional fields,

$$\mathcal{L}^{\mathcal{KE}} = \frac{i}{2} \sum_{\alpha=e,\mu,\tau} N_\alpha \gamma^\delta D_\delta N_\alpha + (D^\delta S)^\dagger (D_\delta S) + (D^\delta \phi)^\dagger (D_\delta \phi) \tag{7.1}$$

where $D_\delta = \partial_\delta + i g_{\mu\tau} Q_{\mu\tau} (Z_{\mu\tau})_\delta$ with $Q_{\mu\tau}$ representing the charge and $Z_{\mu\tau}$ being the gauge boson of $U(1)_{L_\mu - L_\tau}$ symmetry. Next, we write the Lagrangian involving the Yukawa interactions and masses of the additional fermions involved,

$$\begin{aligned}\mathcal{L} =& - \frac{1}{2} h_{e\mu} (\bar{N}_e^c N_\mu + \bar{N}_\mu^c N_e) S^\dagger - \frac{1}{2} h_{e\tau} (\bar{N}_e^c N_\tau + \bar{N}_\tau^c N_e) S - \sum_{\alpha=e,\mu,\tau} y_\alpha \bar{L}_\alpha \tilde{H} N_\alpha \\ & - \frac{1}{2} M_{ee} \bar{N}_e^c N_e - \frac{1}{2} M_{\mu\tau} (\bar{N}_\mu^c N_\tau + \bar{N}_\tau^c N_\mu) S + h.c. \end{aligned} \tag{7.2}$$

Finally, we write the most general scalar potential involving all the scalars in the present setup,

$$\begin{aligned} V(H,S,\phi) =& - \mu_H^2 H^\dagger H - \mu_S^2 S^\dagger S + \mu_\phi^2 \phi^\dagger \phi + \lambda_H (H^\dagger H)^2 + \lambda_S (S^\dagger S)^2 + \lambda_\phi (\phi^\dagger \phi)^2 \\ & + \lambda_{HS} (H^\dagger H)(S^\dagger S) + \lambda_{H\phi} (H^\dagger H)(\phi^\dagger \phi) + \lambda_{S\phi} (S^\dagger S)(\phi^\dagger \phi). \end{aligned} \tag{7.3}$$

The scalar S breaks the $U(1)_{L_\mu - L_\tau}$ symmetry once its CP even component develops a non-zero vacuum expectation value (vev) $v_{\mu\tau}$. As a consequence of this breaking, the gauge boson belonging to the $U(1)_{L_\mu - L_\tau}$ symmetry obtains a non-zero mass, $m_{Z_{\mu\tau}} = g_{\mu\tau} v_{\mu\tau}$.The same breaking also results in an additional non-zero mixing that develops in between the the RHNs as can be seen from Equation 7.2. After the Electroweak Symmetry Breaking (EWSB), the Higgs doublet (H) also develops a non-zero vev $v = 246$ GeV. The scalars after the breaking of the gauge symmetry can be parameterized as,

$$H = \begin{pmatrix} 0 \\ \frac{1}{\sqrt{2}}(v+h) \end{pmatrix}, \quad S = \frac{1}{\sqrt{2}}(v_{\mu\tau} + s). \tag{7.4}$$

Subsequent to the EWSB, a non-zero $h-s$ mixing leads to the following mass terms,

$$V \supset \frac{1}{2} \begin{pmatrix} h & s \end{pmatrix} \begin{pmatrix} \lambda_H v^2 & \lambda_{HS} v v_{\mu\tau} \\ \lambda_{HS} v v_{\mu\tau} & 2\lambda_S v_{\mu\tau}^2 \end{pmatrix} \begin{pmatrix} h \\ s \end{pmatrix}. \tag{7.5}$$

The mass matrix is diagonalised using

$$\begin{pmatrix} h \\ s \end{pmatrix} = \begin{pmatrix} c_\theta & s_\theta \\ -s_\theta & c_\theta \end{pmatrix} \begin{pmatrix} h_1 \\ h_2 \end{pmatrix} \tag{7.6}$$

with

$$\tan 2\theta = \frac{-2\,\lambda_{HS}\, v\, v_{\mu\tau}}{\lambda_H\, v^2 - 2\,\lambda_S\, v_{\mu\tau}^2}. \tag{7.7}$$

The mass eigenstates (h_1, h_2) then have masses

$$m_{h_1,h_2}^2 = \frac{1}{2}\Big[\big(l_H v^2 + 2 l_S v_{\mu\tau}^2\big) \pm \sqrt{\big(l_H v^2 - 2 l_S v_{\mu\tau}^2\big)^2 + 4 l_{\phi S}^2 v^2 v_{\mu\tau}^2}\Big]. \tag{7.8a}$$

The various model parameters are expressible in terms of the physical quantities as follows:

$$\lambda_H = \frac{m_{h_1}^2 c_\theta^2 + m_{h_2}^2 s_\theta^2}{v^2}, \tag{7.9a}$$

$$\lambda_S = \frac{m_{h_1}^2 s_\theta^2 + m_{h_2}^2 c_\theta^2}{v^2}, \tag{7.9b}$$

$$\lambda_{HS} = \frac{2(m_{h_1}^2 - m_{h_2}^2) s_\theta c_\theta}{v v_{\mu\tau}}. \tag{7.9c}$$

Finally, after both the symmetries are broken, the dark matter mass can be expressed as,

$$m_\phi^2 = \mu_\phi^2 + \frac{1}{2}\lambda_{H\phi} v^2 + \frac{1}{2}\lambda_{S\phi} v_{\mu\tau}^2. \tag{7.10}$$

It is convenient to describe a framework in terms of vevs, physical masses and mixing angles. We demand $m_{h_1} = 125$ GeV and tag $\{g_{\mu\tau}, v_{\mu\tau}, m_{h_2}, m_\phi, s_\theta, l_{H\phi}, l_{S\phi}\}$ as the free parameters of the scalar sector.

7.3 Constraints and additional issues

We discuss in this section the various constraints on this model, as well as, the predictions of neutrino mass and the muon anomalous magnetic moment in this model.

7.3.1 Neutrino scattering experiments

Gauging the $U(1)_{L_\mu - L_\tau}$ symmetry leads to severe constraints from neutrino trident production, that is, $\nu_\mu(\bar{\nu}_\mu) + N \to \nu_\mu(\bar{\nu}_\mu) + \mu^+\mu^- + N$. Here N denotes a heavy nucleus. Given the good agreement of the observed results with the SM for this process reported by CHARM-II [269] and CCFR [270, 271], the parameter space in the presence of a new neutral gauge boson gets seriously restricted. A relatively new probe is the coherent elastic neutrino-nucleus scattering (CEνNS) process that at the amplitude-level looks like $\nu N \to \nu N$. CEνNS has recently been measured by the COHERENT collaboration [272–274]. The $Z_{\mu\tau}$ in the gauged $U(1)_{L_\mu - L_\tau}$ model enters CEνNS through the $Z - Z_{\mu\tau}$ kinetic mixing and thereby gets constrained. In fact, the BOREXINO [275, 276] process studies the same scattering process as COHERENT, however using solar neutrinos. The impact of all the constraints is conveniently depicted in the $m_{Z_{\mu\tau}} - g_{\mu\tau}$ plane in Figure 7.1.

7.3.2 LHC constraints

$Z \to 4\mu$ searches by ATLAS [277] and CMS [278] constrains the gauge sector of the model and rules out a portion of the $m_{Z_{\mu\tau}} - g_{\mu\tau}$ plane as shown in Figure 7.1. On another side, an $h - s$ mixing as defined by Equation 7.6 implies that the tree-level couplings of h_1 with the SM fermions and gauge bosons scale by a factor of c_θ *w.r.t.* the corresponding SM ones. This subjects the mixing angle θ from Higgs signal strength constraints and other exclusion limits from the LHC [105, 279]. We adopt $|s_\theta| < 0.1$ in this work to comply with all such constraints. Finally, the reported upper limit on the invisible branching ratio of the 125 GeV Higgs puts a limit on BR$(h \to \phi\phi^\dagger)$ whenever kinematically allowed. However, this constraint is almost trivially satisfied in this setup given a *feeble* $h - \phi - \phi^\dagger$ interaction strength dictated by the freeze-in dynamics.

7.3.3 Dark matter constraints

We demand that the freeze-in relic density predicted by this model must entirely account for the observed relic of the universe. The Planck experiment [12] has reported

$$\Omega_{\rm DM} h^2 = 0.120 \pm 0.001. \tag{7.11}$$

In addition, any dark matter model must abide by the limits imposed by the direct detection experiments such as LUX [167], PANDA [253], XENON1T [169]. It is however much easier to evade such constraints in a freeze-in framework such as the present scenario. In this case, the tiny couplings of the DM ϕ to h_1 and h_2 accordingly predict DM-nucleon scattering (mediated by h_1, h_2 in this model) rates that are well below the stated bounds.

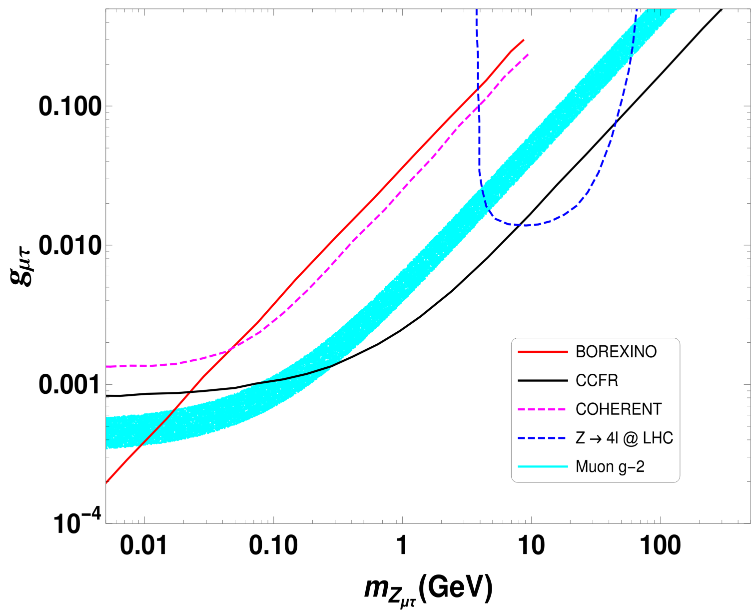

Figure 7.1: The impact of the various experimental constraints on the present model. The region to the left of the red, magenta, and black curves are respectively ruled out by BOREXINO, COHERENT, and CCFR. And the region bound by the blue curve is ruled out by the $Z \to 4l$ searches at the LHC. The cyan band is the region compatible with the 2σ limit of muon $g-2$ as quoted in Eq. 7.13.

7.3.4 Muon $g-2$

The dominant contribution to Δa_μ in this model comes from the 1-loop amplitude mediated by the $Z_{\mu\tau}$ gauge-boson. This contribution can be expressed as [280,281]

$$\Delta a_\mu^{Z_{\mu\tau}} = \frac{g_{\mu\tau}^2}{4\pi^2}\int_0^1 dx \frac{x(1-x)^2}{(1-x)^2+rx}, \tag{7.12}$$

where $r = (m_{Z_{\mu\tau}}/m_\mu)^2$. Following the announcement of the FNAL [282] results on muon $g-2$, a combined measurement of the discrepancy is

$$a_\mu^{\rm exp} - a_\mu^{\rm SM} = (2.51 \pm 0.59) \times 10^{-9}. \tag{7.13}$$

An inspection of Figure 7.1 reveals that apart from the stretch around $m_{Z_{\mu\tau}} \in$ [10 MeV,300 MeV], the parameter space compatible with the observed Δa_μ is almost entirely ruled out by the neutrino scattering experiments.

7.3.5 Neutrino mass

Generation of neutrino mass in the gauged $U(1)_{L_\mu - L_\tau}$ model occurs through Type-I seesaw [13,231–233,283] and has been discussed in detail in [268,284,285]. The light neutrino mass matrix has the familiar Type-I form

$$M_\nu = -M_D M_R^{-1} M_D^T. \tag{7.14}$$

Here, M_D and M_R refer to the Dirac and Majorana mass matrices. Following the spontaneous breaking of the gauge symmetry of the model, one derives

$$M_R = \begin{pmatrix} M_{ee} & \frac{1}{\sqrt{2}} h_{e\mu} v_{\mu\tau} & \frac{1}{\sqrt{2}} h_{e\tau} v_{\mu\tau} \\ \frac{1}{\sqrt{2}} h_{e\mu} v_{\mu\tau} & 0 & M_{\mu\tau} \\ \frac{1}{\sqrt{2}} h_{e\tau} v_{\mu\tau} & M_{\mu\tau} & 0 \end{pmatrix}, \tag{7.15a}$$

$$M_D = \frac{1}{\sqrt{2}} v \times \mathrm{diag}(y_e, y_\mu, y_\tau). \tag{7.15b}$$

We refer the reader to [268, 284, 285] for details of fitting the neutrino data. A similar approach is adopted for this study.

7.4 Freeze-in production and the impact of thermal corrections

This section outlines the impact of $T \neq 0$ on the masses of particles in this model. The formalism we follow is elaborately discussed in the review [286]. Henceforth, the thermal correction to the mass of a particle P will be denoted by $\delta m_P^2(T)$ and its thermally corrected mass by $M_P(T)$. One then notes $M_P(T) = \sqrt{m_P^2 + \delta m_P^2(T)}$ where m_P is the mass for $T = 0$. We first discuss the correction to the $Z_{\mu\tau}$ mass. The contribution coming from a complex scalar carrying a charge q_S (see left panel of Figure 7.2) is given by

$$\delta M_{Z_{\mu\tau}}^2(T)\big|_S = \frac{1}{3} q_S^2 g_{\mu\tau}^2 T^2. \tag{7.16}$$

We add here that only the longitudinal component of a gauge boson receives thermal corrections. Similarly, the contribution coming from a chiral fermion (see right panel of Figure 7.2), say f_L carrying q_f charge reads

$$\delta M_{Z_{\mu\tau}}^2(T)\big|_{f_L} = \frac{1}{6} (q_f)^2 g_{\mu\tau}^2 T^2. \tag{7.17}$$

Thus, summing up the contributions coming from all relevant fields in the model, one obtains

$$\delta M_{Z_{\mu\tau}}^2(T) = \left(\frac{5}{3} + n_{\mu\tau}^2\right) g_{\mu\tau}^2 T^2. \tag{7.18}$$

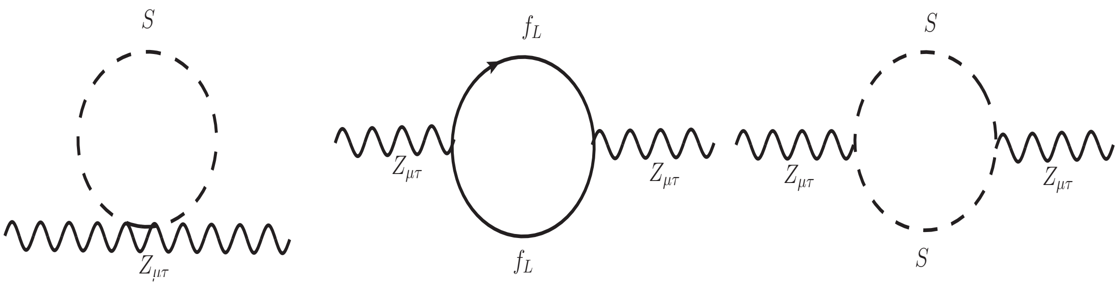

Figure 7.2: The one loop diagrams contributing to the mass of gauge boson $Z_{\mu\tau}$.

As detailed in the previous sections, the DM ϕ has *feeble* interactions with the scalars as well as with the gauge field $Z_{\mu\tau}$. The smallness of such interaction strengths implies that the interaction rate of DM remains smaller than the Hubble expansion rate throughout the thermal course of the Universe. Consequently, the DM ϕ is never in equilibrium with the thermal bath and is injected into the thermal plasma via annihilations and decays of other particles. This is the *freeze-in* mechanism in a nutshell. Of these, the dominant contribution comes from the decay since the annihilations typically undergo suppressions by propagators and additional couplings. The impact of the annihilations is hence neglected in this study hereafter. Also, since the DM ϕ does not enter the thermal bath at any point in its cosmological history, it is *cold*. Therefore, thermal corrections to the DM mass itself become negligible in this setup.

We remind here that some previous studies [266] have looked at the freeze-in dynamics for the $U(1)_{L_\mu-L_\tau}$ model in detail. As mentioned earlier, we shall refer to the standard picture that has emerged from such studies as "standard freeze-in" or SFI. Our goal in this study is to demonstrate the deviation from SFI when thermal corrections to the masses of both the decaying particle and the DM are taken. We assume that all the decaying particles (see Figure 7.3), i.e., the two scalars and $Z_{\mu\tau}$, are throughout in thermal equilibrium.

The Boltzmann equation predicting the DM yield is then given by

$$\frac{dY_\phi}{dx} = \frac{1}{Hx}\left[< \Gamma_{Z_{\mu\tau}\to\phi\phi^\dagger} > (x) Y^{\rm eq}_{Z_{\mu\tau}} + \sum_{i=1,2} < \Gamma_{S_i\to\phi\phi^\dagger} > (x) Y^{\rm eq}_{S_i}\right]. \tag{7.19}$$

Here $x = \frac{m_\phi}{T}$ with T and $H = 1.67\sqrt{g_*}\frac{T^2}{M_{\rm Pl}}$ denoting the temperature and the expansion rate of the Universe respectively. In addition, $Y_\phi = \frac{n_\phi}{s}$ refers to the co-moving number density of the DM with s being the entropy density. $Y_i^{\rm eq}$ signifies the equilibrium densities with $i = Z_{\mu\tau}, S_1, S_2$. Here, in theory, S_1, S_2 generically denote the two neutral scalars. It is pointed out that $\{S_1, S_2\}$ respectively coincide with $\{h, S\}$ and $\{h_1, h_2\}$ before and after the spontaneous breakdown of the gauge symmetry. The thermal decay width for $A \to B\ C$ reads

$$\langle \Gamma_{A\to B\ C}\rangle(x) = \frac{K_1(x)}{K_2(x)}\,\Gamma_{A\to B\ C}, \tag{7.20}$$

where $K_n(x)$ is the nth order modified Bessel function. The late-time DM yield $Y_\phi(x_\infty)$ is calculated by solving the Boltzmann equation. The DM relic density is then obtained using

$$\Omega_\phi h^2 = 2.744 \times 10^8\ m_\phi Y_\phi(x_\infty). \tag{7.21}$$

It is reminded that the parameters controlling the interaction strengths of ϕ

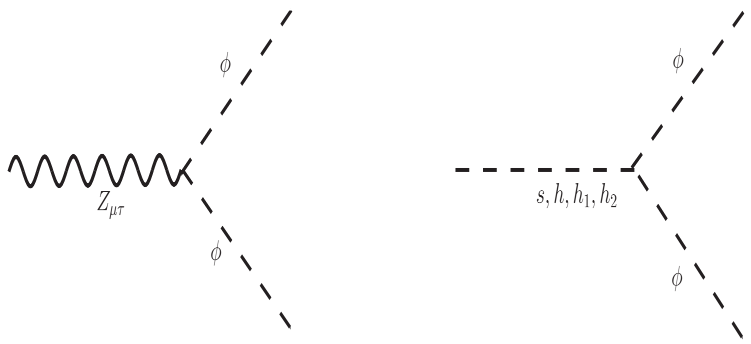

Figure 7.3: Decays responsible for the dark matter production.

and ultimately $Y_\phi(x_\infty)$ are $\lambda_{H\phi}, \lambda_{S\phi}, g_{\mu\tau}$ and $n_{\mu\tau}$. For a clearer understanding of the interplay of the different thermal masses involved, we divide the subsequent analysis into Scenario A: $\lambda_{H\phi}, \lambda_{S\phi} << n_{\mu\tau} g_{\mu\tau}$ and Scenario B: $\lambda_{H\phi}, \lambda_{S\phi} \sim n_{\mu\tau} g_{\mu\tau}$. We further take $g_{\mu\tau} = 5 \times 10^{-4}$ and $v_{\mu\tau} = 80$ GeV for this case which corresponds to the tree level mass $M_{Z_{\mu\tau}} = 0.04$ GeV following the spontaneous breaking of $U(1)_{L_\mu - L_\tau}$. Moreover, this choice predicts $\Delta a_\mu = 1.45 \times 10^{-9}$ and thus is consistent with the latest 2σ experimental limit of Equation 7.13. Explicit verifications establish that the lifetime corresponding to the $Z_{\mu\tau} \to \nu_\mu \bar{\nu}_\mu, \nu_\tau \bar{\nu}_\tau$ decays is smaller than the age of the Universe by several orders of magnitude for the said choice of $g_{\mu\tau}$. Thus $Z_{\mu\tau}$ is not cosmologically stable and thus does not contribute to the relic density. Finally, we would also like to emphasize that the interaction strength of $Z_{\mu\tau}$ with the SM fermions is large enough to keep it in equilibrium in the early Universe.

7.4.1 $\lambda_{H\phi}, \lambda_{S\phi} << n_{\mu\tau} g_{\mu\tau}$

This limit entails that $\Gamma_{S_i \to \phi\phi^\dagger} << \Gamma_{Z_{\mu\tau} \to \phi\phi^\dagger}$ and hence DM is dominantly produced by the $Z_{\mu\tau}$ decay. In order to study the impact of thermal corrections on DM production, we propose m_ϕ = 1 GeV, 30 MeV, and 25 MeV as benchmark values. The rationale behind choosing such values will become clear in the ensuing discussion.

The thermally corrected mass of $Z_{\mu\tau}$ for $T > v_{\mu\tau}$ reads $M_{Z_{\mu\tau}}(T) \simeq \sqrt{\frac{5}{3}} g_{\mu\tau} T$ since $n_{\mu\tau} \ll 1$ for freeze-in. It is once again reminded that while the mass of $Z_{\mu\tau}$ entirely comes from thermal corrections for $T > v_{\mu\tau}$, the DM ϕ does get a bare mass equalling μ_ϕ from the scalar potential in the said temperature range. Figure 7.4 shows the variation of $M_{Z_{\mu\tau}}(x)$ for the chosen values of m_ϕ. At a very high temperature, say $T_{\rm initial} = 10^5$ GeV ($x_{\rm initial} = 10^{-5}$ for $m_\phi = 1$ GeV), one finds $M_{Z_{\mu\tau}}(T_{\rm initial}) = 64.55$ GeV. However, this mass gap diminishes with decreasing T (increasing x) and a crossover is observed at $T = T_1^{\rm cr}$ ($x = x_1^{\rm cr}$) obtainable through $M_{Z_{\mu\tau}}(T_1^{\rm cr}) = 2m_\phi$, beyond which $M_{Z_{\mu\tau}}(T) < 2m_\phi$. We hereafter refer to this as the *first crossover*. Using the expressions for $M_{Z_{\mu\tau}}(T)$ given above, one derives $T_1^{\rm cr} = \sqrt{\frac{12}{5}} \frac{m_\phi}{g_{\mu\tau}}$. This crossover is seen to happen for m_ϕ = 1 GeV and 30 MeV. Table 7.3 displays the corresponding $T_1^{\rm cr}$ values. As an example, m_ϕ = 1 GeV predicts $T_1^{\rm cr} \simeq 3.098 \times 10^3$ GeV. On the other hand, decreasing m_ϕ accordingly postpones the crossover. For instance, as m_ϕ is lowered from 1 GeV to 30 MeV, $T_1^{\rm cr}$ proportionately decreases from $\simeq 3.098 \times 10^3$ GeV to 92.95 GeV.

We next come to discuss the role of $v_{\mu\tau}$ in this scenario. An inspection of Table 7.3 reveals that $T_1^{\rm cr} > v_{\mu\tau} = 80$ GeV for m_ϕ = 1 GeV and 30 MeV. The spontaneous breaking of $U(1)_{L_\mu-L_\tau}$ takes place at $T = v_{\mu\tau}$ thereby generating a squared mass equalling $g_{\mu\tau}^2 v_{\mu\tau}^2$ for $Z_{\mu\tau}$. The thermally corrected mass for the same therefore shows a kink at $T = v_{\mu\tau}$, as can be seen in Figure 7.4. And this kink opens up the possibility of having $M_{Z_{\mu\tau}}(T = v_{\mu\tau}) > 2m_\phi$ for a second time during the thermal evolution of this scenario. We compute the $Z_{\mu\tau}$ thermal mass at this symmetry-breaking threshold in Table 7.3 and discover that this indeed happens in case of m_ϕ = 30 MeV. Moreover, at some $T_2^{\rm cr} < v_{\mu\tau}$, one again might encounter $M_{Z_{\mu\tau}}(T_2^{\rm cr}) = 2m_\phi$ for a second time. This is referred to here as the *second crossover* with the corresponding temperature being $T_2^{\rm cr} = \sqrt{\frac{12m_\phi^2 - 3g_{\mu\tau}^2 v_{\mu\tau}^2}{5g_{\mu\tau}^2}}$. We mention here again that all crossover possibilities and the corresponding temperatures and x-values are summarised in Table 7.3 for each m_ϕ.

We can take a stock at this point. Each m_ϕ value entails a qualitative behavior distinct from the others. For m_ϕ = 1 GeV, the first crossover is seen following which one has $M_{Z_{\mu\tau}}(T) < 2m_\phi$ at all later times. Even the kink at $T = v_{\mu\tau}$ does not flip the hierarchy between $M_{Z_{\mu\tau}}(T)$ and m_ϕ immediately preceding $T = v_{\mu\tau}$. Hence, a second crossover is ruled out for this DM mass. On the other hand, following the first crossover in case of m_ϕ = 30 MeV, the kink at the symmetry

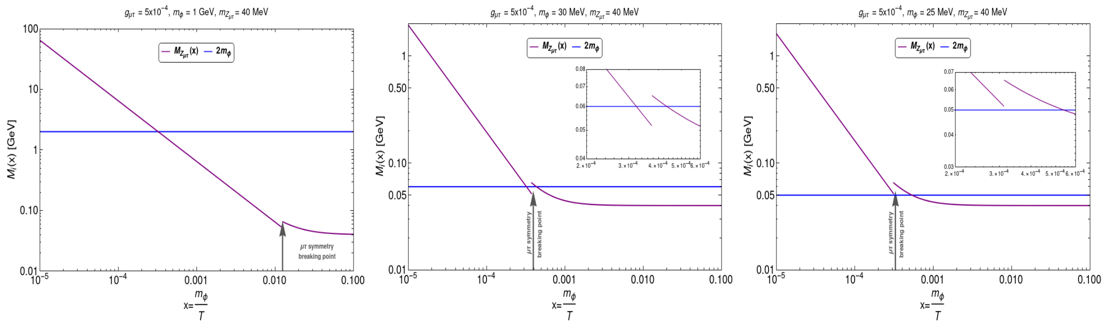

Figure 7.4: Variation of thermal masses of the extra gauge boson($Z_{\mu\tau}$) (green) with the dimensionless variable $x = \frac{m_\phi}{T}$ for three different values of DM masses. The horizontal blue line corresponds to dark matter mass m_ϕ.

m_ϕ	First crossover	$T_1^{\rm cr}$ ($x_1^{\rm cr}$)	$m_X(T = v_{\mu\tau})$	Second crossover	$T_2^{\rm cr}$ ($x_2^{\rm cr}$)
1 GeV	Yes	3098.39 GeV (3.22×10^{-4})	0.065 GeV	No	-
30 MeV	Yes	92.95 GeV (3.22×10^{-4})	0.065 GeV	Yes	69.28 GeV (4.33×10^{-4})
25 MeV	No	-	0.065 GeV	Yes	46.48 GeV (5.37×10^{-4})

Table 7.3: The crossover possibilities and the corresponding temperatures.

breaking temperature again leads to $M_{Z_{\mu\tau}}(T) > 2m_\phi$. And the second crossover also takes place shortly after that. Lastly, for $m_\phi = 25$ MeV, $M_{Z_{\mu\tau}}(T) > 2m_\phi$ is maintained all the way from $T >> v_{\mu\tau}$ to $T = T_2^{\rm cr}$ following which the mass hierarchy flips.

We would like to comment on the representativeness of the chosen benchmarks. Any horizontal line corresponding to a given $2m_\phi$ value that cuts the $M_{Z_{\mu\tau}}(x)$ curve just once for $x < \frac{m_\phi}{v_{\mu\tau}}$ shares the same qualitative features as BP1. Similarly, the $2m_\phi$ line that cuts the $M_{Z_{\mu\tau}}(x)$ curve thrice, i.e., at $x < \frac{m_\phi}{v_{\mu\tau}}$, $x = \frac{m_\phi}{v_{\mu\tau}}$ and $x > \frac{m_\phi}{v_{\mu\tau}}$ would be qualitatively similar to BP2. Finally, the $2m_\phi$ line that cuts the $M_{Z_{\mu\tau}}(x)$ curve once for $x > \frac{m_\phi}{v_{\mu\tau}}$ is the same as BP3 qualitatively.

Next, we plot the DM comoving number densities $Y_\phi(x)$ as a function of x in Figures 7.5,7.6 and 7.7. One key takeaway from this study is that thermal corrections to the mass of the decaying particle can open up new temperature thresholds not encountered in SFI. And the preceding discussion enables an intuitive understanding of the DM yield as a function of temperature. First, we point out that in the absence of thermal corrections, $Z_{\mu\tau}$ is either massless (for $T > v_{\mu\tau}$) or at best has a 40 MeV mass ($T < v_{\mu\tau}$). That is, $m_{Z_{\mu\tau}} \leq 2m_\phi$ in either case for all the m_ϕ values chosen. Therefore, the decay $Z_{\mu\tau} \to \phi\phi^\dagger$ remains kinematically closed, and no DM production must take place in the SFI picture. However, as detailed before, this decay mode kinematically opens up upon incorporating the thermal corrections, and DM production gets triggered and continues up to $x = x_1^{\rm cr}$ for the DM masses permitting the first crossover. The decay threshold closes at $x = x_1^{cr}$, and DM production abruptly stops causing the DM yield to saturate at $Y_\phi(x_1^{\rm cr})$ immediately after. For $m_\phi = 1$ GeV, the $Z_{\mu\tau} \to \phi\phi^\dagger$ threshold does not reopen at any later point. And this explains the horizontal line to the right of $x_1^{\rm cr}$ in Figure 7.5.

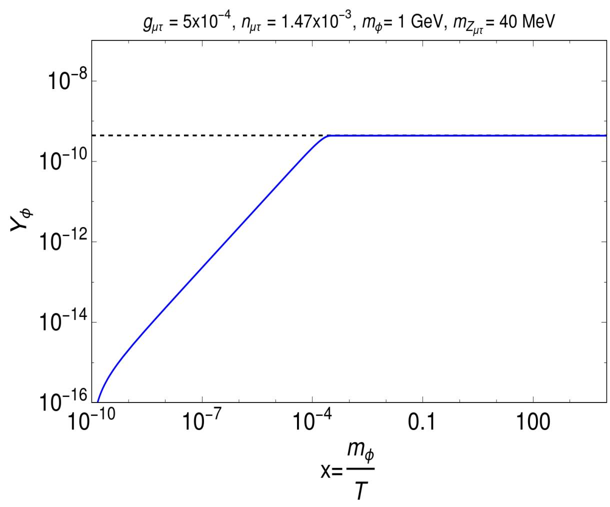

Figure 7.5: Evolution of the DM comoving number density as a function of $x = \frac{m_\phi}{T}$ for $m_\phi = 1$ GeV when DM production from scalar decay is negligible.

For $m_\phi = 30$ MeV, DM production stops at the first crossover point, thereby causing the plateau immediately to the right of $x_1^{\rm cr} = 3.22 \times 10^{-4}$. For this BP, the $Z_{\mu\tau} \to \phi\phi^\dagger$ threshold reopens shortly after at the symmetry breaking point, and freeze-in production kicks in again. This reopening is what shows up as the kink in Figure 7.6 around $x = 3.75 \times 10^{-4}$. However, this second phase of DM production is rather short-lived and terminates permanently at the second crossover point. Hence a second horizontal region $x_2^{\rm cr} = 4.33 \times 10^{-4}$ onwards in Figure 7.6.

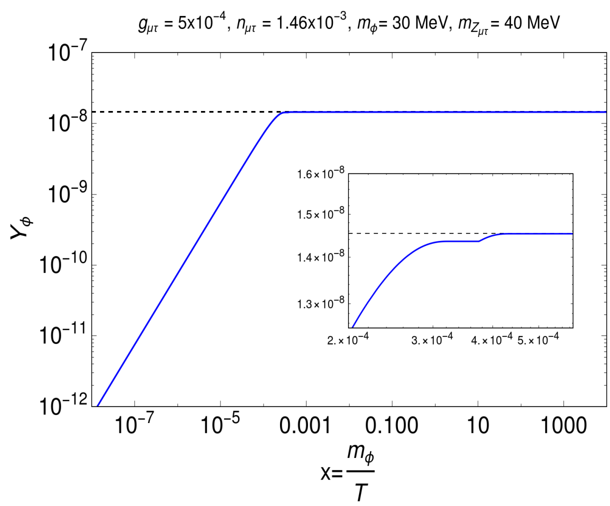

Figure 7.6: Evolution of the DM comoving number density as a function of $x = \frac{m_\phi}{T}$ for $m_\phi = 30$ MeV when DM production from scalar decay is negligible.

Lastly, we discuss the freeze-in production for $m_\phi = 25$ MeV. In this case, DM production is unimpeded up to the second crossover point. Therefore, one expectedly finds a plateau starting at $x_2^{\rm cr} = 5.37 \times 10^{-4}$ in Figure 7.7. The symmetry breaking only leads to the minor cusp around the corresponding x-value, i.e., $x = 3.12 \times 10^{-4}$.

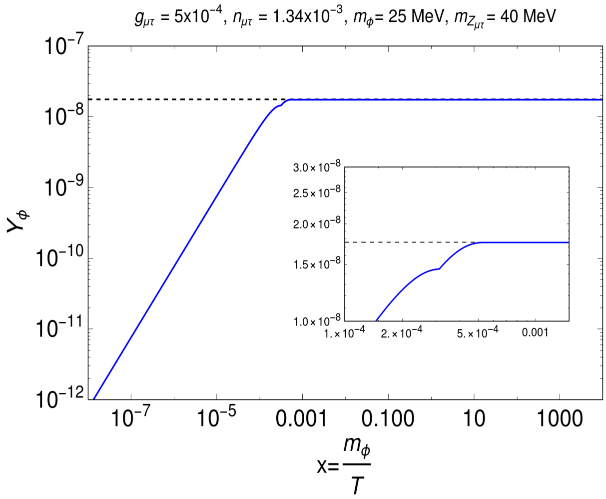

Figure 7.7: Evolution of the DM comoving number density as a function of $x = \frac{m_\phi}{T}$ for $m_\phi = 25$ MeV when DM production from scalar decay is negligible.

For the DM ϕ being generated through the decay of $Z_{\mu\tau}$ only, $Y_\phi(x_\infty)$ and therefore $\Omega_\phi h^2 \propto n_{\mu\tau}^2$. Having displayed the various temperature thresholds in the Figures 7.5, 7.6 and 7.7, it is all about tuning $n_{\mu\tau}$ such that $Y_\phi(x_\infty)$ is in the requisite $\sim 10^{-11}$ ballpark. For example, we find the appropriate $n_{\mu\tau} = 1.47 \times 10^{-3}$, 1.46×10^{-3} and 1.34×10^{-3} for $m_\phi = 1$ GeV, 30 MeV and 25 MeV respectively.

7.4.2 $\lambda_{H\phi}, \lambda_{S\phi} \sim n_{\mu\tau} g_{\mu\tau}$

In this section, we study the impact of the $h_1, h_2 \to \phi\phi^\dagger$ decays on freeze-in production for the chosen m_ϕ values. It, therefore, becomes pertinent here to examine the thermal corrections to the masses of the decaying scalars. A crucial difference between $Z_{\mu\tau} \to \phi\phi^\dagger$ and $h_1, h_2 \to \phi\phi^\dagger$ in this model is that while the former can lead to DM production at very early epochs (or at a very high T) through thermal corrections, the latter is triggered primarily through spontaneous symmetry breaking. Given that we have $v_{\mu\tau} = 80$ GeV in addition to $v = 246$ GeV, one can treat $v_{\rm SB} \sim 100$ GeV as a common symmetry breaking scale, and therefore the scalar decays are activated for $T \leq v_{\rm SB}$. We further take $M_{h_2} = 25$ GeV, $\sin\theta = 0.01$ and $y_{e\mu} = y_{e\tau} = 0.5$ consistently with the collider constraints and neutrino data. And the impact of thermal corrections on the scalar masses becomes subdominant for such a temperature range. We first quote below the thermally corrected masses for $h_{1,2}$ to test this impact. Neglecting the effect of a small s_θ, and the couplings $\lambda_{H\phi}$ and $\lambda_{S\phi}$, one writes

$$M_{h_1}^2(T) \simeq m_{h_1}^2 + \frac{1}{12}\big(6\lambda_H + \lambda_{HS} + 3y_t^2 + \frac{3}{4}(g')^2 + \frac{9}{4}g^2\big)T^2, \tag{7.22a}$$

$$M_{h_2}^2(T) \simeq m_{h_2}^2 + \frac{1}{12}(2\lambda_{HS} + 4\lambda_S + y_{e\mu}^2 + y_{e\tau}^2 + 3g_{\mu\tau}^2)T^2. \tag{7.22b}$$

This choice corresponds to $\lambda_H = 0.258$, $\lambda_S = 0.098$ and $\lambda_{HS} = 0.015$ from Equations 7.9a-7.9c. One then obtains $M_{h_1}(v_{\mu\tau}) = 153.73$ GeV and $M_{h_2}(v_{\mu\tau}) = 33.42$ GeV. Thus, for both $m_{h_1} = 125$ GeV and $m_{h_2} = 25$ GeV, the correction generated from the thermal loops is incremental. Such choices for m_ϕ and m_{h_2},

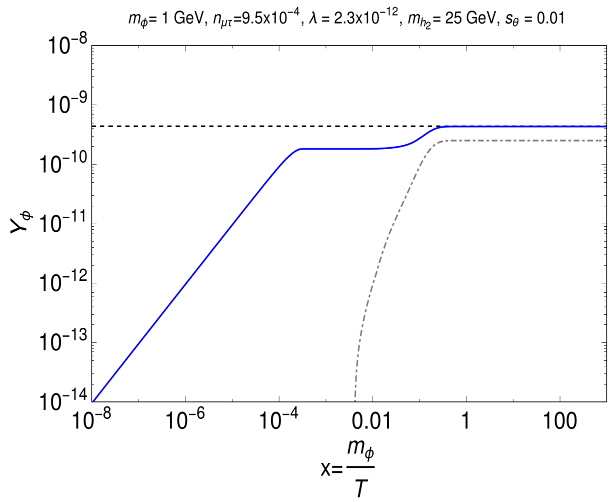

Figure 7.8: Evolution of the DM comoving number density as a function of $x = \frac{m_\phi}{T}$ for $m_\phi = 1$ GeV when scalar decays are not negligible. The dotted line is the corresponding SFI curve.

therefore, imply that unlike $Z_{\mu\tau} \to \phi\phi^\dagger$, the $h_1, h_2 \to \phi\phi^\dagger$ decays can occur even in the absence of temperature effects. Therefore, DM production in the SFI picture is not completely ruled out for this subsection.

Figures 7.8, 7.9 and 7.10 show the impact of scalar decays on the DM yield for $m_\phi = 1$ GeV, 30 MeV, and 25 MeV respectively. For the chosen DM masses, both $M_{h_1}(T)$ and $M_{h_2}(T)$ remain greater than $2m_\phi$ in the $T < v_{\mu\tau}$ range. In other words, the finite temperature corrections do not alter the original hierarchy in this case. We also take $\lambda_{H\phi} = \lambda_{S\phi} \equiv \lambda$ for simplicity. For $m_\phi = 1$ GeV, DM production from scalar decay kicks in around $x \simeq 0.01$, an epoch when the production from $Z_{\mu\tau}$ decay has already ceased long back. As can be seen in Figure 7.8, the scalar decays thus "lift" the horizontal DM yield curve, and the natural freeze-in saturation smoothly is attained around $x \sim \mathcal{O}(0.1)$. No new crossovers are introduced in the process. The cases of BP2 and BP3 are also not very different. For BP2 and BP3, DM production from $Z_{\mu\tau}$ decay stops at $x_2^{\rm cr} = 4.33\times10^{-4}$ and 5.37×10^{-4} respectively. However $h_1, h_2 \to \phi\phi^\dagger$ get activated at a slightly earlier epoch, i.e., $x \simeq 3\times10^{-4}$. So, DM matter production never entirely ceases for BP2 and BP3. This is corroborated by Figures 7.9 and 7.10. We remind now that scalar decays too contribute to DM production; the parameters l and $n_{\mu\tau}$ values need to be chosen carefully so as to obtain the required relic density. These parameter values for each m_ϕ can be read from the corresponding figure.

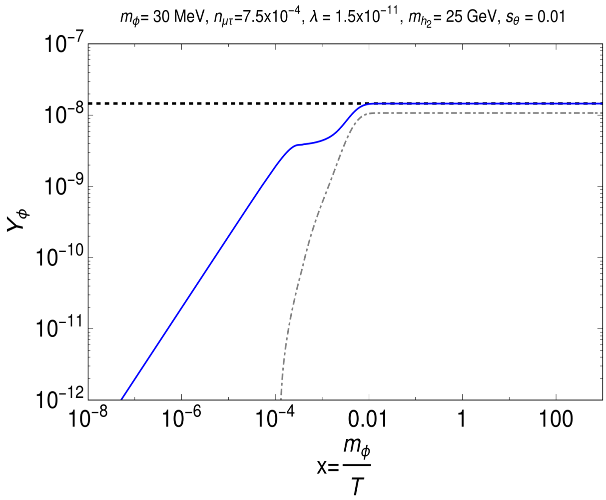

Figure 7.9: Evolution of the DM comoving number density as a function of $x = \frac{m_\phi}{T}$ for $m_\phi = 30$ MeV when scalar decays are not negligible. The dotted line is the corresponding SFI curve.

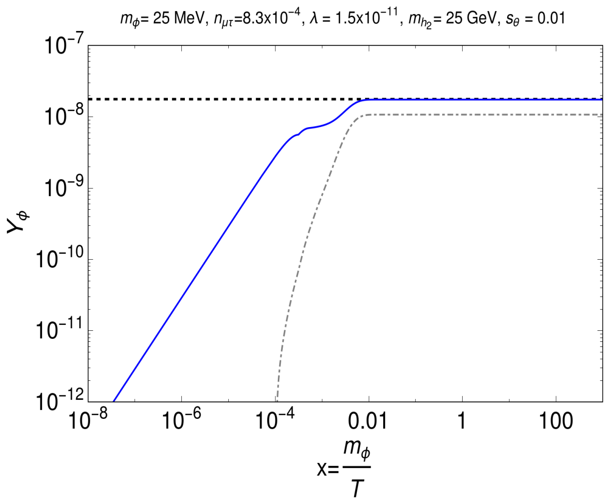

Figure 7.10: Evolution of the DM comoving number density as a function of $x = \frac{m_\phi}{T}$ for $m_\phi = 25$ MeV when scalar decays are not negligible. The dotted line is the corresponding SFI curve.

Finally, we will also like to comment briefly on the possibility of having a large

$v_{\mu\tau}$ with the same choice of $g_{\mu\tau}$ fixed at 5×10^{-4} as discussed above. A large $v_{\mu\tau}$ results in a heavier $Z_{\mu\tau}$. Although this scenario does not remain consistent with the recent $g-2$ data, as can also be seen from Figure 7.1, it still is interesting in terms of DM phenomenology. If the mass hierarchy among the $Z_{\mu\tau}$, the scalar responsible for breaking $U(1)_{L_\mu - L_\tau}$ symmetry, and the DM are appropriately set the scenario can result in the forbidden production of the DM from the decay of this scalar at a very early epoch through thermal corrections. The production of DM from $Z_{\mu\tau}$ decay will always proceed through the SFI even with the thermal mass of $Z_{\mu\tau}$ is taken into account if the DM mass is smaller than half of the $Z_{\mu\tau}$ mass. Discussing this scenario in detail is beyond the scope of the present work, and we wish to take it as a future project.

7.5 Summary and Conclusion

Although the studies of FIMP dark matter in a minimally extended $U(1)_{L_\mu - L_\tau}$ model already exists in the literature, the role of thermal corrections in this setup has never been examined before. In this work, we show that incorporating a thermal mass for the gauge boson $Z_{\mu\tau}$ opens up new temperature thresholds that are not encountered in SFI. For simplicity, we only consider the production of the DM through the decay of the gauge boson of $U(1)_{L_\mu - L_\tau}$ symmetry and two scalars. All the above-mentioned particles remain in equilibrium with the SM bath but couple feebly to the DM. The DM mass does not receive thermal corrections on account of the fact that a FIMP does not equilibrate with the thermal bath at any point. However, the masses of the decaying particles receive such corrections at high temperatures due to their interactions with the thermal bath.

For a better understanding of the role of different thermal masses, we divide our study into two different scenarios: (A) $\lambda_{H\phi}, \lambda_{S\phi} << n_{\mu\tau} g_{\mu\tau}$ and (B) $\lambda_{H\phi}, \lambda_{S\phi} \sim n_{\mu\tau} g_{\mu\tau}$. In the first scenario, the DM is dominantly produced by the decay of $Z_{\mu\tau}$ whereas the second scenario entails the production of DM from the decay of $Z_{\mu\tau}$ as well as the other two scalars. An exciting feature of the first scenario is the existence of two crossovers where the condition $M_{Z_{\mu\tau}}(T) > 2m_\phi$ is satisfied. While the DM production always proceeds via a channel that remains kinematically forbidden in the SFI scenario before the first crossover, and the production of the DM after the second crossover might or might not happen via the forbidden channel. In the second scenario, the impact of the scalars decaying into the DM is also observed on top of its production from the decay of $Z_{\mu\tau}$. Here, the production from the scalar decay is triggered only after the spontaneous symmetry breaking. Finally, we also comment on the possibility of having a larger

$U(1)_{L_\mu - L_\tau}$ breaking scale, which we wish to take as a future endeavor.

The involvement of the feeble interactions of DM with the SM particles in the freeze-in scenario makes the model exceedingly challenging to observe experimentally. With the WIMP DM parameter space almost getting ruled out from the present experiments, the FIMP-type DM has emerged as a new alternative. Hence, providing a detection prospect of such DM is always a compelling task. Keeping this in mind, we focused on a DM parameter of the present setup that remained consistent with the DM relic density but at the same time also provided a solution to the muon $(g-2)$ anomaly. This, in turn, also increases the predictability of the present setup.

Chapter 8

Summary and Conclusions

The standard model of particle physics, one of the remarkable advancements of the present era, successfully describes elementary particles at a fundamental level and all the interactions among them. Decades-long journey in different high-energy experiments directed us to acquire a deep understanding of the fascinating world of electroweak and QCD interactions, measuring different parameters at very high precision. Despite this, several blind spots, such as its inability to describe dark matter, neutrino mass, matter anti-matter asymmetry, etc., and various esthetic issues in its composition compelled us to conceive the standard model as an effective low-energy description of a larger and superior construction. While theoretical physicists around the globe are looking to design such self-consistent edifice, different collider and celestial experiments are scrutinizing for a desperate hint of new physics.

The present thesis studies some new physics models winding around different dark matter scenarios. Interestingly, the evidence of dark matter has spread over a wide range of scales, e.g., from the galactic to the cosmological scale, in various experiments. In addition, the observation of CMB even provides the composition of the present Universe in high precision, confirming that the non-baryonic dark matter constitutes almost 80 percent of the matter density. As this significant component of the Universe, there is no reason not to expect a much-extended family structure in the dark sector. We are primarily oblivious because of their characteristic weaker interaction with the SM particles. Neither we know their fundamental properties, such as mass, spin, interactions, complexity in the dark sector, or production mechanism. Different production paradigms for the DM have been proposed depending on the nature of its interaction.

Our study mainly focuses on the WIMP and FIMP paradigms of dark matter, where the freeze-out and freeze-in mechanisms set the final abundance of dark matter, respectively. Freeze-out mechanism leads to the eventual abundance of the thermal dark matter after maintaining thermal equilibrium with the thermal soup in the early Universe. So this kind of dark matter typically poses a significant interaction rate and is severely constrained from direct detection experiments and sometimes other indirect and collider searches. Different model-dependent studies indicate substantial constraints in the parameter space with the possible mass range of such dark matter in the GeV to TeV scale range.

On the contrary, freeze-in dark matter is never part of the thermal bath because of its feeble interaction strength. Getting any measurable detection signal for such feebly interacting DM is challenging. In this case, one can get dark matter for a wide range from orders of keV to TeV and higher. DM production can occur via the decay of the heavy mediator in the dark sector. In that case, such a mediator can be produced at the collider experiments to study signatures like displaced vertex (DV) or long-lived particle (LLP) searches.

Since the production of dark matter is a phenomenon of the early Universe, it has a connection with cosmology. We have shown that the effects of non-standard cosmology have a stimulating impact on dark matter phenomenology and leptogenesis. The presence of the modified cosmology demands an early freeze-out than the standard case, so one needs a larger interaction rate to satisfy the relic density constraints. In some scenarios, improved signals can be obtained since the interaction strength is enhanced. In the freeze-in scenario also, large annihilation and or/and decays are needed due to the presence of a non-standard Universe which can significantly modify the search strategy for the DM.

In our first study (Chapter 3), we investigate a simple extension of the standard model with a doublet and a singlet fermion. Here, considering a small Majorana mass term for the singlet field splits the Dirac state into two nearly degenerate pseudo-Dirac states. The lightest pseudo-Dirac state serves as the dark matter, which is capable of evading the strong bound of the spin-independent direct detection experiment due to the subdued scattering of the dark matter with the nucleon mediated by the Z boson. We also illustrate the effect of the relaxation in the direct detection constraint on the singlet doublet mixing angle while ensuring that the dark matter fully satisfies the thermal relic. In addition, the same Majorana mass term has the potential to generate Majorana mass for the neutrinos radiatively at one loop, which necessitates the presence of real scalars. In Chapter 4, we further examined into a scalar extended singlet doublet model, which can realize the baryogenesis via the leptogenesis mechanism. Here, the asymmetry is generated first in the lepton sector and then transformed to the baryon sector via the sphelaron process. In this scenario, lepton asymmetry production proceeds via the heavy scalar's decay to the BSM fermion doublet and the SM lepton doublet. We also explore the effects of non-standard cosmology on DM phenomenology and baryogenesis. We have found that generating the correct order baryon asymmetry is impossible in the presence of standard cosmology. However, the consideration of the non-standard cosmology has the potential to address the baryon asymmetry by significantly suppressing the washout of the produced lepton asymmetry.

Decades of null results in different direct detection experiments put forward the question on the scale of the interaction. There are several alternative proposals; among them, the feebly interacting massive particle paradigm is a very exciting one. In this scenario, the DM never thermalizes with the thermal bath and produces non-thermally from the scattering or decays of the bath particles. Interestingly, there are works that describe the self-interaction of dark matter enable to address the small-scale problem of cosmology. Now, we examine the nonthermal production of the singlet doublet dark matter where we extend our scalar sector by a MeV scale singlet scalar to mediate the strong self-interaction of the DM in Chapter 5. Initially, the fermion dark matter is non-thermally produced, and then the conversion of dark matter to scalar occurs. Here, the abundance of dark matter is fixed not by the FI but by the freeze-out of the conversion process occurring in the dark sector. Since the scalar does not have any decay mode, it also contributes to the relic density of dark matter. In the radiation-dominated Universe, the conversion process is so significant that it effectively reduces the abundance of dark matter and remains unsuccessful in making the fermion dark matter the main component. However, the consideration of the kination or faster than kination dominated Universe can circumvent the issue by suppressing the conversion of dark matter to the scalar. We have further discussed that the MeV scalar mediator can generate the sizeable velocity-dependent self-interaction cross-section for the realized parameter space of the dark matter. In the remainder of the thesis, we look at a different aspect of dark matter. We know that the production of dark matter took place in the early Universe when the temperature was very high. So the consideration of thermal effects can play an essential role in dark matter phenomenology. Now we demonstrate the impact of thermal effects on the study of dark matter. In chapter 6, we have studied the FIMP dark matter in a minimal $U(1)_{B-L}$ extension of the SM where the lightest RHN(N_1) serves as the DM candidate and the rest two heavier RHNs can generate the neutrino masses as well as the matter anti-matter asymmetry of the Universe through the Type-I seesaw mechanism. Here, the $B-L$ scalar and the gauge boson become massive after the $B-L$ breaking. In this scenario, we have discussed the impact of thermal effects on the DM phenomenology and seen that the $B-L$ scalar gets significant thermal mass correction at high temperatures. We discuss the DM phenomenology for the mass hierarchy $M_{Z_{BL}} \ll M_1 \ll m_s$ where the production of both N_1 and Z_{BL} proceed via the kinematically forbidden channel at high temperature because of the incorporation of the thermal mass correction. Here, the dark matter is further produced via the late time decays of the Z_{BL} boson. The dark matter production remains impossible through the standard FI for such mass hierarchy. In another mass hierarchy($M_{Z_{BL}} \ll m_s \ll M_1$), though the DM production occurs via SFI, the late time decay of Z_{BL} to DM helps in differentiating SFI from FFI. Finally, we conclude that the consideration of thermal effects actually enlarges the parameter space of DM by allowing DM production from a kinematically forbidden channel.

Finally, we explore FIMP dark matter in the context of $U(1)_{L_\mu - L_\tau}$ model; However, such studies are done earlier, but we are considering thermal corrections to the masses of the particles participating in the dark matter phenomenology and the dark matter for the first time in Chapter 7. Here, the dark matter production can occur through the scalar's decay and the $Z_{\mu\tau}$ boson. We divide our scenario into two cases to facilitate the analysis together with the realization of the thermal effects. At first, we demonstrate the production of dark matter from the kinematically forbidden decay of the $Z_{\mu\tau}$ boson due to the presence of thermal correction while neglecting the scalar contribution. Next, we take into account the contribution of the scalars and found that both the decays open up after the symmetry breakings and produce dark matter further on top of the dark matter production from $Z_{\mu\tau}$ decay. The experimental detections of FIMP dark matter remain highly challenging due to its feeble interaction with the visible particles. Offering a detection prospect of such dark matter is always a fascinating task. Interestingly, our scenario has the potential to address the muon $(g-2)$ anomaly. So, we choose the parameter space for which it can satisfy the $(g-2)$ data while satisfying the relic density constraints of dark matter.

In conclusion, this thesis covers some interesting BSM aspects, mainly focusing on various dark matter scenarios. Apart from the dark matter, other attractive puzzles, the neutrino mass and the baryon asymmetry generated by *Bariogenesis via Leptogenesis mechanism* are also addressed. Besides studying the usual WIMP, and FIMP scenarios, we explore different new exciting possibilities of dark matter production. We perform the dark matter phenomenology in the presence of thermal effects and discuss the freeze-in production of DM from a kinematically forbidden channel due to the significant thermal correction towards mass named as *forbidden freeze-in*(FFI). In addition, we also study another interesting paradigm called reannihilation, where the DM (or mediator) is produced from standard model particles non-thermally (via freeze in the process), and then the conversion process happens inside the dark sector, and the conversion process's freeze-out fixes the abundance of dark matter. We discuss the self-interacting dark matter scenario where the large self-interaction of dark matter comes from

the dark matter interaction with the light scalar mediator, which can solve the small-scale problem of cosmology.
Many of these mechanisms have been proposed just recently, generating euphoria in activities constructing different models and phenomenology around them. Since many such mechanisms were realized in the early phase of the Universe when the temperature was very high, the study of thermal effects is important. It is interesting to follow how it modifies dark matter production. The thermal effects in the case of leptogenesis are also an interesting aspect to explore.

Appendix A

Boltzmann Equation to Study Leptogenesis

Leptogenesis is an out of equllibrium process and it can be described by Boltzmann equation. The evolution of any spices 'X' is given by the following differential equation.

$$\dot{n}_X + 3\frac{\dot{R}}{R}n_X = -\sum[Xa.... \leftrightarrow ij....] \tag{A.1}$$

$$[Xa.... \leftrightarrow ij....] = \frac{n_X n_a....}{n_X^{eq} n_a^{eq}....}\gamma^{eq}(Xa.... \to ij....) - \frac{n_i n_j....}{n_i^{eq} n_j^{eq}....}\gamma^{eq}(ij.... \to Xa....)$$

γ^{eq} is the spacetime density of scattering in thermal equllibrium. It can be considered as the decay rate(Γ) also, for the process like $X \to ij....$. The density of scattering for the process $Xa \to ij$.

$$\gamma^{eq}(Xa \to ij) \equiv \int d\vec{p}_X d\vec{p}_a f_X f_a \int d\vec{p}_i d\vec{p}_j (2\pi)^4 \delta^4(p_X + p_a - p_i - p_j)|\mathcal{M}|^2$$

where, $d\vec{p}_X = \int \frac{d_X^p}{2E_X(2\pi)^3}$. n and n^{eq} are the number density and equllibrium number density respectively.
The Boltzmann equation is purely classical here. Quantum corrections will get importance when the mean distance between collisions is shorter than the wavelengths of the particles. The second term of the equation of L.H.S is called the dilution factor which is coming because of the expansion effect of the universe.
Now we will define the number density in comoving volume i.e. we will absorb the effect of expansion and a dimensionless variable to simplify the above equation. The comoving number density and dimensionless variable are Y and z

respectively.

$$Y = \frac{n}{s}, \qquad\qquad z = \frac{m_X}{T} \tag{A.2}$$

where, s is the entropy density and m_X is the mass of the spice X.
The Boltzmann equation becomes

$$szH\frac{dY_X}{dz} = -\sum[Xa.... \leftrightarrow ij....] \tag{A.3}$$

A.1 Boltzmann equation for Y_N

Let Y_N is the comoving number density of right handed neutrino. We are cosidering only decay and inverse decay in the Boltzmann equation($N \leftrightarrow l\tilde{\phi}^\dagger, N \leftrightarrow \bar{l}\tilde{\phi}$). The Boltzmann equation for righthanded neutrino becomes

$$szH\frac{dY_N}{dz} = -\{[N \leftrightarrow l\tilde{\phi}^\dagger] + [N \leftrightarrow \bar{l}\tilde{\phi}]\} \tag{A.4}$$

For decay $N \rightarrow ij.....$

$$\gamma^{eq}(N \rightarrow ij...) = \gamma^{eq}(ij... \rightarrow N) = n_N^{eq}\frac{K_1(z)}{K_2(z)}\Gamma_N \tag{A.5}$$

Here the particle density distribution function is approximated as the Maxwell-Boltzmann distribution function and are very small to make significant quantum correction.

$$szH\frac{dY_N}{dz} = -\frac{K_1(z)}{K_2(z)}\Gamma_N\left(n_N - n_N^{eq}\frac{n_i n_j...}{n_i^{eq}n_j^{eq}...}\right) \tag{A.6}$$

Decay of heavy neutrino produces the out of equllibrium of the system. The lepton number conserving scattering is occuring very fast to maintain the thermal equillibrium for rest of the system. All the spices are following their equillibrium density distribution except right handed neutrino.

$$zH\frac{dY_N}{dz} = -\frac{K_1(z)}{K_2(z)}\Gamma_N(Y_N - Y_N^{eq}) \tag{A.7}$$

A.2 Boltzmann equation for Y_{B-L}

We will derive the Boltzmann equation for the time evolution of $B - L$. The right handed neutrinos do not carry any lepton number. So all processes involving heavy neutrinos will violate $B - L$ because they conserve baryon number. Here we will take into account only $B-L$ violating interactions. In literature, decay, inverse decays, $\Delta L = 1$ and $\Delta L = 2$ scatterings at tree level are considered in deriving the Boltzmann equation.

We will neglect the $\Delta L = 1$ scattering here since it involves interactions with quark sector and we consider the effects of lepton sector. $\Delta L = 1$ scattering involves Higgs as mediator. The presence of any $\mathbb{Z}_2$ like discrete symmetry forbids any interaction of heavy neutrino with Standard model Higgs. So $\Delta L = 1$ scattering is' relevant for leptogenesis in seesaw type model. Now the Boltzmann equation for $B-L$ evolution can be written as

$$\begin{aligned} zH\frac{dY_{B-L}}{dz} &= -\frac{1}{s}\Big\{[N \leftrightarrow l\tilde{\phi}^\dagger] - [N \leftrightarrow \bar{l}\tilde{\phi}] \\ &- 2[ll \leftrightarrow \tilde{\phi}\tilde{\phi}] - 2[l\tilde{\phi}^\dagger \leftrightarrow \bar{l}\tilde{\phi}] + 2[\bar{l}\bar{l} \leftrightarrow \tilde{\phi}^\dagger\tilde{\phi}^\dagger]\Big\} \end{aligned} \tag{A.8}$$

Two terms of R.H.S of the first line of above equation denotes the contribution of the decay and the inverse deca, where the last three terms are giving the contribution of scattering. The multiplication factor 2 is telling that the lepton number violated by two units fpr scattering but same is violated by one unit for decays and inverse decays. Lets focos on the deacy part.

$$[N \leftrightarrow l\tilde{\phi}^\dagger] = \frac{n_N}{n_N^{eq}}\gamma^{eq}(N \to l\tilde{\phi}^\dagger) - \frac{n_l n_{\tilde{\phi}^\dagger}}{n_l^{eq} n_{\tilde{\phi}^\dagger}^{eq}}\gamma^{eq}(l\tilde{\phi}^\dagger \to N), \tag{A.9}$$

$$[N \leftrightarrow \bar{l}\tilde{\phi}] = \frac{n_N}{n_N^{eq}}\gamma^{eq}(N \to \bar{l}\tilde{\phi}) - \frac{n_{\bar{l}} n_{\tilde{\phi}}}{n_{\bar{l}}^{eq} n_{\tilde{\phi}}^{eq}}\gamma^{eq}(\bar{l}\tilde{\phi} \to N), \tag{A.10}$$

Sakarov's condition says that C and CP violations are needed. Here heavy neutrinos decay are generating CP violation. So all the γ's above are not equal. But CPT conservation will give the following equalities.

$$\gamma^{eq}(N \to l\tilde{\phi}^\dagger) = \gamma^{eq}(\bar{l}\tilde{\phi} \to N) \equiv (1+\epsilon_D)\frac{\gamma_D}{2}, \tag{A.11}$$

$$\gamma^{eq}(N \to \bar{l}\tilde{\phi}) = \gamma^{eq}(l\tilde{\phi}^\dagger \to N) \equiv (1-\epsilon_D)\frac{\gamma_D}{2},, \tag{A.12}$$

where ϵ_D is the measure of CP violation due to the decay and γ_D is the total decay rate.

Initially when we derive the evolution of comoving number density for any spice, we have taken that only the spice is decaying out of equllibrium where as all other spices are maintaing their equllibrium value. Since here we are producing excess in lepton number, so we also take the abundance of lepton doublet to be out of equllibrium. Here only Higgs doublet is in it's equllibrium value. So the number density of lepton doublet is deviating from it's equllirium value such a way

$$\frac{n_l}{n_l^{eq}} = 1 + \chi_l, \qquad \frac{n_{\bar{l}}}{n_{\bar{l}}^{eq}} = 1 + \chi_{\bar{l}}, , \tag{A.13}$$

where, χ_l and $\chi_{\bar{l}}$ are the amount of lepton number violations which are first order small in ϵ_D. Using Equations A.9, A.10, A.11, A.12, A.13 one can write

$$[N \leftrightarrow l\tilde{\phi}^\dagger] - [N \leftrightarrow \bar{l}\tilde{\phi}]$$

$$\begin{aligned} &= \frac{n_N}{n_N^{eq}}(1+\epsilon_D)\frac{\gamma_D}{2} - (1+\chi_l)(1-\epsilon_D)\frac{\gamma_D}{2} \\ &\quad - \frac{n_N}{n_N^{eq}}(1-\epsilon_D)\frac{\gamma_D}{2} + (1+\chi_{\bar{l}})(1+\epsilon_D)\frac{\gamma_D}{2} \end{aligned}$$

$$= \epsilon_D\gamma_D\left(\frac{n_N}{n_N^{eq}} + 1\right) - \frac{\gamma_D}{2}(\chi_l - \chi_{\bar{l}}) \tag{A.14}$$

where we have neglected any second order term in ϵ_D.
Now,

$$[ll \leftrightarrow \tilde{\phi}\tilde{\phi}] = (1+\chi_l)^2\gamma^{eq}(ll \to \tilde{\phi}\tilde{\phi}) - \gamma^{eq}(\tilde{\phi}\tilde{\phi} \to ll) \tag{A.15}$$

$$[l\tilde{\phi}^\dagger \leftrightarrow \bar{l}\tilde{\phi}] = (1+\chi_l)\gamma^{eq}(l\tilde{\phi}^\dagger \to \bar{l}\tilde{\phi}) - (1+\chi_{\bar{l}})\gamma^{eq}(\bar{l}\tilde{\phi} \to l\tilde{\phi}^\dagger) \tag{A.16}$$

$$[\bar{l}\bar{l} \leftrightarrow \tilde{\phi}^\dagger\tilde{\phi}^\dagger] = (1+\chi_{\bar{l}})^2\gamma^{eq}(\bar{l}\bar{l} \to \tilde{\phi}^\dagger\tilde{\phi}^\dagger) - \gamma^{eq}(\tilde{\phi}^\dagger\tilde{\phi}^\dagger \to \bar{l}\bar{l}) \tag{A.17}$$

We know that any process at tree level is CP conserving. Since we are considering that all the $\Delta L = 2$ scattering processes at tree level so these processes are CP invariant. Using CP and CPT invariance property one can get the following relations.

$$\gamma^{eq}(ll \to \tilde{\phi}\tilde{\phi}) = \gamma^{eq}(\tilde{\phi}\tilde{\phi} \to ll) = \gamma^{eq}(\bar{l}\bar{l} \to \tilde{\phi}^\dagger\tilde{\phi}^\dagger) = \gamma^{eq}(\tilde{\phi}^\dagger\tilde{\phi}^\dagger \to \bar{l}\bar{l}) \equiv \gamma_t, \tag{A.18}$$

$$\gamma^{eq}(l\tilde{\phi}^\dagger \to \bar{l}\tilde{\phi}) = \gamma^{eq}(\bar{l}\tilde{\phi} \to l\tilde{\phi}^\dagger) \equiv \gamma_s \tag{A.19}$$

$\Delta L = 2$ scattering involves s channel processes. These processes look like a decay followed by inverse decay when the mediator is satisfying on-shell condition i.e. real particle. In the Boltzmann equation we have considered the decay as well as scattering for the evolution of $B - L$. Decay means the particle is real and also scattering involving on shell mediator means real particle. So we are over counting. We subtract the on shell contribution from the s channel scattering. The contribution to γ_s by the on-shell N as mediator particles using narrow width approximation.

$$\gamma_{OS}^{eq}(l\tilde{\phi}^{\dagger} \rightarrow \bar{l}\tilde{\phi}) = \gamma^{eq}(l\tilde{\phi}^{\dagger} \rightarrow N)BR(N \rightarrow l\tilde{\phi}) \tag{A.20}$$

$$\gamma_{OS}^{eq}(l\tilde{\phi} \rightarrow \bar{l}\tilde{\phi}^{\dagger}) = \gamma^{eq}(l\tilde{\phi} \rightarrow N)BR(N \rightarrow l\tilde{\phi}^{\dagger}) \tag{A.21}$$

The branching ratios for different decay channels of heavy neutrinos

$$BR(N \rightarrow l\tilde{\phi}) \equiv \frac{(1-\epsilon_D)}{2}, \qquad BR(N \rightarrow l\tilde{\phi}^{\dagger}) \equiv \frac{(1+\epsilon_D)}{2} \tag{A.22}$$

Now the substracted or corrected s channel contribution is given by

$$[l\tilde{\phi}^{\dagger} \leftrightarrow \bar{l}\tilde{\phi}]^{sub} = (1+\chi_l)[\gamma_s - (1-\epsilon_D)^2\frac{\gamma_D}{4}] - (1+\chi_{\bar{l}})[\gamma_s - (1-\epsilon_D)^2\frac{\gamma_D}{4}]$$

$$= (\gamma_s + \frac{\gamma_D}{4})(\chi_l - \chi_{\bar{l}}) + \gamma_D\epsilon_D + \frac{\gamma_D\epsilon_D}{2}(\chi_l + \chi_{\bar{l}}) \tag{A.23}$$

We are taking terms upto linear order in ϵ_D. Since χ's are first order in ϵ_D, we neglect the last term also.

$$[l\tilde{\phi}^{\dagger} \leftrightarrow \bar{l}\tilde{\phi}]^{sub} = (\gamma_s + \frac{\gamma_D}{4})(\chi_l - \chi_{\bar{l}}) + \gamma_D\epsilon_D \tag{A.24}$$

One can simplifies the following equations in Equations A.15,A.17 using the relation of Equation A.18 and taking the linear order of χ's.

$$[ll \leftrightarrow \tilde{\phi}\tilde{\phi}] = (1+\chi_l)^2\gamma^{eq}(ll \rightarrow \tilde{\phi}\tilde{\phi}) - \gamma^{eq}(\tilde{\phi}\tilde{\phi} \rightarrow ll)$$

$$= (1+2\chi_l)\gamma_t - \gamma_t = 2\chi_l\gamma_t \tag{A.25}$$

$$[\bar{l}\bar{l} \leftrightarrow \tilde{\phi}^{\dagger}\tilde{\phi}^{\dagger}] = (1+\chi_{\bar{l}})^2\gamma^{eq}(ll \rightarrow \tilde{\phi}\tilde{\phi}) - \gamma^{eq}(\tilde{\phi}\tilde{\phi} \rightarrow ll)$$

$$= (1+2\chi_{\bar{l}})\gamma_t - \gamma_t = 2\chi_l\gamma_t \tag{A.26}$$

After putting all the calculated expression from the Equations A.14,A.25,A.24,A.26 in Equation A.8, the Boltzmann equation for $B-L$ becomes

$$\begin{aligned} zH\frac{dY_{B-L}}{dz} &= -\frac{1}{s}\Bigg[\epsilon_D\gamma_D\left(\frac{n_N}{n_N^{eq}}+1\right) - \frac{\gamma_D}{2}(\chi_l-\chi_{\bar{l}}) - 2\gamma_s(\chi_l-\chi_{\bar{l}}) \\ &\qquad - \frac{\gamma_D}{2}(\chi_l-\chi_{\bar{l}}) - 2\gamma_D\epsilon_D - 4\gamma_t(\chi_l-\chi_{\bar{l}})\Bigg] \\ &= -\frac{1}{s}\Bigg[\epsilon_D\gamma_D\left(\frac{n_N}{n_N^{eq}}-1\right) - (\chi_l-\chi_{\bar{l}})(\gamma_D+2\gamma_s+4\gamma_t)\Bigg] \end{aligned} \tag{A.27}$$

The term $(\chi_l-\chi_{\bar{l}})$ measures the total lepton number violation. One can express it in terms of lepton number vioation in comoving volume and entropy density.

$$\chi_l-\chi_{\bar{l}} = (1+\chi_l)-(1+\chi_{\bar{l}}) = \frac{n_l-n_{\bar{l}}}{n_l^{eq}} = Y_L s \tag{A.28}$$

where, $Y_L = \frac{n_l-n_{\bar{l}}}{n_l^{eq}s} = \frac{n_L-n_{\bar{L}}}{s}$. Here we have taken thet the equillibrium number density of lepton and anti lepton are equal.

Now one can rewrite the above Boltzmann equation in terms of comoving number density and also total decay width with the help of decay width as follows

$$zH\frac{dY_{B-L}}{dz} = -\epsilon_D\Gamma_N\frac{K_1(z)}{K_2(z)}\left(Y_N-Y_N^{eq}\right) + Y_L(\gamma_D+2\gamma_s+4\gamma_t) \tag{A.29}$$

The varriable should be same on both side of the equation so we have to relate L to $B-L$. At very high temparature sphalerons are in equllibrum and these processes conserve $B-L$. After electroweak symmetry breaking those processes become very suppressed. So N_L and N_{B-L} are connected to each other depending on temparature. When the spheleron processes are in equillibrium that time some of the lepton number leaks to baryon number. These are related by the spheleron factor a_{sph}, N_L=-$a_{sph}N_{B-L}$. where $0 < a_{sph} < 1$ is the measure of effectiveness of sphlerons. Now the set of Boltzmann equations for leptogenesis

$$\frac{dY_N}{dz} = -D(Y_N-Y_N^{eq}), \tag{A.30}$$

$$\frac{dY_{B-L}}{dz} = -\epsilon_D D\left(Y_N-Y_N^{eq}\right) - WY_{B-L} \tag{A.31}$$

where,

$$D = \frac{\Gamma_N}{zH}\frac{K_1(z)}{K_2(z)}, \qquad W = a_{sph}\frac{\gamma_D+2\gamma_s+4\gamma_t}{zH} \tag{A.32}$$

Appendix B

Realization of Pseudo-Dirac fermion

Here, we present a brief understanding on the construction of a pseudo-Dirac fermion. The notations to be used are adopted from Ref [287]. In general a Dirac fermion (X) can be expressed in terms of two Weyl fermions.

$$X = \begin{pmatrix} \eta \\ \xi^\dagger \end{pmatrix} \quad \text{with} \quad P_L X = \begin{pmatrix} \eta \\ 0 \end{pmatrix} \quad \text{and} \quad P_R X = \begin{pmatrix} 0 \\ \xi^\dagger \end{pmatrix} \tag{B.1}$$

The charge conjugation of X is given by

$$X^c = \begin{pmatrix} \xi \\ \eta^\dagger . \end{pmatrix} \tag{B.2}$$

Suppose we have a Lagrangian where both Dirac and Majorana mass terms for X field are present.

$$\mathcal{L} = m_D \bar{X} X + \frac{1}{2} m_M^L \overline{X^C} P_L X + h.c. + \frac{1}{2} m_M^R \overline{X^C} P_R X + h.c.. \tag{B.3}$$

For the moment we consider $m_M^{L,R} = m_M$. Now, one can expand $\mathcal{L}$ in terms of the Weyl components and can rewrite the above Lagrangian as,

$$\mathcal{L} = m_D(\eta\xi + \eta^\dagger \xi^\dagger) + \frac{1}{2} m_M(\eta\eta + h.c.) + \frac{1}{2} m_M(\xi\xi + h.c.) \tag{B.4}$$

With this, the mass matrix in the (η, ξ) basis turns out to be

$$\mathcal{M} = \begin{pmatrix} m_M & m_D \\ m_D & m_M \end{pmatrix} . \tag{B.5}$$

After diagonalising $\mathcal{M}$, we obtain the two mass eigenstates as,

$$y_1 = \frac{i}{\sqrt{2}}(\xi - \eta) \tag{B.6}$$

$$y_2 = \frac{1}{\sqrt{2}}(\xi + \eta). \tag{B.7}$$

We notice that the eigenstates y_1 and y_2 are two component in nature. However, we can always form a four component spinor by defining

$$Y_i = \begin{pmatrix} y_i \\ y_i^\dagger \end{pmatrix}. \tag{B.8}$$

With the above definition it is convenient to write the following relations,

$$Y_1 = \frac{i}{\sqrt{2}}(X^c - X) \tag{B.9}$$

$$Y_2 = \frac{1}{\sqrt{2}}(X^c + X). \tag{B.10}$$

It is important to mention that, in the limit $m_M^L \neq m_M^R$, the above four component eigenstates will receive some correction which can be expressed as

$$Y_1 = \frac{i}{\sqrt{2}}(X^c - X) + \mathcal{O}(\delta) \tag{B.11}$$

$$Y_2 = \frac{1}{\sqrt{2}}(X^c + X) + \mathcal{O}(\delta), \tag{B.12}$$

where, $\delta = |m_M^L - m_M^R|$. Now, the states Y_1 and Y_2 are non degenerate and since they have a pseudo-Dirac origin, we call them pseudo-Dirac states in the limit $m_M^{L,R} \ll m_D$.

Appendix C

Analytical formulation of the lepton asymmetry parameter

In this section we present a brief analytical estimate of the lepton asymmetry from the lepton number violating dark sector scalar singlet decay. The asymmetry parameter generally gets non-zero contributions from the interference of the tree level and two 1-loop level diagrams as shown in Figure 4.8. However in the present set up with a vanishing lepton mass limit, the sole contribution to the lepton asymmetry is sourced by the interference of the tree level and vertex diagram only. The invariant amplitude square for the tree level decay of the BSM scalar (ϕ) to SM lepton (l) and the vector like fermion (Ψ) can be expressed as,

$$|\mathcal{M}|^2_{\phi_i \to \bar{l}_{L\alpha} + \Psi} = \sum_{\alpha} \left(h_{\alpha i} h^*_{\alpha i}\right) M^2_{\phi_i}, \tag{C.1}$$

Where $i,\ j$ are the indices specific to the BSM scalar which run as $(1, 2, 3)$ and the $\alpha = e,\ \mu,\ \tau$ refers to SM lepton indices respectively. Considering the limit $M_\phi \gg m_\Psi, m_l$, the corresponding decay width of i'th scalar at tree level can be expressed as:

$$\begin{aligned}\Gamma_{\phi_i \to \bar{l}_{L\alpha} + \Psi} &= \frac{|\mathcal{M}|^2}{16\pi} \frac{1}{M_{\phi_i}} \\ &= \frac{\left(h^\dagger h\right)_{ii} M_{\phi_i}}{16\pi}.\end{aligned} \tag{C.2}$$

Next we proceed to calculate the contribution caused by the interference between the tree level and vertex diagrams to ϵ. The Feynman amplitude square of such kind of interference process (see Figure C.1) is given by (in the vanishing

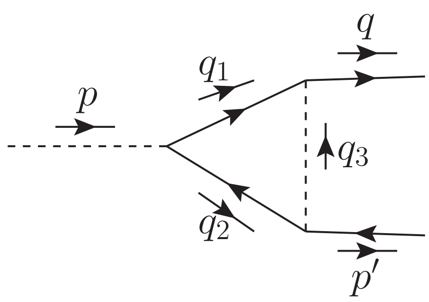

Figure C.1: Particle directions and momenta of the vertex diagram as shown in Figure 4.8.

lepton and DM mass limits):

$$I'_{\text{vertex}} = 2iA_h \int \frac{d^4q_1}{(2\pi)^4} \frac{\overline{u_\Psi}\ P_R\ \not{q}_1\ P_L \not{q}_2\ P_R\ v_l\ \overline{v_l}\ P_L\ u_\Psi}{(q_1^2+i\varepsilon)(q_2^2+i\varepsilon)(q_3^2-M_{\phi_j}^2+i\varepsilon)}, \tag{C.3}$$

where $A_h = h_{\beta j}h^*_{\beta i}h_{\alpha j}h^*_{\alpha i}$. Afterwards, we use the standard trace properties of the Gamma matrices and also consider the imaginary part of the I'_{vertex}/A_h in Equation C.3 (since it solely matters for lepton asymmetry as we will see in a while) to write:

$$I'_{\text{vertex}} = 2iA_h \int \frac{d^4q_1}{(2\pi)^4} \frac{(q_1.q_2)(p'.q) - (q_1.p')(q_2.q) + (q_1.q)(q_2.p')}{(q_1^2+i\varepsilon)(q_2^2+i\varepsilon)(q_3^2-M_{\phi_j}^2+i\varepsilon)}, \tag{C.4}$$

We work in rest frame of the incoming particle ϕ_i. Applying principle of momentum conservation at each vertices we obtain

$$q_1 = \{E_1, \mathbf{q_1}\}, \quad q_2 = \{M_{\phi_i} - E_1, -\mathbf{q_1}\} \text{ with } p = \{M_{\phi_i}, \vec{0}\}, \tag{C.5}$$

$$\text{also,} \quad p' = \left\{\frac{M_{\phi_i}}{2}, -\mathbf{q}\right\} \quad , q = \left\{\frac{M_{\phi_i}}{2}, \mathbf{q}\right\}. \tag{C.6}$$

Next, we implement the famous Cutkosky rule to evaluate the integral $\text{Im}(I_{\text{vertex}})$ and write

$$\text{Disc}\ [I'_{\text{vertex}}] = 2iA_h \int \frac{d^4q_1}{(2\pi)^4} \frac{(-2\pi i)^2\ \delta[q_1^2]\ \delta[(p-q_1)^2]\ \Theta(E_1)\ \Theta(M_{\phi_i}-E_1)}{\left[(q-q_1)^2 - M_{\phi_j}^2\right]} \tag{C.7}$$

Upon further simplifications and performing the integral Equation C.7 we reach at

$$\text{Disc}\ [I'_{\text{vertex}}] = \frac{iA_h M_{\phi_i}^2}{8\pi}\left[1 + x_{ij}\ \log\left(\frac{x_{ij}}{1+x_{ij}}\right)\right], \tag{C.8}$$

where $x_{ij} = \frac{M_j^2}{M_i^2}$. Now, one can use the conversion: $\mathrm{Im}\,(I') = -\frac{1}{2i}$ Disc $[I']$ to attain

$$\mathrm{Im}\,(I') = -\frac{M_{\phi_i}^2}{16\pi}\left[1 + x_{ij}\ \log\left(\frac{x_{ij}}{1+x_{ij}}\right)\right]. \tag{C.9}$$

where we define $I'_{\text{vertex}} = A_h I'$. The general formula for vertex contribution to the lepton asymmetry parameter is,

$$\epsilon_{\text{vertex}} = -\frac{4}{\Gamma_{\text{tot}}}\sum_{i\neq j}\sum_{\alpha}\mathrm{Im}(A_h)\ \mathrm{Im}[I'V_\phi], \tag{C.10}$$

where V_ϕ is the phase space factor for a two body decay process (under discussion) having magnitude $\frac{1}{8\pi M_{\phi_i}}$. The total decay width is the sum of forward and inverse decay widths *i.e.* $\Gamma_{\text{tot}} = \Gamma_{\phi_i} + \bar{\Gamma}_{\phi_i}$ as in Equation C.2. One can further write $\mathrm{Im}(I'V_\phi) = \mathrm{Im}(I')V_\phi$ since V_ϕ is real.

With all the expressions earlier highlighted, finally we note down the explicit form of ϵ_{vertex} in terms of the model parameters,

$$\epsilon^i_{\text{vertex}} = \frac{1}{4\pi}\sum_{j\neq i}\frac{\mathrm{Im}\left[(h^\dagger h)_{ij} h_{\alpha j} h^*_{\alpha i}\right]}{(h^\dagger h)_{ii}}\left[1 + x_{ij}\ \log\left(\frac{x_{ij}}{x_{ij}+1}\right)\right] \tag{C.11}$$

In a similar fashion, one can formulate the contribution to the lepton asymmetry originating from the self energy diagram. Since at vanishing lepton mass limit due to properties of Gamma matrices, the interference amplitude of self energy and the tree level diagrams vanishes at the amplitude level we skip the details here.

Appendix D

Feynmann Diagrams for DM production, Direct Detection and Indirect Detection

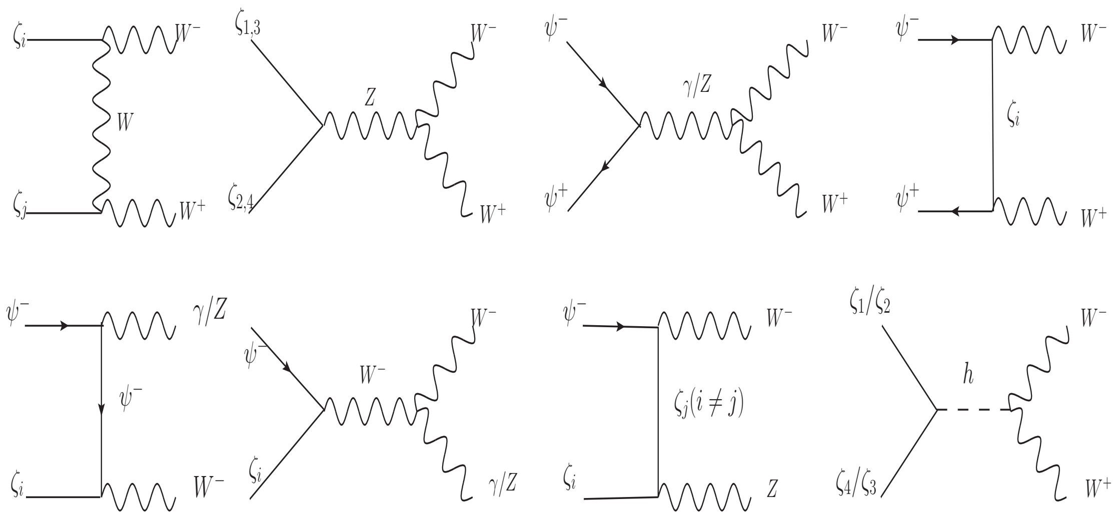

Figure D.1: Annihilation and coannihilation processes dominantly contribute to the relic density of DM.

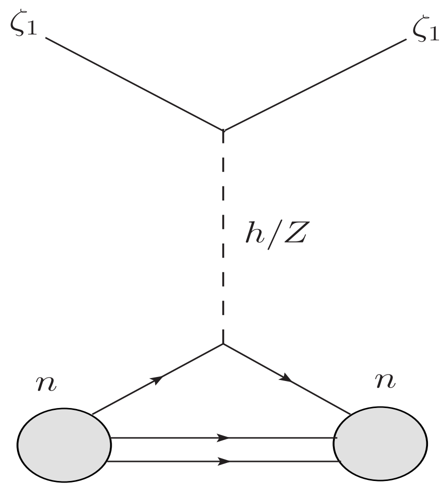

Figure D.2: Process for direct detection of DM.

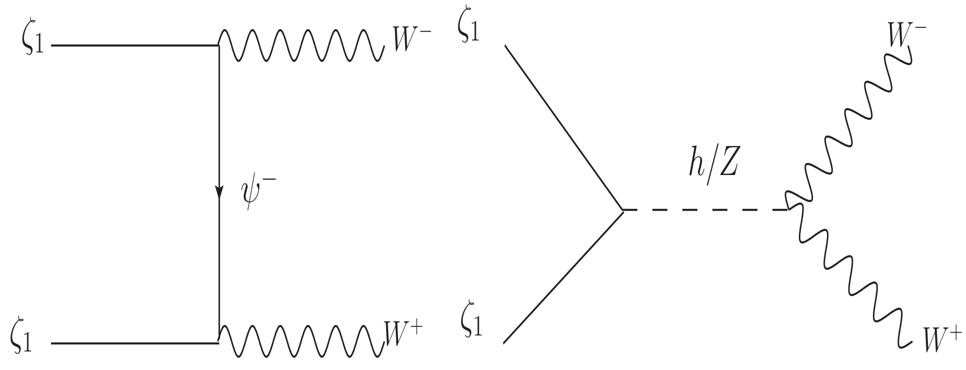

Figure D.3: Process for indirect detection of DM.

Bibliography

[1] S. L. Glashow, *Partial-symmetries of weak interactions*, *Nuclear Physics* **22** (1961) 579–588.

[2] A. Salam and J. Ward, *Electromagnetic and weak interactions*, *Physics Letters* **13** (1964) 168–171.

[3] S. Weinberg, *A model of leptons*, *Phys. Rev. Lett.* **19** (Nov, 1967) 1264–1266.

[4] Particle Data Group collaboration, M. Tanabashi, K. Hagiwara, K. Hikasa, K. Nakamura, Y. Sumino, F. Takahashi et al., *Review of particle physics*, *Phys. Rev. D* **98** (Aug, 2018) 030001.

[5] P. W. Anderson, *Plasmons, gauge invariance, and mass*, *Phys. Rev.* **130** (Apr, 1963) 439–442.

[6] P. W. Higgs, *Broken symmetries and the masses of gauge bosons*, *Phys. Rev. Lett.* **13** (Oct, 1964) 508–509.

[7] F. Englert and R. Brout, *Broken symmetry and the mass of gauge vector mesons*, *Phys. Rev. Lett.* **13** (Aug, 1964) 321–323.

[8] G. S. Guralnik, C. R. Hagen and T. W. B. Kibble, *Global conservation laws and massless particles*, *Phys. Rev. Lett.* **13** (Nov, 1964) 585–587.

[9] KamLAND collaboration, S. Abe et al., *Precision Measurement of Neutrino Oscillation Parameters with KamLAND*, *Phys. Rev. Lett.* **100** (2008) 221803, [0801.4589].

[10] Super-Kamiokande collaboration, Y. Fukuda et al., *Evidence for oscillation of atmospheric neutrinos*, *Phys. Rev. Lett.* **81** (1998) 1562–1567, [hep-ex/9807003].

[11] K2K collaboration, M. H. Ahn et al., *Indications of neutrino oscillation in a 250 km long baseline experiment*, *Phys. Rev. Lett.* **90** (2003) 041801, [hep-ex/0212007].

[12] Planck collaboration, N. Aghanim et al., *Planck 2018 results. VI. Cosmological parameters*, *Astron. Astrophys.* **641** (2020) A6, [1807.06209].

[13] P. Minkowski, *$\mu \to e\gamma$ at a Rate of One Out of 10^9 Muon Decays?*, *Phys. Lett. B* **67** (1977) 421–428.

[14] M. Gell-Mann, P. Ramond and R. Slansky, *Complex Spinors and Unified Theories*, *Conf. Proc. C* **790927** (1979) 315–321, [1306.4669].

[15] R. N. Mohapatra and G. Senjanović, *Neutrino mass and spontaneous parity nonconservation*, *Phys. Rev. Lett.* **44** (Apr, 1980) 912–915.

[16] T. Yanagida, *Horizontal Symmetry and Masses of Neutrinos*, *Prog. Theor. Phys.* **64** (1980) 1103.

[17] J. Schechter and J. W. F. Valle, *Neutrino Masses in SU(2) x U(1) Theories*, *Phys. Rev. D* **22** (1980) 2227.

[18] J. Schechter and J. W. F. Valle, *Neutrino decay and spontaneous violation of lepton number*, *Phys. Rev. D* **25** (Feb, 1982) 774–783.

[19] Z. Maki, M. Nakagawa and S. Sakata, *Remarks on the unified model of elementary particles*, *Prog. Theor. Phys.* **28** (1962) 870–880.

[20] R. N. Mohapatra and G. Senjanović, *Neutrino masses and mixings in gauge models with spontaneous parity violation*, *Phys. Rev. D* **23** (Jan, 1981) 165–180.

[21] G. Lazarides, Q. Shafi and C. Wetterich, *Proton lifetime and fermion masses in an so(10) model*, *Nuclear Physics B* **181** (1981) 287–300.

[22] C. Wetterich, *Neutrino Masses and the Scale of B-L Violation*, *Nucl. Phys. B* **187** (1981) 343–375.

[23] B. Brahmachari and R. N. Mohapatra, *Unified explanation of the solar and atmospheric neutrino puzzles in a minimal supersymmetric SO(10) model*, *Phys. Rev. D* **58** (1998) 015001, [hep-ph/9710371].

[24] R. N. Mohapatra and J. W. F. Valle, *Neutrino mass and baryon-number nonconservation in superstring models*, *Phys. Rev. D* **34** (Sep, 1986) 1642–1645.

[25] R. N. Mohapatra, *Mechanism for Understanding Small Neutrino Mass in Superstring Theories*, *Phys. Rev. Lett.* **56** (1986) 561–563.

[26] A. Zee, *A Theory of Lepton Number Violation, Neutrino Majorana Mass, and Oscillation*, *Phys. Lett. B* **93** (1980) 389.

[27] K. Babu, *Model of "calculable" majorana neutrino masses*, *Physics Letters B* **203** (1988) 132–136.

[28] A. Zee, *Quantum Numbers of Majorana Neutrino Masses*, *Nucl. Phys. B* **264** (1986) 99–110.

[29] K. S. Babu and E. Ma, *Natural hierarchy of radiatively induced majorana neutrino masses*, *Phys. Rev. Lett.* **61** (Aug, 1988) 674–677.

[30] E. Ma, *Verifiable radiative seesaw mechanism of neutrino mass and dark matter*, *Phys. Rev. D* **73** (2006) 077301, [hep-ph/0601225].

[31] L. Lopez Honorez, E. Nezri, J. F. Oliver and M. H. G. Tytgat, *The Inert Doublet Model: An Archetype for Dark Matter*, *JCAP* **02** (2007) 028, [hep-ph/0612275].

[32] L. Lopez Honorez and C. E. Yaguna, *A new viable region of the inert doublet model*, *JCAP* **01** (2011) 002, [1011.1411].

[33] N. G. Deshpande and E. Ma, *Pattern of symmetry breaking with two higgs doublets*, *Phys. Rev. D* **18** (Oct, 1978) 2574–2576.

[34] P. M. Ferreira and D. R. T. Jones, *Bounds on scalar masses in two Higgs doublet models*, *JHEP* **08** (2009) 069, [0903.2856].

[35] A. Ahriche, A. Jueid and S. Nasri, *Radiative neutrino mass and majorana dark matter within an inert higgs doublet model*, *Phys. Rev. D* **97** (May, 2018) 095012.

[36] A. D. Sakharov, *Violation of CP Invariance, C asymmetry, and baryon asymmetry of the universe*, *Pisma Zh. Eksp. Teor. Fiz.* **5** (1967) 32–35.

[37] M. Fukugita and T. Yanagida, *Baryogenesis Without Grand Unification*, *Phys. Lett. B* **174** (1986) 45–47.

[38] A. Ignatiev, N. Krasnikov, V. Kuzmin and A. Tavkhelidze, *Universal cp-noninvariant superweak interaction and bayron asymmetry of the universe*, *Physics Letters B* **76** (1978) 436–438.

[39] M. Yoshimura, *Unified Gauge Theories and the Baryon Number of the Universe*, *Phys. Rev. Lett.* **41** (1978) 281–284.

[40] J. R. Ellis, M. K. Gaillard and D. V. Nanopoulos, *Baryon Number Generation in Grand Unified Theories*, Phys. Lett. B **80** (1979) 360.

[41] I. Affleck and M. Dine, *A New Mechanism for Baryogenesis*, Nucl. Phys. B **249** (1985) 361–380.

[42] M. Dine, L. Randall and S. D. Thomas, *Baryogenesis from flat directions of the supersymmetric standard model*, Nucl. Phys. B **458** (1996) 291–326, [hep-ph/9507453].

[43] M. Losada, *High temperature dimensional reduction of the MSSM and other multiscalar models*, Phys. Rev. D **56** (1997) 2893–2913, [hep-ph/9605266].

[44] M. Carena, M. Quiros and C. E. M. Wagner, *Opening the window for electroweak baryogenesis*, Phys. Lett. B **380** (1996) 81–91, [hep-ph/9603420].

[45] D. Delepine, J. M. Gerard, R. Gonzalez Felipe and J. Weyers, *A Light stop and electroweak baryogenesis*, Phys. Lett. B **386** (1996) 183–188, [hep-ph/9604440].

[46] A. Riotto and M. Trodden, *Recent progress in baryogenesis*, Ann. Rev. Nucl. Part. Sci. **49** (1999) 35–75, [hep-ph/9901362].

[47] M. Dine and A. Kusenko, *The Origin of the matter - antimatter asymmetry*, Rev. Mod. Phys. **76** (2003) 1, [hep-ph/0303065].

[48] W. Buchmuller, P. Di Bari and M. Plumacher, *Leptogenesis for pedestrians*, Annals Phys. **315** (2005) 305–351, [hep-ph/0401240].

[49] A. Anisimov, S. Blanchet and P. Di Bari, *Viability of Dirac phase leptogenesis*, JCAP **04** (2008) 033, [0707.3024].

[50] S. Davidson, E. Nardi and Y. Nir, *Leptogenesis*, Phys. Rept. **466** (2008) 105–177, [0802.2962].

[51] W. Buchmuller, R. D. Peccei and T. Yanagida, *Leptogenesis as the origin of matter*, Ann. Rev. Nucl. Part. Sci. **55** (2005) 311–355, [hep-ph/0502169].

[52] P. Konar, A. Mukherjee, A. K. Saha and S. Show, *Linking the pseudo-Dirac dark matter and radiative neutrino mass in a singlet doublet scenario*, Phys. Rev. D **102** (2020) 015024, [2001.11325].

[53] P. Konar, A. Mukherjee, A. K. Saha and S. Show, *A dark clue to seesaw and leptogenesis in a pseudo-Dirac singlet doublet scenario with (non)standard cosmology*, *JHEP* **03** (2021) 044, [2007.15608].

[54] P. Ghosh, P. Konar, A. K. Saha and S. Show, *Self-interacting freeze-in dark matter in a singlet doublet scenario*, 2112.09057.

[55] P. Konar, R. Roshan and S. Show, *Freeze-in dark matter through forbidden channel in U(1)B-L*, *JCAP* **03** (2022) 021, [2110.14411].

[56] N. Chakrabarty, P. Konar, R. Roshan and and S. Show, *Thermally corrected masses and freeze-in dark matter: a case study*, 2206.02233.

[57] F. Zwicky, *Die Rotverschiebung von extragalaktischen Nebeln*, *Helv. Phys. Acta* **6** (1933) 110–127.

[58] H. W. Babcock, *The rotation of the Andromeda Nebula*, *Lick Observatory Bulletin* **498** (Jan., 1939) 41–51.

[59] J. Jeans, *The dynamical theory of gases*. University Press, 1921.

[60] T. Hill, "Statistical Mechanics. 1956."

[61] K. G. Begeman, A. H. Broeils and R. H. Sanders, *Extended rotation curves of spiral galaxies: Dark haloes and modified dynamics*, *Mon. Not. Roy. Astron. Soc.* **249** (1991) 523.

[62] D. Clowe, M. Bradac, A. H. Gonzalez, M. Markevitch, S. W. Randall, C. Jones et al., *A direct empirical proof of the existence of dark matter*, *Astrophys. J. Lett.* **648** (2006) L109–L113, [astro-ph/0608407].

[63] S. W. Randall, M. Markevitch, D. Clowe, A. H. Gonzalez and M. Bradac, *Constraints on the Self-Interaction Cross-Section of Dark Matter from Numerical Simulations of the Merging Galaxy Cluster 1E 0657-56*, *Astrophys. J.* **679** (2008) 1173–1180, [0704.0261].

[64] R. Gavazzi, T. Treu, J. D. Rhodes, L. V. Koopmans, A. S. Bolton, S. Burles et al., *The Sloan Lens ACS Survey. 4. The mass density profile of early-type galaxies out to 100 effective radii*, *Astrophys. J.* **667** (2007) 176–190, [astro-ph/0701589].

[65] B. Paczyński, *Gravitational microlensing by the galactic halo*, *The Astrophysical Journal* **304** (1986) 1–5.

[66] Planck collaboration, R. Adam et al., *Planck 2015 results. I. Overview of products and scientific results*, *Astron. Astrophys.* **594** (2016) A1, [1502.01582].

[67] G. Arcadi, M. Dutra, P. Ghosh, M. Lindner, Y. Mambrini, M. Pierre et al., *The waning of the WIMP? A review of models, searches, and constraints*, *Eur. Phys. J. C* **78** (2018) 203, [1703.07364].

[68] N. Bernal, M. Heikinheimo, T. Tenkanen, K. Tuominen and V. Vaskonen, *The Dawn of FIMP Dark Matter: A Review of Models and Constraints*, *Int. J. Mod. Phys. A* **32** (2017) 1730023, [1706.07442].

[69] M. M. Pierre, *Dark Matter phenomenology : from simplified WIMP models to refined alternative solutions*. PhD thesis, U. Paris-Saclay, 2018. 1901.05822.

[70] M. Schumann, *Direct Detection of WIMP Dark Matter: Concepts and Status*, *J. Phys. G* **46** (2019) 103003, [1903.03026].

[71] J. M. Gaskins, *A review of indirect searches for particle dark matter*, *Contemp. Phys.* **57** (2016) 496–525, [1604.00014].

[72] F. Kahlhoefer, *Review of LHC Dark Matter Searches*, *Int. J. Mod. Phys. A* **32** (2017) 1730006, [1702.02430].

[73] M. W. Goodman and E. Witten, *Detectability of certain dark-matter candidates*, *Phys. Rev. D* **31** (Jun, 1985) 3059–3063.

[74] J. D. Lewin and P. F. Smith, *Review of mathematics, numerical factors, and corrections for dark matter experiments based on elastic nuclear recoil*, *Astropart. Phys.* **6** (1996) 87–112.

[75] D. G. Cerdeno and A. M. Green, *Direct detection of WIMPs*, 1002.1912.

[76] T. Lin, *Dark matter models and direct detection*, *PoS* **333** (2019) 009, [1904.07915].

[77] M. J. Reid, *The distance to the center of the galaxy*, *Ann. Rev. Astron. Astrophys.* **31** (1993) 345–372.

[78] J. I. Read, *The Local Dark Matter Density*, *J. Phys. G* **41** (2014) 063101, [1404.1938].

[79] M. Kuhlen, M. Vogelsberger and R. Angulo, *Numerical Simulations of the Dark Universe: State of the Art and the Next Decade*, *Phys. Dark Univ.* **1** (2012) 50–93, [1209.5745].

[80] F. J. Kerr and D. Lynden-Bell, *Review of galactic constants*, *Mon. Not. Roy. Astron. Soc.* **221** (1986) 1023.

[81] M. C. Smith et al., *The RAVE Survey: Constraining the Local Galactic Escape Speed*, *Mon. Not. Roy. Astron. Soc.* **379** (2007) 755–772, [astro-ph/0611671].

[82] QCDSF collaboration, G. S. Bali et al., *Strangeness Contribution to the Proton Spin from Lattice QCD*, *Phys. Rev. Lett.* **108** (2012) 222001, [1112.3354].

[83] COMPASS collaboration, M. G. Alekseev et al., *Quark helicity distributions from longitudinal spin asymmetries in muon-proton and muon-deuteron scattering*, *Phys. Lett. B* **693** (2010) 227–235, [1007.4061].

[84] COMPASS collaboration, M. Alekseev et al., *The Polarised Valence Quark Distribution from semi-inclusive DIS*, *Phys. Lett. B* **660** (2008) 458–465, [0707.4077].

[85] C. A. Aidala, S. D. Bass, D. Hasch and G. K. Mallot, *The Spin Structure of the Nucleon*, *Rev. Mod. Phys.* **85** (2013) 655–691, [1209.2803].

[86] R. J. Hill and M. P. Solon, *Standard model anatomy of wimp dark matter direct detection. ii. qcd analysis and hadronic matrix elements*, *Phys. Rev. D* **91** (Feb, 2015) 043505.

[87] M. I. Gresham and K. M. Zurek, *Effect of nuclear response functions in dark matter direct detection*, *Phys. Rev. D* **89** (2014) 123521, [1401.3739].

[88] J. Engel, *Nuclear form-factors for the scattering of weakly interacting massive particles*, *Phys. Lett. B* **264** (1991) 114–119.

[89] R. H. Helm, *Inelastic and elastic scattering of 187-mev electrons from selected even-even nuclei*, *Phys. Rev.* **104** (Dec, 1956) 1466–1475.

[90] J. R. Ellis, K. A. Olive and C. Savage, *Hadronic Uncertainties in the Elastic Scattering of Supersymmetric Dark Matter*, *Phys. Rev. D* **77** (2008) 065026, [0801.3656].

[91] J. Ellis, N. Nagata and K. A. Olive, *Uncertainties in WIMP Dark Matter Scattering Revisited*, *Eur. Phys. J. C* **78** (2018) 569, [1805.09795].

[92] J. Billard, L. Strigari and E. Figueroa-Feliciano, *Implication of neutrino backgrounds on the reach of next generation dark matter direct detection experiments*, *Phys. Rev. D* **89** (2014) 023524, [1307.5458].

[93] J. E. Gunn, B. W. Lee, I. Lerche, D. N. Schramm and G. Steigman, *Some Astrophysical Consequences of the Existence of a Heavy Stable Neutral Lepton*, *Astrophys. J.* **223** (1978) 1015–1031.

[94] Y. B. Zeldovich, A. A. Klypin, M. Y. Khlopov and V. M. Chechetkin, *Astrophysical constraints on the mass of heavy stable neutral leptons*, *Sov. J. Nucl. Phys.* **31** (1980) 664–669.

[95] J. Silk and M. Srednicki, *Cosmic-ray antiprotons as a probe of a photino-dominated universe*, *Phys. Rev. Lett.* **53** (Aug, 1984) 624–627.

[96] F. W. Stecker and A. J. Tylka, *The Cosmic Ray Anti-proton Spectrum From Dark Matter Annihilation and Its Astrophysical Implications: A New Look*, *Astrophys. J. Lett.* **336** (1989) L51–L54.

[97] H. Baer and S. Profumo, *Low energy antideuterons: shedding light on dark matter*, *JCAP* **12** (2005) 008, [astro-ph/0510722].

[98] F. Donato, N. Fornengo and D. Maurin, *Antideuteron fluxes from dark matter annihilation in diffusion models*, *Phys. Rev. D* **78** (Aug, 2008) 043506.

[99] M. Cirelli, N. Fornengo, T. Montaruli, I. A. Sokalski, A. Strumia and F. Vissani, *Spectra of neutrinos from dark matter annihilations*, *Nucl. Phys. B* **727** (2005) 99–138, [hep-ph/0506298].

[100] M. Cirelli, G. Corcella, A. Hektor, G. Hutsi, M. Kadastik, P. Panci et al., *PPPC 4 DM ID: A Poor Particle Physicist Cookbook for Dark Matter Indirect Detection*, *JCAP* **03** (2011) 051, [1012.4515].

[101] Fermi-LAT, DES collaboration, A. Albert et al., *Searching for Dark Matter Annihilation in Recently Discovered Milky Way Satellites with Fermi-LAT*, *Astrophys. J.* **834** (2017) 110, [1611.03184].

[102] Fermi-LAT collaboration, M. Ackermann et al., *Searching for Dark Matter Annihilation from Milky Way Dwarf Spheroidal Galaxies with Six Years of Fermi Large Area Telescope Data*, *Phys. Rev. Lett.* **115** (2015) 231301, [1503.02641].

[103] M. Lisanti, S. Mishra-Sharma, N. L. Rodd and B. R. Safdi, *Search for Dark Matter Annihilation in Galaxy Groups*, *Phys. Rev. Lett.* **120** (2018) 101101, [1708.09385].

[104] L. J. Chang, M. Lisanti and S. Mishra-Sharma, *Search for dark matter annihilation in the Milky Way halo*, *Phys. Rev. D* **98** (2018) 123004, [1804.04132].

[105] ATLAS collaboration, M. Aaboud et al., *Combination of searches for invisible Higgs boson decays with the ATLAS experiment*, *Phys. Rev. Lett.* **122** (2019) 231801, [1904.05105].

[106] C. E. Yaguna, *Singlet-Doublet Dirac Dark Matter*, *Phys. Rev.* **D92** (2015) 115002, [1510.06151].

[107] J. Fiaschi, M. Klasen and S. May, *Singlet-doublet fermion and triplet scalar dark matter with radiative neutrino masses*, *JHEP* **05** (2019) 015, [1812.11133].

[108] D. Restrepo, A. Rivera and W. Tangarife, *Singlet-Doublet Dirac Dark Matter and Neutrino Masses*, *Phys. Rev.* **D100** (2019) 035029, [1906.09685].

[109] G. Arcadi, *2HDM portal for Singlet-Doublet Dark Matter*, *Eur. Phys. J.* **C78** (2018) 864, [1804.04930].

[110] S. Esch, M. Klasen and C. E. Yaguna, *A singlet doublet dark matter model with radiative neutrino masses*, *JHEP* **10** (2018) 055, [1804.03384].

[111] L. Calibbi, L. Lopez-Honorez, S. Lowette and A. Mariotti, *Singlet-Doublet Dark Matter Freeze-in: LHC displaced signatures versus cosmology*, *JHEP* **09** (2018) 037, [1805.04423].

[112] N. Maru, N. Okada and S. Okada, *Fermionic Minimal Dark Matter in 5D Gauge-Higgs Unification*, *Phys. Rev.* **D96** (2017) 115023, [1801.00686].

[113] N. Maru, T. Miyaji, N. Okada and S. Okada, *Fermion Dark Matter in Gauge-Higgs Unification*, *JHEP* **07** (2017) 048, [1704.04621].

[114] Q.-F. Xiang, X.-J. Bi, P.-F. Yin and Z.-H. Yu, *Exploring Fermionic Dark Matter via Higgs Boson Precision Measurements at the Circular Electron Positron Collider*, *Phys. Rev.* **D97** (2018) 055004, [1707.03094].

[115] T. Abe, *Effect of CP violation in the singlet-doublet dark matter model*, *Phys. Lett.* **B771** (2017) 125–130, [1702.07236].

[116] S. Banerjee, S. Matsumoto, K. Mukaida and Y.-L. S. Tsai, *WIMP Dark Matter in a Well-Tempered Regime: A case study on Singlet-Doublets Fermionic WIMP*, *JHEP* **11** (2016) 070, [1603.07387].

[117] S. Horiuchi, O. Macias, D. Restrepo, A. Rivera, O. Zapata and H. Silverwood, *The Fermi-LAT gamma-ray excess at the Galactic Center in the singlet-doublet fermion dark matter model*, *JCAP* **1603** (2016) 048, [1602.04788].

[118] L. Calibbi, A. Mariotti and P. Tziveloglou, *Singlet-Doublet Model: Dark matter searches and LHC constraints*, *JHEP* **10** (2015) 116, [1505.03867].

[119] C. Cheung and D. Sanford, *Simplified Models of Mixed Dark Matter*, *JCAP* **1402** (2014) 011, [1311.5896].

[120] T. Cohen, J. Kearney, A. Pierce and D. Tucker-Smith, *Singlet-Doublet Dark Matter*, *Phys. Rev.* **D85** (2012) 075003, [1109.2604].

[121] R. Enberg, P. J. Fox, L. J. Hall, A. Y. Papaioannou and M. Papucci, *LHC and dark matter signals of improved naturalness*, *JHEP* **11** (2007) 014, [0706.0918].

[122] F. D'Eramo, *Dark matter and Higgs boson physics*, *Phys. Rev.* **D76** (2007) 083522, [0705.4493].

[123] B. Barman, D. Borah, P. Ghosh and A. K. Saha, *Flavoured gauge extension of singlet-doublet fermionic dark matter: neutrino mass, high scale validity and collider signatures*, *JHEP* **10** (2019) 275, [1907.10071].

[124] A. Dutta Banik, A. K. Saha and A. Sil, *Scalar assisted singlet doublet fermion dark matter model and electroweak vacuum stability*, *Phys. Rev.* **D98** (2018) 075013, [1806.08080].

[125] B. Barman, S. Bhattacharya, P. Ghosh, S. Kadam and N. Sahu, *Fermion Dark Matter with Scalar Triplet at Direct and Collider Searches*, *Phys. Rev.* **D100** (2019) 015027, [1902.01217].

[126] S. Bhattacharya, P. Ghosh, N. Sahoo and N. Sahu, *Mini Review on Vector-Like Leptonic Dark Matter, Neutrino Mass, and Collider Signatures*, *Front.in Phys.* **7** (2019) 80, [1812.06505].

[127] S. Bhattacharya, N. Sahoo and N. Sahu, *Minimal vectorlike leptonic dark matter and signatures at the LHC*, *Phys. Rev.* **D93** (2016) 115040, [1510.02760].

[128] S. Bhattacharya, N. Sahoo and N. Sahu, *Singlet-Doublet Fermionic Dark Matter, Neutrino Mass and Collider Signatures*, *Phys. Rev.* **D96** (2017) 035010, [1704.03417].

[129] D. Restrepo, A. Rivera, M. Sánchez-Peláez, O. Zapata and W. Tangarife, *Radiative Neutrino Masses in the Singlet-Doublet Fermion Dark Matter Model with Scalar Singlets*, *Phys. Rev.* **D92** (2015) 013005, [1504.07892].

[130] A. Freitas, S. Westhoff and J. Zupan, *Integrating in the Higgs Portal to Fermion Dark Matter*, *JHEP* **09** (2015) 015, [1506.04149].

[131] G. Cynolter, J. Kovács and E. Lendvai, *Doublet–singlet model and unitarity*, *Mod. Phys. Lett.* **A31** (2016) 1650013, [1509.05323].

[132] S. Bhattacharya, B. Karmakar, N. Sahu and A. Sil, *Unifying the flavor origin of dark matter with leptonic nonzero θ_{13}*, *Phys. Rev.* **D93** (2016) 115041, [1603.04776].

[133] S. Bhattacharya, B. Karmakar, N. Sahu and A. Sil, *Flavor origin of dark matter and its relation with leptonic nonzero θ_{13} and Dirac CP phase δ*, *JHEP* **05** (2017) 068, [1611.07419].

[134] J.-W. Wang, X.-J. Bi, P.-F. Yin and Z.-H. Yu, *Impact of Fermionic Electroweak Multiplet Dark Matter on Vacuum Stability with One-loop Matching*, *Phys. Rev.* **D99** (2019) 055009, [1811.08743].

[135] T. Abe and R. Sato, *Current status and future prospects of the singlet-doublet dark matter model with CP-violation*, *Phys. Rev.* **D99** (2019) 035012, [1901.02278].

[136] B. Barman, A. Dutta Banik and A. Paul, *Singlet-Doublet Fermionic Dark Matter and Gravitational Wave in Two Higgs Doublet Extension of the Standard Model*, 1912.12899.

[137] A. De Simone, V. Sanz and H. P. Sato, *Pseudo-Dirac Dark Matter Leaves a Trace*, *Phys. Rev. Lett.* **105** (2010) 121802, [1004.1567].

[138] N. Narendra, N. Sahoo and N. Sahu, *Dark matter assisted Dirac leptogenesis and neutrino mass*, *Nucl. Phys.* **B936** (2018) 76–90, [1712.02960].

[139] E. Ma, *Radiative inverse seesaw mechanism for nonzero neutrino mass*, *Phys. Rev.* **D80** (2009) 013013, [0904.4450].

[140] K. Kannike, *Vacuum Stability Conditions From Copositivity Criteria*, *Eur. Phys. J. C* **72** (2012) 2093, [1205.3781].

[141] J. Chakrabortty, P. Konar and T. Mondal, *Copositive Criteria and Boundedness of the Scalar Potential*, *Phys. Rev. D* **89** (2014) 095008, [1311.5666].

[142] J. Horejsi and M. Kladiva, *Tree-unitarity bounds for THDM Higgs masses revisited*, *Eur. Phys. J. C* **46** (2006) 81–91, [hep-ph/0510154].

[143] G. Bhattacharyya and D. Das, *Scalar sector of two-Higgs-doublet models: A minireview*, *Pramana* **87** (2016) 40, [1507.06424].

[144] Planck collaboration, N. Aghanim et al., *Planck 2018 results. VI. Cosmological parameters*, 1807.06209.

[145] XENON collaboration, E. Aprile et al., *First Dark Matter Search Results from the XENON1T Experiment*, *Phys. Rev. Lett.* **119** (2017) 181301, [1705.06655].

[146] D. Barducci, G. Belanger, J. Bernon, F. Boudjema, J. Da Silva, S. Kraml et al., *Collider limits on new physics within* $micrOMEGAs_4.3$, *Comput. Phys. Commun.* **222** (2018) 327–338, [1606.03834].

[147] Y. Cui, D. E. Morrissey, D. Poland and L. Randall, *Candidates for Inelastic Dark Matter*, *JHEP* **05** (2009) 076, [0901.0557].

[148] L. J. Hall, T. Moroi and H. Murayama, *Sneutrino cold dark matter with lepton number violation*, *Phys. Lett.* **B424** (1998) 305–312, [hep-ph/9712515].

[149] D. Tucker-Smith and N. Weiner, *Inelastic dark matter*, *Phys. Rev.* **D64** (2001) 043502, [hep-ph/0101138].

[150] A. Davoli, A. De Simone, T. Jacques and V. Sanz, *Displaced Vertices from Pseudo-Dirac Dark Matter*, *JHEP* **11** (2017) 025, [1706.08985].

[151] F. Halzen and A. D. Martin, *QUARKS AND LEPTONS: AN INTRODUCTORY COURSE IN MODERN PARTICLE PHYSICS*. 1984.

[152] MAGIC, Fermi-LAT collaboration, M. Ahnen et al., *Limits to Dark Matter Annihilation Cross-Section from a Combined Analysis of MAGIC and Fermi-LAT Observations of Dwarf Satellite Galaxies*, *JCAP* **02** (2016) 039, [1601.06590].

[153] K. Griest and M. Kamionkowski, *Unitarity Limits on the Mass and Radius of Dark Matter Particles*, *Phys. Rev. Lett.* **64** (1990) 615.

[154] S. Fraser, E. Ma and O. Popov, *Scotogenic Inverse Seesaw Model of Neutrino Mass*, *Phys. Lett.* **B737** (2014) 280–282, [1408.4785].

[155] G. 't Hooft and M. J. G. Veltman, *Scalar One Loop Integrals*, *Nucl. Phys.* **B153** (1979) 365–401.

[156] R. K. Ellis and G. Zanderighi, *Scalar one-loop integrals for QCD*, *JHEP* **02** (2008) 002, [0712.1851].

[157] T. Abe, M. Fujiwara and J. Hisano, *Loop corrections to dark matter direct detection in a pseudoscalar mediator dark matter model*, *JHEP* **02** (2019) 028, [1810.01039].

[158] J. A. Casas and A. Ibarra, *Oscillating neutrinos and muon → e, gamma*, *Nucl. Phys.* **B618** (2001) 171–204, [hep-ph/0103065].

[159] Particle Data Group collaboration, M. Tanabashi et al., *Review of Particle Physics*, *Phys. Rev.* **D98** (2018) 030001.

[160] D. N. Dinh, A. Ibarra, E. Molinaro and S. T. Petcov, *The* $\mu - e$ *Conversion in Nuclei,* $\mu \to e\gamma, \mu \to 3e$ *Decays and TeV Scale See-Saw Scenarios of Neutrino Mass Generation*, *JHEP* **08** (2012) 125, [1205.4671].

[161] D. Tommasini, G. Barenboim, J. Bernabeu and C. Jarlskog, *Nondecoupling of heavy neutrinos and lepton flavor violation*, *Nucl. Phys.* **B444** (1995) 451–467, [hep-ph/9503228].

[162] A. Ilakovac and A. Pilaftsis, *Flavor violating charged lepton decays in seesaw-type models*, *Nucl. Phys.* **B437** (1995) 491, [hep-ph/9403398].

[163] MEG II collaboration, A. M. Baldini et al., *The design of the MEG II experiment*, *Eur. Phys. J.* **C78** (2018) 380, [1801.04688].

[164] F. D'Eramo, N. Fernandez and S. Profumo, *When the Universe Expands Too Fast: Relentless Dark Matter*, *JCAP* **05** (2017) 012, [1703.04793].

[165] J. Herrero-Garcia, E. Molinaro and M. A. Schmidt, *Dark matter direct detection of a fermionic singlet at one loop*, *Eur. Phys. J. C* **78** (2018) 471, [1803.05660].

[166] G. Cynolter and E. Lendvai, *Electroweak Precision Constraints on Vector-like Fermions*, *Eur. Phys. J. C* **58** (2008) 463–469, [0804.4080].

[167] LUX collaboration, D. Akerib et al., *Results from a search for dark matter in the complete LUX exposure*, Phys. Rev. Lett. **118** (2017) 021303, [1608.07648].

[168] PandaX-II collaboration, X. Cui et al., *Dark Matter Results From 54-Ton-Day Exposure of PandaX-II Experiment*, Phys. Rev. Lett. **119** (2017) 181302, [1708.06917].

[169] XENON collaboration, E. Aprile et al., *Dark Matter Search Results from a One Ton-Year Exposure of XENON1T*, Phys. Rev. Lett. **121** (2018) 111302, [1805.12562].

[170] CMS collaboration, V. Khachatryan et al., *Searches for invisible decays of the Higgs boson in pp collisions at $\sqrt{s}$ = 7, 8, and 13 TeV*, JHEP **02** (2017) 135, [1610.09218].

[171] R. Caldwell, R. Dave and P. J. Steinhardt, *Cosmological imprint of an energy component with general equation of state*, Phys. Rev. Lett. **80** (1998) 1582–1585, [astro-ph/9708069].

[172] E. W. Kolb and M. S. Turner, *The Early Universe*, vol. 69. 1990.

[173] A. Alloul, N. D. Christensen, C. Degrande, C. Duhr and B. Fuks, *FeynRules 2.0 - A complete toolbox for tree-level phenomenology*, Comput. Phys. Commun. **185** (2014) 2250–2300, [1310.1921].

[174] G. Bélanger, F. Boudjema, A. Pukhov and A. Semenov, *micrOMEGAs4.1: two dark matter candidates*, Comput. Phys. Commun. **192** (2015) 322–329, [1407.6129].

[175] S. Pascoli, S. Petcov and C. Yaguna, *Quasidegenerate neutrino mass spectrum, $\mu \to e + \gamma$ decay and leptogenesis*, Phys. Lett. B **564** (2003) 241–254, [hep-ph/0301095].

[176] S. Petcov and T. Shindou, *Charged lepton decays $l(i) \to l(j) + \gamma$, leptogenesis CP-violating parameters and Majorana phases*, Phys. Rev. D **74** (2006) 073006, [hep-ph/0605151].

[177] F. Capozzi, E. Lisi, A. Marrone and A. Palazzo, *Current unknowns in the three neutrino framework*, Prog. Part. Nucl. Phys. **102** (2018) 48–72, [1804.09678].

[178] I. Esteban, M. Gonzalez-Garcia, A. Hernandez-Cabezudo, M. Maltoni and T. Schwetz, *Global analysis of three-flavour neutrino oscillations:*

synergies and tensions in the determination of θ_{23}, δ_{CP}, and the mass ordering, JHEP **01** (2019) 106, [1811.05487].

[179] T2K collaboration, K. Abe et al., *Constraint on the matter–antimatter symmetry-violating phase in neutrino oscillations*, Nature **580** (2020) 339–344, [1910.03887].

[180] M. Plumacher, *Baryogenesis and lepton number violation*, Z. Phys. C **74** (1997) 549–559, [hep-ph/9604229].

[181] W. Buchmuller, P. Di Bari and M. Plumacher, *Some aspects of thermal leptogenesis*, New J. Phys. **6** (2004) 105, [hep-ph/0406014].

[182] G. Giudice, A. Notari, M. Raidal, A. Riotto and A. Strumia, *Towards a complete theory of thermal leptogenesis in the SM and MSSM*, Nucl. Phys. B **685** (2004) 89–149, [hep-ph/0310123].

[183] E. Giusarma, M. Gerbino, O. Mena, S. Vagnozzi, S. Ho and K. Freese, *Improvement of cosmological neutrino mass bounds*, Phys. Rev. D **94** (2016) 083522, [1605.04320].

[184] S. Vagnozzi, E. Giusarma, O. Mena, K. Freese, M. Gerbino, S. Ho et al., *Unveiling ν secrets with cosmological data: neutrino masses and mass hierarchy*, Phys. Rev. D **96** (2017) 123503, [1701.08172].

[185] C. Kouvaris, I. M. Shoemaker and K. Tuominen, *Self-Interacting Dark Matter through the Higgs Portal*, Phys. Rev. D **91** (2015) 043519, [1411.3730].

[186] K. Kainulainen, K. Tuominen and V. Vaskonen, *Self-interacting dark matter and cosmology of a light scalar mediator*, Phys. Rev. D **93** (2016) 015016, [1507.04931].

[187] B. Zhu and M. Abdughani, *Thermal relic of self-interacting dark matter with retarded decay of mediator*, JHEP **12** (2021) 059, [2103.06050].

[188] M. Duch, B. Grzadkowski and D. Huang, *Strongly self-interacting vector dark matter via freeze-in*, JHEP **01** (2018) 020, [1710.00320].

[189] Y. Du, F. Huang, H.-L. Li and J.-H. Yu, *Freeze-in Dark Matter from Secret Neutrino Interactions*, JHEP **12** (2020) 207, [2005.01717].

[190] G. Krnjaic, *Freezing In, Heating Up, and Freezing Out: Predictive Nonthermal Dark Matter and Low-Mass Direct Detection*, JHEP **10** (2018) 136, [1711.11038].

[191] J. Berger, D. Croon, S. El Hedri, K. Jedamzik, A. Perko and D. G. E. Walker, *Dark matter amnesia in out-of-equilibrium scenarios*, *JCAP* **02** (2019) 051, [1812.08795].

[192] C. Cheung, G. Elor, L. J. Hall and P. Kumar, *Origins of Hidden Sector Dark Matter I: Cosmology*, *JHEP* **03** (2011) 042, [1010.0022].

[193] C. Cheung, G. Elor, L. J. Hall and P. Kumar, *Origins of Hidden Sector Dark Matter II: Collider Physics*, *JHEP* **03** (2011) 085, [1010.0024].

[194] X. Chu, T. Hambye and M. H. G. Tytgat, *The Four Basic Ways of Creating Dark Matter Through a Portal*, *JCAP* **05** (2012) 034, [1112.0493].

[195] B. Barman, P. Ghosh, F. S. Queiroz and A. K. Saha, *Scalar multiplet dark matter in a fast expanding Universe: Resurrection of the desert region*, *Phys. Rev. D* **104** (2021) 015040, [2101.10175].

[196] J. M. No, P. Tunney and B. Zaldivar, *Probing Dark Matter freeze-in with long-lived particle signatures: MATHUSLA, HL-LHC and FCC-hh*, *JHEP* **03** (2020) 022, [1908.11387].

[197] N. Bernal, X. Chu, C. Garcia-Cely, T. Hambye and B. Zaldivar, *Production Regimes for Self-Interacting Dark Matter*, *JCAP* **03** (2016) 018, [1510.08063].

[198] A. Tapadar, S. Ganguly and S. Roy, *Non-adiabatic evolution of dark sector in the presence of $U(1)_{L\mu} - {}_{L\tau}$ gauge symmetry*, *JCAP* **05** (2022) 019, [2109.13609].

[199] S. Heeba, F. Kahlhoefer and P. Stöcker, *Freeze-in production of decaying dark matter in five steps*, *JCAP* **11** (2018) 048, [1809.04849].

[200] K.-C. Yang, *Thermodynamic Evolution of Secluded Vector Dark Matter: Conventional WIMPs and Nonconventional WIMPs*, *JHEP* **11** (2019) 048, [1905.09582].

[201] T. Binder, T. Bringmann, M. Gustafsson and A. Hryczuk, *Early kinetic decoupling of dark matter: when the standard way of calculating the thermal relic density fails*, *Phys. Rev. D* **96** (2017) 115010, [1706.07433].

[202] A. Hryczuk and M. Laletin, *Dark matter freeze-in from semi-production*, *JHEP* **06** (2021) 026, [2104.05684].

[203] L. J. Hall, K. Jedamzik, J. March-Russell and S. M. West, *Freeze-In Production of FIMP Dark Matter*, *JHEP* **03** (2010) 080, [0911.1120].

[204] ATLAS collaboration, M. Aaboud et al., *Search for long-lived charginos based on a disappearing-track signature in pp collisions at $\sqrt{s} = 13$ TeV with the ATLAS detector*, *JHEP* **06** (2018) 022, [1712.02118].

[205] CMS collaboration, A. M. Sirunyan et al., *Search for disappearing tracks as a signature of new long-lived particles in proton-proton collisions at $\sqrt{s} = 13$ TeV*, *JHEP* **08** (2018) 016, [1804.07321].

[206] ATLAS collaboration, M. Aaboud et al., *Search for long-lived, massive particles in events with displaced vertices and missing transverse momentum in $\sqrt{s} = 13$ TeV pp collisions with the ATLAS detector*, *Phys. Rev. D* **97** (2018) 052012, [1710.04901].

[207] D. Curtin et al., *Long-Lived Particles at the Energy Frontier: The MATHUSLA Physics Case*, *Rept. Prog. Phys.* **82** (2019) 116201, [1806.07396].

[208] MATHUSLA collaboration, C. Alpigiani et al., *A Letter of Intent for MATHUSLA: A Dedicated Displaced Vertex Detector above ATLAS or CMS.*, 1811.00927.

[209] S. Tulin and H.-B. Yu, *Dark Matter Self-interactions and Small Scale Structure*, *Phys. Rept.* **730** (2018) 1–57, [1705.02358].

[210] S. Tulin, H.-B. Yu and K. M. Zurek, *Beyond Collisionless Dark Matter: Particle Physics Dynamics for Dark Matter Halo Structure*, *Phys. Rev. D* **87** (2013) 115007, [1302.3898].

[211] M. R. Buckley and P. J. Fox, *Dark Matter Self-Interactions and Light Force Carriers*, *Phys. Rev. D* **81** (2010) 083522, [0911.3898].

[212] J. L. Feng, M. Kaplinghat and H.-B. Yu, *Halo Shape and Relic Density Exclusions of Sommerfeld-Enhanced Dark Matter Explanations of Cosmic Ray Excesses*, *Phys. Rev. Lett.* **104** (2010) 151301, [0911.0422].

[213] R. N. Mohapatra, S. Nussinov and V. L. Teplitz, *Mirror matter as selfinteracting dark matter*, *Phys. Rev. D* **66** (2002) 063002, [hep-ph/0111381].

[214] W. G. Vincenti and C. H. Kruger, *Introduction to physical gas dynamics*. 1965.

[215] B. Colquhoun, S. Heeba, F. Kahlhoefer, L. Sagunski and S. Tulin, *Semiclassical regime for dark matter self-interactions*, *Phys. Rev. D* **103** (2021) 035006, [2011.04679].

[216] M. Kaplinghat, S. Tulin and H.-B. Yu, *Dark Matter Halos as Particle Colliders: Unified Solution to Small-Scale Structure Puzzles from Dwarfs to Clusters*, *Phys. Rev. Lett.* **116** (2016) 041302, [1508.03339].

[217] L. Darmé, A. Hryczuk, D. Karamitros and L. Roszkowski, *Forbidden frozen-in dark matter*, *JHEP* **11** (2019) 159, [1908.05685].

[218] E. Braaten and D. Segel, *Neutrino energy loss from the plasma process at all temperatures and densities*, *Phys. Rev. D* **48** (1993) 1478–1491, [hep-ph/9302213].

[219] H. Eberl, I. D. Gialamas and V. C. Spanos, *Gravitino thermal production revisited*, *Phys. Rev. D* **103** (2021) 075025, [2010.14621].

[220] V. S. Rychkov and A. Strumia, *Thermal production of gravitinos*, *Phys. Rev. D* **75** (2007) 075011, [hep-ph/0701104].

[221] A. Strumia, *Thermal production of axino Dark Matter*, *JHEP* **06** (2010) 036, [1003.5847].

[222] M. J. Baker, M. Breitbach, J. Kopp and L. Mittnacht, *Dynamic Freeze-In: Impact of Thermal Masses and Cosmological Phase Transitions on Dark Matter Production*, *JHEP* **03** (2018) 114, [1712.03962].

[223] S. Biondini and J. Ghiglieri, *Freeze-in produced dark matter in the ultra-relativistic regime*, *JCAP* **03** (2021) 075, [2012.09083].

[224] A. Davidson, *$b-l$ as the fourth color within an $\mathrm{SU}(2)_L \times \mathrm{U}(1)_R \times \mathrm{U}(1)$ model*, *Phys. Rev. D* **20** (Aug, 1979) 776–783.

[225] R. N. Mohapatra and R. E. Marshak, *Local B-L Symmetry of Electroweak Interactions, Majorana Neutrinos and Neutron Oscillations*, *Phys. Rev. Lett.* **44** (1980) 1316–1319.

[226] A. Davidson and K. C. Wali, *Universal seesaw mechanism?*, *Phys. Rev. Lett.* **59** (Jul, 1987) 393–395.

[227] A. Biswas, S. Choubey and S. Khan, *Galactic gamma ray excess and dark matter phenomenology in a $U(1)_{B-L}$ model*, *JHEP* **08** (2016) 114, [1604.06566].

[228] A. Biswas and A. Gupta, *Freeze-in Production of Sterile Neutrino Dark Matter in U(1)$_{\rm B-L}$ Model*, *JCAP* **09** (2016) 044, [1607.01469].

[229] A. Biswas, S. Choubey and S. Khan, *Neutrino mass, leptogenesis and FIMP dark matter in a* $\mathrm{U}(1)_{B-L}$ *model*, *Eur. Phys. J. C* **77** (2017) 875, [1704.00819].

[230] P. Fileviez Pérez, C. Murgui and A. D. Plascencia, *Neutrino-Dark Matter Connections in Gauge Theories*, *Phys. Rev. D* **100** (2019) 035041, [1905.06344].

[231] M. Gell-Mann, P. Ramond and R. Slansky, *Complex Spinors and Unified Theories*, *Conf. Proc. C* **790927** (1979) 315–321, [1306.4669].

[232] R. N. Mohapatra and G. Senjanovic, *Neutrino Mass and Spontaneous Parity Nonconservation*, *Phys. Rev. Lett.* **44** (1980) 912.

[233] J. Schechter and J. W. F. Valle, *Neutrino Decay and Spontaneous Violation of Lepton Number*, *Phys. Rev. D* **25** (1982) 774.

[234] V. Brdar, A. J. Helmboldt, S. Iwamoto and K. Schmitz, *Type-I Seesaw as the Common Origin of Neutrino Mass, Baryon Asymmetry, and the Electroweak Scale*, *Phys. Rev. D* **100** (2019) 075029, [1905.12634].

[235] Super-Kamiokande collaboration, Y. Fukuda et al., *Evidence for oscillation of atmospheric neutrinos*, *Phys. Rev. Lett.* **81** (1998) 1562–1567, [hep-ex/9807003].

[236] SNO collaboration, Q. R. Ahmad et al., *Direct evidence for neutrino flavor transformation from neutral current interactions in the Sudbury Neutrino Observatory*, *Phys. Rev. Lett.* **89** (2002) 011301, [nucl-ex/0204008].

[237] G. L. Fogli, E. Lisi, A. Marrone, A. Palazzo and A. M. Rotunno, *Neutrino masses and neutrino mixing*, *Nucl. Phys. B Proc. Suppl.* **155** (2006) 5–9.

[238] K2K collaboration, M. H. Ahn et al., *Indications of neutrino oscillation in a 250 km long baseline experiment*, *Phys. Rev. Lett.* **90** (2003) 041801, [hep-ex/0212007].

[239] A. Dutta Banik, R. Roshan and A. Sil, *Neutrino mass and asymmetric dark matter: study with inert Higgs doublet and high scale validity*, *JCAP* **03** (2021) 037, [2011.04371].

[240] A. Datta, R. Roshan and A. Sil, *Scalar Triplet Flavor Leptogenesis with Dark Matter*, 2110.03914.

[241] M. Escudero, S. J. Witte and N. Rius, *The dispirited case of gauged U(1)$_{B-L}$ dark matter*, *JHEP* **08** (2018) 190, [1806.02823].

[242] T. Basak and T. Mondal, *Constraining Minimal $U(1)_{B-L}$ model from Dark Matter Observations*, *Phys. Rev. D* **89** (2014) 063527, [1308.0023].

[243] S. Bhattacharya, N. Chakrabarty, R. Roshan and A. Sil, *Multicomponent dark matter in extended $U(1)_{B-L}$: neutrino mass and high scale validity*, *JCAP* **04** (2020) 013, [1910.00612].

[244] N. Okada and O. Seto, *Higgs portal dark matter in the minimal gauged $U(1)_{B-L}$ model*, *Phys. Rev. D* **82** (2010) 023507, [1002.2525].

[245] S. Khalil and O. Seto, *Sterile neutrino dark matter in B - L extension of the standard model and galactic 511-keV line*, *JCAP* **10** (2008) 024, [0804.0336].

[246] O. Seto and T. Shimomura, *Signal from sterile neutrino dark matter in extra $U(1)$ model at direct detection experiment*, *Phys. Lett. B* **811** (2020) 135880, [2007.14605].

[247] Q. Decant, J. Heisig, D. C. Hooper and L. Lopez-Honorez, *Lyman-α constraints on freeze-in and superWIMPs*, 2111.09321.

[248] J. C. Montero and V. Pleitez, *Gauging U(1) symmetries and the number of right-handed neutrinos*, *Phys. Lett. B* **675** (2009) 64–68, [0706.0473].

[249] A. Hook, E. Izaguirre and J. G. Wacker, *Model Independent Bounds on Kinetic Mixing*, *Adv. High Energy Phys.* **2011** (2011) 859762, [1006.0973].

[250] LHC Higgs Cross Section Working Group collaboration, D. de Florian et al., *Handbook of LHC Higgs Cross Sections: 4. Deciphering the Nature of the Higgs Sector*, 1610.07922.

[251] M. E. Carrington, *Effective potential at finite temperature in the standard model*, *Phys. Rev. D* **45** (Apr, 1992) 2933–2944.

[252] D. Comelli and J. R. Espinosa, *Bosonic thermal masses in supersymmetry*, *Phys. Rev. D* **55** (1997) 6253–6263, [hep-ph/9606438].

[253] PandaX collaboration, H. Zhang et al., *Dark matter direct search sensitivity of the PandaX-4T experiment*, *Sci. China Phys. Mech. Astron.* **62** (2019) 31011, [1806.02229].

[254] T. Robens and T. Stefaniak, *LHC Benchmark Scenarios for the Real Higgs Singlet Extension of the Standard Model*, *Eur. Phys. J. C* **76** (2016) 268, [1601.07880].

[255] M. Carena, A. Daleo, B. A. Dobrescu and T. M. P. Tait, *Z' gauge bosons at the Tevatron*, *Phys. Rev. D* **70** (2004) 093009, [hep-ph/0408098].

[256] G. Cacciapaglia, C. Csaki, G. Marandella and A. Strumia, *The Minimal Set of Electroweak Precision Parameters*, *Phys. Rev. D* **74** (2006) 033011, [hep-ph/0604111].

[257] A. Das, P. S. B. Dev, Y. Hosotani and S. Mandal, *Probing the minimal $U(1)_X$ model at future electron-positron colliders via the fermion pair-production channel*, 2104.10902.

[258] MAGIC, Fermi-LAT collaboration, M. L. Ahnen et al., *Limits to Dark Matter Annihilation Cross-Section from a Combined Analysis of MAGIC and Fermi-LAT Observations of Dwarf Satellite Galaxies*, *JCAP* **02** (2016) 039, [1601.06590].

[259] L. Bian, X. Liu and K.-P. Xie, *Probing superheavy dark matter with gravitational waves*, 2107.13112.

[260] M. A. McLaughlin, *The North American Nanohertz Observatory for Gravitational Waves*, *Class. Quant. Grav.* **30** (2013) 224008, [1310.0758].

[261] R. M. Shannon et al., *Gravitational waves from binary supermassive black holes missing in pulsar observations*, *Science* **349** (2015) 1522–1525, [1509.07320].

[262] M. Kramer and D. J. Champion, *The European Pulsar Timing Array and the Large European Array for Pulsars*, *Class. Quant. Grav.* **30** (2013) 224009.

[263] G. Hobbs et al., *The international pulsar timing array project: using pulsars as a gravitational wave detector*, *Class. Quant. Grav.* **27** (2010) 084013, [0911.5206].

[264] LISA collaboration, P. Amaro-Seoane et al., *Laser Interferometer Space Antenna*, 1702.00786.

[265] LIGO Scientific, Virgo collaboration, B. P. Abbott et al., *Search for the isotropic stochastic background using data from Advanced LIGO's second observing run*, *Phys. Rev. D* **100** (2019) 061101, [1903.02886].

[266] A. Biswas, S. Choubey and S. Khan, *FIMP and Muon $(g-2)$ in a $U(1)_{L_\mu - L_\tau}$ Model*, *JHEP* **02** (2017) 123, [1612.03067].

[267] H. Okada, Y. Orikasa and Y. Shoji, *Radiative dark matter and neutrino masses from an alternative U(1) B-L gauge symmetry*, *JCAP* **07** (2021) 006, [2102.10944].

[268] H. Banerjee, P. Byakti and S. Roy, *Supersymmetric gauged $U(1)_{L_\mu - L_\tau}$ model for neutrinos and the muon $(g-2)$ anomaly*, *Phys. Rev. D* **98** (2018) 075022, [1805.04415].

[269] CHARM-II collaboration, D. Geiregat et al., *First observation of neutrino trident production*, *Phys. Lett. B* **245** (1990) 271–275.

[270] CCFR collaboration, S. R. Mishra et al., *Neutrino tridents and W Z interference*, *Phys. Rev. Lett.* **66** (1991) 3117–3120.

[271] W. Altmannshofer, S. Gori, M. Pospelov and I. Yavin, *Neutrino Trident Production: A Powerful Probe of New Physics with Neutrino Beams*, *Phys. Rev. Lett.* **113** (2014) 091801, [1406.2332].

[272] COHERENT collaboration, D. Akimov et al., *Observation of Coherent Elastic Neutrino-Nucleus Scattering*, *Science* **357** (2017) 1123–1126, [1708.01294].

[273] I. M. Shoemaker, *Coherent search strategy for beyond standard model neutrino interactions*, *Phys. Rev. D* **95** (Jun, 2017) 115028.

[274] J. Liao and D. Marfatia, *Coherent constraints on nonstandard neutrino interactions*, *Physics Letters B* **775** (2017) 54–57.

[275] T. Araki, S. Hoshino, T. Ota, J. Sato and T. Shimomura, *Detecting the $L_\mu - L_\tau$ gauge boson at belle ii*, *Phys. Rev. D* **95** (Mar, 2017) 055006.

[276] M. Abdullah, J. B. Dent, B. Dutta, G. L. Kane, S. Liao and L. E. Strigari, *Coherent elastic neutrino nucleus scattering as a probe of a z' through kinetic and mass mixing effects*, *Phys. Rev. D* **98** (Jul, 2018) 015005.

[277] ATLAS Collaboration collaboration, G. Aad, B. Abbott, J. Abdallah, S. Abdel Khalek, O. Abdinov, R. Aben et al., *Measurements of four-lepton production at the z resonance in pp collisions at $\sqrt{s} = 7$ and 8 tev with atlas*, *Phys. Rev. Lett.* **112** (Jun, 2014) 231806.

[278] CMS collaboration, S. Chatrchyan et al., *Observation of Z Decays to Four Leptons with the CMS Detector at the LHC*, JHEP **12** (2012) 034, [1210.3844].

[279] ATLAS, CMS collaboration, G. Aad et al., *Measurements of the Higgs boson production and decay rates and constraints on its couplings from a combined ATLAS and CMS analysis of the LHC pp collision data at $\sqrt{s} = 7$ and 8 TeV*, JHEP **08** (2016) 045, [1606.02266].

[280] S. N. Gninenko and N. V. Krasnikov, *The Muon anomalous magnetic moment and a new light gauge boson*, Phys. Lett. B **513** (2001) 119, [hep-ph/0102222].

[281] S. Baek, N. G. Deshpande, X. G. He and P. Ko, *Muon anomalous g-2 and gauged L(muon) - L(tau) models*, Phys. Rev. D **64** (2001) 055006, [hep-ph/0104141].

[282] Muon g-2 collaboration, B. Abi et al., *Measurement of the Positive Muon Anomalous Magnetic Moment to 0.46 ppm*, Phys. Rev. Lett. **126** (2021) 141801, [2104.03281].

[283] J. Schechter and J. W. F. Valle, *Neutrino masses in su(2) $\bigotimes$ u(1) theories*, Phys. Rev. D **22** (Nov, 1980) 2227–2235.

[284] S. Patra, S. Rao, N. Sahoo and N. Sahu, *Gauged $U(1)_{L_\mu - L_\tau}$ model in light of muon $g-2$ anomaly, neutrino mass and dark matter phenomenology*, Nucl. Phys. B **917** (2017) 317–336, [1607.04046].

[285] A. Biswas, S. Choubey and S. Khan, *Neutrino Mass, Dark Matter and Anomalous Magnetic Moment of Muon in a $U(1)_{L_\mu - L_\tau}$ Model*, JHEP **09** (2016) 147, [1608.04194].

[286] M. Laine and A. Vuorinen, *Basics of Thermal Field Theory*, vol. 925. Springer, 2016, 10.1007/978-3-319-31933-9.

[287] H. K. Dreiner, H. E. Haber and S. P. Martin, *Two-component spinor techniques and Feynman rules for quantum field theory and supersymmetry*, Phys. Rept. **494** (2010) 1–196, [0812.1594].